Omid Emadinia

Micro hot embossing of metallic reinforced powders

A dissertation to the fulfilment of doctorate degree in

Advanced Materials and Processing

Supervisor: Professor Manuel Fernando Gonçalves Vieira

Co-supervisor: Professor Maria Teresa Freire Vieira

Porto, June 2018

U.PORTO
FEUP FACULDADE DE ENGENHARIA
UNIVERSIDADE DO PORTO

If one does know to which port one is sailing, no wind is favourable.

Lucius Annaeus Seneca

Abstract

Metal matrix nanocomposites are important advanced materials that benefit from the properties of nanoreinforcements, e.g. high modulus and strength of carbon nanotubes or graphene nanosheets. Powder metallurgy processing routes are attractive due to their low energy consumption and avoidance of possible reactions in liquid states; these are also considered as near net shape processes. Micro hot embossing is a recently adapted technique for producing metallic components. Similar to powder injection moulding it involves preparing a proper feedstock (powder-binder mixture), shaping, debinding and sintering. The nanoreinforcements can be added to the metal powder before feedstock preparation and the shaping can be carried out under uniaxial pressure in an elastomer die. Thus, micro hot embossing is more acceptable than powder injection moulding for the production of low series and less complex geometries.

In this study, aluminium and 316L stainless steel powders, with or without 1 vol.% multiwalled carbon nanotubes, were used for feedstock preparation. Feedstock characteristics are a fundamental aspect in metal powder shaping since optimized feedstocks can ensure shape replicability. The conditions for optimization of feedstocks preparation depends on powder concentration and additives (stearic acid or multiwalled carbon nanotubes). Torque rheometer mixing technique is used for the determination of the critical powder volume concentration and the homogeneity of the prepared feedstock. The presence of nanotubes in the feedstocks ensures homogeneity as well. Shaping geometries with similar aspect ratios is dependent on whether they are convex or concave. Plastic deformation of elastomer die greatly influences roughness, dimensions, and reproducibility. When the elastomer is replaced by a more rigid one or a metallic die, microgear geometry and a microwall feature are produced, respectively. The sensibility to segregation in the metallic die is reduced by changing the shaping conditions.

Thermal debinding in a flowing Ar-H_2 atmosphere resulted in a perfect shape retention; however, it seemed to leave some residues. Oxidation of Al powder was attributed to the thermal cycle rather than the binder decomposition. Aluminium was sintered at the most feasible sintering temperature by high vacuum application (up to 640 °C and $< 5\times10^{-3}$ Pa). The porosities and presence of nanotube aggregates contributed to the shrinkage level, and the strengthening effect was not attained. Unlike Ar-H_2 atmosphere, a high vacuum can overcome the porosity of the low compacted powder during sintering. Moreover, the grain size of pressed and sintered Al was dependent on the compaction pressure. This sintering method was also able to densify micro hot embossed 316L powders, whose microfeatures were preserved perfectly

after sintering. The composition of the sintered part was equal to the pristine powder and the microtensile test showed an ultimate strength and ductility equivalent to a bulk alloy. Carbon nanotubes were not observed but they led to a lower carbide formation in the microstructure.

As a case study, the dispersion of different reinforcements (multiwalled carbon nanotube, graphene nanosheets, nanoalumina and ultrafine tungsten carbide) was evaluated in the aluminium powder. Raman spectroscopy revealed that the sonication technique assisted by ultrasonication was the best technique for dispersing the carbon nanotubes. The presence of powder during an equal mixing procedure introduced structural defects to the nanotubes. This study also indicates that, for identical volume portions and an equal processing route, the Al-WC was hardened the most, increasing the yield strength, ultimate tensile and flexural strength of the matrix. These achievements were attributed to the $Al_{12}W$ phase formation. However, this composite did not show a good wear abrasive resistance.

Resumo

Os nanocompósitos de matriz metálica são importantes materiais avançados que beneficiam das propriedades únicas dos nanoreforços como, por exemplo, o elevado módulo de elasticidade e resistência mecânica de nanotubos de carbono ou nanofolhas de grafeno. As técnicas de pulverometalurgia são atrativas porque requerem um baixo consumo energético e evitam reações que poderiam ocorrer no estado líquido; além disso, estas técnicas são consideradas como processos que produzem peças com forma próxima da final. A microgravação a quente é uma técnica recentemente adaptada à produção de componentes metálicos. Esta técnica é semelhante à moldação por injeção de pós metálicos e envolve a preparação de uma mistura de pó metálico com um ligante, a conformação por microgravação, a remoção do ligante e a sinterização. Os nanoreforços podem ser adicionados ao pó metálico antes da mistura e a conformação pode ser feita simplesmente comprimindo uniaxialmente a mistura em uma matriz de silicone. Com estas condições, a microgravação a quente é mais adequada do que a moldação por injeção para a produção de pequenas series de components com geometrias pouco complexas.

Neste trabalho foram preparadas misturas com pós de alumínio e de aço inoxidável 316L. Algumas destas misturas foram reforçadas com 1 vol.% de nanotubos de carbono. As caraterísticas das misturas são determinantes na conformação sendo a replicação da forma pretendida assegurada pelas misturas otimizadas. As condições ótimas para a preparação das misturas dependem das concentrações de pó metálico e de aditivos (ácido esteárico e nanotubos de carbono). A reometria de binário foi a técnica utilizada para a otimização da mistura, em particular, para a determinação do volume crítico de pó metálico e da homogeneidade da mistura. A presença de nanotubos de carbono nas misturas facilita a homogeneidade da mistura. A conformação de componentes com razões de aspeto semelhantes depende da sua forma ser côncava ou convexa. A deformação plástica da matriz de silicone influencia fortemente a rugosidade, dimensões e reprodutibilidade dos componentes. A utilização de matrizes metálicas ou silicones mais rígidos permite a produção de formas mais complexas, como micro paredes ou micro engrenagens, respetivamente. Na matriz metálica, a sensibilidade para a segregação foi reduzida ajustando as condições de conformação.

A remoção térmica do ligante em uma atmosfera de árgon hidrogenado permitiu uma perfeita retenção da forma mas não conseguiu eliminar todos os resíduos do ligante. Foi observada oxidação do alumínio que resulta do ciclo térmico de remoção do ligante e não da sua

decomposição. A sinterização do alumínio só foi conseguida a temperaturas muito próximas do ponto de fusão e em alto vácuo (até 640 ºC e < 5×10^{-3} Pa). A utilização de árgon hidrogenado na sinterização não permitiu eliminar a porosidade em pós compactados com baixa pressão de compactação na etapa da microgravação dos pós de alumínio; esta pressão mostrou ser determinante no mecanismo de densificação durante a sinterização dos pós de alumínio. Durante a sinterização, a contração foi determinada pelas porosidades e pelos agregados de nanotubos. Não foi detetado nenhum aumento da resistência mecânica associado à presença dos nanoreforços. A sinterização em alto vácuo também se mostrou eficaz na densificação de componentes obtidos por microgravação a quente de pós de aço inoxidável 316L tendo sido perfeitamente preservados os microdetalhes. A composição do aço não se alterou no processo de microgravação e microprovetes de tração exibem uma resistência à tração e uma ductilidade semelhante à do material maciço. Os nanotubos de carbon não foram observados após sinterização mas induzem uma menor formação de carbonetos/óxidos.

Como caso de estudo complementar a este trabalho foi avaliada a dispersão em pós de alumínio de diferentes reforços (nanotubos de carbono, nanofolhas de grafeno, nanoalumina e carboneto de tungsténio ultrafino). A análise por espectroscopia Raman mostrou que a ultrassonicação assistida por banho de ultrassons foi a técnica mais eficiente na dispersão dos nanotubos de carbono. No entanto, se a técnica for utilizada na presença do pó metálico são introduzidos defeitos estruturais nos nanotubos. Este estudo também indica que, utilizando a mesma fração volúmica de reforço e o mesmo processamento, o carboneto de tungsténio ultrafino foi o reforço que mais aumentou a resistência mecânica da matriz. Este endurecimento foi associado à formação da fase $Al_{12}W$. No entanto, e apesar do aumento da dureza, este compósito não revelou uma boa resistência ao desgaste.

Acknowledgements

I appreciate Fundação para a Ciência e a Tecnologia for the scholarship to accomplish the tasks of my PhD during last four years.

Many sincere and wholehearted thanks go to my supervisor, Professor Manuel Gonçalves Vieira, for his supervision, supporting me in my academic life, and being available at any time to answer my questions and commenting without any stress. I also thank him for all the freedom he provided me, allowing me to follow my own path and to grow enormously both as a researcher and human being, especially when I faced struggles with debinding and sintering and he provided facilities and supported me to overcome the difficulties.

I am very grateful to work under the supervision of Professor Maria Teresa Freire Vieira for her support during this period, for sharing ideas and discussions, especially for the edition time during which she commuted from Coimbra to Porto.

I thank Dr Elsa Sequeiros at DEMM/FEUP and Dr Telma Ferreira at IPN in Coimbra, they showed me how to do micro hot embossing and how to prepare feedstock for the first time. Thanks to Eng. Claudia Lopes for teaching me how to run the equipment needed at DEMM. Thanks to CEMUP for microscopy analyses, especially Eng. Rui Rocha for his assistance and comments, it was a great opportunity and I will not forget that. In addition, CEMMPRE for TEM availability and the help of Dr Sonia Simões and Dr Ruben Santos to acquire TEM images; Eng. Carlos Patacas at IPN for topography analyses; Dr Jorge Ferreira at LNEG for XRD analysis; Eng. Fernando Barbosa for die preparation at Cinfu; Dr André Cavaleiro at INEGI for elastomer die preparations. I also thank Professor Filomena Viana for her helpful comments.

Many thanks to my beloved wife, Laleh, and my lovely daughter, Mandana, for their understandings. My father, Masoud, and my mother, Parvaneh, whose support were endless even from far distances, I also thank my brothers, Arash and Ashkan.

I like to appreciate the welcoming of Portuguese society, FEUP community, especially DEMM staff, and I thank anyone who helped me to progress and fulfil my goals. I will not forget my friends, for their positive talks.

Omid Emadinia

Porto

24th June 2018

Table of Contents

List of Figures

List of Tables

List of Abbreviations and Symbols

Abbreviations

AISI – American Iron and Steel Institute

CNT – Carbon Nanotube

CPVC – Critical Powder Volume Concentration

EBSD – Electron Backscattered Diffraction

EDS – Energy Dispersive Spectroscopy

ICDD – International Centre for Diffraction Data

ICSD – Inorganic crystal Structure Database

IPF – Inverse pole figure

MMC – Metal Matrix Composites

MWCNT – Multiwall or Multiwalled, Multi-Wall, or Multi-Walled Carbon Nanotube

µPIM – Micro Powder Injection Moulding

OM – Optical Microscopy

PIM – Powder Injection Moulding

PM – Powder Metallurgy

PSD – Particle Size Distribution

rpm – rotation per minute

SA – Stearic Acid

SEM – Scanning Electron Microscopy

TEM – Transmission electron Microscopy

TGA – Thermal Gravimetric Analysis

UTS – Ultimate Tensile Strength

XRD – X-Ray Diffraction

YS – Yield Strength

µMIM – Micro Metal Injection Moulding

Symbols

316L – low carbon stainless steel alloy

Al – Aluminium

Al_2O_3 – Aluminium oxide or alumina

Al_4C_3 – Aluminium carbide

M1 – Commercial binder

min – Minute(s)

μ – Micron

P Pressure

S – Seconds

T – Temperature

T – Time

vol.% – Volume percentage

wt.%– Weight percentage

θ – Bragg angle

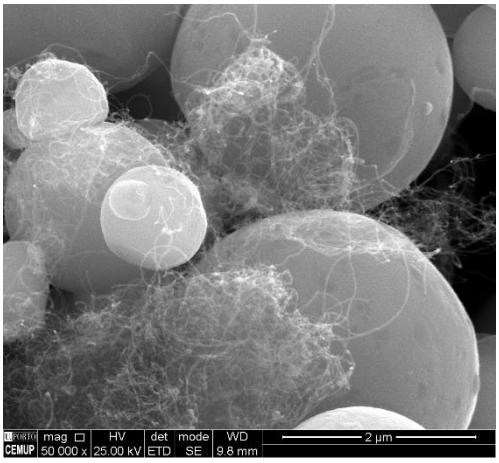

Chapter 1 – Metallic nanocomposites in micropowder hot embossing process

1.1 Introduction

Powder metallurgy (PM) is an interesting processing approach for producing metal matrix composites (MMC). A related study reported the production of 30% MMC through PM approach between 2005 and 2015 [1]. This study also indicates that PM techniques can reduce the challenges faced during machining MMCs. There is also a great expectation regarding the industrialization of MMCs, such as aluminium matrix composites [2], and any study highlighting the potential of PM applications for composite production is welcomed. PM involves mixing the constituents, shape forming and sintering, this is sometimes followed by post processing, like hot isostatic pressing. PM technologies can produce near-net-shape parts with simple to complex geometries, by compacting and sintering, (micro)powder injection moulding ((µ)PIM), micro hot embossing or selective laser melting, etc. Each technique has a specific field of application. The first technique is suitable for producing simple geometries. The second one is used for large series of small pieces with complex shapes and features up to submillimetre scale [3-7]. Micro hot embossing metal powders, which was adapted from a well-known micromoulding process of polymeric parts, can be useful for the production of small series of less complex forms at low cost, due to the inexistence of mould [8, 9]. In this technique, shaping is carried out using a compression machine assembled with a heating system. This technology is easy to process, is not expensive and can be a solution for different parts/systems. Moreover, a feedstock similar to what is used for PIM is needed, this is a mixture of inorganic powders with a binder, the powder can be a metal, a ceramic or a composite. Production of

multi-layered components starting with a material and ending with other can also be considered for future applications.

The production of MMCs based on aluminium, copper, magnesium, titanium, iron, and nickel was reported [10-16], using different reinforcement composition and particle size (micro or nanoscale). In the last two decades, the tendency has been towards using nano reinforcements due to their unusual properties. These reinforcements are normally intermetallic compounds, ceramics or carbon allotropes [17, 18]. The use of carbon allotropes nanoparticles, such as carbon nanotubes (CNT) or Graphene nanosheets, is widely reported because of their extraordinary strength and stiffness [19-22]. However, nanoparticles tend to agglomerate which reduces the mechanical properties of the composite [23-25], for example, CNTs agglomerate strongly due to the intrinsic Van der Waals forces [26] (Figure 1.1a and 1.1b). Nevertheless, there is a hypothesis that PM can outpace casting approach because the flotation tendency and the week wettability of the reinforcements are high in the molten bath [21].

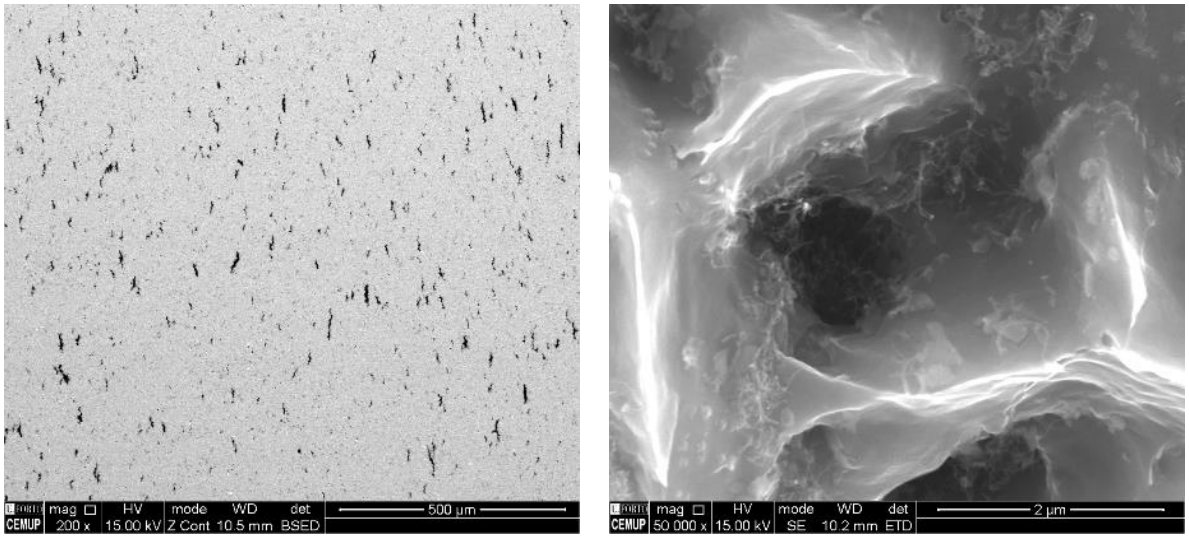

(a) (b)

Figure 1.1 *Electron microscopy images from the MWCNT agglomerations observed on the cross section (a) and fracture surface of a tensile specimen (b) (Al with D_{50} of 10 µm with 1.00 vol.% MWCNT (0.75 wt.% MWCNT[1]) compacted at ~300 MPa and sintered at 640 ºC in high vacuum for 2h).*

For this study, pure aluminium (Al) and an austenitic stainless steel (AISI 316L) were selected, representing nonferrous and ferrous metals with low carbon content, respectively. The former has a low melting temperature (660 ºC), while latter melts at a temperature more than two times

[1] The measured densities of these Al and MWCNT powders are 2670 kg/m^3 and 2013 kg/m^3, respectively.

higher (1390 – 1440 °C). These metals have good workability and corrosion resistance, due to the crystalline structures and the stability of the intrinsic oxide layers. There are many publications on the reinforcement of Al matrix, while a few studies have stated this effect for 316L stainless steel. On the contrary, many studies have reported the production, characterization and use of AISI 316L feedstock, while few highlighted the production of Al parts through feedstock processing. In this regard, no study reported the micro hot embossing of metal matrix composite feedstocks with micro or nanoscale reinforcements; in particular, a study using multiwalled carbon nanotubes (MWCNT) dispersed in a feedstock, as the metal-reinforcement mixture, can add value to this micromanufacturing technique.

1.2 Dissertation structure

This dissertation is organized as follows:

- State of the art on the reinforcing of pure Al by MWCNT or Graphene nanosheets through PM techniques, reinforcing of AISI 316L matrix through PM, feedstock preparation in pure Al, and Al and 316L composites, and finally shaping, debinding and sintering.
- Materials and techniques: this chapter presents and characterizes all the input materials, techniques and methodologies for processing and measuring properties.
- Feedstock preparation includes: optimisation of the feedstocks for Al and 316L powders, preparation and characterization of feedstocks, dispersion and homogeneity evaluation and correlation of torque values with feedstock composition (concentrations of metal powder, MWCNT and stearic acid additive).
- Shaping green specimens: the highlighted topics include the replicability evaluation (shape retention and surface roughness) affected by different geometries, the feedstock characteristics, such as particulate size and composition, and the die assembly. It is also emphasized the evaluation of green specimens homogeneity that is affected by the feedstock composition or processing conditions. The capability of micro hot embossing through changing the shaping methodology (e.g. sequences of pressure application or using metallic die) is also discussed.
- The chapter on thermal debinding and sintering of Al and 316L green specimens analyse the debinding, densification, replicability, hardness and phase evolution in parts affected by the processing conditions, composition and MWCNT. The effect of powder compaction is also evaluated.
- Comparative study with other reinforcements: this chapter presents how the dispersion of MWCNT with the as purchased Al powder was a challenge, it also shows how the combination of mixing techniques can function. Dispersion and strengthening of Al with graphene nanosheets, nanoalumina and ultrafine tungsten carbide will also be analysed.
- Conclusions and future works.

1.3 State of the art

This section reviews the state of the art concerning the mixing methods and hardening of pure Al by multiwalled carbon nanotube (MWCNT) and Graphene nanosheets, this also summarizes the effect of carbon allotropes or ceramic reinforcements on AISI 316L stainless steel powder. The processing of these advanced materials through (μ)PIM or micro hot embossing is also summarized.

1.3.1 Mixing pure aluminium with MWCNT or Graphene nanosheets

Aluminium is used as alloy and composite for structural, automotive and aeronautic applications, presenting attractive high-specific stiffness [12, 27, 28]. Reinforcing pure Al is very interesting because the ductile matrix can provide workability [29], no heat treatment is needed, and the realization of the strengthening mechanism, in the absence of any phase formation by alloying elements, is easier. Table 1.1 presents some properties of a commercial pure Al.

Table 1.1 Properties of commercially high pure Al (99.8% purity) at room temperature in the annealed condition [30].

Density ($kg.m^{-3}$)	**Modulus of elasticity (GPa)**	**Yield stress (YS) at 0.2% offset (MPa)**	**Tensile strength (TS) (MPa)**	**Elongation (%)**	**Melting temperature (°C)**
2699	62	20	60	45	660.4

As above mentioned, the strengthening of pure Al through the application of MWCNT or Graphene nanosheets is widely reported (some examples are listed in Table 1.2) [21, 22, 31-34]. Some authors highlighted the increase of the tensile strength of pure Al which is influenced by processing conditions [35-38]; however, this increase is generally reported at the expense of ductility (Figure 1.2) [21, 39, 40]. The usage of MWCNT and Graphene was also reported for creating self-lubricating Al matrix [41].

The load transferring is the most recognized strengthening mechanism, as this is emphasized in Table 1.2. Meanwhile, the association of the nanotube aspect ratio with strengthening is also suggested: the larger the aspect ratio of the nanotube, the higher the strengthening potential [42], however, the chance of entanglement of CNTs also increases [43]. The same table also highlights that the ball milling has been used the most for dispersing the constituents. There are

also other techniques such as magnetic stirring, ultrasonication bath, sonication probe or ultra-dispersing. Moreover, the polyester binder assisted, and in-situ formation methods were reported as well [18, 21, 44, 45]. A solution treatment is sometimes used to increase the surface interaction of CNT or Graphene with metal powder. This is carried out through a liquid media, e.g. stablishing a superficial bonding between CNTs and powder surface, so called functionalization. This uses an acid treatment, and it is sometimes followed by electroless plating of a metallic ion on the CNTs [46-49]. Functionalization resulted in the formation of a carboxyl group (-COOH) on the CNTs surfaces through which the wettability increases. In this way, the best dispersion is achieved in a hydrophilic media, like polyvinyl alcohol. Electroless deposition is carried out to implant the best dispersed nanotubes among metal powder particles. However, these preparation processes influence the integrity of CNTs, and their defected zones are prone to carbide formation in aluminium matrix [50-53], although this was not always reported [36, 54].

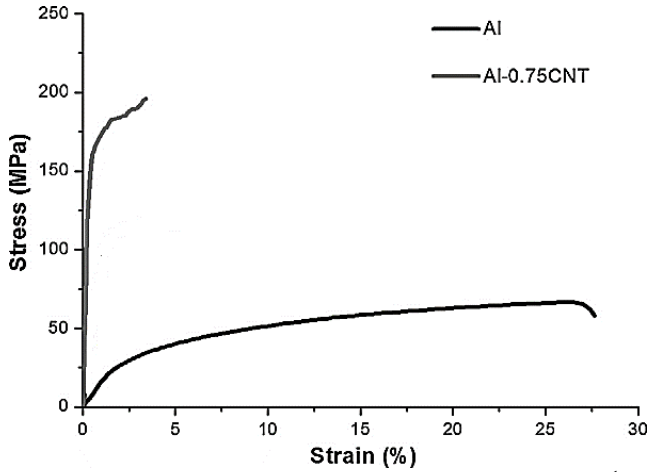

Figure 1.2 *Tensile tests showing the effect of 1.00 vol.% (0.75 wt.% CNT[1]) on strength and ductility (adapted from [40]).*

The integrity evaluation of MWCNTs, in a bulk and non-destructive scale, is carried out by Raman spectroscopy through considering the ratio between the intensities of the defect and graphitic bands (D and G, respectively), I_D/I_G determines the aggressivity of the processing conditions, i.e. the smallest the ratio, the least the damage [51, 55, 56].

Figure 1.3 illustrates the D and G bands of a pristine CNT, and the ball milled one with and without Al powder. It illustrates that in the presence of the powder during milling (CNTs+Al powder) the peaks were broaden, which was attributed to the amorphisation of the nanotubes, and their integrity reduced. Table 1.3 presents the changes of the intensity ratio affected by

some processing conditions, having pristine material as reference. In the same table, it is also seen that the pristine nanotubes have different ratios, which can be attributed to the wavelength of the laser incident beam and the characteristics of the nanotubes, e.g. graphitization, initial defects, level of impurity, and size of the tubes [57-60].

Table 1.2 Summary of studies reporting the composition, dispersing procedures, parameters and strengthening mechanisms of Al-MWCNT and Al-Graphene.

Composition	Dispersing method	Properties	Strengthening mechanism	Reference
0.00 & 1.00 wt.% CNT	Ball milling	Tensile strength	Load transferring	[37]
0.00, 1.00 & 5.00 vol.% CNT (0.00, 0.75 & 3.82 wt.%)[2]	Acid treated & ultrasonication	Tensile strength	Load transferring	[36]
0.00 & 1.00 vol.% CNT (0.00 & 0.75 wt.%)[2]	Ultrasonication	Tensile strength	Load transferring (pulled out CNTs)	[39]
0.00, 1.00, 3.00, 5.00 & 7.00 vol.% CNT (0.00, 0.75, 2.28, 3.82 & 5.37 wt.%)[2] 0.00, 0.30, 0.50 & 0.70 vol.% Graphene (0.00, 0.25, 0.41 & 0.58 wt.%)[2]	Ball milling	Compressive strength	Load transferring	[61]
0.00, 0.50, 1.00, 1.50 & 2.00 wt.% Graphene	Cryomilling	Tensile strength	Direct mechanism Grain refinement & Load transfer	[62]
0.00, 0.25, 0.50 & 1.00 wt.% Graphene	Ultrasonication + ball milling	Hardness & tensile strength - Presence of Al_4C_3	Load transferring & Dislocation strengthening	[63]
0.00, 0.10, 0.50 & 1.00 wt.% Graphene	Ultrasonication + Cryomilling	Hardness & grain size	Grain refinement & Precipitated impurities	[64]
0.00 & 1.00 wt.% Graphene	Stirring and ball milling	Grain size & tensile strength	Dislocation strengthening, Grain refinement & Load transferring	[65]
0.00, 0.10, 0.20, 0.40 & 0.90 wt.% Graphene	Milling, pressing, infiltration	Tensile strength	Load transferring (pulled out sheets)	[66]

[2] Calculated by the rule of mixtures and considering the densities of the Al, CNT and Graphene equal with 2670 kg/m^3, 2013 kg/m^3 and 2200 kg/m^3, respectively.

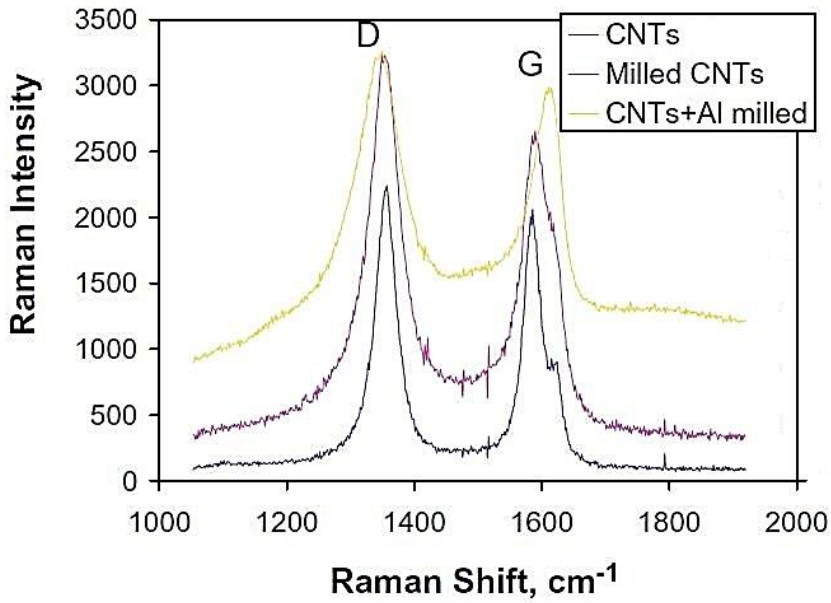

Figure 1.3 *Effect of processing conditions on the integrity of CNTs [51].*

It was already mentioned that AISI 316L stainless steel is interesting for this study, representing a high melting temperature metallic material [67]; the following section presents a general point of view, the types of reinforcements used for strengthening this alloy and the processing conditions applied through PM approach.

Table 1.3 Effect of dispersing techniques on CNTs measured through Raman intensity ratio.

Conditions	**I_D/I_G**	**Ratio increase (%)**	**Reference**
Pristine	0.858	Reference	[45]
Polymer assisted	0.903	5.2	
Low energy ball milled	1.100	28.2	
High energy ball milled	1.608	87.4	
Pristine	1.27	Reference	[68]
Functionalized	1.60	26	
Pristine	1.08	Reference	[40]
Sonicated	1.18	9.3	

1.3.2 AISI 316L stainless steel for composite

The AISI 316L stainless steel is interesting for having a combination of good corrosion and oxidation resistance and mechanical properties. However, corrosion resistance will be affected by the porosity inherited from the powder processing [69, 70]. Some authors [71] highlighted the effect of cooling rate on corrosion resistance, the best result was reported for cooling at 10 °C/min, in comparison with 5 °C/min, and this was attributed to the depletion of Cr for the lowest cooling rate, in addition to this the high cooling rate yielded the highest mechanical properties (Table 1.4). The alloy performance, processed by PIM, is very dependent on the sensitization (formation of chromium carbide, oxide or nitride) which occurs during sintering [72]. The 316L stainless steel parts processed by PM routes, such as PIM, are applied in the automotive, medical, water pipe, chemical processing, aerospace, clock and other industries [67, 69].

Reinforcing AISI 316L alloy is not as common as that of Al, but some studies pointed out an improvement in the properties of the matrix by the addition of micro or nano reinforcements [73-75]. The reinforcements were dispersed using rotary or high energy ball milling, shaped and densified through cold compaction and sintering, PIM or selective laser sintering. With regard to the addition of carbon allotropes, Graphene has not been mentioned so far, and a few studies have reported the interaction of 316L powders and MWCNT. These composites were produced by PIM, pressureless low temperature sintering, or chemical vapor deposition of MWCNT directly into stainless steel pellets [76-78].

Table 1.4 Properties of an AISI 316L processed by PIM and sintered at 1325 °C in high vacuum and cooled at 10 °C/min [71].

Powder loading (vol.%)	Tensile strength (MPa)	Elongation (%)	Hardness (HRB)	Density (%)
65	481	22	76	96

1.3.3 Strengthening mechanisms in nanocomposites

Many studies related to the production of metal matrix nanocomposites reported several factors contributing to matrix strengthening; however, the materials, concentrations of the reinforcements and processing conditions analysed in these studies were different. In a general perspective, the strengthening or stiffening of a metal matrix can be caused directly, or indirectly, by the simultaneous activation of several mechanisms which are difficult to identify

separately [79]. The most commonly reported mechanism involves the transfer of the load by matrix to the stiff reinforcements (e.g. hard ceramic particles); mechanisms including microstructural changes, e.g. interaction of dislocations generated by the thermal mismatch, are also mentioned [80].

It must be emphasised that the high stacking fault energy of aluminium enables the activation of dynamic recovery mechanisms which makes it more difficult to identify the mechanisms of strengthening in Al-CNT composites.

1.3.3.1 Thermal mismatch

The big difference between the thermal expansion coefficients of the constituents (matrix and reinforcement) will result in the generation of dislocations at their interface to accommodate this thermal mismatch, [81, 82], i.e. thermal mismatches occur during solidifications or cooling stages and dislocations are produced through the relaxation of thermal residual stresses (so-called thermal relaxation). This mechanism was also reported for the Al-CNT due to the dominant differences between the Coefficients of Thermal Expansion (CTE) of the Al and the CNT: $23.6*10^{-6}$ K^{-1} and $\sim10^{-6}$ K^{-1}, respectively. It was also indicated that the dislocation density is influenced by the surface area of the reinforcement, i.e. the small diameter of CNT induces a pronounced effect [31].

1.3.3.2 Load transferring

Under a tensile stress, the matrix role is to transfer the load to the reinforcement through the interfacial shear stress, e.g. so-called shear lag model [80]. This model was also suggested for carbon nanotubes, considering their aspect ratio (< 100) and their wettability as important factors for reinforcing [31, 83]. In this model, the interface plays an important role, e.g. in the Al-CNT, the formation of Al_4C_3 at the interface influences the load transferring mechanism [84]. However, this interface can function most effectively if this is formed at the ends of the opened nanotubes [50]. This mechanism cannot be effective when agglomerates exist, since CNTs move and slide over each other. Regarding Al-Graphene composite, a related study reported the load transfer as the strengthening mechanism since no grain refinement and no dislocation density increase were observed in the nanocomposite matrix [85], other authors also agreed on the function of this mechanism in Al-MWCNT and Al-Graphene composites (Table 1.2).

1.3.3.3 Orowan mechanism

When reinforcements in a matrix are strong, fine and closely spaced enough to obstacle dislocations movements, this mechanism is activated [86]; for the same volume fraction of nanoparticles, the relative contribution of the Orowan strengthening effect increases as the nanoparticles size decreases to a critical particle size (typically of the order of 2.0 nm) [87]. A related study indicates that the looped dislocations will generate a back stress through which the movement of other dislocations are inhibited and the yield stress increases [31].

1.3.3.4 Grain refinement

When there is a large enough content of reinforcements, grain growth is hindered by the interaction of grain boundaries with the dispersed reinforcements, which contributes to the strength by the Hall-Petch formula. The grain size in a metal matrix is dependent on the proportion of the solid particle radius over the volume fraction in the matrix, so-called Zener formula [82, 88]. Some authors (Table 1.2) reported the grain refinement as the strengthening mechanism of a copper matrix [89].

1.3.4 Shaping the nanocomposite powders

The simplest technique to perform powder shaping is to compact it in a die. However, this method is limited to simple geometries, such as disks or small plates. Feedstock preparation facilitates the powder shaping into complex configurations. In this process, the mouldability of a shape is dependent on powder concentration in the feedstock. In the following, it is highlighted for Al and 316L composites how the best compositions were determined and the composites that have been processed by PIM or hot-embossing.

1.3.4.1 Feedstock preparation for the (µ)PIM or micro hot embossing

For producing green specimens, the feedstock constituents must be correctly mixed [4, 90]. Shaping can be done using (µ)PIM or µhot embossing processes and reinforcements can be added to the mixture. Injecting temperature and shear stress rate should be adjusted to allow a perfect injection without the segregation of the powder and binder, mould clogging, or any other defects; in addition, the feedstock composition should also assure a proper viscosity [91, 92]. These conditions are evaluated through the analyses of rheological properties before shaping [93, 94]. The most acceptable feedstock preparation method involves finding a proper amount of metal powder for the feedstock, this quantity is based on a critical powder volume

concentration (CPVC) at which feedstock finds an infinite relative viscosity (being the relative viscosity defined as the viscosity of the feedstock in relation to the viscosity of the binder) and shows no fluidity [91, 92]. The proper powder concentration should be slightly smaller than the CPVC, in this way the maximum packing density is ensured [95]. The CPVC determination has been reported through indirect or direct approaches. In the first one, feedstocks with different powder concentrations are prepared and their rheological behaviour or the replicability of the produced components are evaluated [90, 96] thus, the best powder concentration is selected. The second approach involves finding the absolute value of CPVC prior to producing any component. This value is determined through different techniques: binder thermal softening by a torque mixer equipment (Figure 1.4a) and plotting the torque mixing values (Figure 1.4b) against the powder concentrations (Figure 1.4c), CPVC is the volume at which the slope of the torque growth increases suddenly (the star inset in Figure 1.4c) [97, 98]; torque mixing by an oil absorption approach and plotting the torque values versus the corresponding powder concentrations [99]; rheological properties such as flow activation energy and plotting the powder concentrations against the levels of energy [100, 101]; other rheological properties such as shear viscosity and shear rate obtained by capillary rheometer [95, 98, 102].

Since the torque mixer equipment (Plastisizer) consumes the least possible material and this is more friendly to be analysed, this technique was used to determine the CPVC values and the optimal feedstocks for this study [97]. Related studies with micro hot embossing have reported the feedstock preparation based on the optimisation process [103-105].

Regarding the material characteristics, rather than the processing conditions, the CPVC value is affected by several factors such as binder composition [98, 105, 106], particle size distribution (PSD), and powder shape [91, 107-109]. Some authors have indicated that the CPVC decreases when the PSD diminishes (due to the viscosity increase), and this will rise when the powder shape becomes almost spherical [91]. These conclusions are not supported by the results of other authors who showed that it was not possible to establish a general trend (Table 1.5) [109].

Table 1.5 Effect of PSD and atomization routes on the CPVC values.

PSD (μm)	3		8		11		20	
Atomizing route	Gas	Water	Gas	Water	Gas	Water	Gas	Water
CPVC (vol.%)	67	68	66	70	70	66	70	66

(a)

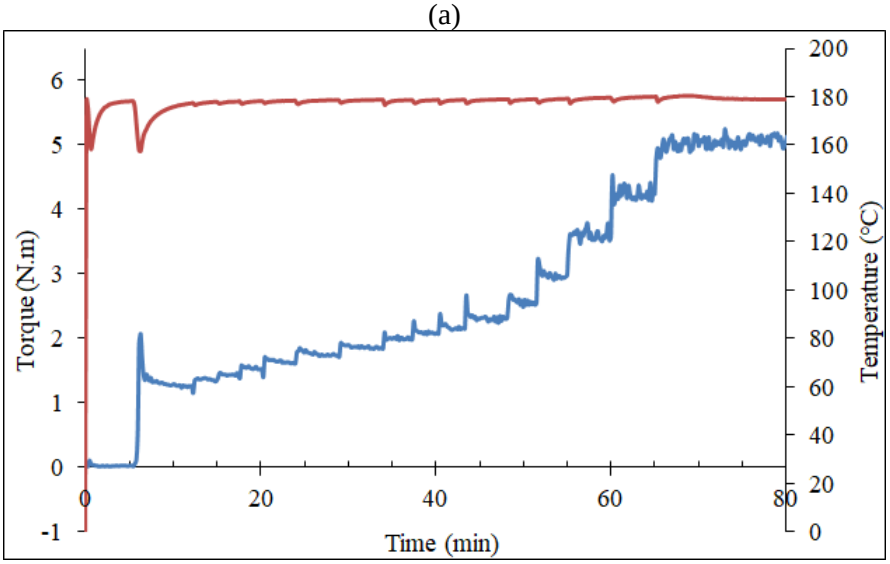

(b)

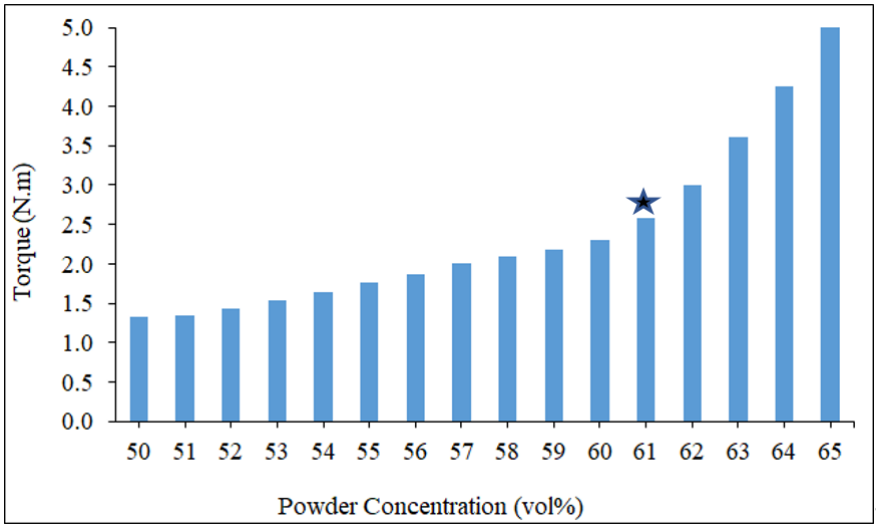

(c)

Figure 1.4 *Torque mixer equipment (Plasticizer) used for the optimisation process and feedstock preparation (a); torque evolution against time (b), torque changes versus powder concentration (c) for a 316L stainless steel powder mixed with a commercialized binder system mixed at 30 rpm and 175 °C, during the incremental addition of the powder to the torque mixing chamber.*

The homogeneity of prepared feedstocks should be evaluated in order to ensure the production of a perfect part. This could be attained by the analyses of torque evolution versus time during mixing preparation, supported by scanning electron microscopy (SEM). The latter technique benefits the effect of atomic mass differences of the constituents through backscattered electron beam in SEM/BSE [94]. In the approach of the torque graph, it is assumed that the homogeneity of feedstock is achieved when the torque variations reach a steady state. However, this is affected by binder composition [98, 110], mixing speed and time, and powder concentration [94, 111, 112].

1.3.4.2 Feedstock preparation for nanocomposites

There are many studies about AISI 316L feedstock preparation and characterization (for example [94, 110, 113]); however, this number is quite small for Al and metal matrix micro/nanocomposites [99, 114-121]. The usage of a polymer, such as polyester, was reported to facilitate the dispersion of CNTs among Al powders, being strengthened more efficiently than a ball milling dispersing route [45]; this method is not expected to deteriorate the dispersion of the nanoreinforcements through feedstock preparation. A related study reported the best composition for an Al feedstock, through plotting the viscosity against shear rate for several temperatures [99, 101].

Regarding Al composites, the effect of SiC, AlN and Al_2O_3 reinforcements (at micron and nanoscale ranges) were reported [101, 122-127]. Nevertheless, none of these studies discussed the effect of adding reinforcements on the feedstock homogeneity and on the rheological properties. The 316L composite feedstocks with TiC, TiCN, Si_3N_4 (at micro size), and nano Al_2O_3 were reported [73, 93, 128-130]. One study indicated that, for specific conditions of shear rate, powder loading and temperature, the replicability of the 316L-TiC feedstock can be better than that of the 316L, that was explained by the reduction of the viscosity of the composite feedstock justified by the effectiveness of the binder material after the addition of ceramic particles [93]. Other related studies, through capillary rheometer measurement, reported the viscosity increase for iron and copper feedstocks with Fe-0.20 wt.% CNT and Cu-2.50 vol.% CNT (Cu-0.57 wt.% CNT)[3] concentrations, respectively, in these feedstocks the production of perfect green specimens was achieved by increasing the injection pressure to overcome the viscosity increase [115, 118, 131]. Assuming that the torque mixing value indicates the

[3] Calculated by the rule of mixtures and considering the densities of the Cu and CNT equal to 8930 kg/m^3, and 2013 kg/m^3, respectively.

viscosity, the addition of 10 vol.% stearic acid (SA) to the AISI 316L-CNT feedstock reduced the torque by 50%, thus facilitating the injection [132-134]; however, this addition could change the thermal debinding conditions due to the SA degradation.

1.3.4.3 Micro hot embossing/(μ)PIM of Al powder and the Al and AISI 316L composite feedstocks

Shaping a feedstock to a configuration is well carried out through (μ)PIM, even for high series production [3, 7, 135]. Despite needing expensive equipment and mould [136], (μ)PIM is still attractive for new developments [137]. However, for low series production, less complex parts and short lifespan components micro hot embossing can be a good alternative since it needs less expensive equipment and die assembly [9, 138, 139].

The production of components with micro or nanoreinforced composites has been reported, in some cases such as tensile test specimen made of 316L feedstocks with micro size TiC, Si_3N_4 and nanoalumina by PIM [73, 129, 130], and microgear made of 316L-nanoalumina through microsoft moulding technique [140]. The production of few geometries, e.g. small disks, thin walled parts, rectangular blocks, gear, or tensile test specimens with Al, Al-SiC, Al-nanoalumina and Al-AlN, through PIM, was also described [114, 120-122, 127, 141]. Related studies with micro hot embossing reported the use of a silicon wafer as die for replicating 316L pins (with 100*200 μm features) [9]; other authors proceeded this micromanufacturing technique using an elastomer die and they showed the replication of some microgeometries such as: a set of Cu blocks (with 200*200 μm in width and height) [142]; convex and concave circle-like structures, and interconnected walls and channels (Figure 1.5a to 1.5d) made of Fe-Ni, WC-Co, 316L and Cu [96, 143]; concave and convex hemispherical-like specimens (Figures 1.5e and 1.5f) of 316L [144, 145]. Moreover, the failure of a micro hot embossed gear specimen was reported [146].

Studies reported the replicability (shape retention and surface roughness) being affected by critical conditions such as pressure [90, 96, 103, 144, 146], temperature [9, 90, 96, 103, 104, 112, 143, 145], and holding time [9, 103, 143, 145, 147], e.g. the higher the pressure and temperature, the less the surface roughness and the better the replicability. The replicability may be attributed to the pseudoplastic flow behavior and mouldability of the feedstock, being affected through micro hot embossing conditions [105, 112]. These assessments were carried out by viscosity measurements, obtained with a capillary rheometer through which a torque is applied.

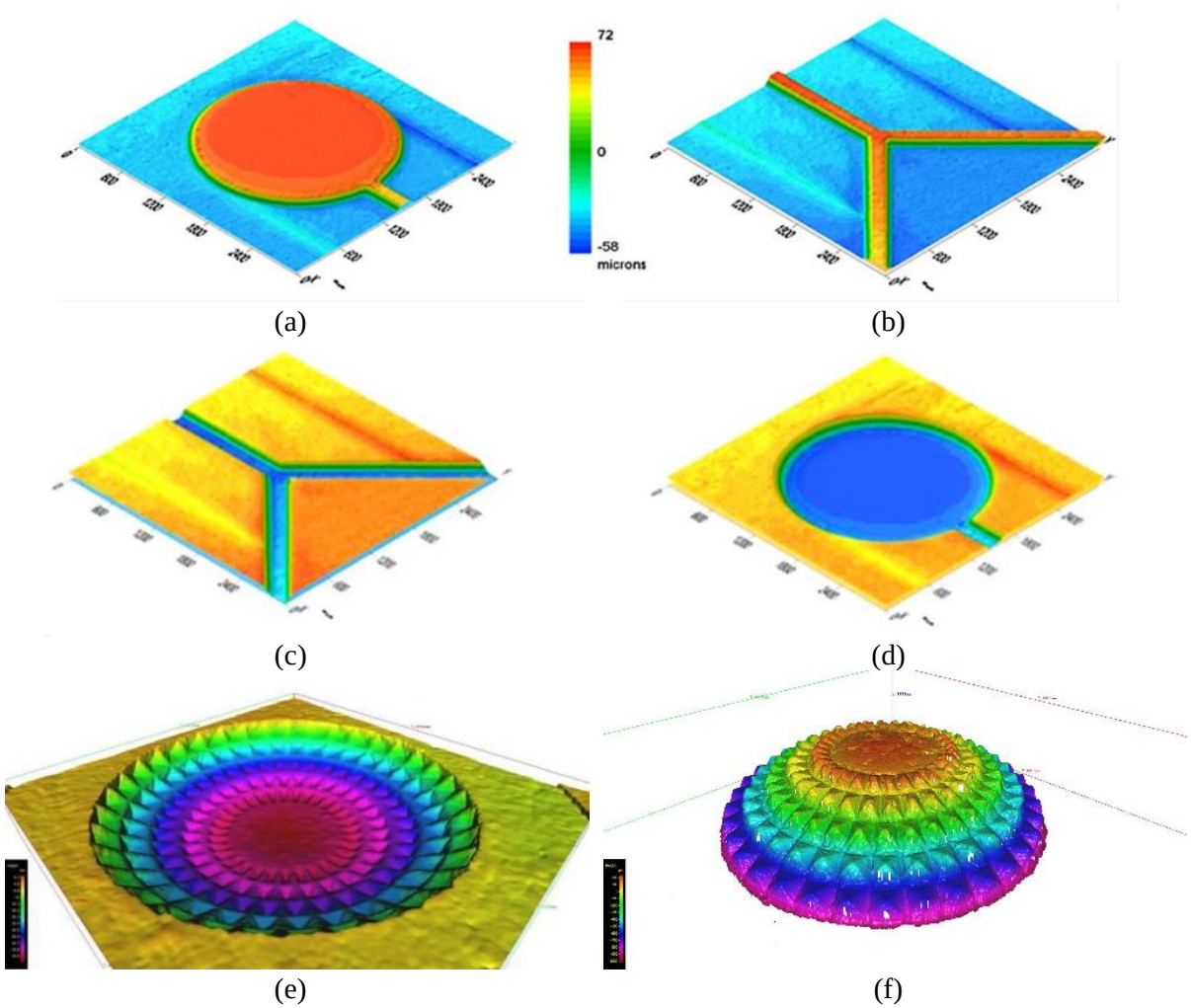

Figure 1.5 *IFM images from micro hot embossed specimens (a) to (d) convex and concave circle-like and interconnected structures [96, 143] (the circles with 2000*100 µm in diameter and height, and the channels with 100*100 µm in width and height); (e) concave and (f) convex hemispherical-like geometry with features of 100 µm [139, 144].*

1.3.5 Debinding and sintering Al and Al micro/nanocomposite mixtures

Sintering is a vital process in PM to realize a component and this is carried out in (µ)PIM or micro hot embossing processes after debinding. So far, no study has reported the sintering of Al specimens produced by micro hot embossing. A few studies reported the sintering of aluminium [114, 116, 121, 148], and premixed Al powder with AlN, SiC and nanoalumina [122, 123, 125, 127, 141, 149], processed by PIM. These studies used a two-step debinding approach, first solvent and then thermal, to decompose the binder material of green specimens (to produce brown parts). The debinding initiated by dissolving binder in hexane or heptane (6

to 48 hours depending on the specimen size), followed by heating in a high-purity nitrogen (N_2) atmosphere (with holding times up to 20 hours, and various flowing rates of N_2, 1 to 10 L/min). Then the brown specimens were sintered at different temperatures (620 °C to 740 °C[4]) and different holding times (from half an hour to two hours) in N_2 atmosphere. The formation of AlN as the by-product of the sintering atmosphere, and the usage of Sn and Mg to increase the sintering efficiency were reported as well.

A great problem about sintering Al is attributed to the presence of the Al oxide superficial layer; this film acts as a barrier to the diffusion of Al atoms to the neighbouring particles which makes sintering difficult. The effective disruption of the oxide layer can be brought about by the use of a high purity N_2 atmosphere since at high temperature and extremely low oxygen partial pressure in N_2, the AlN phase is thermodynamically more stable than the Al_2O_3 [150]. The application of high vacuum ($<10^{-3}$ Pa) can be an alternative to increase the sinterability without the formation of intermediate phases in the Al matrix, for example AlN compound [151]. Using high concentration Hydrogen atmosphere for sintering can cause the diffusion of hydrogen in Al [152, 153].

Table 1.6 presents the conditions to obtain the best results for Al composites, produced by PIM. One study justified the strengthening by preventing the dislocation movement by the nanoalumina particles [127]. The shrinkage and density were influenced by the addition of the reinforcement, e.g. a density decrease in the Al-nanoalumina composite was reported. The effectiveness of increasing the sintering temperature was also highlighted.

1.3.6 Sintering the AISI 316L micro/nanocomposite mixtures after debinding

There are plenty of studies about sintering 316L powder after debinding, being processed by (μ)PIM or micro hot embossing [9, 104, 144, 154, 155]. A few studies reported the processing of the stainless steel composites through PIM or soft moulding [73, 128-130, 140], being reinforced with TiC, TiC(N), ultrafine or nanoscale Alumina, and Si_3N_4 particles. These studies reported different debinding approaches, e.g. thermal debinding in Argon or N_2-10%H_2, dissolution in water or heptane followed by thermal debinding in vacuum or H_2. Sintering was carried out at temperatures between 1050 °C and 1405 °C for 60, 90 or 120 minutes, in the same atmosphere used for the thermal debinding step. Optimised mechanical properties and the

[4] Although the authors mentioned sintering, but this should involve a liquid phase densification.

highest density was reported through sintering in Argon-Hydrogen atmosphere although the shrinkage for the longitudinal direction was larger than other directions [156]. Another study reports the effectiveness of the N_2 atmosphere, over the Argon, considering the increase of the tensile strength and hardness of the 316L alloy after sintering [157]; however, a difference of 75 °C in the sintering temperature is observed between these two studies.

Table 1.6 Selected aspects of some studies reporting the production of Al matrix composite by PIM.

Reinforcement/Feedstock composition	**Dispersing method**	**Behaviour of sintered component**	**Reference**
30.00 vol.% SiC_p (33.04 wt.%)[5], in 52 & 55 vol.% powder concentration	Attrition milling	Hardness and density increased by increasing the sintering temperature (740 °C) and powder concentration.	[125]
10.00 vol.% SiC (11.34 wt.%)[4], in 55 vol.% powder concentration	Ball milling	Not a significant difference in wear resistance.	[141]
0.00, 3.00, 6.00 & 9.00 wt.% nanoalumina, in 54 & 60 vol.% powder concentration	Ball milling	Best mechanical properties obtained at 6% by 54 vol.% powder concentration.	[127, 149]
10.00 wt.% AlN, in 61 vol.% powder concentration	Turbula mixer	Best properties at the highest sintering temperature (640 °C).	[122]

Table 1.7 presents the compositions, mixing techniques to prepare the 316L-reinforcement mixture and the feedstock, and the conditions ended up to the best results. The improvement of the properties was attributed to the increase of the sintering temperature. The reinforcement content did not ensure the increase of all properties, e.g. reductions of density and wear resistance. However, it was reported that the addition of the Si_3N_4 increased the relative density, with respect to the non-reinforced specimen. That can be attributed to the dissolution of the Si_3N_4 and the formation of a low melting temperature phase [130].

Near net-shape production processes require shape retention and sometime controlling the surface roughness, and this becomes very important for micromanufacturing. These evaluations

[5] Calculated according to the rule of mixtures based on the density values indicated in reference [142].

were carried out by light stereoscopy, SEM equipment [158] and 3D topography measurements [112, 147, 155, 159] such as infinite focus or confocal microscopies.

As regards the MWCNT, the stability of this carbon allotrope was attested at high temperature in a high rich Argon atmosphere [160]; however, some structural changes were reported by heating in high vacuum [161].

Table 1.7 Selected aspects of some studies reporting the production of AISI 316L matrix composite through powder processing, like PIM.

Reinforcement/Feedstock compositions	**Dispersing method**	**Best results obtained by:**	**Reference**
0.00, 5.00 & 10.00 wt.% Si_3N_4, in 55 vol.% powder concentration	Milling	Increasing temperature (1350 °C) and 5% Si_3N_4	[130]
2.50 & 5.00 wt.% nanoalumina, in 60 vol.% powder concentration	Turbula mixer	Increasing temperature and time (1405 °C 2h), 5% for HV, 2.5% for UTS, Wear resistance reduction	[129]
2.50, 5.00, 7.50 & 10.00 wt.% ultrafine alumina	Stirring the slurry	10% for HV Gave the poorest density	[140]
3.00 wt.% TiC & TiCN, in 62.5% powder concentration	Turbula mixer	Increasing temperature (1385 °C) Except hardness all properties reduced	[128]
3.00 & 5.00 wt.% TiC; in 53, 55, 56 wt.% powder concentration	Blade mixer	Increasing temperature (1350 °C) and heating rate (10 °C/min) 3% TiC by 53%	[73]

1.4 Summary

Powder metallurgy is reliable to produce metal matrix nanocomposites. The constituents can be dispersed with or without using any assisting environment such as alcohol or a polymer mixture, although the last one is needed to produce complex shapes and microgeometries. The micro or nanoreinforcements may be mixed with metal powder prior to adding binder. Carbon nanotubes and Graphene nanosheets are strongly affected through ball milling and/or functionalization, and in the Al matrix their defected zones are prone to form carbides. Nanocomposite properties are influenced by several factors: chemical composition, size, morphology, volume fraction, distribution and structure of the nanoreinforcement; interface of the nanoreinforcement and matrix; porosity; and the thermomechanical history of the material. There is a strong agreement upon the load transferring as the strengthening mechanism of Al matrices by MWCNT and Graphene nanosheets.

Successful sintering of Al was reported in a N_2 atmosphere; however, there was a chance of AlN formation. Application of low-pressure for Al and 316L powder can eliminate the possibility of phase formation and give rise to a good densification. For 316L powder, this atmosphere can cause the superficial depletion of Cr due to evaporation. This problem can be removed by finishing process. After sintering, a high cooling rate is suggested for 316L steel to prevent sensitization.

The feedstock properties and behaviours depend on the powder characteristics. Meanwhile, the addition of MWCNT should have a pronounced influence on the feedstock, and replicability is expected to decrease when the feedstock viscosity increases. The stability of MWCNT during thermal debinding and sintering is essential to ensure the reinforcement of the matrix, this is particularly critical for the 316 L matrix. The hypothesis of having an accumulated porosity after sintering can affect final properties, this can be caused by the agglomeration of the nanoparticles and the PM processing heritage. These porosities may influence the dimensional and surface roughness as well.

References:

[1] P.S. Bains, S.S. Sidhu, H.S. Payal, **Materials and Manufacturing Processes**, **31** (2016) 553-573, 10.1080/10426914.2015.1025976.

[2] A. Schmidt, S. Siebeck, U. Götze, G. Wagner, D. Nestler, **Metals**, **8** (2018) 143, 10.3390/met8020143.

[3] Z.Y. Liu, N.H. Loh, S.B. Tor, K.A. Khor, Y. Murakoshi, R. Maeda, T. Shimizu, **Journal of Materials Processing Technology**, **127** (2002) 165-168, 10.1016/s0924-0136(02)00119-x.

[4] H.Z. Ye, X.Y. Liu, H.P. Hong, **Journal of Materials Processing Technology**, **200** (2008) 12-24, 10.1016/j.jmatprotec.2007.10.066.

[5] U.M. Attia, J.R. Alcock, **Journal of Micromechanics and Microengineering**, **21** (2011) 10.1088/0960-1317/21/4/043001.

[6] V. Piotter, 13 - Micro metal injection molding (MicroMIM) A2 - Heaney, Donald F, Handbook of Metal Injection Molding, Woodhead Publishing2012, pp. 307-337.

[7] D.F. Heaney, C.D. Greene, 6 - Molding of components in metal injection molding (MIM), Handbook of Metal Injection Molding, Woodhead Publishing2012, pp. 109-133e.

[8] M. Heckele, W.K. Schomburg, **Journal of Micromechanics and Microengineering**, **14** (2004) R1-R14, 10.1088/0960-1317/14/3/r01.

[9] G. Fu, S. Tor, N. Loh, D. Hardt, **Applied Physics A: Materials Science & Processing**, **97** (2009) 925-931, 10.1007/s00339-009-5363-3.

[10] S.F. Moustafa, Z. Abdel-Hamid, A.M. Abd-Elhay, **Materials Letters**, **53** (2002) 244-249, 10.1016/s0167-577x(01)00485-2.

[11] A. Paesano, C.K. Matsuda, J.B.M. da Cunha, M.A.Z. Vasconcellos, B. Hallouche, S.L. Silva, **Journal of Magnetism and Magnetic Materials**, **264** (2003) 264-274, 10.1016/s0304-8853(03)00215-4.

[12] J.M. Torralba, C.E. da Costa, F. Velasco, **Journal of Materials Processing Technology**, **133** (2003) 203-206, 10.1016/s0924-0136(02)00234-0.

[13] K. Kondoh, T. Threrujirapapong, H. Imai, J. Umeda, B. Fugetsu, **Composites Science and Technology**, **69** (2009) 1077-1081, 10.1016/j.compscitech.2009.01.026.

[14] M.K. Habibi, S.P. Joshi, M. Gupta, **Acta Materialia**, **58** (2010) 6104-6114, 10.1016/j.actamat.2010.07.028.

[15] K. Chu, Q.Y. Wu, C.C. Jia, X.B. Liang, J.H. Nie, W.H. Tian, G.S. Gai, H. Guo, **Composites Science and Technology**, **70** (2010) 298-304, 10.1016/j.compscitech.2009.10.021.

[16] M.K. Habibi, A.M.S. Hamouda, M. Gupta, **Composites Science and Technology**, **72** (2012) 290-298, 10.1016/j.compscitech.2011.11.015.

[17] F. He, Ceramic nanoparticles in metal matrix composites, Ceramic Nanocomposites, Woodhead Publishing2013, pp. 185-207.

[18] R. Casati, M. Vedani, **Metals**, **4** (2014) 65-83, 10.3390/met4010065.

[19] B.G. Demczyk, Y.M. Wang, J. Cumings, M. Hetman, W. Han, A. Zettl, R.O. Ritchie, **Materials Science and Engineering a-Structural Materials Properties Microstructure and Processing**, **334** (2002) 173-178, 10.1016/s0921-5093(01)01807-x.

[20] C. Lee, X. Wei, J.W. Kysar, J. Hone, **science**, **321** (2008) 385-388, 10.1126/science.1157996.

[21] S.R. Bakshi, D. Lahiri, A. Agarwal, **International Materials Reviews**, **55** (2010) 41-64, 10.1179/095066009x12572530170543.

[22] A. Nieto, A. Bisht, D. Lahiri, C. Zhang, A. Agarwal, **International Materials Reviews**, **62** (2017) 241-302, 10.1080/09506608.2016.1219481.

[23] C.F. Deng, D.Z. Wang, X.X. Zhang, A.B. Li, **Materials Science and Engineering a-Structural Materials Properties Microstructure and Processing**, **444** (2007) 138-145, 10.1016/j.msea.2006.08.057.

[24] M.F. Ashby, P.J. Ferreira, D.L. Schodek, Nanomaterials: Properties, Nanomaterials, Nanotechnologies and Design, Butterworth-Heinemann, Boston, 2009, pp. 199-255.

[25] M.K. Akbari, H.R. Baharvandi, K. Shirvanimoghaddam, **Materials & Design**, **66** (2015) 150-161, 10.1016/j.matdes.2014.10.048.

[26] L. Vaisman, H.D. Wagner, G. Marom, **Advances in Colloid and Interface Science**, **128** (2006) 37-46, 10.1016/j.cis.2006.11.007.

[27] J.C. Williams, E.A. Starke, **Acta Materialia**, **51** (2003) 5775-5799, 10.1016/j.actamat.2003.08.023.

[28] D.K. Koli, G. Agnihotri, R. Purohit, **Materials Today-Proceedings**, **2** (2015) 3032-3041, 10.1016/j.matpr.2015.07.290.

[29] Fundamentals of aluminium metallurgy Production, processing and applications, Woodhead Publishing Limited, Cambridge CB21 6AH, UK, 2011.

[30] Properties and Selection: Nonferrous Alloys and Special Purpose Materials, 10th ed., ASM International.

[31] R. George, K.T. Kashyap, R. Raw, S. Yamdagni, **Scripta Materialia**, **53** (2005) 1159-1163, 10.1016/j.scriptamat.2005.07.022.

[32] A.M.K. Esawi, K. Morsi, A. Sayed, A.A. Gawad, P. Borah, **Materials Science and Engineering a-Structural Materials Properties Microstructure and Processing**, **508** (2009) 167-173, 10.1016/j.msea.2009.01.002.

[33] Z. Hu, G. Tong, D. Lin, C. Chen, H. Guo, J. Xu, L. Zhou, **Materials Science and Technology**, **32** (2016) 930-953, 10.1080/02670836.2015.1104018.

[34] Z. Baig, O. Mamat, M. Mustapha, **Critical Reviews in Solid State and Materials Sciences**, **43** (2018) 1-46, 10.1080/10408436.2016.1243089.

[35] H. Kwon, D.H. Park, J.F. Silvain, A. Kawasaki, **Composites Science and Technology**, **70** (2010) 546-550, 10.1016/j.compscitech.2009.11.025.

[36] H. Kurita, H. Kwon, M. Estili, A. Kawasaki, **Materials Transactions**, **52** (2011) 1960-1965, 10.2320/matertrans.M2011146.

[37] B. Chen, K. Kondoh, H. Imai, J. Umeda, M. Takahashi, **Scripta Materialia**, **113** (2016) 158-162, 10.1016/j.scriptamat.2015.11.011.

[38] B. Chen, J. Shen, X. Ye, H. Imai, J. Umeda, M. Takahashi, K. Kondoh, **Carbon**, **114** (2017) 198-208, 10.1016/j.carbon.2016.12.013.

[39] B. Boesl, D. Lahiri, S. Behdad, A. Agarwal, **Carbon**, **69** (2014) 79-85, 10.1016/j.carbon.2013.11.061.

[40] S. Simões, F. Viana, M.A.L. Reis, M.F. Vieira, **Composite Structures**, **108** (2014) 992-1000, 10.1016/j.compstruct.2013.10.043.

[41] A.D. Moghadam, E. Omrani, P.L. Menezes, P.K. Rohatgi, **Composites Part B-Engineering**, **77** (2015) 402-420, 10.1016/j.compositesb.2015.03.014.

[42] A.M.K. Esawi, K. Morsi, A. Sayed, M. Taher, S. Lanka, **Composites Part a-Applied Science and Manufacturing**, **42** (2011) 234-243, 10.1016/j.compositesa.2010.11.008.

[43] A.M.K. Esawi, K. Morsi, A. Sayed, M. Tahera, S. Lanka, **Composites Science and Technology**, **70** (2010) 2237-2241, 10.1016/j.compscitech.2010.05.004.

[44] T. Noguchi, A. Magario, S. Fukazawa, S. Shimizu, J. Beppu, M. Seki, **Materials Transactions**, **45** (2004) 602-604, 10.2320/matertrans.45.602.

[45] J.Z. Liao, M.J. Tan, **Powder Technology**, **208** (2011) 42-48, 10.1016/j.powtec.2010.12.001.

[46] L. Jiang, G.L. Fan, Z.Q. Li, X.Z. Kai, D. Zhang, Z.X. Chen, S. Humphries, G. Heness, W.Y. Yeung, **Carbon**, **49** (2011) 1965-1971, 10.1016/j.carbon.2011.01.021.

[47] B. Abbasipour, S.M. Monirvaghefi, B. Niroumand, **Metals and Materials International**, **18** (2012) 1015-1021, 10.1007/s12540-012-6014-3.

[48] A. Maqbool, F.A. Khalid, M.A. Hussain, N. Bakhsh, Synthesis of copper coated carbon nanotubes for aluminium matrix composites, in: S. Qaisar, A.N. Khan, E.A. Mukhtar (Eds.) 13th International Symposium on Advanced Materials2014.

[49] S.-H. Joo, S.C. Yoon, C.S. Lee, D.H. Nam, S.H. Hong, H.S. Kim, **Journal of Materials Science**, **45** (2010) 4652-4658, 10.1007/s10853-010-4382-y.

[50] L.J. Ci, Z.Y. Ryu, N.Y. Jin-Phillipp, M. Ruhle, **Acta Materialia**, **54** (2006) 5367-5375, 10.1016/j.actamat.2006.06.031.

[51] D. Poirier, R. Gauvin, R.A.L. Drew, **Composites Part A: Applied Science and Manufacturing**, **40** (2009) 1482-1489, https://doi.org/10.1016/j.compositesa.2009.05.025.

[52] R.P. Bustamante, M.M. Yoshida, R.M. Sánchez, J.B. Martinez, J.G. Cantu, **Microscopy and Microanalysis**, **18** (2012) 1914, 10.1017/S1431927612011427.

[53] V.T. Pham, V.A. Nguyen, H.T. Bui, D.C. Le, V.C. Nguyen, V.L. Nguyen, D.P. Doan, N.M. Phan, **Advances in Natural Sciences-Nanoscience and Nanotechnology**, **4** (2013) 10.1088/2043-6262/4/2/025015.

[54] D.S. Li, Y. Ye, X.J. Liao, Q.H. Qin, **Nano Research**, **11** (2018) 1642-1650, 10.1007/s12274-017-1779-9.

[55] M.A. Pimenta, G. Dresselhaus, M.S. Dresselhaus, L.G. Cancado, A. Jorio, R. Saito, **Physical Chemistry Chemical Physics**, **9** (2007) 1276-1291, 10.1039/b613962k.

[56] S. Costa, E. Borowiak-Palen, M. Kruszynska, A. Bachmatiuk, R.J. Kalenczuk, **Materials Science-Poland**, **26** (2008) 433-441.

[57] L.G. Cancado, K. Takai, T. Enoki, M. Endo, Y.A. Kim, H. Mizusaki, A. Jorio, L.N. Coelho, R. Magalhaes-Paniago, M.A. Pimenta, **Applied Physics Letters**, **88** (2006) 10.1063/1.2196057.

[58] R.A. DiLeo, B.J. Landi, R.P. Raffaelle, **Journal of Applied Physics**, **101** (2007) 10.1063/1.2712152.

[59] R. Saito, M. Hofmann, G. Dresselhaus, A. Jorio, M.S. Dresselhaus, **Advances in Physics**, **60** (2011) 413-550, 10.1080/00018732.2011.582251.

[60] Y.C. Choi, K.I. Min, M.S. Jeong, **Journal of Nanomaterials**, (2013) 10.1155/2013/615915.

[61] S.E. Shin, H.J. Choi, J.Y. Hwang, D.H. Bae, **Scientific Reports**, **5** (2015) 10.1038/srep16114.

[62] J.L. Li, Y.C. Xiong, X.D. Wang, S.J. Yan, C. Yang, W.W. He, J.Z. Chen, S.Q. Wang, X.Y. Zhang, S.L. Dai, **Materials Science and Engineering a-Structural Materials Properties Microstructure and Processing**, **626** (2015) 400-405, 10.1016/j.msea.2014.12.102.

[63] G. Li, B. Xiong, **Journal of Alloys and Compounds**, **697** (2017) 31-36, https://doi.org/10.1016/j.jallcom.2016.12.147.

[64] M. Tabandeh-Khorshid, J.B. Ferguson, B.F. Schultz, C.-S. Kim, K. Cho, P.K. Rohatgi, **Materials & Design**, **92** (2016) 79-87, https://doi.org/10.1016/j.matdes.2015.12.007.

[65] S.J.N. Kumar, R. Keshavamurthy, M.R. Haseebuddin, P.G. Koppad, **Transactions of the Indian Institute of Metals**, **70** (2017) 605-613, 10.1007/s12666-017-1070-5.

[66] W. Yang, Q. Zhao, L. Xin, J. Qiao, J. Zou, P. Shao, Z. Yu, Q. Zhang, G. Wu, **Journal of Alloys and Compounds**, **732** (2018) 748-758, https://doi.org/10.1016/j.jallcom.2017.10.283.

[67] Powder Metal Technologies and Applications, ASM International1998.

[68] V.T. Pham, V.A. Nguyen, H.T. Bui, D.C. Le, V.C. Nguyen, V.L. Nguyen, D.P. Doan, N.M. Phan, **Advances in Natural Sciences: Nanoscience and Nanotechnology**, **4** (2013) 10.1088/2043-6262/4/2/025015.

[69] E. Klar, P.K. Samal, Powder Metallurgy Stainless Steels - Processing, Microstructures, and Properties, **ASM International**.

[70] J. Shankar, A. Upadhyaya, R. Balasubramaniam, **Corrosion Science**, **46** (2004) 487-498, 10.1016/s0010-938x(03)00144-6.

[71] M.R. Raza, F. Ahmad, M.A. Omar, R.M. German, **Journal of Materials Processing Technology**, **212** (2012) 164-170, 10.1016/j.jmatprotec.2011.08.019.

[72] J.M. Torralba, 16 - Metal injection molding (MIM) of stainless steel A2 - Heaney, Donald F, Handbook of Metal Injection Molding, Woodhead Publishing2012, pp. 393-414.

[73] N.H. Loh, S.B. Tor, K.A. Khor, **Journal of Materials Processing Technology**, **108** (2001) 398-407, 10.1016/S0924-0136(00)00855-4.

[74] J. Abenojar, F. Velasco, J.M. Torralba, J.A. Bas, J.A. Calero, R. Marce, **Materials Science and Engineering a-Structural Materials Properties Microstructure and Processing**, **335** (2002) 1-5, 10.1016/s0921-5093(01)01941-4.

[75] S.M. Zhao, X.F. Shen, J.L. Yang, W.H. Teng, Y.Y. Wang, **Optics and Laser Technology**, **103** (2018) 239-250, 10.1016/j.optlastec.2018.01.005.

[76] R.B. Patel, J.W. Liu, J.V. Scicolone, S. Roy, S. Mitra, R.N. Dave, Z. Iqbal, **Journal of Materials Science**, **48** (2013) 1387-1395, 10.1007/s10853-012-6885-1.

[77] M.A. Hussain, A. Maqbool, F.A. Khalid, M.U. Farooq, I.H. Abidi, N. Bakhsh, W. Amin, J.Y. Kim, **Ceramics International**, **41** (2015) 10125-10132, 10.1016/j.ceramint.2015.04.110.

[78] T.J. Ferreira, M.T. Vieira, **Advances in Materials and Processing Technologies**, **3** (2017) 640-650, 10.1080/2374068X.2017.1365281.

[79] J. Singh, A. Chauhan, **Journal of Materials Research and Technology-Jmr&T**, **5** (2016) 159-169, 10.1016/j.jmrt.2015.05.004.

[80] T.W. Clyne, P.J. Withers, An Introduction to Metal Matrix Composites, Cambridge University Press, Cambridge, 1993.

[81] R.J. Arsenault, N. Shi, **Materials Science and Engineering**, **81** (1986) 175-187, 10.1016/0025-5416(86)90261-2.

[82] C.S. Goh, J. Wei, L.C. Lee, A. Gupta, **Acta Materialia**, **55** (2007) 5115-5121, 10.1016/j.actamat.2007.05.032032.

[83] H.J. Choi, G.B. Kwon, G.Y. Lee, D.H. Bae, **Scripta Materialia**, **59** (2008) 360-363, 10.1016/j.scriptamat.2008.04.006.

[84] J.G. Park, D.H. Keum, Y.H. Lee, **Carbon**, **95** (2015) 690-698, 10.1016/j.carbon.2015.08.112.

[85] J.Y. Wang, Z.Q. Li, G.L. Fan, H.H. Pan, Z.X. Chen, D. Zhang, **Scripta Materialia**, **66** (2012) 594-597, 10.1016/j.scriptamat.2012.01.012.

[86] Z. Zhang, D.L. Chen, **Scripta Materialia**, **54** (2006) 1321-1326, 10.1016/j.scriptamat.2005.12.017.

[87] Z. Zhang, D.L. Chen, **Materials Science and Engineering a-Structural Materials Properties Microstructure and Processing**, **483-84** (2008) 148-152, 10.1016/j.msea.2006.10.184.

[88] A. Sanaty-Zadeh, **Materials Science and Engineering a-Structural Materials Properties Microstructure and Processing**, **531** (2012) 112-118, 10.1016/j.msea.2011.10.043.

[89] K. Chu, C.C. Jia, **Physica Status Solidi a-Applications and Materials Science**, **211** (2014) 184-190, 10.1002/pssa.201330051.

[90] M. Sahli, J.C. Gelin, T. Barriere, **Materials Science & Engineering C-Materials for Biological Applications**, **55** (2015) 252-266, 10.1016/j.msec.2015.05.019.

[91] R.K. Enneti, V.P. Onbattuvelli, S.V. Atre, 4 - Powder binder formulation and compound manufacture in metal injection molding (MIM) A2 - Heaney, Donald F, Handbook of Metal Injection Molding, Woodhead Publishing2012, pp. 64-92.

[92] D.F. Heaney, 3 - Powders for metal injection molding (MIM), Handbook of Metal Injection Molding, Woodhead Publishing2012, pp. 50-63.

[93] M. Khakbiz, A. Simchi, R. Bagheri, **Powder Metall.**, **48** (2005) 144-150, 10.1179/003258905x37747.

[94] L. Liu, N.H. Loh, B.Y. Tay, S.B. Tor, Y. Murakoshi, R. Maeda, **Materials Characterization**, **54** (2005) 230-238, 10.1016/j.matcher.2004.11.014.

[95] J.J. Reddy, N. Ravi, M. Vijayakumar, **Journal of the European Ceramic Society**, **20** (2000) 2183-2190, 10.1016/S0955-2219(00)00096-0.

[96] M. Sahli, J.C. Gelin, T. Barriere, **Powder Technology**, **246** (2013) 284-302, 10.1016/j.powtec.2013.05.026.

[97] F.M. Barreiros, M.T. Vieira, **Ceramics International**, **32** (2006) 297-302, 10.1016/j.ceramint.2005.03.006.

[98] X. Kong, C. Quinard, T. Barrière, J.-C. Gelin, **International Journal of Material Forming**, **2** (2009) 709-712, 10.1007/s12289-009-0652-0.

[99] H. Abdoos, H. Khorsand, A.A. Yousefi, **Iranian Polymer Journal**, **23** (2014) 745-755, 10.1007/s13726-014-0268-1.

[100] J.M. Contreras, A. Jimenez-Morales, J.M. Torralba, **Powder Metall.**, **53** (2010) 34-40, 10.1179/003258909x12450768327225.

[101] A. Ghanbari, M. Alizadeh, E. Ghasemi, R.Y. Rad, S. Ghaffari, **Science and Engineering of Composite Materials**, **22** (2015) 549-554, 10.1515/secm-2013-0209.

[102] Y.M.M. Li, L.J.J. Li, K.A. Khalil, **Journal of Materials Processing Technology**, **183** (2007) 432-439, 10.1016/j.jmatprotec.2006.10.039.

[103] E.W. Sequeiros, T.J. Ferreira, M.T. Vieira, M.F. Vieira, **Euro PM 2011**, Barcelona, Spain, 9 - 12 October 2011.

[104] J. Zhang, J.-C. Gelin, M. Sahli, T. Barrière, **Journal of Micro and Nano-Manufacturing**, **1** (2013) 041003, 10.1115/1.4025554.

[105] M. Sahli, J.C. Gelin, **International Journal of Advanced Manufacturing Technology**, **69** (2013) 2139-2148, 10.1007/s00170-013-5170-z.

[106] S. Ahn, S.J. Park, S. Lee, S.V. Atre, R.M. German, **Powder Technology**, **193** (2009) 162-169, 10.1016/j.powtec.2009.03.010.

[107] S.-J. Park, Y. Wu, D.F. Heaney, X. Zou, G. Gai, R.M. German, **Metallurgical and Materials Transactions A**, **40** (2009) 215-222, 10.1007/s11661-008-9690-3.

[108] M. Sotomayor, A. Várez, B. Levenfeld, **Powder Technology**, **200** (2010) 30-36, 10.1016/j.powtec.2010.02.003.

[109] B. Hausnerova, B.N. Mukund, D. Sanetrnik, **Powder Technology**, **312** (2017) 152-158, 10.1016/j.powtec.2017.02.023.

[110] X. Kong, T. Barriere, J. Gelin, **Journal of Materials Processing Technology**, **212** (2012) 2173-2182, 10.1016/j.jmatprotec.2012.05.023.

[111] R. Supati, N. Loh, K. Khor, S. Tor, **Materials Letters**, **46** (2000) 109-114, 10.1016/S0167-577X(00)00151-8.

[112] J. Zhang, M. Sahli, J.C. Gelin, T. Barriere, **International Journal of Advanced Manufacturing Technology**, **77** (2015) 2135-2149, 10.1007/s00170-014-6595-8.

[113] R. Asmawi, M.H.I. Ibrahim, A.M. Amin, N. Mustafa, Iop, **International Engineering Research and Innovation Symposium, IRIS 2016;** , Kings Green Hotel MelakaMelaka; Malaysia;, 24 November 2016 through 25 November 2016.

[114] Z.Y. Liu, T.B. Sercombe, G.B. Schaffer, **Powder Metall.**, **51** (2008) 78-83, 10.1179/174329008x284859.

[115] A.S. Muhsan, F. Ahmad, M. Rafi Raza, **2011 IEEE Colloquium on Humanities, Science and Engineering, CHUSER 2011**.

[116] L. Acar, H.O. Gulsoy, **Powder Metall.**, **54** (2011) 427-431, 10.1179/003258910x12740974839558.

[117] A.S. Muhsan, F. Ahmad, N.M. Mohamed, P.S.M.B.T.M. Yusoff, M.R. Raza, **Journal of Applied Sciences**, **12** (2012) 2397-2403, 10.3923/jas.2012.2397.2403.

[118] F. Ahmad, A.S. Muhsan, M.R. Raza, **7th International Conference on MEMS, NANO and Smart Systems, ICMENS 2011;** , **Advanced Materials Research**, **403-408** (2012) 5335-5340, 10.4028/www.scientific.net/AMR.403-408.5335.

[119] A.S. Muhsan, F. Ahmad, N.M. Mohamed, M.R. Raza, **4th International Conference on Applied Mechanics and Mechanical Engineering, ICAMME 2013**, **Applied Mechanics and Materials**, **459** (2013) 11-17, 10.4028/www.scientific.net/AMM.459.11.

[120] H. Saidin, M. Azuddin, **4th International Conference on Mechanical and Manufacturing Engineering, ICME 2013;** , **Applied Mechanics and Materials**, **465-466** (2014) 1250-1254, 10.4028/www.scientific.net/AMM.465-466.1250.

[121] A. Hossain, I.A. Choudhury, N. Nahar, I. Hossain, A. Bin Mamat, **Materials and Manufacturing Processes**, **30** (2015) 41-46, 10.1080/10426914.2014.930955.

[122] Z.Y. Liu, D. Kent, G.B. Schaffer, **Materials Science and Engineering A**, **513-514** (2009) 352-356, 10.1016/j.msea.2009.02.001.

[123] D. Kent, M. Qian, G.B. Schaffer, **Powder Metall.**, **53** (2010) 118-124, 10.1179/003258909X12523294330154.

[124] T. Udomphol, B. Inpanya, N. Chuankrerkkul, **2011 International Conference on Manufacturing Science and Technology, ICMST 2011;** , **Advanced Materials Research**, **383-390** (2012) 3234-3240, 10.4028/www.scientific.net/AMR.383-390.3234.

[125] T. Patcharawit, S. Klahan, P. Rupkrathok, N. Chuankrerkkul, **3rd International Conference on Advanced Materials Design and Mechanics, ICAMDM 2014;**, **Applied Mechanics and Materials**, **597** (2014) 103-108, 10.4028/www.scientific.net/AMM.597.103.

[126] T. Patcharawit, B. Inpanya, N. Chuankrerkkul, **International Journal of Materials Engineering Innovation**, **5** (2014) 151-158, 10.1504/IJMATEI.2014.060318.

[127] H. Abdoos, H. Khorsand, A.A. Yousefi, **Mechanics of Advanced Composite Structures**, **3** (2016) 45 - 51.

[128] H.O. Gulsoy, **Materials Science and Technology**, **24** (2008) 1484-1491, 10.1179/174328408x270239.

[129] H.Ö. Gulsoy, T. Baykara, S. Özbek, **Powder Metall.**, **54** (2011) 360-365, 10.1179/003258910X12678035166692.

[130] D.D. Guan, X.B. He, X.H. Qu, **2nd International Conference on Advanced Engineering Materials and Technology, AEMT 2012;**, **Advanced Engineering Materials Ii, Pts 1-3**, **535-537** (2012) 133-138, 10.4028/www.scientific.net/AMR.535-537.133.

[131] S. Liang, Y. Tang, Y. Zhang, J. Zhong, **2nd International Conference on Multi-Functional Materials and Structures,**, **Advanced Materials Research**, **79-82** (2009) 469-472, 10.4028/www.scientific.net/AMR.79-82.469.

[132] J.-P. Choi, H.-G. Lyu, W.-S. Lee, J.-S. Lee, **Powder Technology**, **261** (2014) 201-209, https://doi.org/10.1016/j.powtec.2014.04.047.

[133] T.J. Ferreira, M.T. Vieira, **Euro PM 2014 Congress and Exhibition, Proceedings**.

[134] T.J. Ferreira, M.T. Vieira, **Ciencia e Tecnologia dos Materiais**, **29** (2017) e87-e91, 10.1016/j.ctmat.2016.07.010.

[135] R.M. German, 1 - Metal powder injection molding (MIM): key trends and markets A2 - Heaney, Donald F, Handbook of Metal Injection Molding, Woodhead Publishing2012, pp. 1-25.

[136] A. Rota, T.V. Duong, T. Hartwig, **Microsystem Technologies**, **8** (2002) 323-325, 10.1007/s00542-002-0157-y.

[137] J.-P. Choi, J.-S. Park, J.-I. Song, W.-S. Lee, J.-S. Lee, **Powder Technology**, **317** (2017) 1-5, https://doi.org/10.1016/j.powtec.2017.04.051.

[138] M. Heckele, W. Bacher, K.D. Muller, **Microsystem Technologies**, **4** (1998) 122-124, 10.1007/s005420050112.

[139] E.W. Sequeiros, M.T. Vieira, M.F. Vieira, **Euro PM2017** Milan Italy, 1-5 October 2017.

[140] M.F. Imbaby, K. Jiang, **Acta Materialia**, **57** (2009) 4751-4757, 10.1016/j.actamat.2009.06.034.

[141] T. Patcharawit, A. Ngeekoh, N. Chuankrekkul, Iop, **2017 International Conference on Materials and Intelligent Manufacturing ; ICMIM 2017**, **244** (2017) 10.1088/1757-899x/244/1/012012.

[142] M. Sahli, C. Millot, J.C. Gelin, T. Barrière, **AIP Conference Proceedings**.

[143] M. Sahli, C. Millot, J.C. Gelin, T. Barrière, **Journal of Materials Processing Technology**, **213** (2013) 913-925, 10.1016/j.jmatprotec.2012.11.007.

[144] E.W. Sequeiros, V.C. Neto, M.T. Vieira, M.F. Vieira, **Powder Metall.**, **57** (2014) 241-244, 10.1179/0032589914z.000000000193.

[145] E.W. Sequeiros, T.J. Ferreira, V.C. Neto, M.T. Vieira, M.F. Vieira, **Euro PM 2014 Congress and Exhibition, Proceedings**.

[146] E.W. Sequeiros, M.T. Vieira, M.F. Vieira, **Proceedings of the International Euro Powder Metallurgy Congress and Exhibition, Euro PM 2012**.

[147] O. Emadinia, E.W. Sequeiros, M.T. Vieira, M.F. Vieira, **World PM2016 Proceedings**, **WorldPM**, Hamburg, Germany, 9-13 October.

[148] I. Pinwill, M. Edirisinghe, M. Bevis, **Journal of materials science letters**, **10** (1991) 1107-1110.

[149] H. Abdoos, H. Khorsand, A.A. Yousefi, **International Journal of Materials Research**, **108** (2017) 237-244, 10.3139/146.111468.

[150] Q. M., S.G. B., Sintering of aluminium and its alloys, in: Z.Z. Fang (Ed.) Sintering of Advanced Materials - Fundamentals and Processes, Woodhead Publishing2010.

[151] Z.Z. Fang, Sintering of advanced materials, Elsevier2010.

[152] K. Hirose, Handbook of hydrogen storage: new materials for future energy storage, John Wiley & Sons2010.

[153] I.B. Ulanovskiy, Hydrogen diffusion and porosity formation in aluminium, National University of Science and Technology" MISIS"2015.

[154] G. Fu, N.H. Loh, S.B. Tor, B.Y. Tay, Y. Murakoshi, R. Maeda, **Applied Physics a-Materials Science & Processing**, **81** (2005) 495-500, 10.1007/s00339-005-3273-6.

[155] J.H. Meng, N.H. Loh, G. Fu, S.B. Tor, B.Y. Tay, **Journal of Alloys and Compounds**, **496** (2010) 293-299, 10.1016/j.jallcom.2010.01.147.

[156] S. Li, B. Huang, D. Li, Y. Li, S. Liang, H. Zhou, **Powder Metall.**, **46** (2003) 241-245, 10.1179/003258903225005394.

[157] N. Kurgan, **Materials & Design**, **52** (2013) 995-998, 10.1016/j.matdes.2013.06.035.

[158] B.Y. Tay, L. Liu, N.H. Loh, S.B. Tor, Y. Murakoshi, R. Maeda, **Materials Science and Engineering a-Structural Materials Properties Microstructure and Processing**, **396** (2005) 311-319, 10.1016/j.msea.2005.01.033.

[159] O. Emadinia, M.T. Vieira, M.F. Vieira, **Euro PM2017 Proceedings**, **EuroPM2017**, Milan, Italy, 1–5 October.

[160] A. Mahajan, A. Kingon, A. Kukovecz, Z. Konya, P.M. Vilarinho, **Materials Letters**, **90** (2013) 165-168, 10.1016/j.matlet.2012.08.120.

[161] E. Kowalska, P. Kowalczyk, J. Radomska, E. Czerwosz, H. Wronka, M. Bystrzejewski, **Journal of Thermal Analysis and Calorimetry**, **86** (2006) 115-119, 10.1007/s10973-006-7585-3.

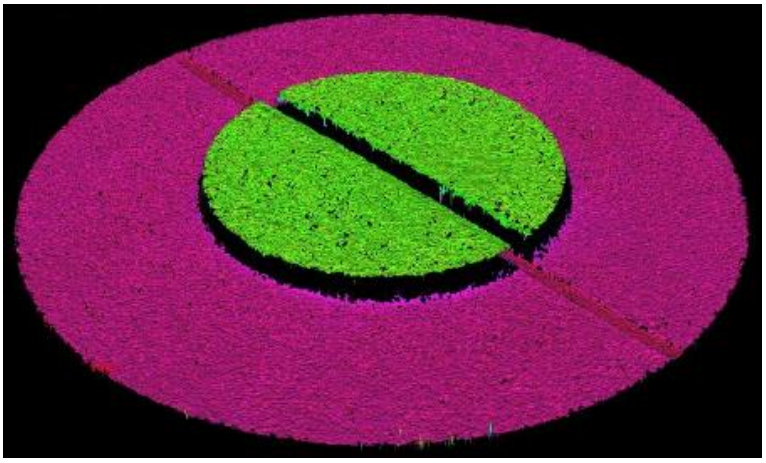

Chapter 2 – Materials and Methods

2.1 Introduction

The key point in materials science and engineering includes correlating the characteristics and properties of materials with the processing conditions being applied. For this purpose, researchers use mechanical tests complemented with analysis techniques such as Scanning Electron Microscopy (SEM) techniques (including Backscattered Electron (BSE), Secondary Electron (SE), Electron Dispersive Spectroscopy (EDS), and Electron Backscattered diffraction (EBSD)), X-ray diffraction (XRD), Infinite Focus microscopy (IFM), Transmission Electron Microscopy (TEM), Raman Spectroscopy, Differential Scanning Calorimetry (DSC) and Thermogravimetric analysis (TG).

In this study the nanocomposite preparation was carried out as follows:

Input materials → *Mixing* → *Filtering* → *Drying* → *Compacting* → *Sintering*

The sequences of micro hot embossing are listed as follow:

Input materials → *Feedstocks* → *Granulating* → *Sieving* → *Shaping (Green part)* → *Debinding (Brown part)* → *Sintering (Final part)*

The preliminary experiments and the primary optimizations were carried out with the aluminium powder, and then the best processing conditions were applied to the 316L stainless steel powder.

2.2 Equipment and tests

Table 2.1 list the equipment used to characterize the input and processed materials.

Table 2.1 List of the equipment for tests and characterization.

Techniques	Equipment	Purpose
Laser diffraction analyser	Mastersizer 3000	Particle size distribution
X-ray fluorescence spectrometer	PANalytical AXIOS^{max}	Chemical analysis
X-ray diffractometer	PANalytical using CuK_{α}, (1.540598 Å), scanning rate of one second per step	Phase evolution
Helium pycnometer	AccuPyc 1330 Micromeritics	Powder and particulate density
SEM/SE, SEM/BSE, SEM/ESD, EBSD	Quanta 400 FEG ESEM/EDAX Genesis X4M	Morphology, microstructure, semi quantitative chemical analysis, structure (grain size and texture)
Thermal analysis (DSC/TG)	Setaram SetSys Evolution up to 1600 ºC & Labsys^{TM} Setaram	Phase transformation and binder degradation
3D coordinate system (IFM)	Alicona IFM G4	Replicability including dimension and topography[6]
Light microscopy	Leica DM 4000 M	Microstructure and porosity
Light stereoscopy	Zeiss Stemi 2000-C	Shape retention
Transmission electron microscopy	FEI, TECNAI G2 20 S-TWIN	Morphology of nanoparticles
Raman spectroscopy	Horiba HR800, laser incident beam with 442 nm wavelength	Integrity of MWCNT
Microhardness	Struers Duramin	Hardness of sintered specimens
Shore A	Teclock GS-719N	Elastomer hardness
Archimedes[7]	METTLER TOLEDO 33360 210260	Density of sintered specimens
Ball cratering	PLINT TE 66 Micro-Scale Abrasion tester	Abrasion wear
Microtensile test	Table top universal tensile tester (Shimadzu)	Tensile strength

[6]This includes dimensional measurements and determining two roughness parameters: Sa and Sz (presented as the arithmetical average of the absolute values of the roughness profile, and the difference between the highest peak and deepest valley in the analyzed area, respectively).

[7] The scale was a METTLER TOLEDO AB204-S with 1 mg error.

In the case of semi-quantitative chemical analysis by SEM/EDS technique, same conditions were applied when a comparison between different samples was intended, e.g. the voltage of 5 keV was selected when it was intended to receive superficial information to evaluate oxidation during process. For this SEM/EDS evaluation, it was also tried to select similar topographies [1].

Densification was evaluated through measurements of density or porosity, the latter was carried out using metallographic images. The dimensional measurements of shaped specimens were performed by IFM analysis or by optical microscopy and ImageJ software. The IFM was also assisted to obtain surface roughness information from rectangular areas positioned on the intended surfaces. The IFM technique was also used to control shrinkage after sintering [2] and also roughness changes between die and parts [3, 4]. In this study, IFM was used to evaluate the effects of the die type and composition on the micro hot embossed specimens.

All the processing equipment used in the present study is summarized in Table 2.2. As regards the mixing and dispersion system of the sonication equipment, it is assembled with a S25D-14G-KS dispersing plastic blade. it can generate a wide range of 3000 to 25000 rpm (50 to 340 Hz) in 1 to 2 liters of water. Magnetic stirring can produce 1000 rpm. The ultrasonication bath generates shock waves with a frequency of 35 kHz (2100000 rpm).

Table 2.2 List of the equipment for material preparation.

Equipment (model)	Purpose
Plastograph with double Z-blades (Brabender torque rheometer)	Feedstock optimization and preparation
A single screw extruder (Brabender)	Eliminating porosities in feedstock
Turbula	Mixing solid constituents
Ultrasonic bath (Sonorex 35 kHz)	Dispersion
Sonication (IKA T 25 Digital)	Dispersion
Magnetic stirring (multiple speed)	Dispersion
Tensile test equipment (LIOYD LR 30K)	Shaping during micro hot embossing
Infrared radiation furnace	Shaping during micro hot embossing
Resistance furnaces with low vacuum and flowmeter[8] or high vacuum	Debinding, Sintering

[8] With alumina recrystallized tubes.

The outputs of the torque rheometer experiment, mixing torque vs powder concentrations or time, were used to identify CPVC and to characterize the homogeneity of optimized feedstocks.

2.3 Materials

2.3.1 Materials for micro hot embossing

Two metal powders, aluminium and stainless steel, were processed separately for feedstock preparation. For studying the strengthening effect of MWCNT, each powder was mixed with 1.00 vol.% MWCNT. This concentration was selected in line with a previous study in which the strengthening of pure Al by MWCNT was evaluated after sonication, compaction and sintering [5]. Micro hot embossing was performed by a die assembly, which included metallic and elastomer dies. Table 2.3 summarizes all the materials used and suppliers. The main characteristics of powders are in Tables 2.4 to 2.6.

Table 2.3 List of materials used for micro hot embossing and nanocomposite production.

Material	Supplier
AISI 316L	Sandvik Osprey Ltd
Aluminium	Alfa Aesar
Binder system (so-called *M1*)	Atect® Corporation
Stearic acid	Sigma Aldrich
MWCNT	FIBERMAX composites
Isopropyl alcohol (> 99.8%)	Sigma Aldrich
Dark blue elastomer (HB FLEX 5550 A+B)	HB Quimica, LDA
Transparent elastomer (HB FLEX RTV2 T4 S A+B)	HB Quimica, LDA
Light blue elastomer (260 A)	Quantum Silicones, LLC - a CHT Group
Beige elastomer (270 A)	Quantum Silicones, LLC - a CHT Group
Cold resin	Presi GmbH

Table 2.4 Metal powder characteristics.

Material	D_{10} (µm)	D_{50} (µm)	D_{90} (µm)	Density (kg/m^3)	Specific surface area (m^2/kg)	Shape factor
Al	5.4	10.1	16.7	2670	695	>1
AISI 316L	1.8	3.5	5.9	7937	2120	~1

Table 2.5 Chemical composition of the Al powder (XRF).

Elements	Al	Ti	V	Fe	Ni	Zn	Ga
wt.%	99.800	0.008	0.011	0.104	0.011	0.005	0.017

Table 2.6 Chemical composition of the AISI 316L powder (Supplier).

Elements	Fe	Si	Mo	Cr	Ni	Mn	P	S	C
wt.%	67.61	0.57	2.40	17.10	11.10	1.17	0.020	0.013	0.012

DSC analysis of the Al powder (Figure 2.1a) revealed two peaks: an exothermic reaction with an onset point at ~590 ℃, followed by melting at 638 ℃. When the cycle was repeated, the first peak was not detected and the onset point of melting increased for 2 ℃. This suggests that during the first heating cycle the primary oxygen or moisture in the loose powder was not removed at low temperatures, and at higher temperatures the oxygen reacted with aluminium and formed the oxide. Similar conclusion was pointed out by other authors who related a similar exothermic reaction of an A1050 powder at ~580 ℃ and associated it to oxidation during heating in air [6].

The DSC test did not reveal any important reaction for the 316L powder heated up to 1350 ℃, only a small exothermic peak at ~609 ℃ was detected and it could be attributed to microstructural changes during heating. In fact, some authors indicated an exothermic reaction at a similar temperature during annealing of a highly deformed 316L specimen, and this was related to the recovery of the structure [7]. In addition, according to the XRD analysis, the 316L powder is not completely austenitic (Figure 2.2a). The indexation process was carried out by X'Pert High Score Plus software and peaks at 43.4º and 50.6º correspond to austenite, and the one at 44.4º matches ferrite/martensite, in accordance to ICDD cards of 00-033-0397 and 01-087-0721, respectively. This powder has been submitted to cooling rates during atomization that contributed to martensite formation due to the high stresses introduced. Therefore, the powder can show a transformation of martensite to austenite during heating up to 600 ℃ (Figure 2.1b).

The EBSD boundary maps (Figure 2.2b and 2.2c) of the stainless-steel and aluminium powders reveal the presence of a larger fraction of subgrains and low-angle boundaries (Table 2.7), which indicates that the producing process has induced a large deformation in the metallic powders. The powder morphologies are illustrated in Figure 2.3.

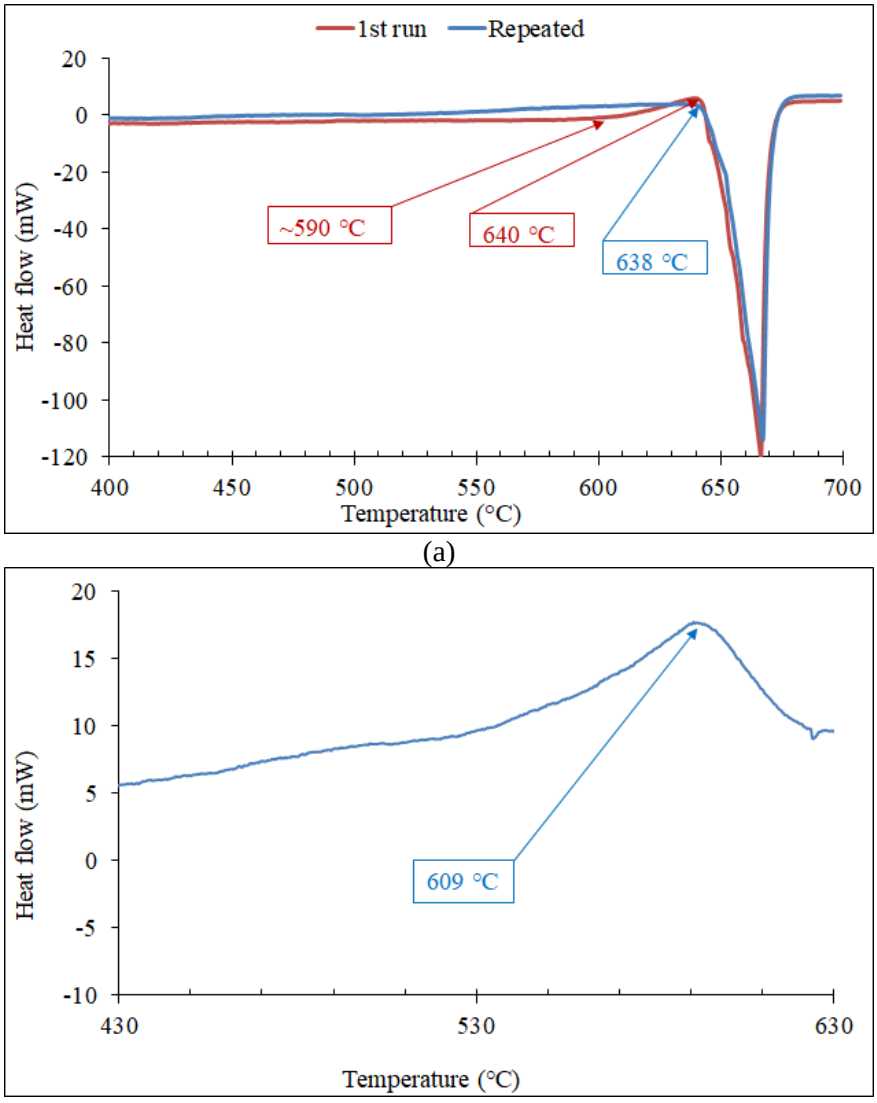

(a)

(b)

Figure 2.1 *DSC graphs of the Al (a) and 316L (b) powders, acquired in flowing Argon (99.999%) at a heating rate of 5 °C/minute.*

Thermal analysis was used to evaluate the loss of weight associated to the identification of the phase transformation in the binder material (M1), using heating rate of 10 °C/min in Argon atmosphere (Figure 2.4). It must be highlighted that the binder is completely eliminated at 500 °C. This binder has a density of 970 kg/m^3, measured by Helium pycnometer.

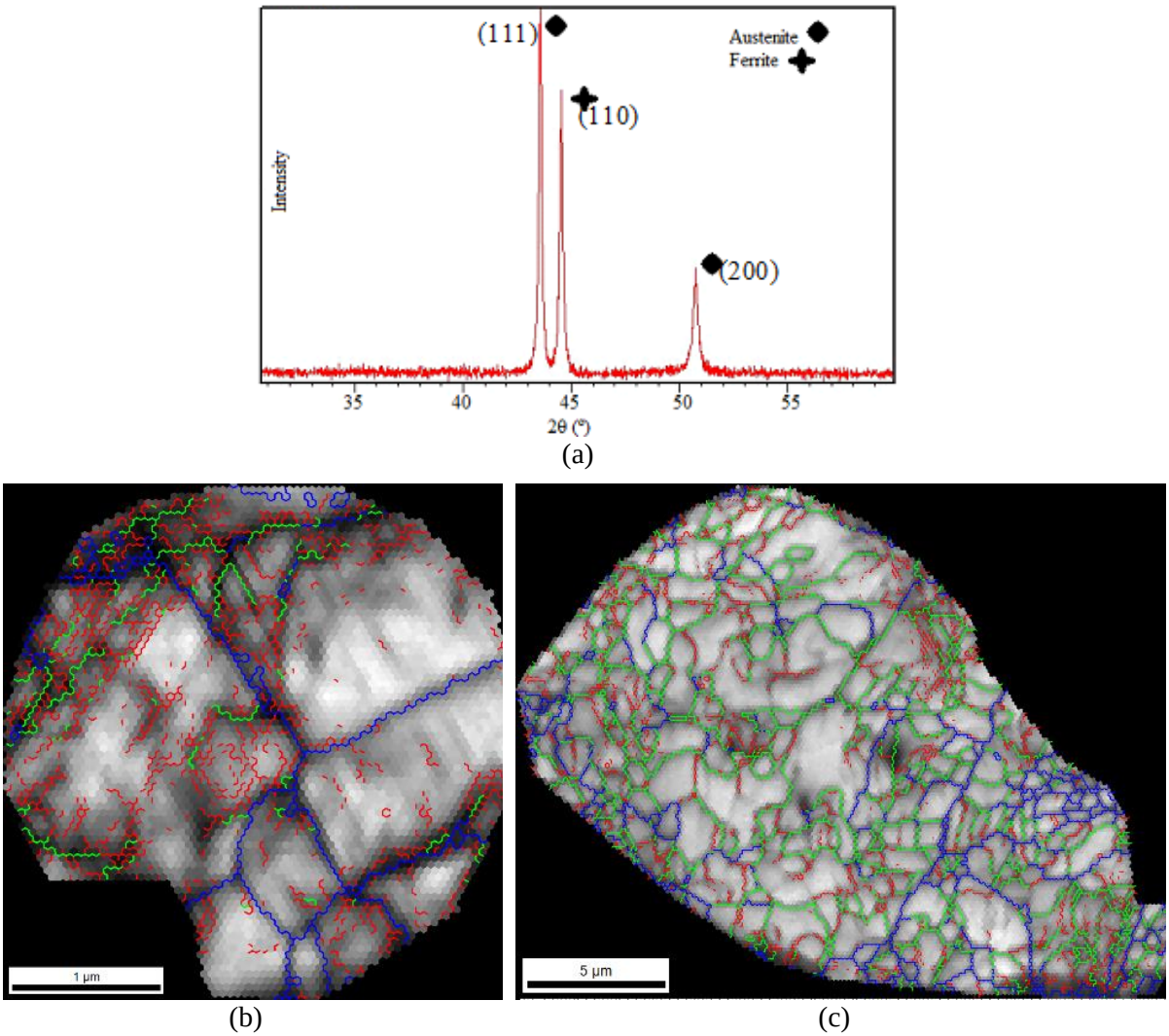

(a) (b) (c)

Figure 2.2 *XRD diffractogram showing the characteristic peaks of the 316L powder, (a); EBSD boundary maps from two individual 316L stainless-steel (b) and Al (c) powder, acquired by 0.05 and 0.15 µm scanning step, respectively (SEM/EBSD).*

Table 2.7 Boundaries characteristics of two individual 316L and Al particulate, analysed by EBSD.

Boundary colour	Min	Max	Representative	Fraction in 316L	Fraction in Al	Average grain size of 316L	Average grain size of Al
-----	2º	5º	Subgrain	0.60	0.31	0.25 µm	0.77 µm
-----	5º	15º	Low angle boundary	0.16	0.44		
-----	15º	180º	High angle boundary	0.24	0.25		

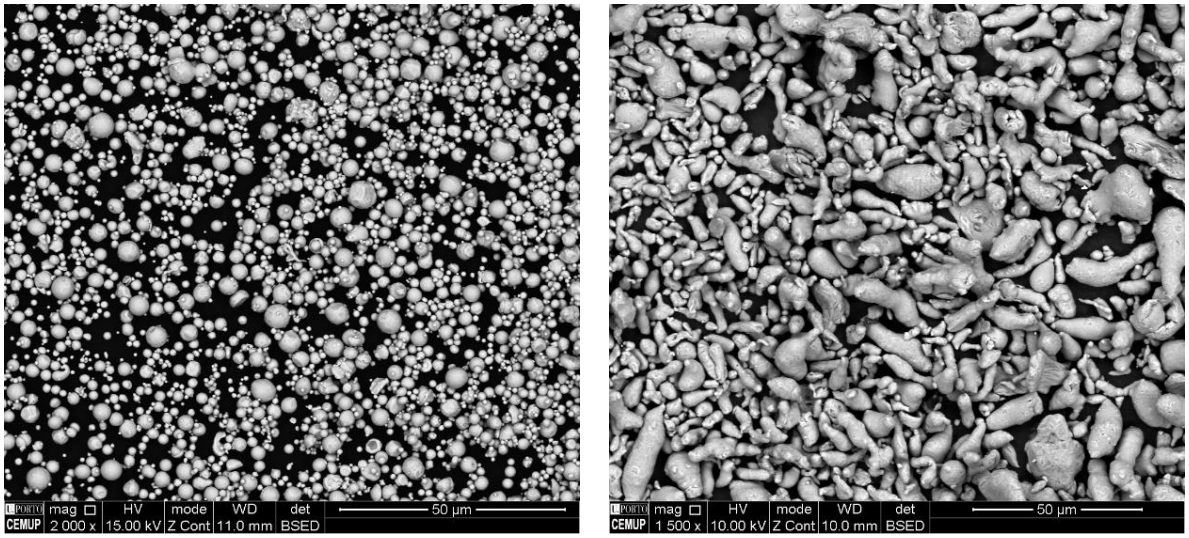

(a) (b)

Figure 2.3 *Powder morphology of 316L (a) and Al (b) with shape factor close to one and far from one, respectively (SEM/BSE).*

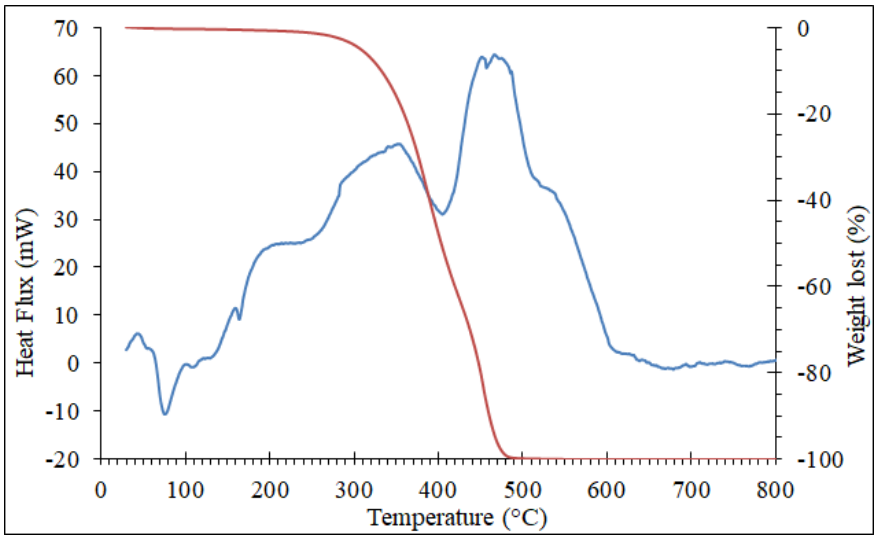

Figure 2.4 *DSC/TG analyses of the binder material.*

The pristine MWCNTs exist in strong large agglomerates (Figure 2.5a) and have a density of 2013.3 kg/m^3 (measured by Helium pycnometer) with an average external diameter of 23±7 nm (measured by ImageJ from SEM images).

The Raman spectra of this pristine MWCNT is illustrated in Figure 2.5b, the main characteristic peaks are observed at 1365.5 cm^{-1}, 1566.9 cm^{-1}, and 2709.8 cm^{-1}, representing the D, G, and G' (or 2D). The presence of each band has a specific meaning, the D band indicates that there is a

level of disorder in the structure of the nanomaterial, the G represents the crystallinity of the graphitic structure, and the 2D band confirms the long range order generated by MWCNTs [8].

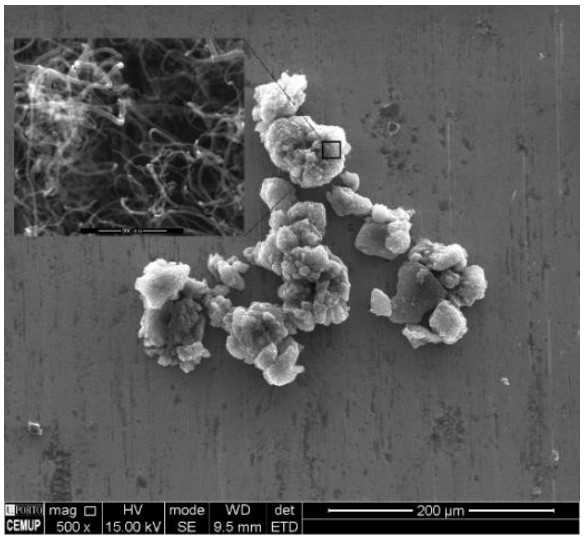

(a)

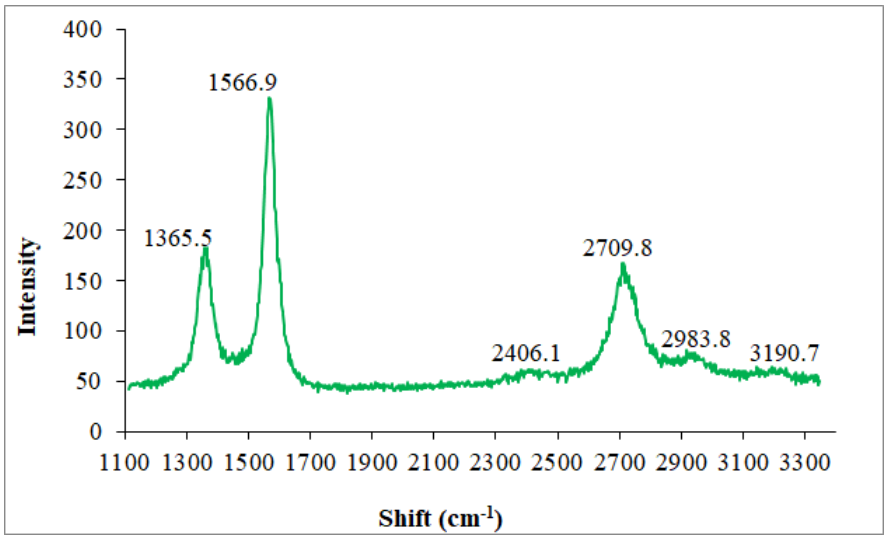

(b)

Figure 2.5 *Pristine MWCNTs morphology (SEM/SE) (a) and the Raman spectra (b).*

2.3.2 Nanoreinforcements

Reinforcements used for the study included MWCNT, also utilized for micro hot embossing, and Graphene nanosheets, Nanoalumina, and Ultrafine Tungsten Carbides (Table 2.8). These different materials, being processed equally, allow to evaluate the effects of reinforcement characteristics such as density, particle size, particle size distribution, shape and structure on the dispersing efficiency and reinforcing. Some characteristics and the morphology of these reinforcements are presented in Table 2.9 and Figure 2.6. For this study theoretical densities

were considered: 2200 kg/m^3, 3955 kg/m^3, and 15630 kg/m^3 for Graphene, alumina and WC, respectively.

Table 2.8 List of reinforcement suppliers.

Material	Supplier
Graphene nanosheet	Graphene Supermarket
Nanoalumina	Sigma Aldrich
Ultrafine Tungsten Carbide	H.C. Starck Tungsten GmbH

Table 2.9 Characteristics of the reinforcements declared by the suppliers.

Material	Particle size	Surface area (m^2/kg)	Purity (%)
Graphene	Average plate thickness 60 nm, Lateral size ≤ 7μm	≤40000	98.5
Al_2O_3	Particle size <50 nm	>40000	-
WC	D_{50}[9] = 330 nm	190005	99.8

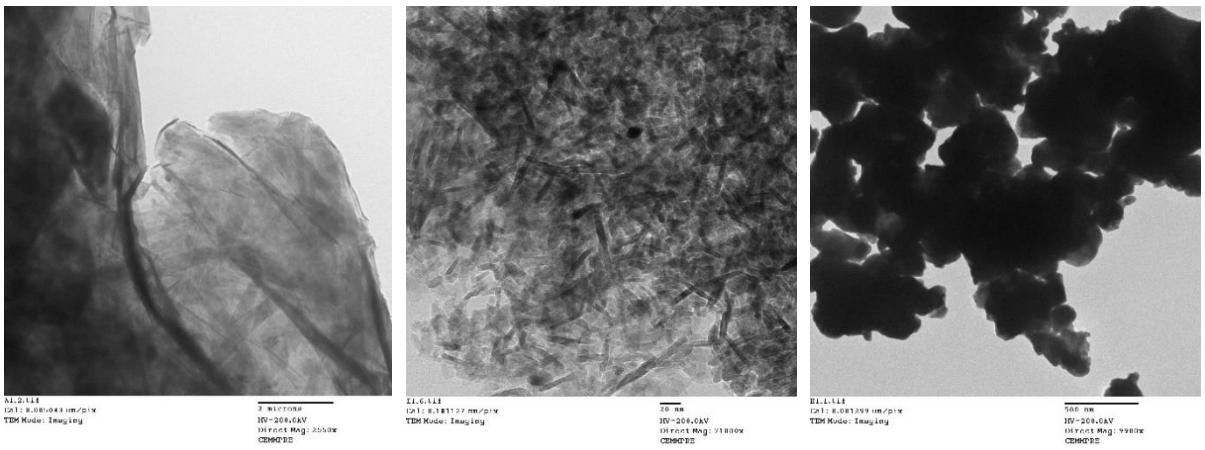

(a) (b) (c)

Figure 2.6. *Nanoreinforcements: pristine Graphene nanosheets (a), nanoalumina (b), and ultrafine WC (c) (TEM).*

2.4 Processing nanocomposites

Pristine MWCNTs are available in large agglomerations (Figure 2.5a) and these should be disentangled as much as possible (Figures 2.7a to 2.7d). The feasibility of the sonication technique (20400 rpm) was already attested, however, some damage could be introduced in the

[9] Measured values.

structure of the nanotubes [5]. The same procedure, simultaneously sonicating the powder and MWCNT, was applied for the preparation of preliminary specimens with different contents of the MWCNT: 0.00, 0.25, 0.50, 0.75, 1.00 and 2.00 wt.% (0.00, 0.33, 0.66, 1.00, 1.32 and 2.64 vol.%) in isopropanol with ~0.02 g/ml solid concentration, considering 20400 rpm (340 Hz) for the optimized time, 15 minutes)[10] [9]. This was followed by draining through a glass fibre filter, with 2 μm of retention, and drying at 80 °C for 60 minutes in normal atmosphere (Figure 2.7e). The result of this sequence is illustrated in Figure 2.7f.

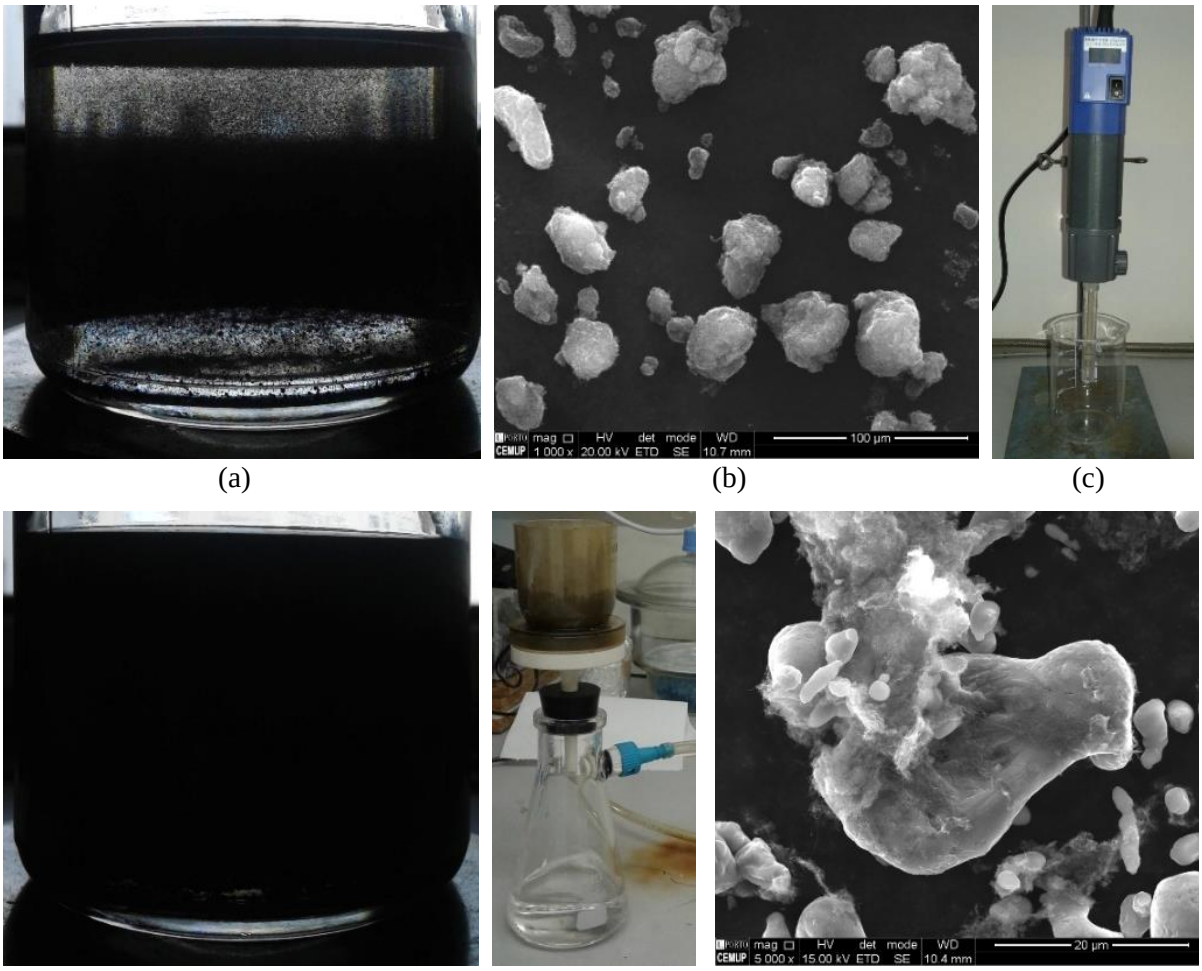

(a) (b) (c)

(d) (e) (f)

Figure 2.7. *Sequences of dispersing through sonication, i.e. MWCNT in alcohol before dispersion (a), pristine MWCNT in large agglomerates (SEM/SE) (b), sonication equipment with the plastic blade (c), dispersed MWCNT after dispersion without Al powder (d), draining assembly to filter the dispersion from alcohol (e), presence of small fine MWCNT agglomerations among Al powder (SEM/SE) (f).*

[10] The mixture was prepared, considering the total weight/volume constant, e.g. 0.75% of the Al powder was replaced by MWCNT.

Afterwards, the dried mixture was mixed in a Turbula shaker for 15 minutes and cold compacted by a hydraulic manual press or by a uniaxial tensile test machine, operating in compression mode. The specimens are disks with 10 mm or 25 mm diameter and ~2 mm thickness densified by sintering. The theoretical density of any prepared composite was calculated according to the rule of mixtures (2.1), excluding the effect of interface (porosity or phase formation):

$$\textit{Powder vol. content} \times \textit{Powder density} + \textit{Additive volume content} \times \textit{Additive density} \quad (2.1)$$

The evaluation of reinforcing effect was controlled by microhardness measurements. In the nanocomposites section (Chapter 6), the change in dispersion methodology to optimize the reinforcement effect of MWCNT will be explained in detail. Afterwards, the best dispersing condition was applied for Graphene, nanoalumina, and ultrafine WC particles. The mechanical evaluation of the hardest material will be proceeded by tensile and abrasion wear tests.

2.5 Feedstock preparation

Feedstocks were prepared based on the CPVC values obtained by binder softening approach through a torque mixer (Figure 1.4a), at 30 rpm and 175 ℃, temperature was measured inside the mixture. Incremental batches, each with 1 vol.% of powder, were added to the pre-softened binder (Figure 1.4b), almost 5 minutes, until the Plastograph chamber becam full. These sequences of addition started from 50 vol.% of powder and the last batch led to 65 vol.% powder. Each interval took a while (at least 5 minutes) for the torque mixture to be stabilized. As already mentioned, CPVC is the torque value for which the torque mixing started to increase at a higher rate than the previous points (Figure 1.4c), i.e. the feedstock loses its flowability due to the great interaction of powders [10]. The powder concentration of the optimized feedstock is 1% smaller than the CPVC. The preparation of the optimized feedstock was also carried out at 30 rpm and 175 ℃ for enough time until the torque stabilized (Figure 2.8).

The content of MWCNT added to the Al and 316L feedstocks was equal to 1 vol.% of the powder concentration. The mixture of metallic powder and MWCNT was prepared as previously mentioned (section 2.4). However, the solid concentration of the mixture in the isopropyl alcohol was almost ten times bigger. In case of any other additives, such as stearic acid (SA) as a diluting agent, the concentration observes the same approach, and this was mixed with the powder by Turbula shaker for 30 minutes before being added to the binder.

Some feedstocks were also extruded by a single screw equipment at 15 rpm and 175 °C (Figure 2.9a) to eliminate porosity. The evaluations of homogeneity, torque evolution during mixing and composition effect will be discussed later in the feedstock section.

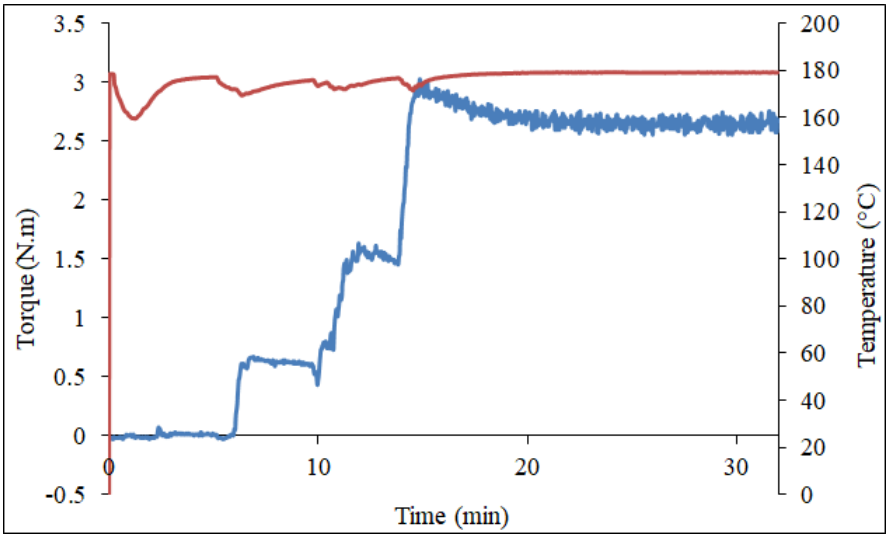

Figure 2.8 *Graph showing the change of torque (blue line) and temperature (red line) against time, the mixing stopped when the torque value stabilized.*

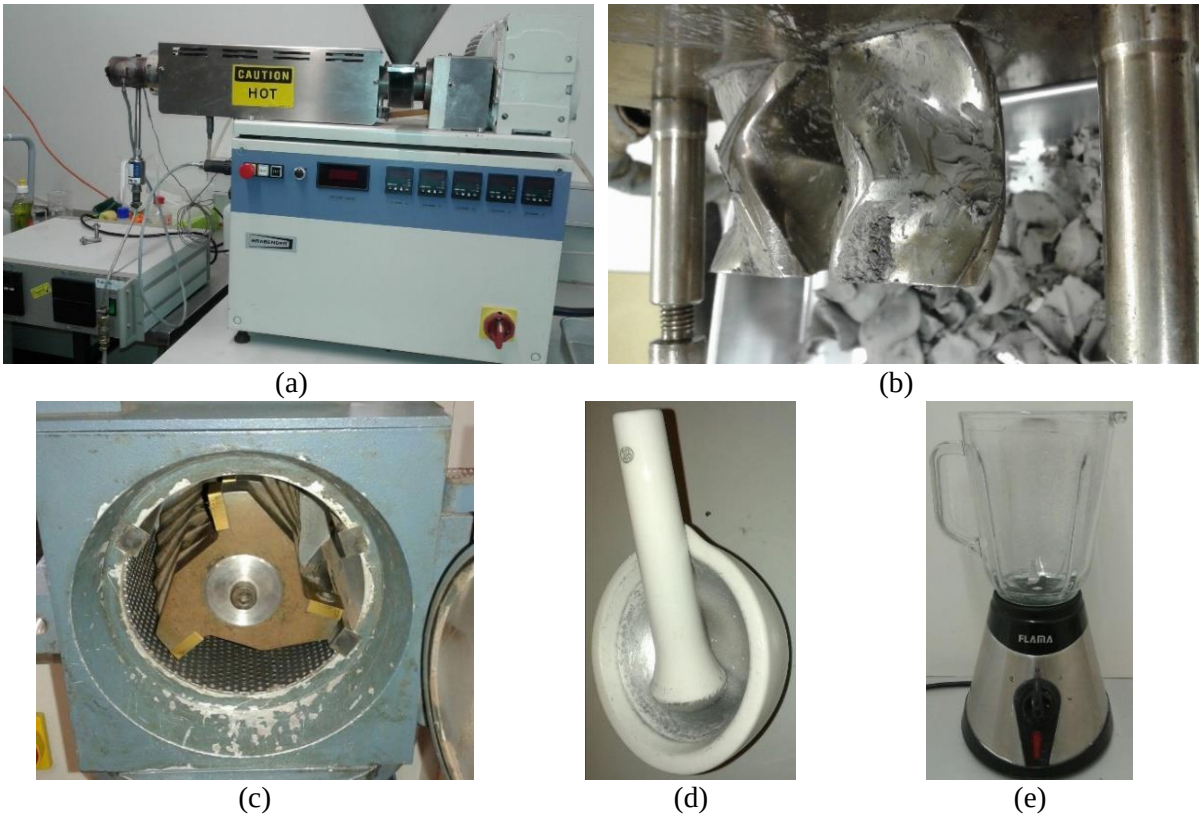

(a) (b)

(c) (d) (e)

Figure 2.9 *Brabender single extruder equipment (a), double Z-blade of the torque mixing equipment with the feedstock pieces beneath the blade (b); industrial granulator (c), mortar and pestle (d), and blender (e).*

The feedstocks are pieces or rods after passing through the torque mixer (Figure 2.9b) or the extruder, respectively. For the Al feedstock, these fragments were crushed down to obtain small particles for which using different equipment was evaluated: first an industrial granulator (Figure 2.9c), then a mortar and pestle (Figure 2.9d), and finally a blender (Figure 2.9e).

The granulating process was proceeded only by the blender for other feedstocks, it will be discussed in section 3.5. The crushed particulates of feedstocks were sieved and the particles smaller than 500 µm (so-called fine) were selected for micro hot embossing. However, green specimens made of coarse particles are presented later in the shaping section to analyse the effect of particle size.

2.6 Die preparation

In this study micro hot embossing started by replicating a preliminary geometry, so-called "microblind flange". First a metallic master die with this geometry was made by machining (Figure 2.10), then it was replicated by an elastomer material, being casted and cured (Figure 2.11). Finally, the micro hot embossing was done using the elastomer die. This geometry encompasses the replication of the height and surface of concentric circles.

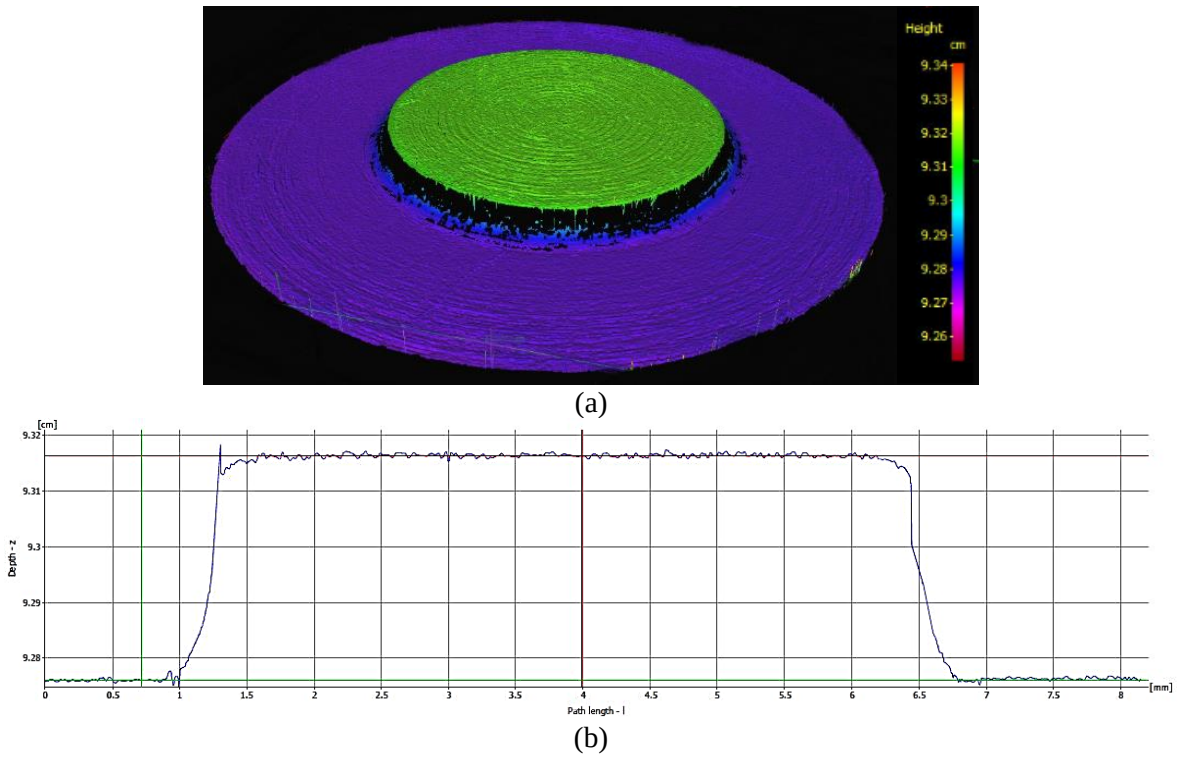

Figure 2.10 *Preliminary metallic master die, a microblind flange with concentric circles on the surface: the roughness map image (a) and the cross-section profile (b) (IFM).*

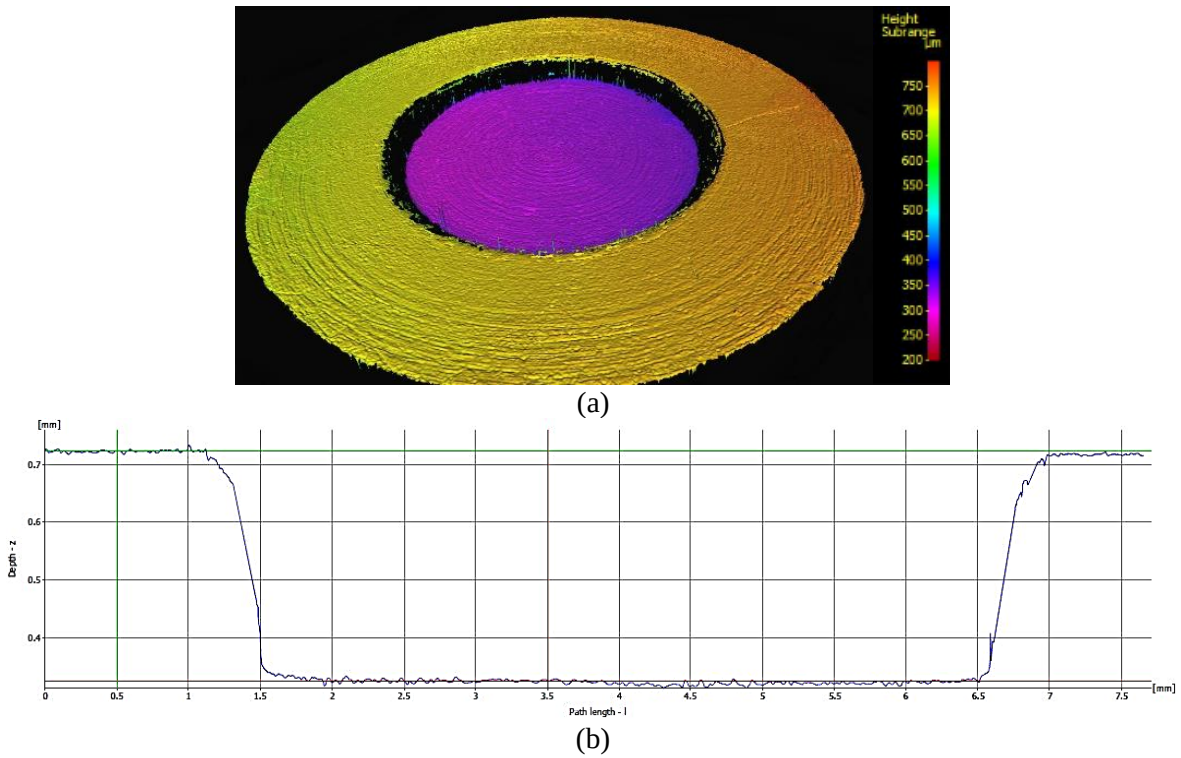

Figure 2.11 *Dark blue elastomer die for replicating the microblind flange with concentric circles on the surface: the roughness map image (a) and the cross-section profile (b) (IFM).*

The characteristics of the matrices are presented in Table 2.10, in the replication of the metal matrix by the elastomer it is verified that the diameter of the flange was slightly shrunk, the height did not change and the roughness of the surface was smoothed.

The other metallic master die with an extra microaspect was made by micromilling a hard metal. This was used to replicate geometries so-called “microchannel-half-flanges” and “microwall-half-reservoirs” (Figure 2.12 and 2.13). These geometries are different, concave and convex geometries, but they have almost equal aspect ratios (Table 2.11). The “microwall-half-reservoirs” geometry was replicated by an elastomer die produced using an intermediate one made of an epoxy resin. Micro hot embossing was also applied for producing three more geometries representing a microtensile specimen (Figure 2.14a) and two more complex geometries, so called concave and convex microgears (Figure 2.14b and 2.14c). Table 2.12 presents all geometries with the corresponding aspect ratios.

Table 2.10 Dimensional characteristics (in µm) of the dies illustrated in Figures 2.10 and 2.11.

Material	Diameter	Height	Sa	Sz
Metal master die	5039	~400	2	64
Dark blue elastomer die	4918	~<400	2	36

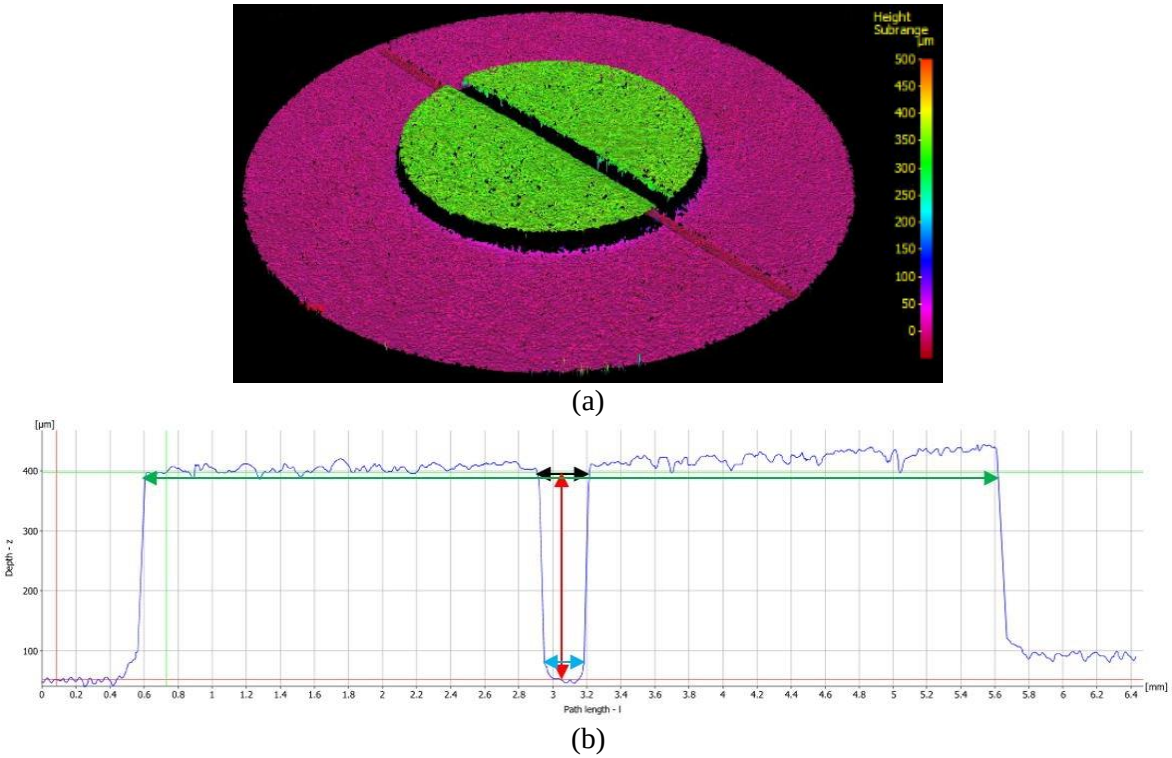

Figure 2.12 *Hard metal master die with microchannel and half-flanges configuration: the roughness map (a) and a cross-sectional profile (b) (IFM). In (b) the green arrow represents the diameter and the black and light blue arrows the maximum and minimum widths, respectively, indicating a conical-like channel.*

Table 2.11 Dimensional characteristics (in µm) of the dies illustrated in Figure 2.12 and 2.13.

Material	Diameter	Height	Maximum width	Minimum width	Sa	Sz
Metallic master die	4983	408±18	321±14	220±21	6.4	166.7
Transparent elastomer die[11]	4896	355±9	326±10	204±13	8.7	679.7
Transparent elastomer die[12]	5000	-	-	-	-	-

[11] This information belongs to a pristine die (Figures 2.13a and 2.13b) to produce the microchannel-half-flanges and it was directly made by replicating elastomer from the metallic master die (Figure 2.12).

[12] This information belongs to a pristine die to produce the microwall-half-reservoirs (replicated by using epoxy intermediate die), measured by ImageJ software from images taken by light stereoscopy (Figure 2.13c).

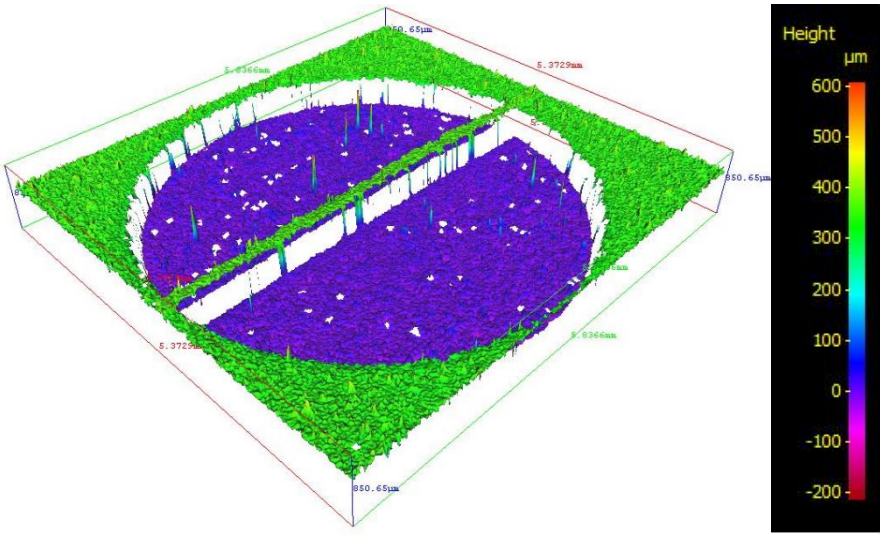

(a)

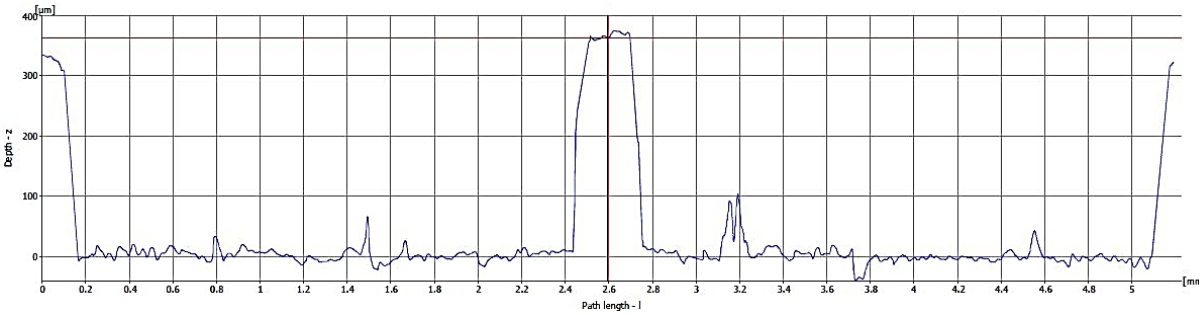

(b)

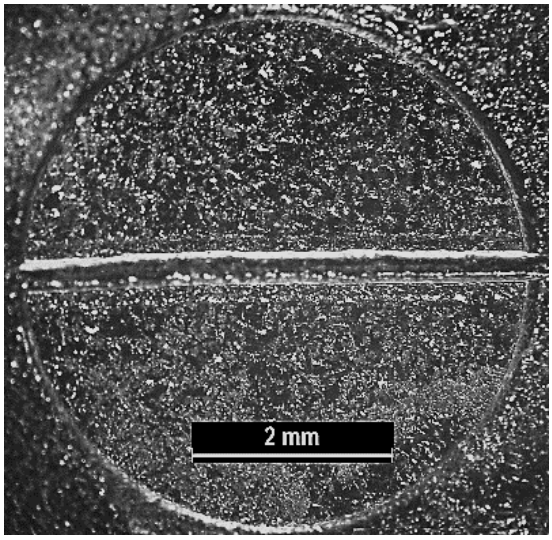

(c)

Figure 2.13 *Transparent elastomer die for replicating microchannel and half-flanges configuration: roughness map (a), cross-section profile (b) (IFM); same elastomer die for replicating microwall-half-reservoirs configuration (c) (stereoscopy).*

(a)

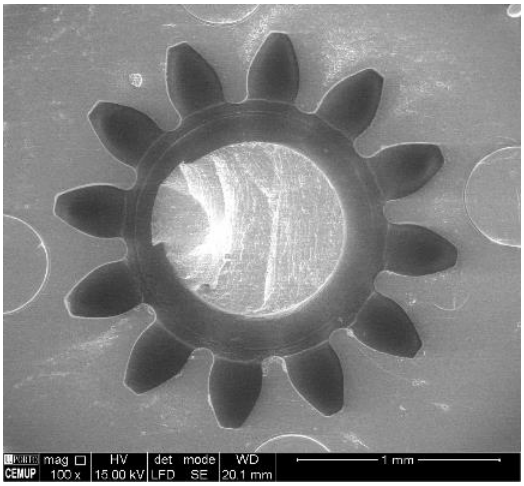

(b)

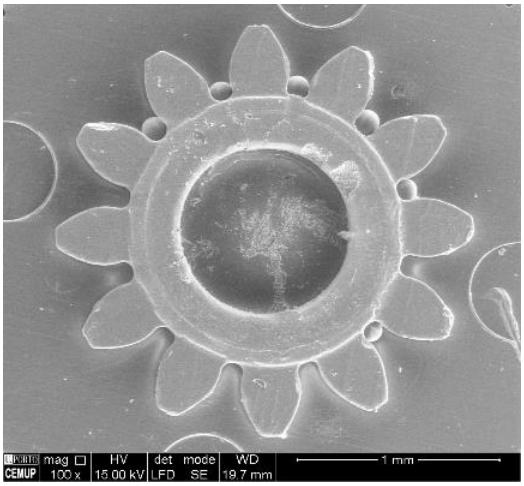

(c)

Figure 2.14 *Dark blue elastomer die to replicate microbone-like tensile specimen (Stereoscopy) (a); beige elastomer dies to replicate convex (b) and concave microgear shapes (c) (SEM/SE).*

Table 2.12. The characteristics of the dies illustrated in Figure 2.10 to 2.14; the aspect ratio is the proportion of the depth/height over the width.

Replicating geometry	**Die material**	**Hardness (pristine die)**	**Aspect ratios**
Microblind flange	Dark blue elastomer	46±1 Shore A	0.08
Microwall-half-reservoirs	Hard metal	40 HRC	1.27 to 1.85 (max to min for wall), 0.08 (for reservoir)
Microchannel-half-flanges	Transparent	38±1 Shore A	1.08 to 1.74 (max to min for wall), 0.07 (for flange)
Microwall-half-reservoirs	Transparent & beige elastomer	38±1 & 69±1 Shore A	~1.08 to ~1.74 (max to min for wall), 0.07 (for reservoir)
Microtensile specimen	Dark and light blue elastomer	46±1 & 64±1 Shore A	~0.2 (the depth over the smallest width)
Convex gear	Transparent & beige elastomer	38±1 & 69±1 Shore A	~1.4 & ~3.3 (the largest to the thinnest width)
Concave gear	Beige elastomer	69±1 Shore A	~1.4 & ~3.3 (the largest to the thinnest width)

2.7 Shaping

The shaping temperature was performed at a temperature of 230 ℃ to ensure maximum benefit from the moulding efficiency of the feedstock (Figure 2.4). The common shaping methodology includes filling the die cavity completely, collecting the die assembly, and then applying temperature and pressure simultaneously to the die assembly until they reach the set points. Afterwards these values are kept constant for a certain time, so-called "holding time", and then the assembly starts cooling down. According to the optimized results of a related study [11], the starting points for pressure and holding time, for the elastomer die, comprise 8.5 MPa and 30 minutes. In this study, the level of pressure is a compromise between the shaping conditions, replicability and the die lifetime. This will be discussed later in the shaping section. Meanwhile, the heating and cooling rates were considered constant for all experiments, close to 15 ℃/min.

Green specimens are produced in a laboratory tensile test equipment, assembled with a vertical furnace (the yellow arrow in Figure 2.15a). The die assembly (Figure 2.15b) is placed between the jaws of the tensile machine (the red rectangle in Figure 2.15a), and heated under the selected temperature, pressure and time conditions (temperature= T, pressure= P & holding time= t). The die assembly encompasses a holding cylinder (part A in Figure 2.15b), this embeds one lower and two upper supports (parts B, G and H in Figure 2.15b), the elastomer die (parts C or D in Figure 2.15b), with lid or back-cover (parts E or F Figure 2.15b). The order of the die parts inside the cylinder in common shaping method includes, from the bottom up, the parts B-C(D)-E(F)-G-H. The die cavity (parts C or D in Figure 2.15b) embeds the replicating geometry that is placed on the bottom face of the cavity, this arrangement is consistent with the earliest study [12]. The die cavity is filled with the feedstock powders, and the lid (part E in Figure 2.15b) or the back-cover (part F in Figure 2.15b) is used depending on whether the cavity is partially or completely filled, respectively.

The weight is not absolutely constant for all specimens because these feedstock particles are affected by the electrostatic force on the surface of the elastomer die (Figure 2.15c). The back cover (E or F in Figure 2.15b) cannot be metallic otherwise there will be an adhesion to the green specimen (Figure 2.15d).

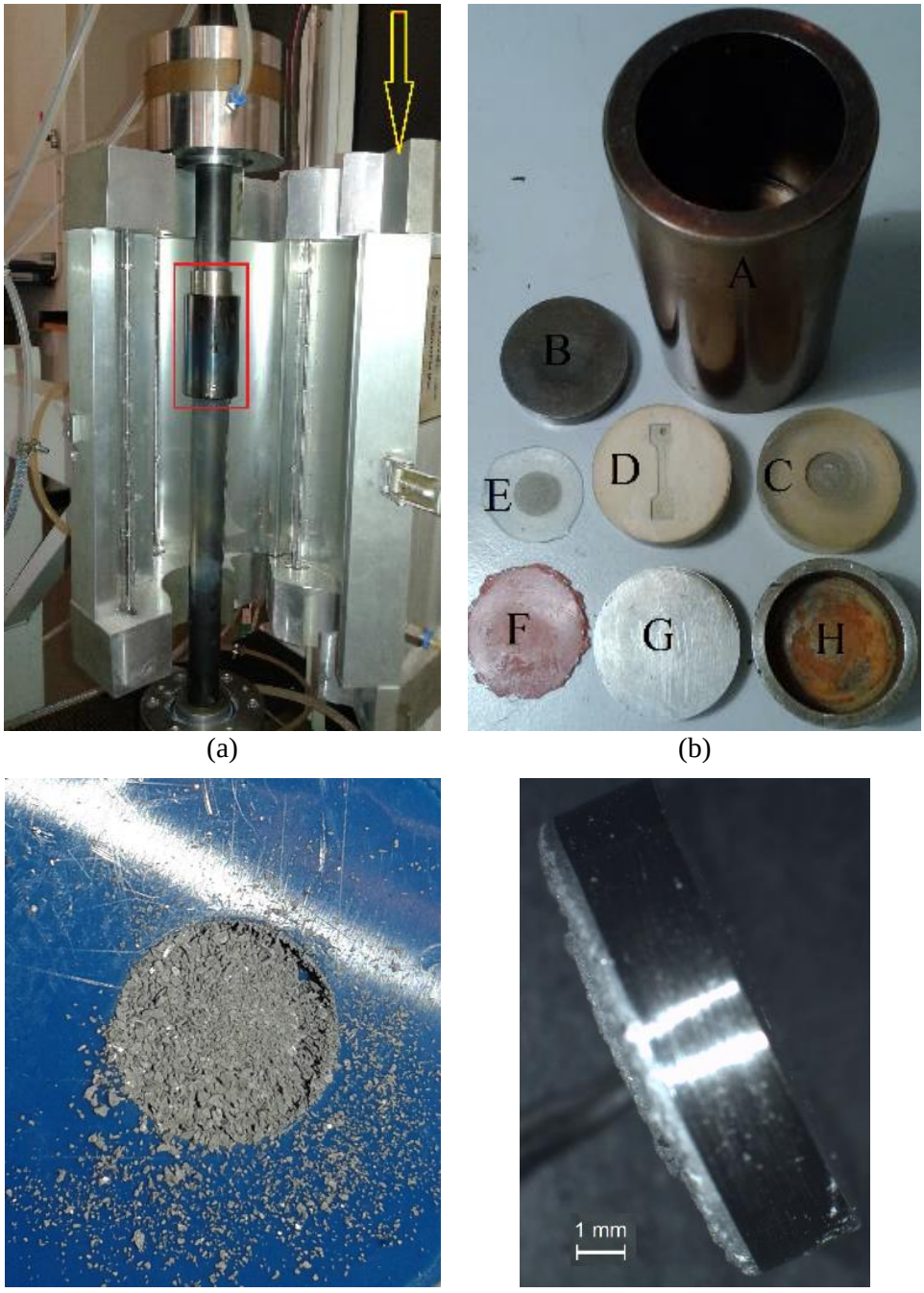

(a) (b)

(c) (d)

Figure 2.15 *Shaping equipment includes the tensile test machine assembled with a furnace (a), die assemblies (b); scattered fine particles on the dark blue elastomer surface (c); adhesion of green Al specimen to a metal back cover (d).*

The study will be proceeded to overcome the shortcomings of the replicability through applying temperature and pressure sequentially or by replacing the elastomer die. Nevertheless, the last one requires a complete change of processing conditions, as will be discussed later in the shaping section.

2.8 Debinding

The binder is a multicomponent material and its thermal decomposition must be achieved through a stepwise treatment (Figure 2.16a). This is a long process because the burnt-out products need to diffuse out from the specimen without changing the part geometry/dimensions.

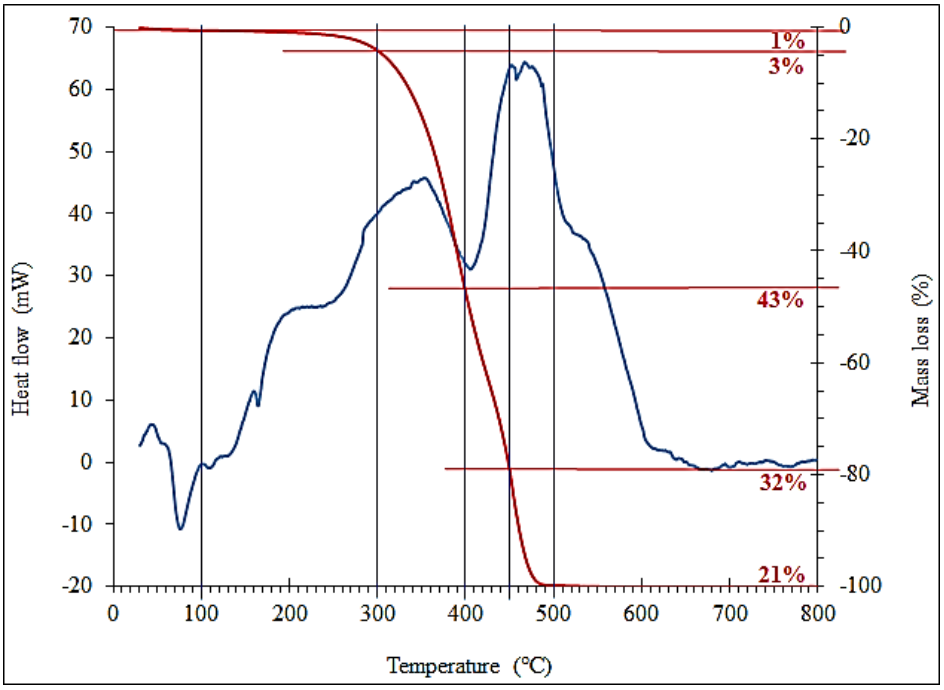

(a)

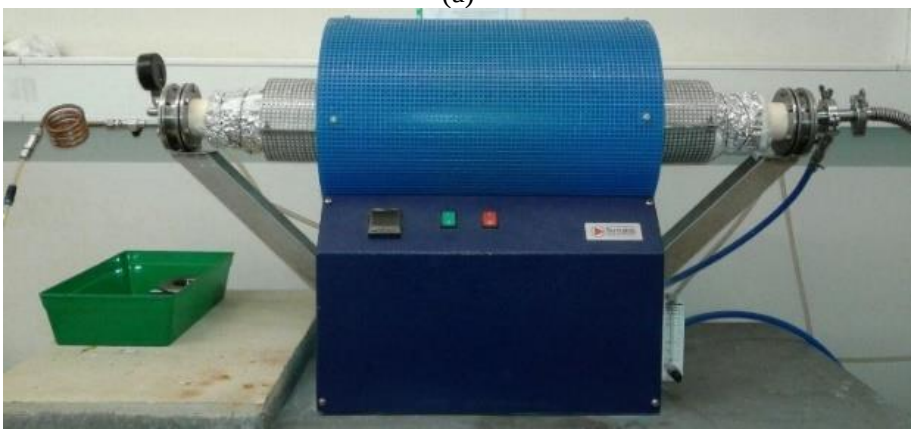

(b)

Figure 2.16 *Determination of the critical degradation temperature steps (red lines) and the weight loss portion (in %) at each step (a); horizontal resistance furnace for debinding or sintering with a controlled atmosphere (b).*

Two atmospheres were evaluated: Argon (99.999% purity) and Argon-Hydrogen (5 vol.% H_2). Each experiment comprised a primary evacuation, until almost 0.1 Pa, purging gas inside the tube until the pressure reaches slightly higher than the atmospheric (101 kPa < P < 150 kPa), this action was repeated three times, afterwards, a gas flow rate of 0.833×10^{-5} m^3s^{-1} and a pressure slightly greater than the atmospheric runs throughout the debinding process (heating and cooling), this process was performed in a debinding furnace illustrated in Figure 2.16b.

The effect of holding time and two heating rates, 1 ℃/min and 5 ℃/min, were evaluated on the debinding efficiency. This was carried out using equation 2.2, a weight control approach, by which the amount of binder remaining in a brown specimen after debinding is calculated. These calculations are based on the theoretical weight of the powder in the green specimen obtained by equation 2.3. In this evaluation it is assumed that the powder and binder are perfectly distributed in the feedstock.

$$\textit{Remaining binder} = ((\textit{Brown weight} - \textit{Powder concentration weight})/\textit{Powder concentration weight})\times 100 \quad (2.2)$$

$$\textit{Powder concentration weight} = \textit{powder density} \times \textit{powder concentration} \times (\textit{green weight}/\textit{green density}^{13}) \quad (2.3)$$

Different sintering trays were used to minimize the presence of the trapped oxygen in the debinding environment, these included porous ceramic, dense pure alumina, Ti6Al4V or AISI 304 sheets.

2.9 Sintering

The brown parts or any other compacted specimens, such as disk-like compacted metal powders or nanocomposite mixtures, were sintered in a horizontal resistance furnace (Figure 2.17) which is connected to a high vacuum turbo molecular pump ($\leq 5\times10^{-3}$ Pa). The heating and cooling rates were always 5 ℃/min and the heating cycle was started after evacuation.

The sintering temperature was selected as 640 ℃ [5, 13] and 1250 ℃ for the Al and 316L specimens, respectively, with a holding time of 120 minutes. Later, the effects of compaction pressure, by a uniaxial pressure, and sintering atmosphere on the densification of the disk-like specimens with 10 mm diameter and ~2 mm thickness, will be discussed in chapter five.

[13] This can be measured by pycnometer or calculated through Equation 2.1.

Figure 2.17 *Horizontal furnace for sintering, assembled with high vacuum system.*

References:

[1] T. Ronnhult, B. Brox, G. Fritze, **Scanning**, **9** (1987) 81-87.

[2] E.W. Sequeiros, V.C. Neto, M.T. Vieira, M.F. Vieira, **Powder Metall.**, **57** (2014) 241-244, 10.1179/0032589914z.000000000193.

[3] J.H. Meng, N.H. Loh, G. Fu, S.B. Tor, B.Y. Tay, **Journal of Alloys and Compounds**, **496** (2010) 293-299, 10.1016/j.jallcom.2010.01.147.

[4] J. Zhang, M. Sahli, J.C. Gelin, T. Barriere, **International Journal of Advanced Manufacturing Technology**, **77** (2015) 2135-2149, 10.1007/s00170-014-6595-8.

[5] S. Simões, F. Viana, M.A.L. Reis, M.F. Vieira, **Composite Structures**, **108** (2014) 992-1000, 10.1016/j.compstruct.2013.10.043.

[6] P. Krizik, M. Balog, E. Illekova, P. Svec, I. Matko, M. Stepanek, M. Nosko, F. Simancik, **Journal of Materials Processing Technology**, **214** (2014) 1165-1172, 10.1016/j.jmatprotec.2014.01.003.

[7] M. El-Tahawy, Y. Huang, T. Um, H. Choe, J.L. Lábár, T.G. Langdon, J. Gubicza, **Journal of Materials Research and Technology**, **6** (2017) 339-347, https://doi.org/10.1016/j.jmrt.2017.05.001.

[8] R.A. DiLeo, B.J. Landi, R.P. Raffaelle, **Journal of Applied Physics**, **101** (2007) 10.1063/1.2712152.

[9] S. Simões, F. Viana, M.A.L. Reis, M.F. Vieira, **Composite Structures**, **126** (2015) 114-122, 10.1016/j.compstruct.2015.02.062.

[10] R.K. Enneti, V.P. Onbattuvelli, S.V. Atre, 4 - Powder binder formulation and compound manufacture in metal injection molding (MIM) A2 - Heaney, Donald F, Handbook of Metal Injection Molding, Woodhead Publishing2012, pp. 64-92.

[11] E.W. Sequeiros, Microfabricação de Componentes Metálicos por Microgravação, Department of Materials and Metallurgical Engineering, **University of Porto**, 2014.

[12] G. Fu, S. Tor, N. Loh, D. Hardt, **Applied Physics A: Materials Science & Processing**, **97** (2009) 925-931, 10.1007/s00339-009-5363-3.

[13] L. Acar, H.O. Gulsoy, **Powder Metall.**, **54** (2011) 427-431, 10.1179/003258910x12740974839558.

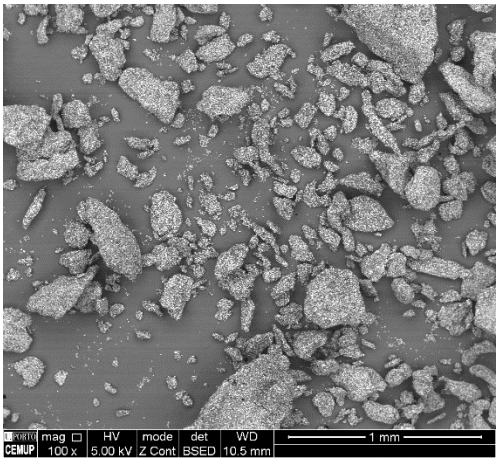

Chapter 3 – Feedstocks

3.1 Introduction

Micro hot embossing is a well-known replicating technique to produce polymeric microcomponents [1]. This technique could be adapted to produce metallic parts from powder [2], following a homothetic path to that of injection moulding and powder injection moulding. In this adaptation, the feedstock preparation is then necessary which is followed by shaping, debinding and sintering.

Related studies reported the replication of components using 316L, Cu, Fe-Ni, and WC-Co feedstocks [2-6], their compositions were prepared based on their CPVC values. This parameter can be measured through the optimization process by plotting the torque mixing values versus powder contents [7]. As already mentioned, CPVC value is determined as the content of powder at which the torque rate increases significantly with respect to the previous concentration.

Micro hot embossing can be helpful for different applications as long as it will be demonstrated its application for different powders, particularly Al and its alloys and nanocomposites based on Al and stainless steel [8]. This study discusses the preparation and characterization of Al and stainless-steel 316L feedstocks, with and without MWCNT. This allotrope of carbon was selected because it is a strong and stiff nanomaterial, widely used for strengthening metal matrices [9]. The evaluation of the MWCNT effects on the feedstock characteristics and replicability is of crucial importance.

In this section, the torque rheometer was used for the feedstock preparation. The homogeneity was evaluated through controlling the torque change during the mixing, i.e. it is considered that the mixture is uniformly dispersed when the torque reaches a steady state [10]. The

homogeneity[14] evaluation was complemented by microstructural analysis. The as prepared feedstocks were granulated, sieved and their homogeneity and dispersion were analysed by SEM as well.

3.2 The effect of powder on the optimization process

Torque value represents the energy required for mixing materials at a certain volume and specified processing conditions and it can be used to evaluate the behaviour of the constituents during mixing. Meanwhile, this value can also represent the viscosity, in terms of powder concentration, considering that the torque value grows with increasing the viscosity of powder-binder mixture [10]. Figure 3.1 illustrates the optimization results and how the CPVC values of Al and 316L powders were determined, the preparation procedure was explained in Section 2.5.

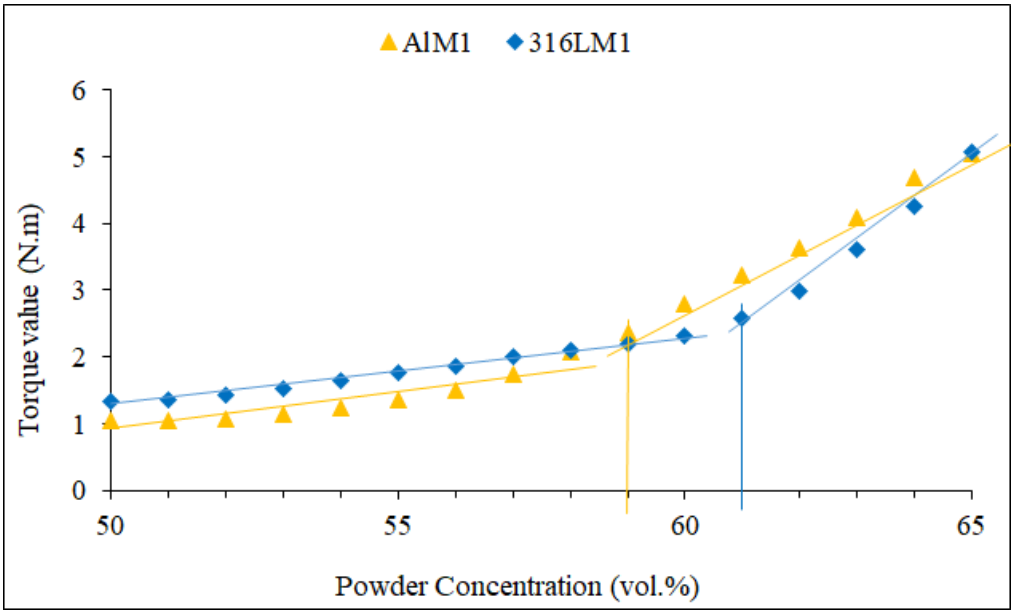

Figure 3.1 *Torque values function of powder concentration for Al and 316L mixed with the M1 binder, using Z-blade mixer at 30 rpm, 175 °C and the atmospheric pressure (101 kPa).*

Figure 3.1 illustrates that as the powder content increases the required mixing torque rises, as expected. The graph presents two regions: in the first region, for values smaller than 59 vol.% powder concentration, in which the torque values of 316L are higher than those of Al, while in the second region this order inverts. In the former one, the difference can be attributed to the

[14] The homogeneity of a feedstock in SEM microstructures was evaluated by the distribution of dark regions (representing a higher binder concentration).

particle size, that is, the finer powder (316L) has higher viscosity [11] and this effect was expected to be accentuated for higher powder concentration due to the increase of the friction caused by the powder interactions [12]. However, this difference is practically constant up to a powder concentration close to 59%, after which the Al torque value grows faster with the powder concentration and exceeds the 316L value. This behaviour can be attributed to the powder shape, i.e. irregular shaped particles lead to higher viscosities due to friction increase [11]. Moreover, the optimization process was longer (120 minutes) for the Al than for the 316L (80 minutes). This difference was resulted from the time required for the stabilization of the torque value for each incremental step. The results indicate that the difference in torque stabilization time can be attributed to the powder shape of the particulates, although the Al powder was larger than the 316L meaning less surface area and sooner interaction with binder, but the Al required larger time (more than 5 minutes for most increments) to interact with the binder to reach stability. Therefore, it is expected that the 316L feedstock can be homogenized faster than the Al one.

The CPVC values of the Al and 316L powders are defined as 59 and 61 vol.% (the orange and blue lines in Figure 3.1, respectively), this selection was easier for the 316L than for the Al because a sudden change and 61 vol.% is easily distinguished for the stainless steel powder. Although the 316L powder has a smaller PSD (meaning higher surface area) than the Al, it obtained a larger CPVC. This can be the consequence of having a shape factor very close to one (spherical) unlike the Al powder which has a larger one (see Figure 2.3). A small surface area justifies the more availability of binder to lubricate powder particles` surfaces but, in this study the irregular shaped Al particles diminished the effect of surface area of 316L powder. The effect of powder shape observed in this study is consistent with other researches [11, 13]. From the CPVC points onwards, the increase rate in the torque of the 316L-binder system exceeded that of the Al-binder. This different response could also be attributed to particles interactions being more affected by the powder shape and size for larger powder concentrations. The difference between the CPVC value of the 316L in the present study and others, using similar PSD, which reported values close to 66% [6, 14-16], can be attributed to the use of different types of binder or processing conditions (mixing temperature or speed). Regarding the PSD, a related study showed that the finer the powder, the smaller the CPVC obtained [12], i.e. providing a greater number of powder particles means more contact and friction between them. However, this was not observed in the present study, which indicates that CPVC is strongly

affected by the particle shape. This is consistent with a study in which it was shown that a powder size reduction (for half) did not influence the CPVC [16].

As above mentioned, it was difficult to distinguish a sudden torque change in the Al system (orange line in Figure 3.1). Therefore, the increment of two consecutive torque values as a function of powder content was plotted (Figure 3.2) in order to determine a proper powder concentration. This information was extracted from the same experiment performed for Figure 3.1. Thus, as it is seen in Figure 3.2, for the Al curve, there are two points, 59 and 63 vol.%, where the torque variation increases further in respect to their neighbouring points. This indicates that the optimum Al concentration of powder volume should be validated by the production of green parts, and it can be either 58 or 62 vol.% of powder. Regarding the 316L powder, the intersect of 60-61 vol.% belongs to the zone where the slope of the torque variation grows faster and 60 vol.% value can guarantee the replicability of components.

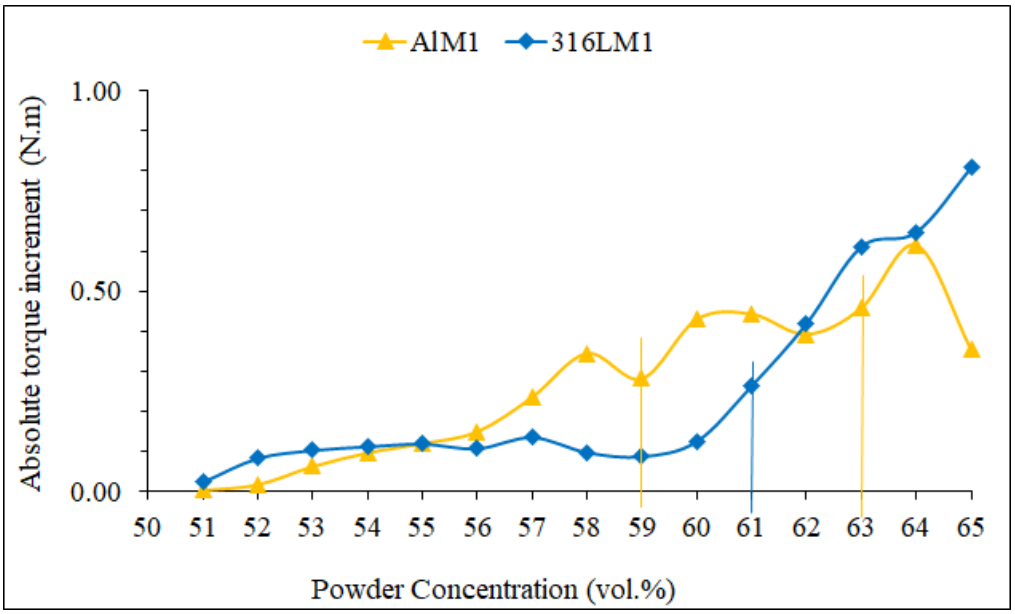

Figure 3.2 *Difference between two consecutive torques for the Al and AISI 316L powder-binder system.*

3.3 Effect of the composition on the torque value

Table 3.1 presents the acronym and some characteristics of the optimized Al and 316L feedstocks (58 vol.% and 60 vol.%, respectively). The major result concerns the effect of the addition of MWCNTs on the increase of the feedstocks viscosity, which is consistent with other studies [17-19]. In the Al-binder system the effect of 1 vol.% MWCNT is more pronounced than the increase of the powder by 4 vol.%. This increasing is attributed to the strengthening

effect of the nanotubes in the binder material [20]. The addition of SA decreased the viscosity of the Al and Al-MWCNT feedstocks. However, the increase of the SA from 1.6% to 5.0% did not result in a strong viscosity reduction [21-23]. Table 3.1 also showed no significant differences between the standard deviations, exception for Al65M1. Moreover, the average torque values of the Al65M1 and 316L65M1 are almost equal. The microstructure analysis of Al feedstocks with SA, prepared with the torque mixer, shows the presence of large porosities when SA is added to the feedstock (Figure 3.3). This reveals that the porosity may assist the viscosity reduction.

Table 3.1 Acronyms, compositions and mean torque values required for mixing of feedstocks, the mean values and the standard deviations were measured after the stabilization (almost 12 minutes).

Acronym	Constituents	Concentration (vol.%)	Torque (N.m)	Standard deviation
Al58M1	Al & M1	58:42	2.66	0.06
Al-MWCNT58M1	Al, CNT & M1	58(1):42	3.92	0.04
Al-MWCNT58M1SA5	Al, CNT, M1 & SA	58(1):425	1.97	0.07
Al62M1	Al & M1	62:38	3.63	0.08
Al62M1SA1.6	Al, M1 & SA	62:38(1.6)	2.00	0.05
Al62M1SA5	Al, M1 & SA	62:38(5)	1.58	0.04
Al65M1	Al & M1	65:35	5.05	0.13
316L60M1	316L & M1	60:40	2.76	0.05
316L-MWCNT60M1	316L, CNT & M1	60(1):40	3.79	0.07
316L65M1	316L & M1	65:35	5.06	0.09

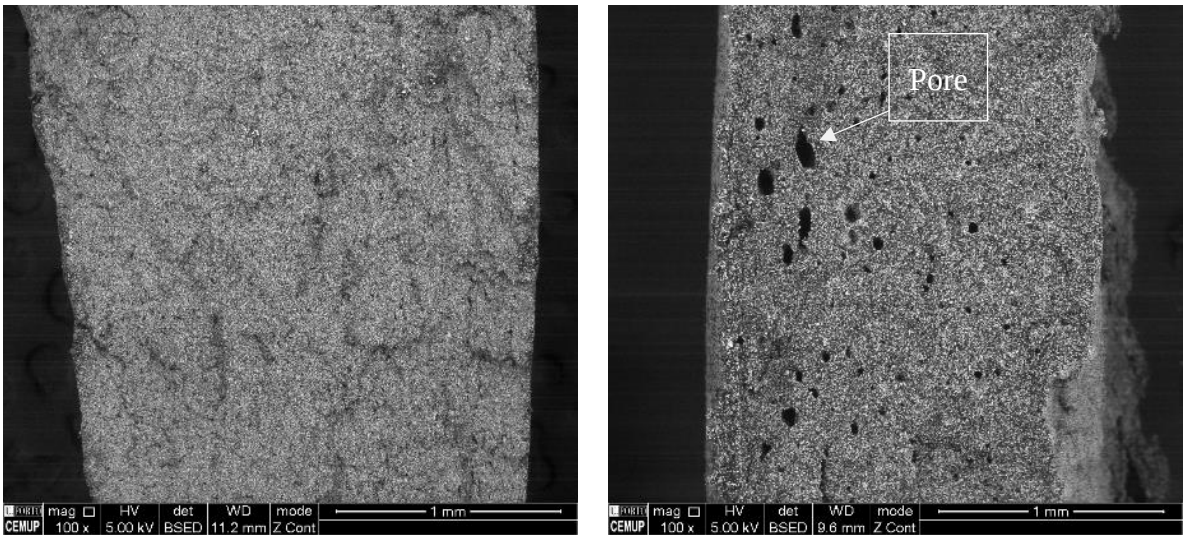

(a) (b)

Figure 3.3 *Feedstocks prepared by torque mixer of Al62M1 (a) and Al62M1SA1.6 (b) (SEM/BSE).*

3.4 Torque values and homogeneity

Figure 3.4a illustrates the torque variations of the Al58M1, Al-MWCNT58M1 and Al-MWCNT58M1SA5 feedstocks. The unstable initial stage belongs to Al-MWCNT58M1 and the great fluctuation could be attributed to the dispersion and interaction of the MWCNT with the binder during the earliest mixing period. The addition of SA delayed the stabilization stage, however, all feedstocks reached steady state after 17 minutes which will be considered as the typical mixing time for Al feedstocks. The mixing time was not prolonged further to avoid losing the binder properties. The microstructure confirmed no differences in the dispersion of the feedstocks constituents. Although some authors reported a good wettability of CNTs in some polymeric materials feedstocks, like polypropylene and polyethylene glycol [24], in the present study the MWCNT aggregations still existed after torque mixing and extrusion, with or without SA (Figure 3.4b), due to the difference of the polymeric materials constituting the binder.

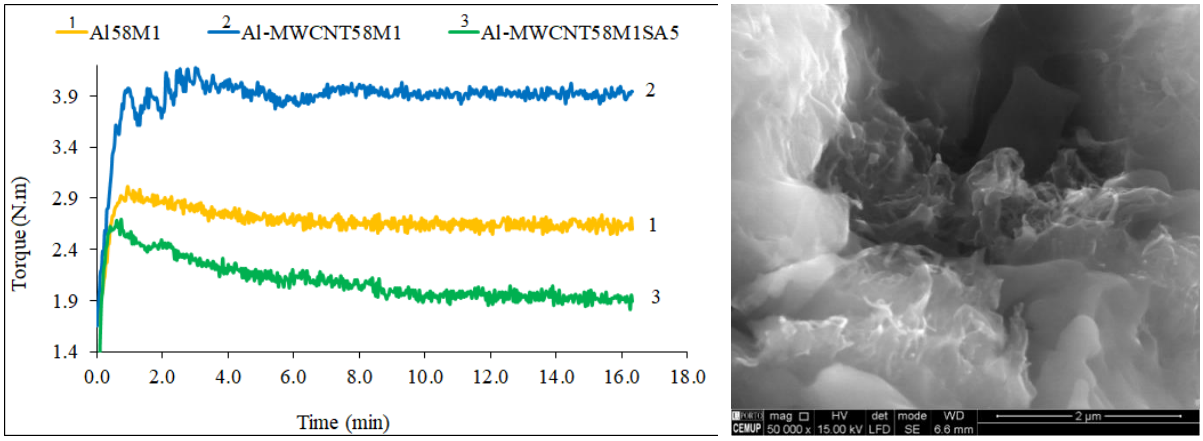

(a) (b)

Figure 3.4 *Torque variation in the optimization of Al feedstocks, with and without additives, during mixing (a); the microstructure of the MWCNT clusters in the binder material (SEM/BSE) (b).*

The torque changes during mixing of the 316L60M1 and 316L-MWCNT60M1 feedstocks are shown in Figure 3.5a. The addition of the MWCNT delayed the torque stabilization. However, the steady state was attained and even maintained until 25 minutes (typical mixing time for 316L feedstocks) (Figure 3.5a). The effect of the MWCNT presence on the viscosity of the 316L-MWCNT feedstock is an increase of the torque value, as already mentioned. This difference can be attributed to the untangling of MWCNTs during torque mixing, although this untangling is not complete, since the microstructure revealed the presence of nanotube clusters (Figure 3.5b). The comparison of torque values for Al and 316L, with and without MWCNTs,

shows a similarity in values between them (Figure 3.5c), which highlights the effect of using the same binder system for all feedstocks [25].

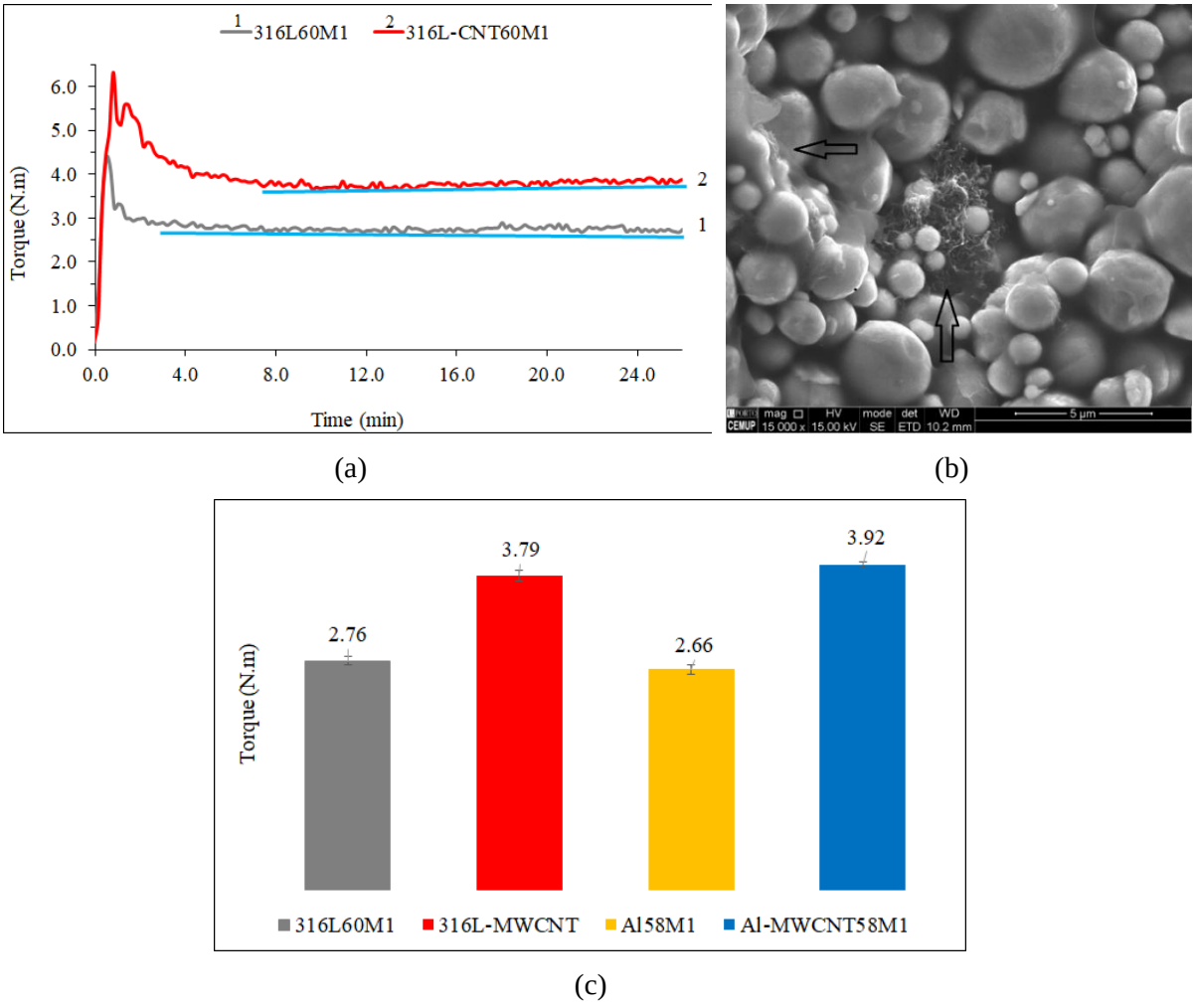

Figure 3.5 *Torque variation in the 316L and 316L-MWCNT feedstocks (a); microstructure of 316L-MWCNT60M1 (the arrows indicate the MWCNT agglomerates) (b); comparing the torque values of the optimized Al and 316L systems (c).*

3.5 Dispersion and homogeneity of the feedstocks

Figure 3.6 shows the distribution of the Al powder and binder in the feedstock, highlighting that the SEM/BSE mode contributes to a better understanding of the dispersion than the SEM/SE mode. Figure 3.7 illustrates the distribution of the constituents of the Al58M1 feedstock before and after extrusion. The extrusion increased the dispersion and eliminated the porosity; however, some Al powder plastic deformation occurred (Figure 3.7c). Crushing Al feedstock through the application of an industrial granulator (Figure 2.9c) required three batches of feedstocks prepared by Plastograph and also had a low producing efficiency, ~12

wt.%, of fine particles (< 500 µm) (Figure 3.8), and induced powder cutting (Figure 3.9a and 3.9b). This latter problem produces fresh Al surfaces, meaning more superficial oxide formation, with no binder in the surface.

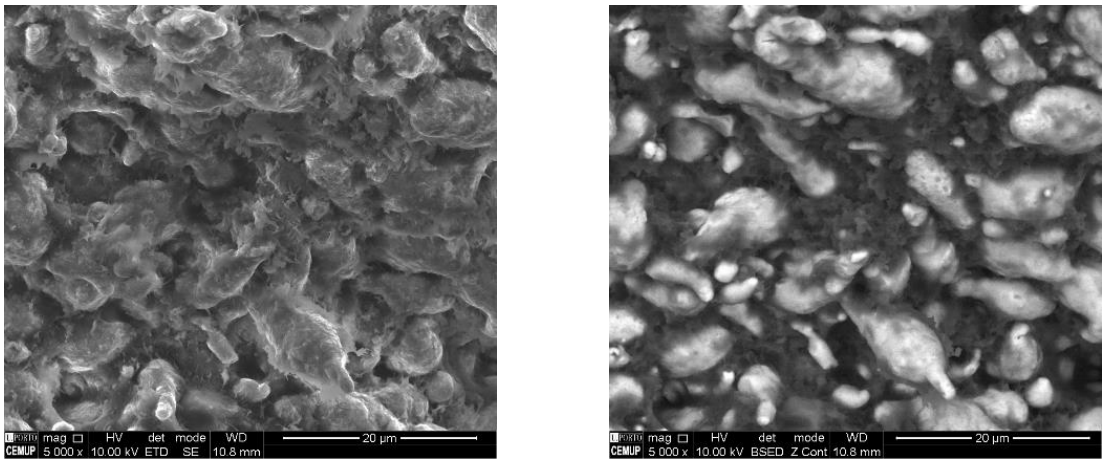

(a) (b)

Figure 3.6. *Microstructure of Al58M1 feedstock by SE (a) and BSE (b) modes, respectively, from same position (SEM).*

The use of another crushing process, like mortar and pestle, did not depend on any minimum feedstock mass. Most of the feedstock was crushed down to fine particulates, but the technique deformed the Al powder more than the granulator (Figure 3.9c). The blender (Figure 2.9e) was the last piece of equipment used to crush the raw material, it required no minimum quantity of feedstock either. With this process almost half of the feedstock was reduced to fine particles (< 500 µm). Three blending sequences were made, in a total of one-minute, and then the crushed particles were sieved. Microstructural analysis after blending revealed this technique introduced less damage to the particles (Figure 3.9d) than the other two. The relative density values (Table 3.2) confirm that the powder and binder separation after blending is not significant; the slightly lower relative density for the AlMWCNT58M1 could be attributed to a slight separation, aggregations or porosity. A more detailed microstructural analysis of the extruded Al-MWCNT feedstock (after crushing) revealed the presence of the nanotube clusters (Figure 3.10a). The same analysis of AISI 316L feedstocks showed that after torque mixing the constituents were well distributed with a negligible amount of voids (Figure 3.10b to 3.10f). Therefore, the 316L60M1 and 316L-MWCNT60M1 feedstocks were not extruded, and this is attributed to the extension of the mixing time to 25 minutes.

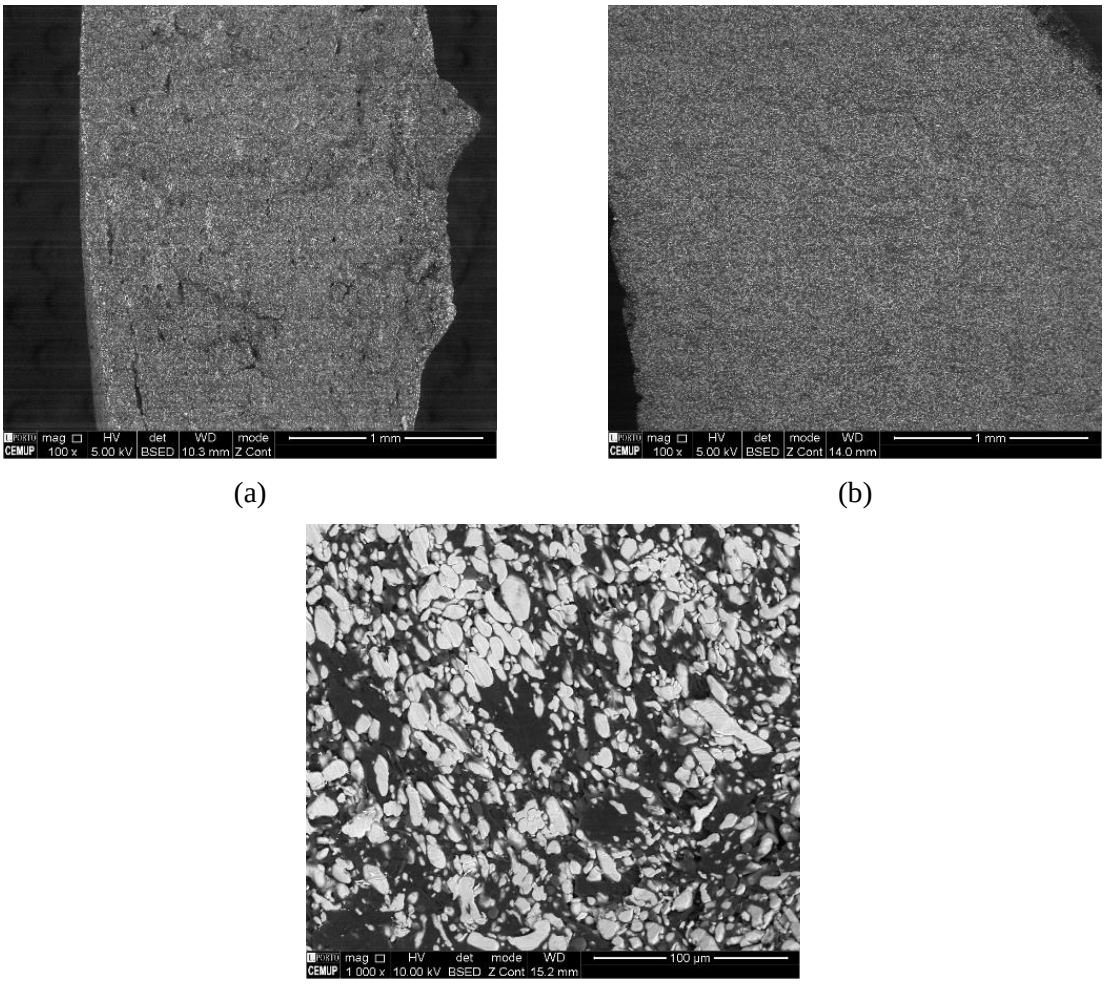

(a) (b)

(c)

Figure 3.7 *Microstructure of Al58M1 feedstock from the cross sections after torque mixing (a) after extrusion (b); the deformed Al powders after extrusion (c) (SEM/SE).*

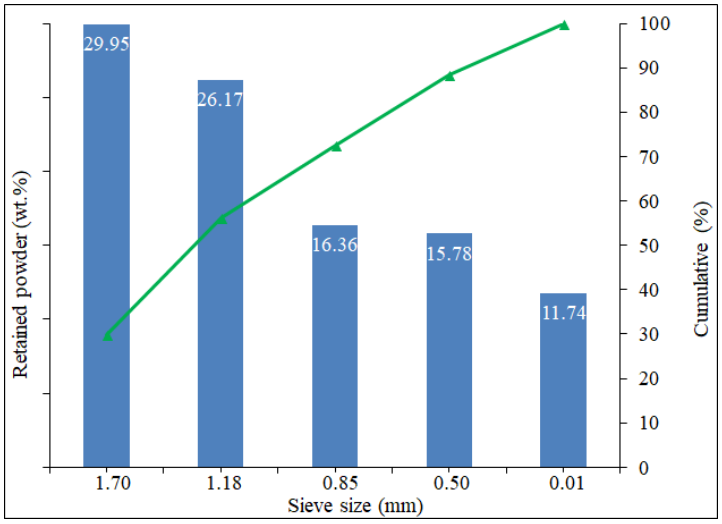

Figure 3.8 *Sieve analysis from the Al62M1 feedstock (three batched prepared by torque mixing) granulated by the industrial granulator equipment.*

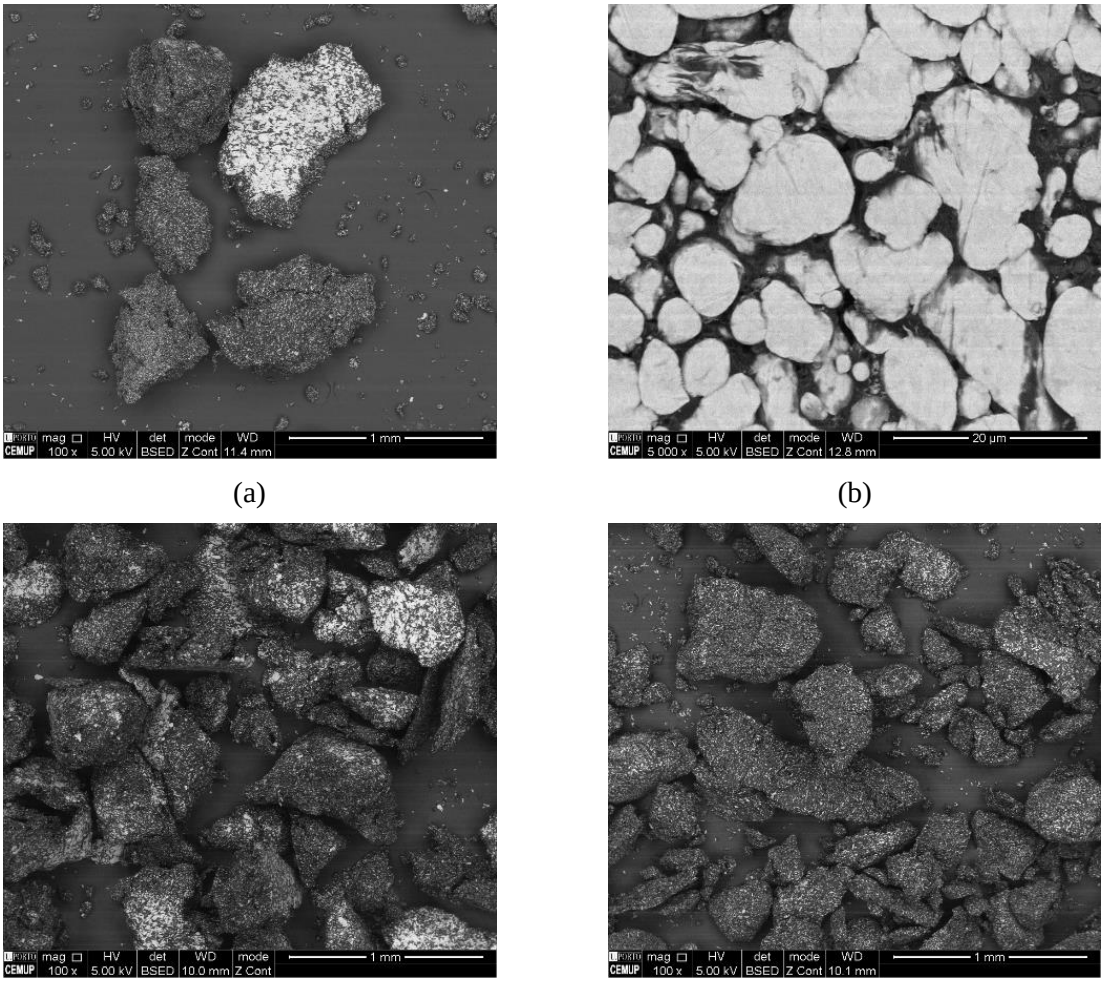

(a) (b)

(c) (d)

Figure 3.9 *Microstructure of granulated AlM1 feedstock (<500 µm) prepared by industrial granulator (a) and (b), mortar and pestle (c), and blender (d), white regions represent deformed Al powder particles found without binder.*

Table 3.2 Density evaluation of two Al feedstocks.

Feedstock	**Measured density[15] (kg/m^3)**	**Theoretical density[16] (kg/m^3)**	**Relative density[17] (%)**
Al58M1	1937	1955	99
AlMWCNT58M1	1907	1951	98

[15] From feedstock particles (< 500 µm), measured by gas pycnometer.

[16] Cf. Table 2.4, section 2.3.1, and equation 2.1, the effect of losing volatile components during preparation is excluded.

[17] Measured density over the theoretical density.

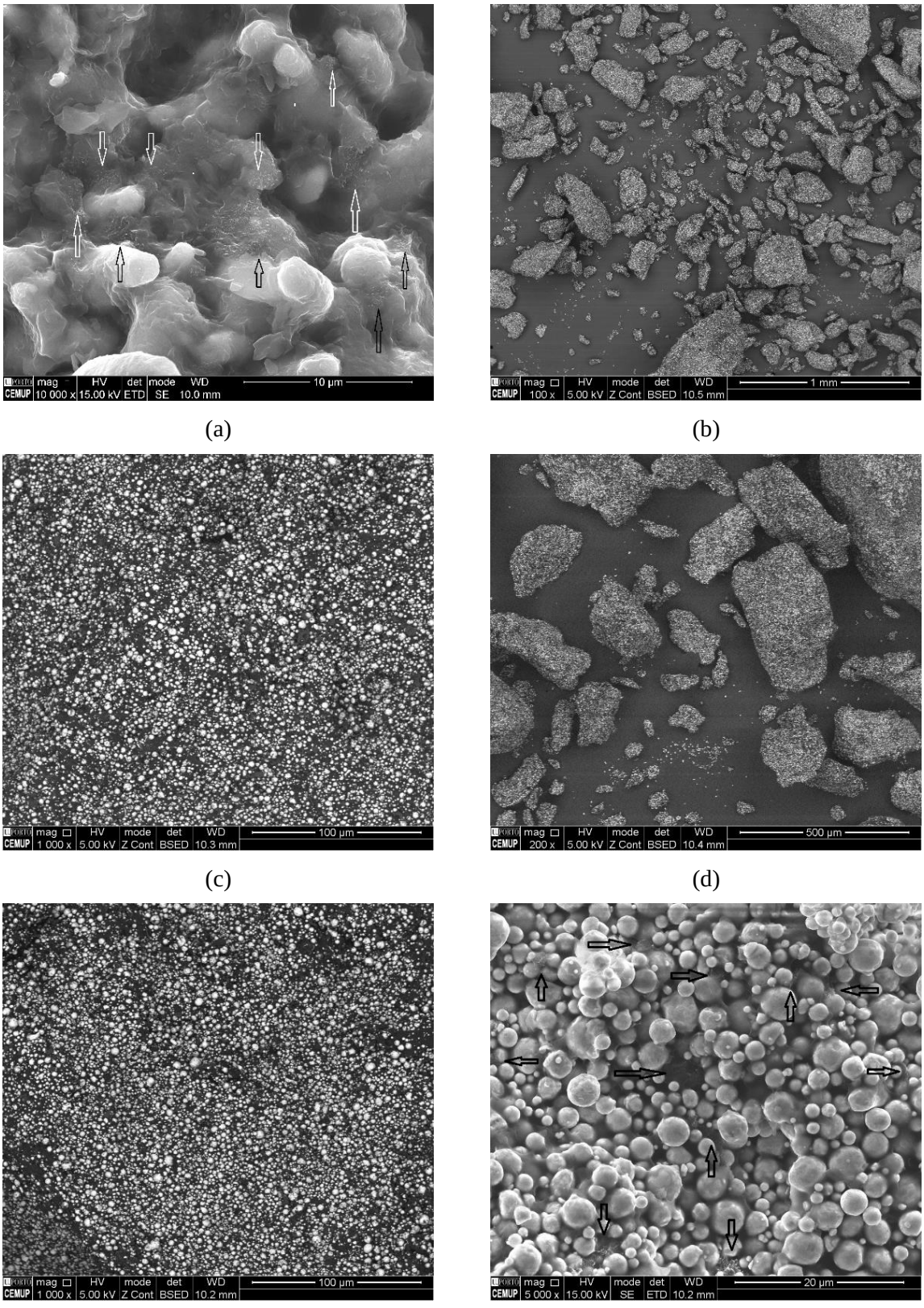

(a) (b)

(c) (d)

(e) (f)

Figure 3.10 *Microdispersion in feedstocks: Al-MWCNT after extrusion (a); 316L60M1 (b) and (c); 316L-MWCNT60M1 (d), (e) and (f), (the arrows indicate the MWCNT agglomerates), (SEM).*

3.6 Conclusions

Feedstocks based on Al and 316L powders, with and without MWCNT, were prepared. The selection of powder concentration for feedstock was based on the CPVC value through an optimized process (Plastograph). The control of the torque variations during feedstock mixing showed that the different compositions reached the steady state at the typical mixing time. In this study the optimized Al and 316L feedstocks, with 1 vol.% MWCNT, and the feedstocks with 65 vol.% powder concentrations required similar torque mixing values. The addition of 1 vol.% of MWCNT increased the initial torque fluctuations and the viscosity of the feedstocks, which was overcome by the addition of the SA. The torque variations also revealed that the interaction of the MWCNT in the Al and AISI 316L feedstocks was similar.

Microstructural analysis confirmed the apparent homogeneity of the feedstocks. MWCNT agglomerations were observed even after extrusion, this technique contributed to decreasing the porosity of the feedstocks due to mixing process. The granulation of the Al feedstocks is more critical than for the 316L stainless steel ones. The blender is a feasible granulating technique for feedstock preparation.

References:

[1] M. Heckele, W. Bacher, K.D. Muller, **Microsystem Technologies**, **4** (1998) 122-124, 10.1007/s005420050112.

[2] G. Fu, S. Tor, N. Loh, D. Hardt, **Applied Physics A: Materials Science & Processing**, **97** (2009) 925-931, 10.1007/s00339-009-5363-3.

[3] E.W. Sequeiros, V.C. Neto, M.T. Vieira, M.F. Vieira, **Powder Metall.**, **57** (2014) 241-244, 10.1179/0032589914z.000000000193.

[4] M. Sahli, C. Millot, J.C. Gelin, T. Barrière, **Journal of Materials Processing Technology**, **213** (2013) 913-925, 10.1016/j.jmatprotec.2012.11.007.

[5] M. Sahli, C. Millot, J.C. Gelin, T. Barrière, **AIP Conference Proceedings**.

[6] M. Sahli, J.C. Gelin, T. Barriere, **Powder Technology**, **246** (2013) 284-302, 10.1016/j.powtec.2013.05.026.

[7] F.M. Barreiros, M.T. Vieira, **Ceramics International**, **32** (2006) 297-302, 10.1016/j.ceramint.2005.03.006.

[8] H.Z. Ye, X.Y. Liu, H.P. Hong, **Journal of Materials Processing Technology**, **200** (2008) 12-24, 10.1016/j.jmatprotec.2007.10.066.

[9] S.R. Bakshi, D. Lahiri, A. Agarwal, **International Materials Reviews**, **55** (2010) 41-64, 10.1179/095066009x12572530170543.

[10] R. Supati, N. Loh, K. Khor, S. Tor, **Materials Letters**, **46** (2000) 109-114, 10.1016/S0167-577X(00)00151-8.

[11] R.K. Enneti, V.P. Onbattuvelli, S.V. Atre, 4 - Powder binder formulation and compound manufacture in metal injection molding (MIM) A2 - Heaney, Donald F, Handbook of Metal Injection Molding, Woodhead Publishing2012, pp. 64-92.

[12] M. Sotomayor, A. Várez, B. Levenfeld, **Powder Technology**, **200** (2010) 30-36, 10.1016/j.powtec.2010.02.003.

[13] D.F. Heaney, 3 - Powders for metal injection molding (MIM), Handbook of Metal Injection Molding, Woodhead Publishing2012, pp. 50-63.

[14] F.M. Barreiros, M.T. Vieira, J.M. Castanho, **Metal Powder Report**, **64** (2009) 18-21, 10.1016/S0026-0657(09)70215-2.

[15] X. Kong, T. Barriere, J. Gelin, **Journal of Materials Processing Technology**, **212** (2012) 2173-2182, 10.1016/j.jmatprotec.2012.05.023.

[16] E.W. Sequeiros, Microfabricação de Componentes Metálicos por Microgravação, Department of Materials and Metallurgical Engineering, **University of Porto**, 2014.

[17] T.J. Ferreira, M.T. Vieira, **Euro PM 2014 Congress and Exhibition, Proceedings**.

[18] F. Ahmad, A.S. Muhsan, M.R. Raza, **7th International Conference on MEMS, NANO and Smart Systems, ICMENS 2011;** , **Advanced Materials Research**, **403-408** (2012) 5335-5340, 10.4028/www.scientific.net/AMR.403-408.5335.

[19] S.Q. Liang, Y. Tang, Y. Zhang, J. Zhong, The rheologyical effect of carbon nanotubes on the iron based metal powder injection molding feedstock, in: Y.S. Yin, X. Wang (Eds.) Multi-Functional Materials and Structures Ii, Pts 1 and 22009, pp. 469-472.

[20] Z. Spitalsky, D. Tasis, K. Papagelis, C. Galiotis, **Progress in Polymer Science**, **35** (2010) 357-401, 10.1016/j.progpolymsci.2009.09.003.

[21] Y.M. Li, X.Q. Liu, F.H. Luo, J.L. Yue, **Transactions of Nonferrous Metals Society of China**, **17** (2007) 1-8, 10.1016/s1003-6326(07)60039-9.

[22] T.J. Ferreira, M.T. Vieira, **Ciencia e Tecnologia dos Materiais**, **29** (2017) e87-e91, 10.1016/j.ctmat.2016.07.010.

[23] M. Sahli, J.C. Gelin, **International Journal of Advanced Manufacturing Technology**, **69** (2013) 2139-2148, 10.1007/s00170-013-5170-z.

[24] S. Nuriel, L. Liu, A.H. Barber, H.D. Wagner, **Chemical Physics Letters**, **404** (2005) 263-266, 10.1016/j.cplett.2005.01.072.

[25] S. Ahn, S.J. Park, S. Lee, S.V. Atre, R.M. German, **Powder Technology**, **193** (2009) 162-169, 10.1016/j.powtec.2009.03.010.

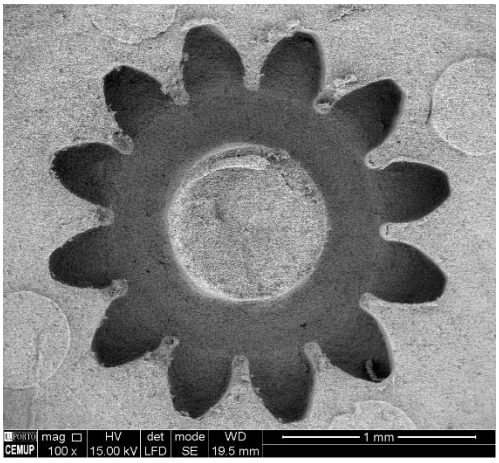

Chapter 4 – Shaping

4.1 Introduction

The production of microparts, with at least one dimension at microscale, through micro hot embossing of metal powder is feasible but only few types of geometries were reported. These involved micropins with dimensions of 100*200 μm [1]; microblocks with width and height of 200*200 μm [2]; circle-like convex and concave structures with depth/height of 100 μm and interconnected walls and channels of 100*100 μm [3, 4]; and, finally, concave and convex hemispherical-like geometries with features of 100 μm [5, 6]. The failure of a micro hot embossed gear specimen was also reported [7]. The processed materials included 316L stainless steel, Cu, Fe-Ni, and WC-Co [1-6].

These studies correlated replicability (shape retention and surface roughness) with processing conditions, such as temperature [1, 3, 4, 6, 8-11], pressure [3, 5, 7-9], and holding time [1, 4, 6, 8]. The replicability was associated with the pseudoplastic behavior and the mouldability of the feedstock, mixture of powder and binder with predetermined concentration, analyzed by capillary rheometry [11, 12].

The potential of micro hot embossing as a near net-shape micromanufacturing technology will increase when it will be extended to the shaping of different geometries of parts in advanced materials, such as Al nanocomposites [13]. The MWCNT were selected as the nanoreinforcement because they have extraordinary properties, such as high strength and stiffness, which make them especially appealing to reinforce metallic matrices [14, 15]. Micro hot embossing involves feedstock preparation (Chapter 3), shaping (by a warm uniaxial pressure compaction), debinding and sintering. Shaping is discussed in this chapter in detail,

and it involves the shaping evaluation, i.e. shape retention, dimensional control and surface roughness. This evaluation was carried out through qualitative and quantitative observations by Stereoscopy, SEM and IFM. Shore A hardness was performed to evaluate the stiffness of the elastomer die during shaping. Moreover, the ImageJ software was used to measure some dimensions in the acquired images.

4.2 Shaping through conventional methodology

The conventional shaping sequence by micro hot embossing using elastomer die comprises:

- filling the die cavity with feedstock particles,
- applying compaction pressure and temperature simultaneously until they reach the set points (the pressure reaches this point much faster than the temperature),
- holding the conditions for a certain time,
- cooling and demoulding.

This section evaluates how the shaping is affected by several factors: arrangement of the feedstock particle size, die filling, die assembly, granulation technique, feedstock composition (powder type and MWCNT addition), shaping geometries, and the elastomer die stiffness.

4.2.1 Effect of feedstock particle size

The evaluation of the shaping process started with the analysis of the effects of the feedstock particles. Figure 4.1 shows that the use of fine particles (< 500 μm) is required for better shaping through micro hot embossing with elastomer die. The image highlights that replicability and surface waviness were strongly dependent on the feedstock particle size independent of shaping pressure and holding time. However, the microscale concentric circles were replicated by both feedstocks, regardless of particle size.

4.2.2 Filling the die cavity

The shaping evaluation was proceeded observing the formation of the edge and the concentric circle configurations of the microblind flange. It was observed that during the conventional shaping methodology, if the die cavity is completely filled, without using the lid, the green specimen does not form straight profiles, as it is evident in the cross-section of Figure 4.2a, which will cause an extra machining process for the final part.

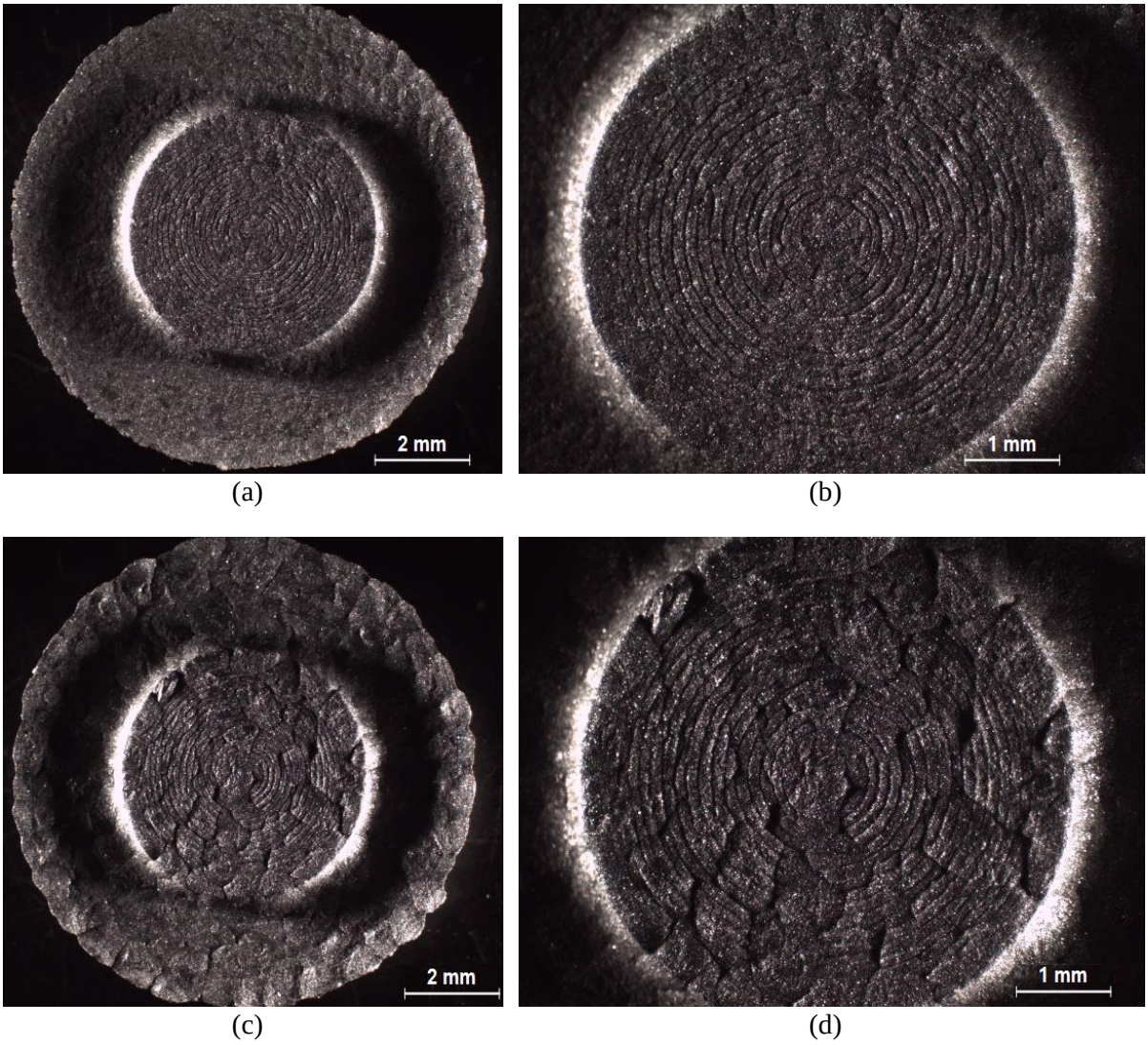

Figure 4.1 *Al58M1 microblind flange parts (shaped by dark blue elastomer die at 230 ℃ and 8.5 MPa for 30 minutes) with feedstock different particle sizes: <500 µm (a) and (b), 500 µm <particles< 850 µm (c) and (d) (stereoscopy).*

The roughness map (Figure 4.2b) illustrates a strong color gradient on the lowest platform, the cross-section profile (Figure 4.2c) also shows that the upper face is not completely flat. If this component is compared with the corresponding elastomer die (Figure 2.11), the shape and roughness are well replicated, but the profiles (sides) have a large difference (being of concave-like shape). This problem was eliminated by changing the shaping methodology, by partially filling the die cavity and placing a lid-like structure to cover the feedstock particles (Figure 4.3a). In this way, the green specimen will present parallel faces (Figure 4.3b to 4.3e) approaching the desired shape.

IFM observations of the concentric circles of the elastomer die and the green specimen (Figure 4.4) confirm the good shaping capability of the Al powder. However, the topography of the green specimen is comparatively larger. These colored maps illustrate that, although the surface is not flat, it is possible to distinguish grooves and valleys individually.

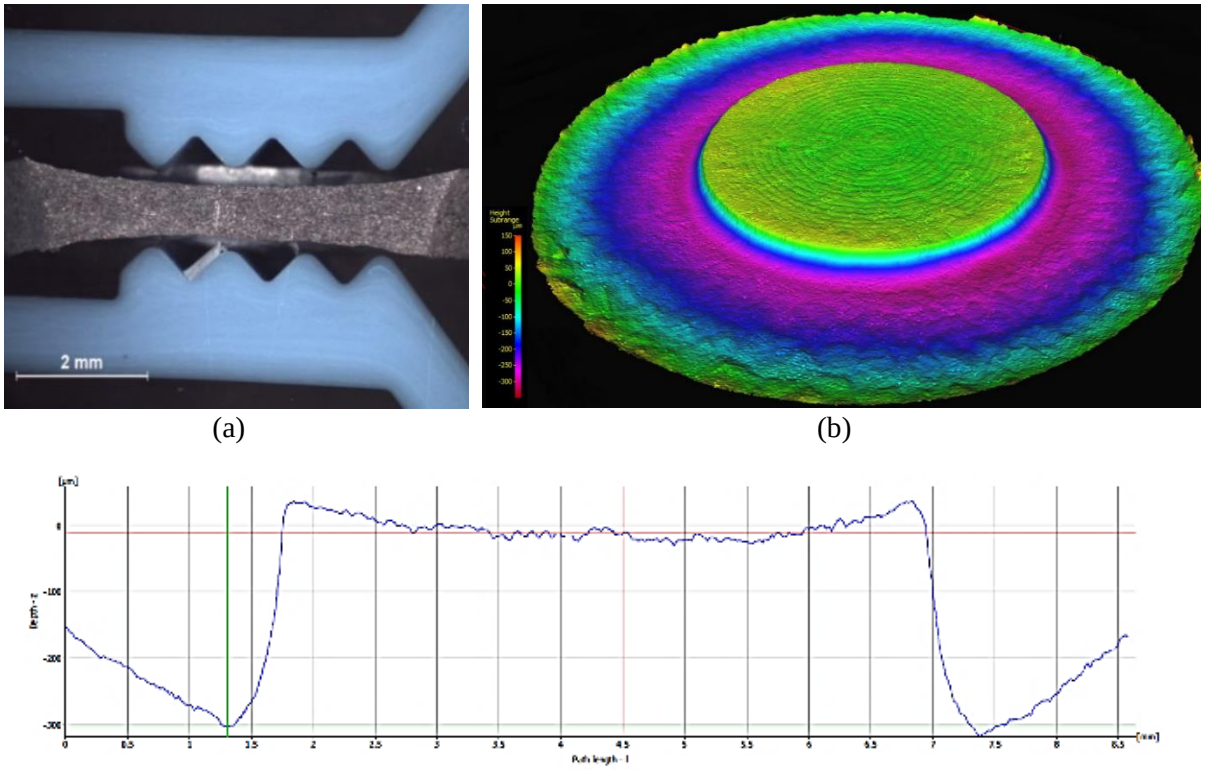

(a) (b)

(c)

Figure 4.2 *Concave distortion on a green microblind flange of an Al specimen (Al58M1), shaped by dark blue elastomer die at 230 °C and 8.5 MPa for 30 minutes as show in the image (a), the roughness map (b) and a cross section profile (c) (stereoscopy and IFM).*

The roughness parameters revealed that the green parts made of Al58M1 feedstocks have rougher surfaces than the dies and that the use of the lid gives a smoother surface (Figure 4.5a). The addition of carbon nanotubes to the feedstock also influenced the roughness and attenuated the importance of using the lid. The diameters of the green flanges were larger than those of the die while its height was smaller (Figure 4.5b). The use of the lid increased the diameter difference between the green specimen and the elastomer die.

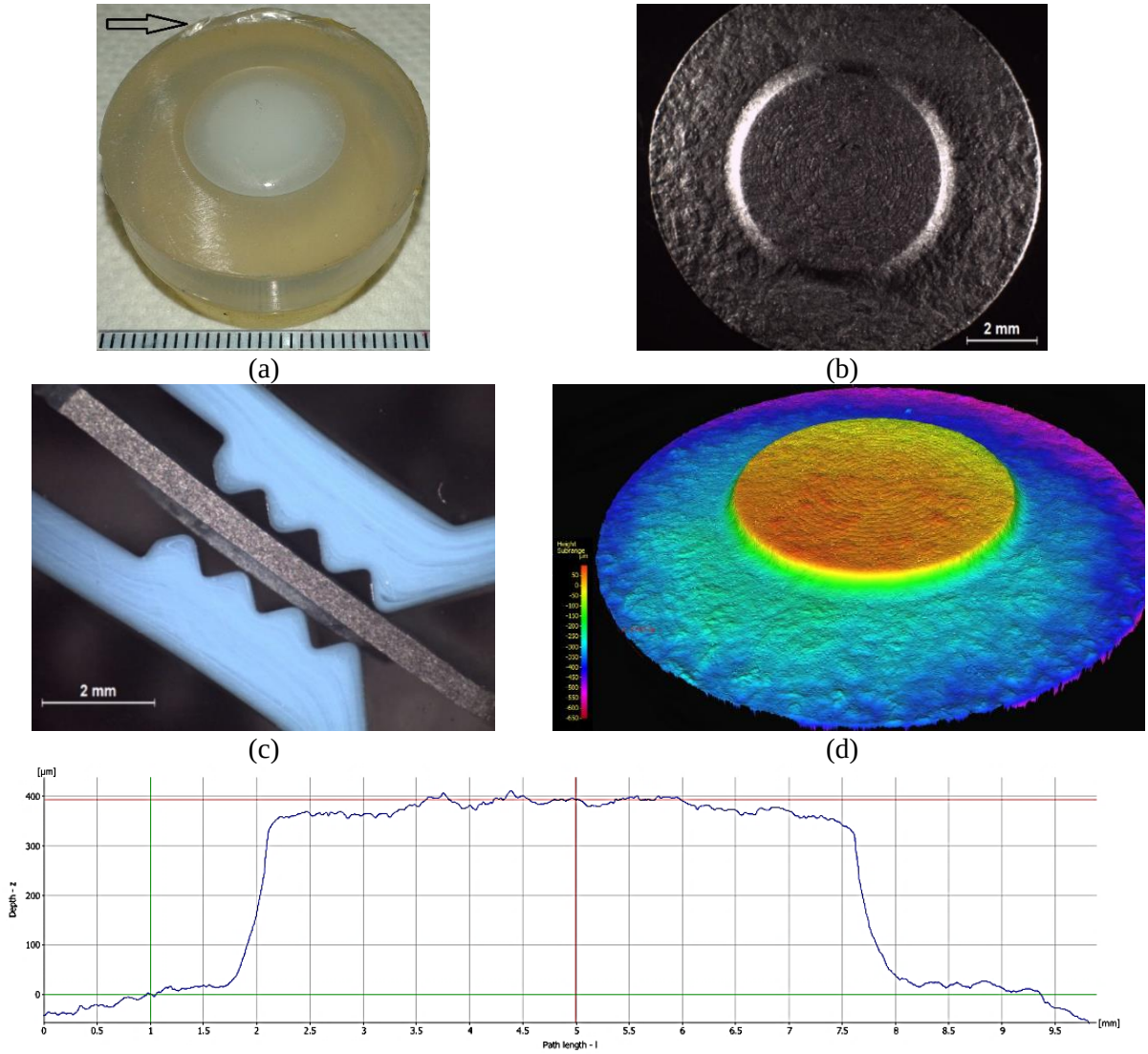

(a) (b) (c) (d) (e)

Figure 4.3 *Transparent elastomer die cavity partially filled and covered with a lid (a), microblind flange green specimen (Al58M1) with straight cross section profiles, shaped by the dark blue elastomer die (cf. 2.5) at 230 °C and 8.5 MPa for 30 minutes (b), (c); roughness map (d) and cross section profile (e) (stereoscopy and IFM).*

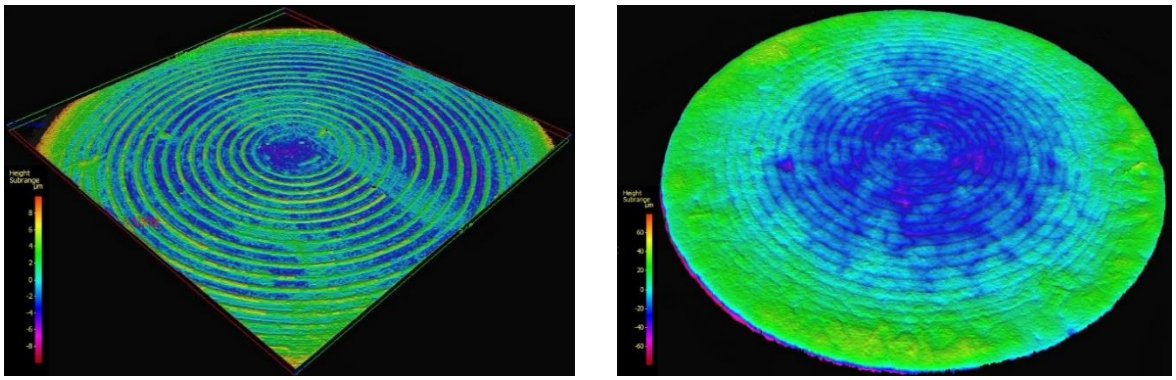

(a) (b)

Figure 4.4 *Dark blue elastomer die surface (a), and the corresponding green part surface (Al58M1), shaped at 230 °C and 8.5 MPa for 45 minutes using complete filling approach (b) (IFM).*

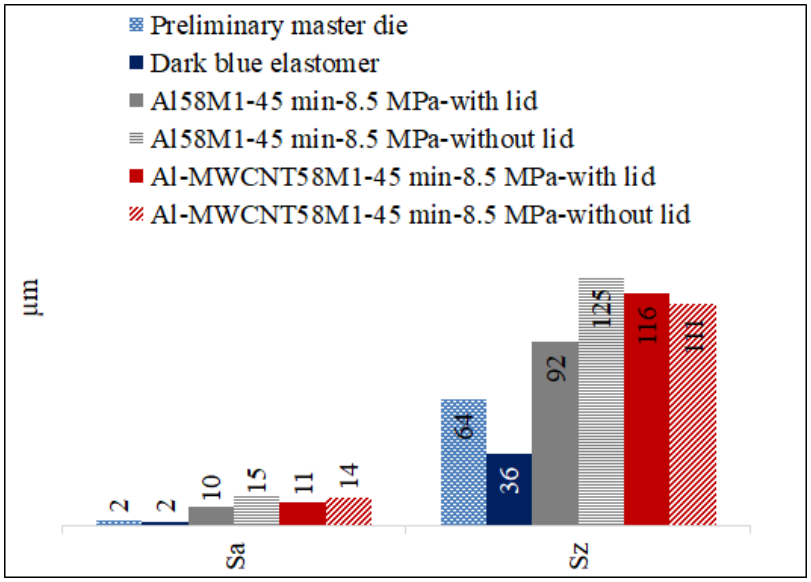

(a)

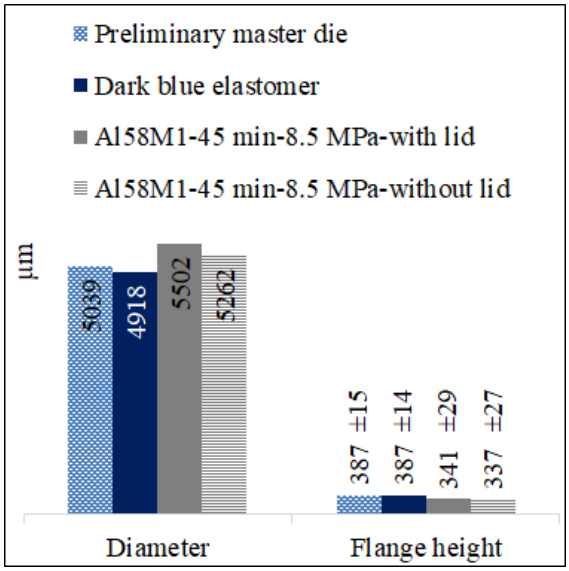

(b)

Figure 4.5 *Comparison of the roughness parameters (a) and dimensions (b) between the metal master die, the dark blue elastomer die and the green specimens made with Al-based feedstocks (obtained by IFM evaluation).*

4.2.3 Die assembling and lifetime

The elastomer die started to degrade from the circumferential edge after the second test (Figure 4.3a) and its degradation increases after each application. The duration of the elastomer die increased significantly when the upper support disk (part G in Figure 2.15b) was used. This disk should have parallel faces well fitted inside the holding cylinder so that the elastomer does

not flow out from the assembly during shaping. This correction can contribute to decreasing the distortion of the parts during compacting step avoiding shear forces in the elastomer die.

4.2.4 Effect of the granulation technique

The granulation technique greatly influences the homogeneity of the feedstock (Chapter 3). In addition to the deformation of the powders, the granulation using an industrial granulator or a mortar and pestle caused powder-binder separation, which is highlighted in the green parts shown in Figure 4.6. In this figure, the dark regions are rich in binder that indicates heterogeneous distribution and will lead to an increase in topography after debinding and sintering. This problem was not observed in the green specimens made of feedstock granulated by blender (Figure 4.7), with which the most homogeneous green part is obtained.

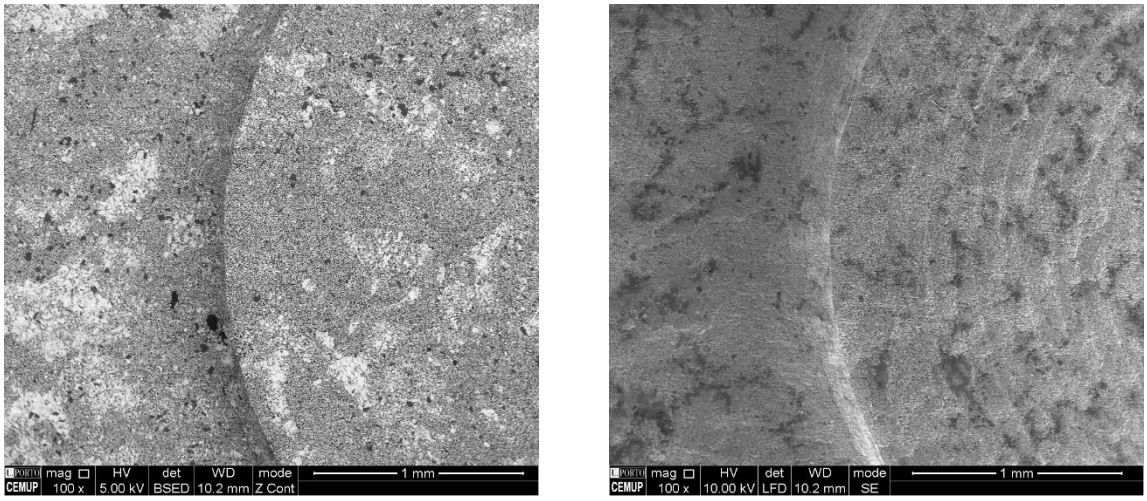

(a) (b)

Figure 4.6 *Microstructure of microblind flange green specimens (Al58M1) shaped at 230 ℃ and 8.5 MPa for 30 minutes in dark blue elastomer die granulated by mortar and pestle: SEM/BSE image (a) same region by SEM/SE mode (b).*

4.2.5 Effect of feedstock composition

The suitable Al powder concentration may range from 58 vol.% to 62 vol.% (Al58M1 and Al62M1), as mentioned in section 3.2. To find the optimal powder concentration, microscopic evaluation of the green specimens, made with different Al feedstock compositions, was performed. The microblind flange was used as the standard die.

The analysis of the green surfaces (Figure 4.8) shows that the best shaping was obtained only for the Al58M1 feedstock, the sharp edge and concentric circles were replicated by this

feedstock, with or without MWCNTs (Figures 4.8a and 4.8b, respectively). Thus, the powder concentration of 58 vol.% of Al was selected as the optimum composition.

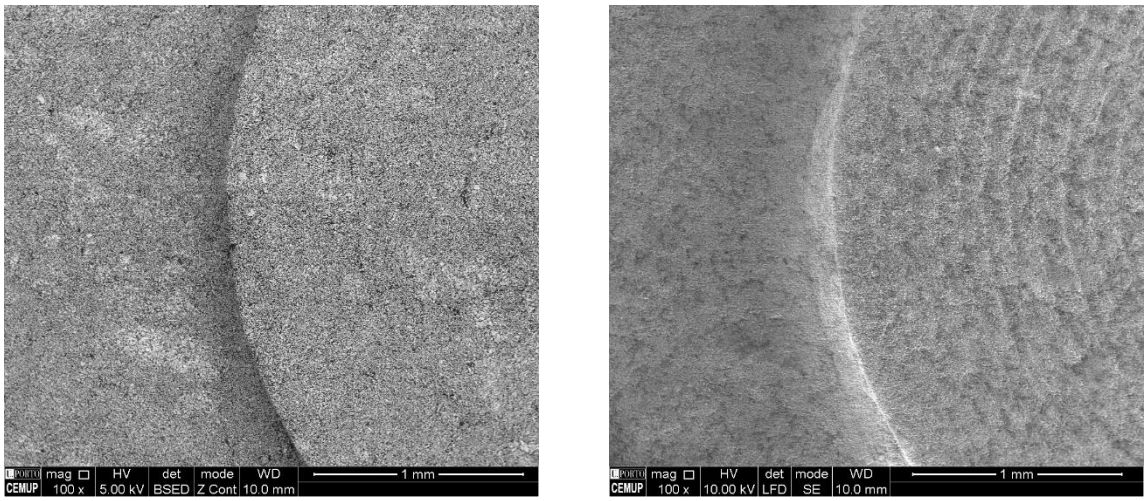

(a) (b)

Figure 4.7 *Microstructure of microblind flange green specimens (Al58M1) shaped at 230 ℃ and 8.5 MPa for 30 minutes in dark blue elastomer die granulated by blender: SEM/BSE image (a) same region by SEM/SE mode (b).*

The images of Figure 4.8 conjugated with the viscosity of the feedstocks (deduced from the torque values given in Table 3.1) indicate that the shaping by micro hot embossing is much more influenced by the powder concentration than by the viscosity. In fact, although the presence of MWCNT induced an increase in viscosity, Al-MWCNT58M1 feedstock was replicated better than Al62M1 (Figures 4.8b and 4.8c) which had a lower viscosity. Similar conclusion can be drawn analysing the influence of the addition of SA, which decreased the viscosity of feedstocks but did not increase their replicability (Figures 4.8d to 4.8f).

In relation to the influence of MWCNT on the homogeneity of the green specimens, Figure 4.9 illustrates that the Al-MWCNT58M1 green specimen is more homogeneous than Al58M1 (without nanotubes). In addition, some microcracks were observed in Al58M1 green specimens (white arrow in Figure 4.9a) and not in specimens with MWCNT (Figure 4.9b). This improvement can be attributed to the nanoreinforcement of the material that better tolerated the demoulding stresses. This homogeneity was also attained using a long holding time (Figure 4.9c). Figures 4.9d and 4.9e show that the problems associated with the addition of SA may be due to the separation of the powder-binder for these very low viscosities [16], and it was more pronounced in the presence of MWCNT rather than for high powder content.

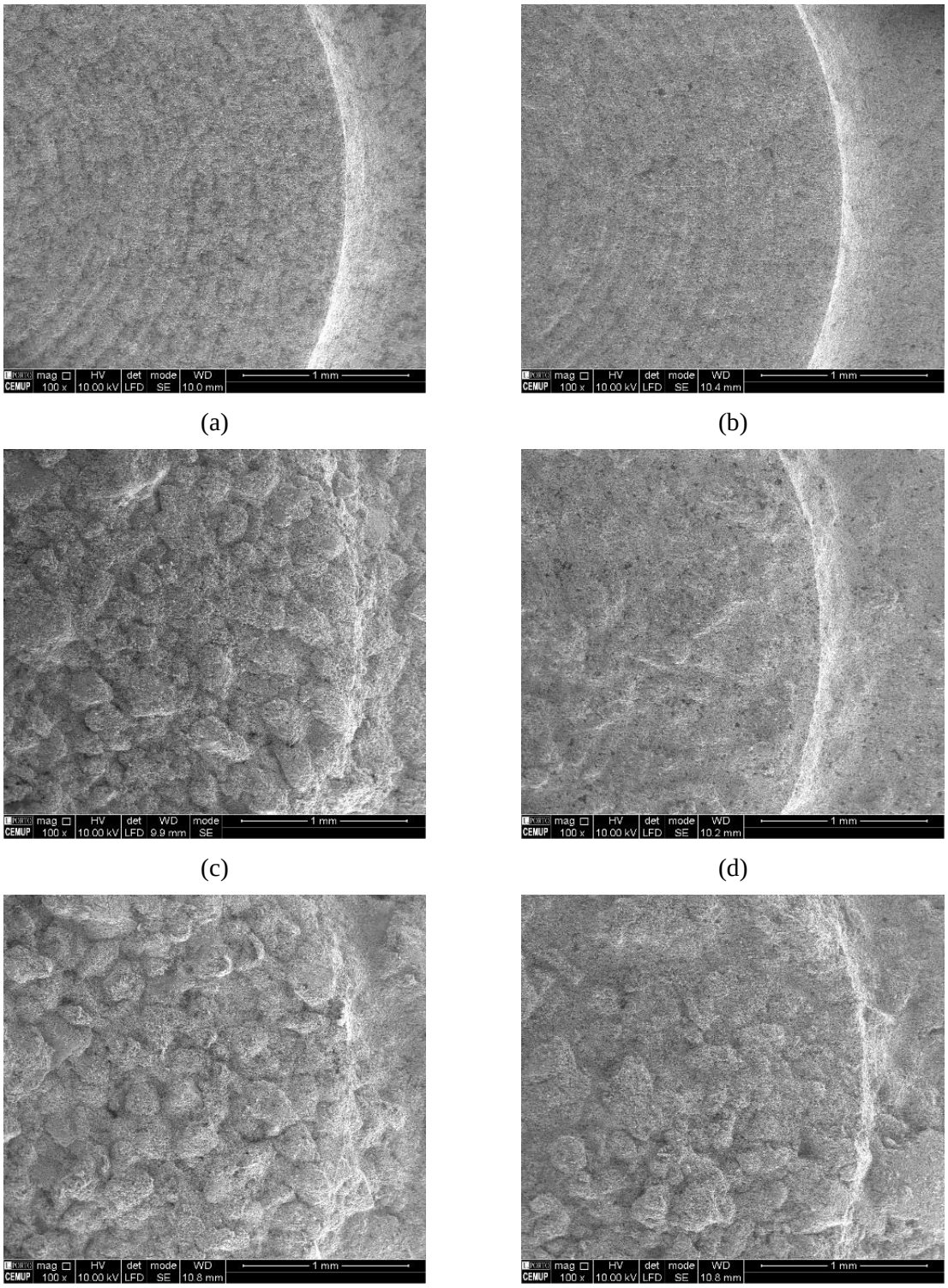

Figure 4.8 *Microstructure of microblind flange green specimens shaped at 230 °C, 8.5 MPa for 30 minutes by dark blue elastomer die, through partially filling the die cavity and covering with the lid, made of: Al58M1 (a), Al-MWCNT58M1 (b), Al62M1 (c), Al-MWCNT58M1SA5 (d), Al62M1SA1.6 (e), and Al62M1SA5 feedstocks (f) (SEM/SE).*

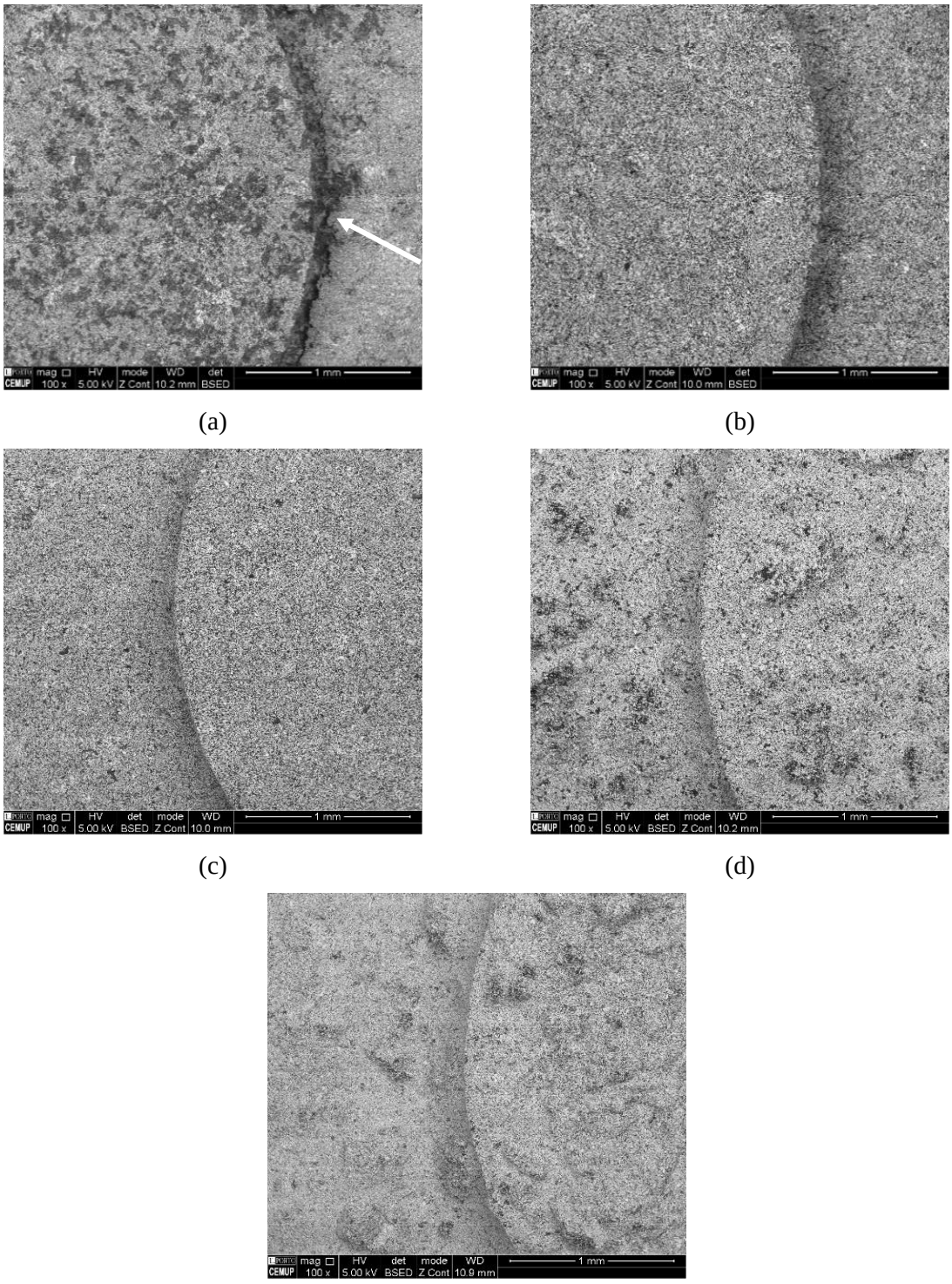

Figure 4.9 *Microstructure of microblind flange green specimens of: Al58M1 (a) and Al-MWCNT58M1 (b), shaped at 230 °C, 11.3 MPa for 15 minutes; Al-MWCNT58M1 (c), Al-MWCNT58MSA5 (d) and Al62M1SA5 (e), shaped at 230 °C, 11.3 MPa for 45 minutes (SEM/BSE).*

4.2.6 Effect of aspect ratio

Microchannel and microwall are different geometries, but with similar aspect ratios (Table 2.12). Figure 4.10 illustrates microchannel-half-flanges green specimens made using a transparent elastomer die and the two optimized feedstocks, Al58M1 and 316L60M1. The replicability of the microaspects was achieved. However, the maximum channel width of the 316L green specimen is larger than that of the Al (363 and 327 microns, respectively), the latter one is almost equal to the corresponding size of the elastomer die (326 microns). This difference can be attributed to the deformation of the elastomer die during compaction; since the stainless-steel powder is intrinsically stronger than the pure Al powder, the steel powder deforms less and more deformation is accommodated by the elastomer material.

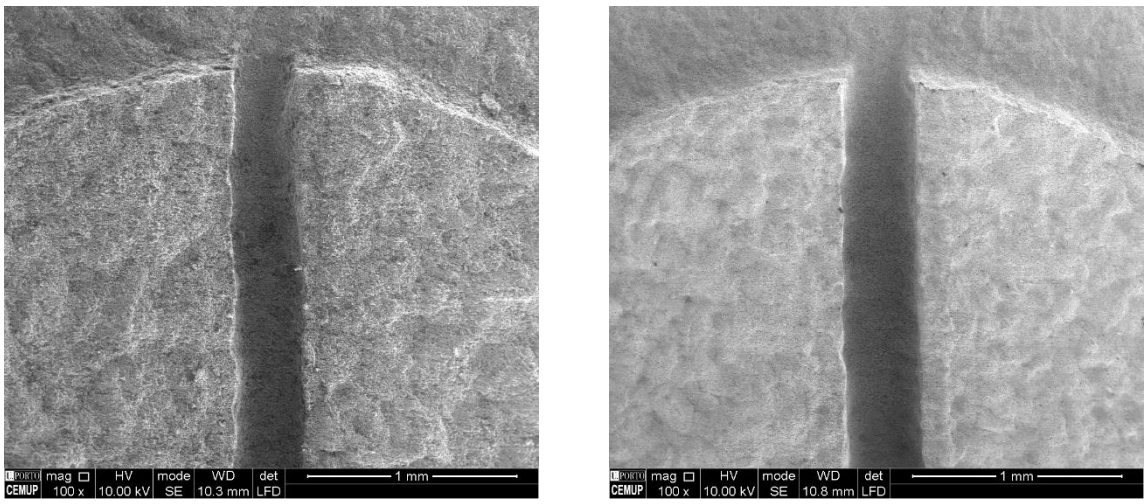

(a) (b)

Figure 4.10 *Microstructure of microchannel-half-flanges green specimens shaped, through the conventional methodology, at 230 ℃, 11.3 MPa for 45 minutes using: Al58M1 (a), and 316L60M1 (b) feedstocks (SEM/SE).*

Regarding the production of microwall-half-reservoirs parts, the shaping was limited (Figure 4.11), with replication being more efficient by 316L60M1 than by Al58M1. This difference between both feedstocks is attributed to the powder characteristics, the steel powder has a smaller shape factor (close to one) and finer particles. The width of the 316L microwall is half the corresponding aspect in the elastomer die (0.15±0.03 mm and 0.30±0.02 mm, respectively). This shortcoming was not surpassed even for the most critical processing conditions, above which the elastomer die was damaged. This was also not overcome using a more rigid die (beige elastomer, Table 2.12). Therefore, it can be concluded that micro hot embossing is suitable for replicating thin concave-like geometries, rather than thin convex-like configurations. This conclusion is also consistent with an earlier study [17].

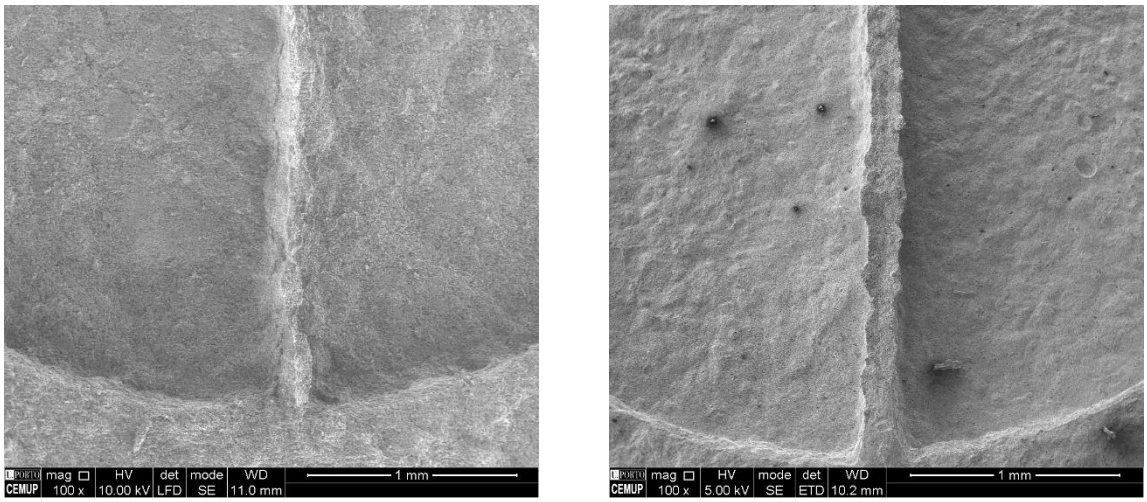

(a) (b)

Figure 4.11 *Microstructure of microwall reservoirs green specimens made by the transparent elastomer die through the conventional shaping sequence at 230 ºC, 11.3 MPa for 45 minutes using: Al58M1 (a), and 316L60M1 (b) feedstocks (SEM/SE).*

Similar to that observed in Al-based feedstocks, the dispersion of the constituents in the 316L-MWCNT60M1 green specimen was better than for 316L60M1 (Figure 4.12a and 4.12b); however, homogeneity decreased with increasing holding time (Figure 4.12c and 4.12d).

The topography of 316L60M1 and 316L-MWCNT60M1 green specimens is shown in Figure 4.13. The colour gradients of the half-flanges parts reveal that 316L surfaces have a greater roughness than 316L-MWCNT ones. The microchannel width of both parts is larger than that of the master die, which may be due to the deformation of the elastomer die during shaping (Figure 4.14a). The Sa parameter of the green parts is larger than that of the die whilst the Sz values are smaller, that can also be due to the elastomer behaviour and the presence of the binder material (Figure 4.14b). However, it seems that the presence of the MWCNT in the feedstock is more effective in the dimensions, mostly affected by the diameter, than in the roughness (Figure 4.14c).

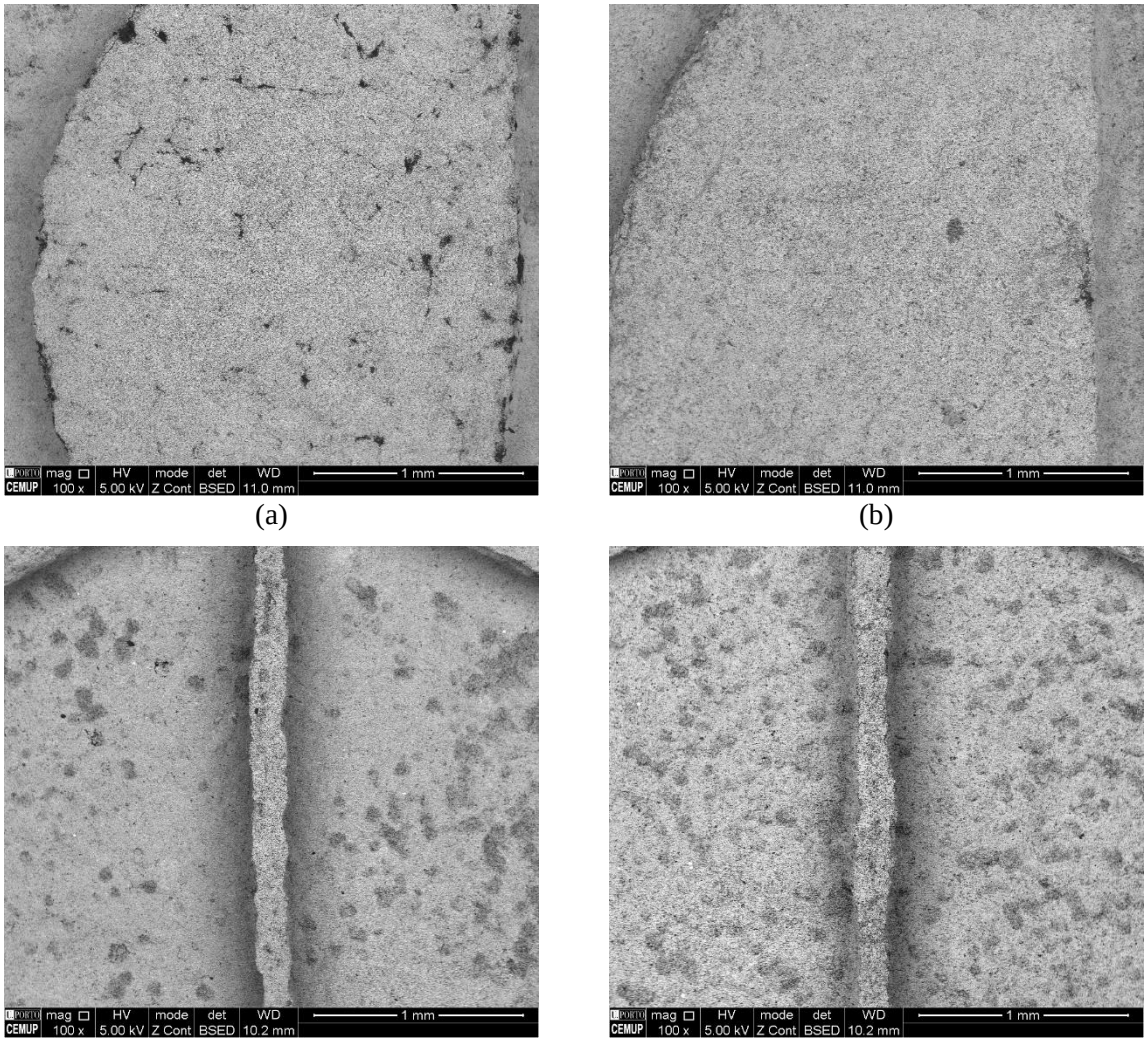

Figure 4.12 *Microstructure of green specimens made of: 316L60M1 (a) and 316L-MWCNT60M1 (b), shaped at 230 ℃, 11.3 MPa for 30 minutes; 316L60M1 (c) and 316L-MWCNT60M1 (d), shaped at 230 ℃, 11.3 MPa for 45 minutes.*

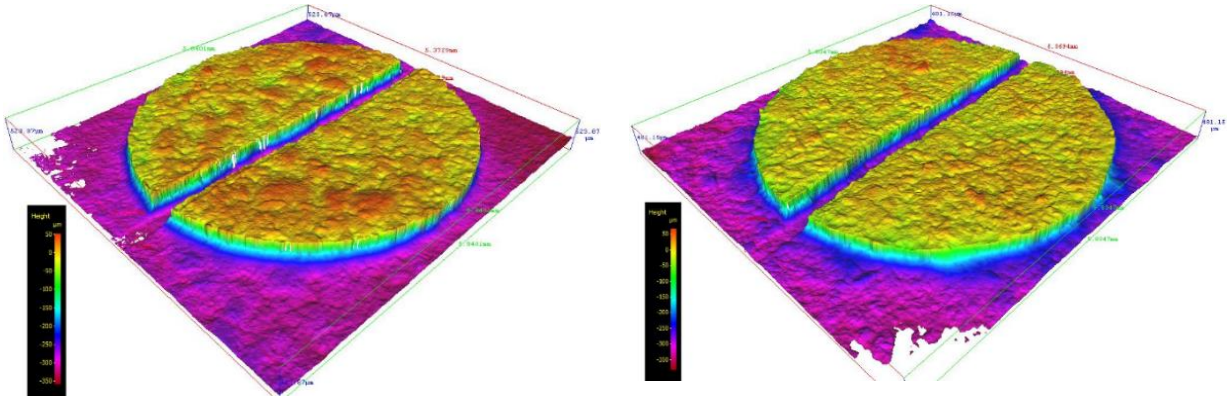

Figure 4.13 *Roughness of microchannel-half-flanges green parts made of: 316L60M1 using a new transparent elastomer die (a), and 316L-MWCNT60M1 made thereafter with the same die (b) (shaping at 230 ℃, 8.5 MPa for 30 minutes) (IFM).*

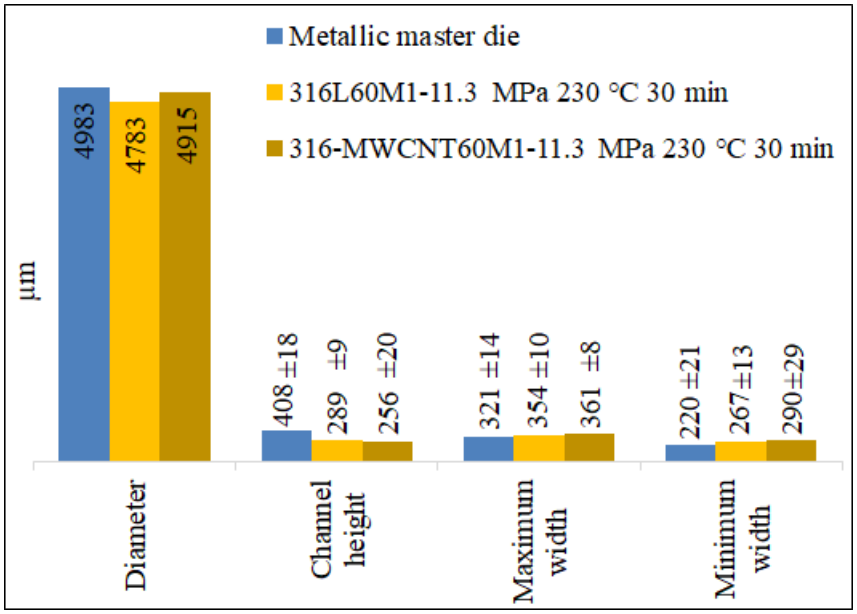

(a)

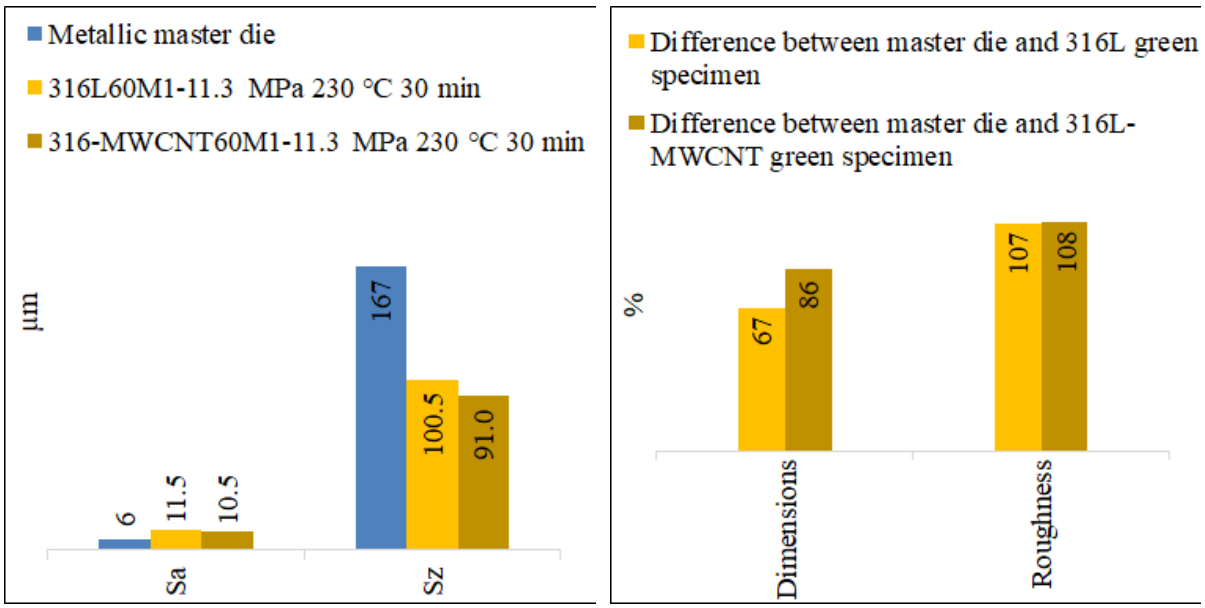

(b) (c)

Figure 4.14 *Dimensions (a) and surface roughness parameters (b) of the metallic master die, 316L and 316L-MWCNT green specimens (cf. Figure 4.13); accumulative of relative differences*[18] *(%) between the parts and die (c).*

[18] The difference in percentage of the four dimensions and of the two roughness parameters was considered for the determination of the accumulative of the relative differences (in absolute values) for the dimensions and roughness, respectively.

4.2.7 Effect of the elastomer dies

According to the IFM analysis (Figure 4.13), the 316L-MWCNT specimen appeared to have less roughness than the 316L one. However, since they were replicated sequentially with the same die, the number of times the die is used may affect its replicability. Another IFM evaluation was performed on two specimens with same composition, being processed consecutively by the same die (Figure 4.15).

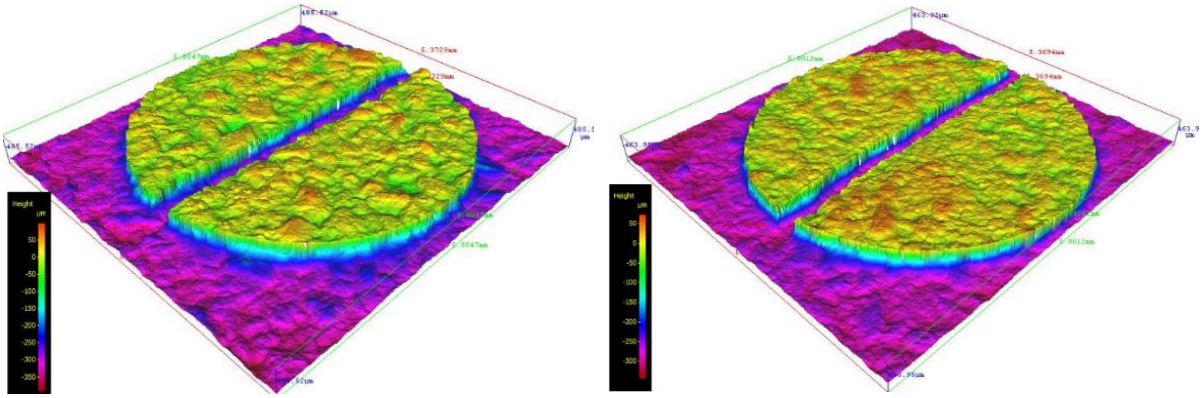

(a) (b)

Figure 4.15 *Roughness maps from Al-MWCNT58M1 specimens shaped at 11.3 MPa at 230 ℃ for 30 minutes, by the pristine die (a) and the same die that already was used (b).*

The dimensions and roughness of green parts changed in consecutive shaping as a consequence of the deterioration of the elastomer die (Figures 4.16 and 4.17).

Therefore, the reproducibility of green specimens is influenced using the elastomer die. This can be caused mainly by the erosion or deformation of the elastomer die and adhesion of the feedstock material to the die surface. Since the elastomer stiffness is dependent on the hardness [18], therefore the die deformation was evaluated from hardness measurements, accepting that the shaping conditions (temperature and pressure) harden the elastomers (Table 4.1). This hardening occurred for all elastomer materials used in this study.

Table 4.1. Shore A values at room temperature of the elastomer die surfaces.

Condition	Transparent	Light blue	Beige
Pristine	38±1	64±1	69±1
After shaping	40±1	70±1	73±2

Another configuration was studied, microtensile specimens. The production of this shape was limited by the composition of the elastomer die. No specimens were made using a transparent or dark blue die, because they were not suitable due to the stiffness, and the green specimens quickly broke during demoulding (Figure 4.18a). However, when these dies were replaced by the light blue elastomer die, no green specimen failed, although trimming was always needed (Figure 4.18b).

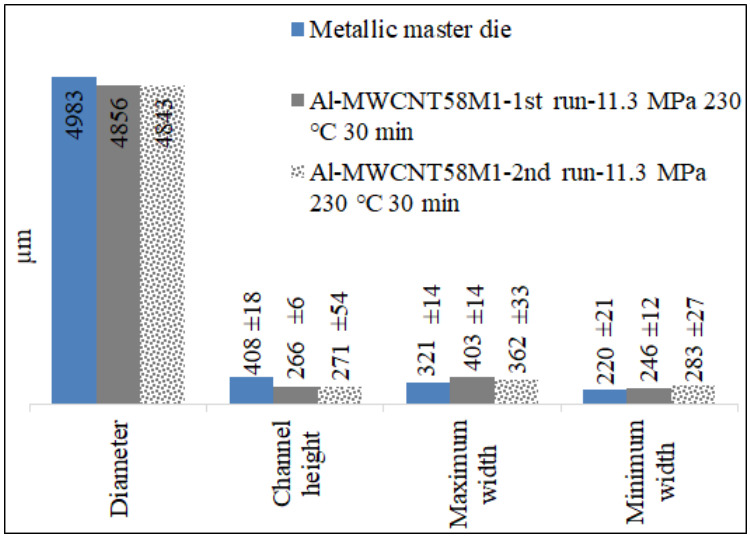

(a)

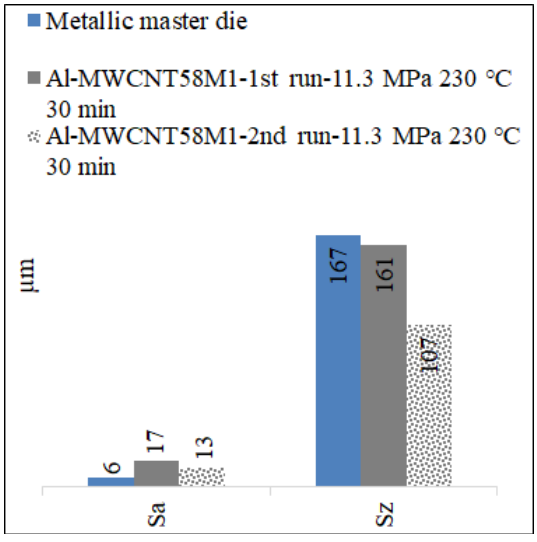

(b)

Figure 4.16 *Dimensions (a) and surface roughness parameters (b) of two Al-MWCNT58M1 specimens produced consecutively by the same die (cf. Figure 4.15).*

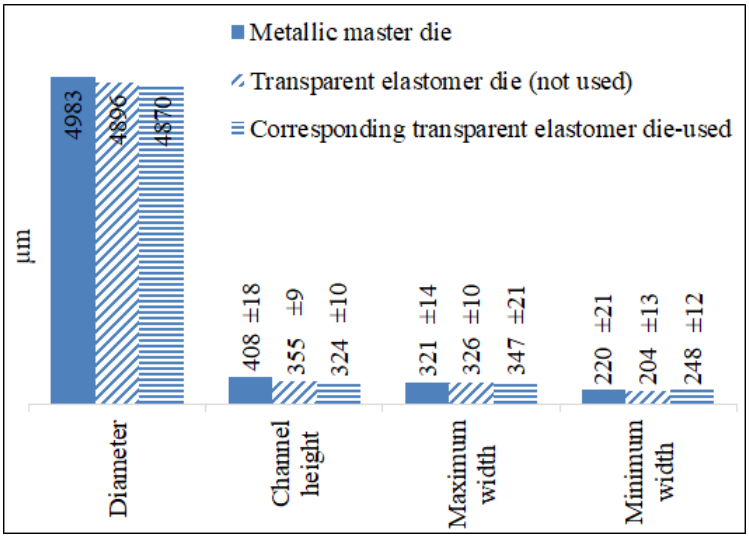

(a)

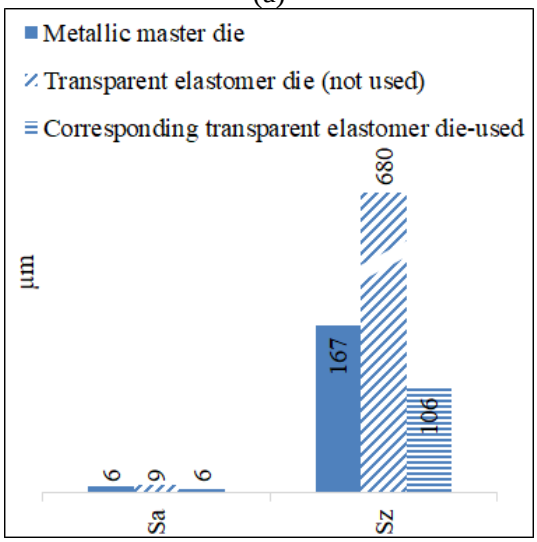

(b)

Figure 4.17 *Dimensions (a) and surface roughness parameters (b) of a new and used elastomer die compared with the metallic die.*

(a)

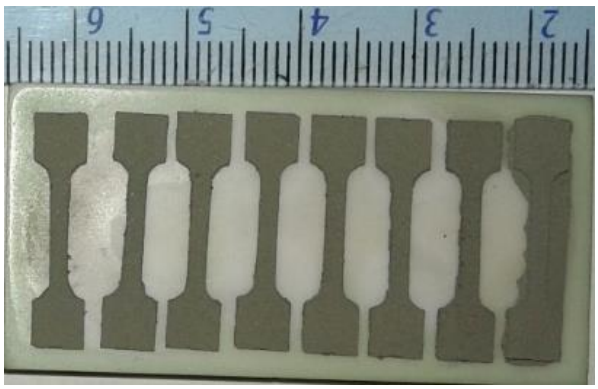

(b)

Figure 4.18 *Green microtensile specimens shaped at 230 °C and 8.5 MPa for 30 minutes using different dies: dark blue elastomer (broken sample) (a), and light blue elastomer (the last specimen is not trimmed) (b).*

4.3 Changing the conventional shaping methodology

This section discusses the replication of different microgear geometries. A related study had reported failure in replication of a microgear geometry through micro hot embossing with elastomer die [7]. However, this geometry was perfectly produced by µPIM [19, 20], in which the pseudoplastic behavior of the feedstock is very helpful, namely by reducing the feedstock viscosity with the increase of shear rate (behavior typical of shear thinning fluids) [21].

The replicability of microwall-half-reservoirs (as a convex geometry) failed. Even using a feedstock with a fine particle size and shape factor close to one (AISI 316L powder) and increasing the critical shaping conditions (temperature, pressure and time), for which a stiffer elastomer was used, did not result in replicating a perfect microwall configuration.

A green specimen is composed of bonded feedstock particles which, at the most initial stage of the conventional shaping approach, are compacted together while they are not yet soft. The compaction of this system affects the elastomer die thus inducing die deformation. This binder is expected to become soft at the shaping temperature (considering that the silicone is not intrinsically a good thermal conductive material, there is some delay until the feedstock reaches the softening temperature, and in meantime, the shear thinning behavior is absent). However, since the reduction of the feedstock viscosity (section 4.2.5) did not increase the replicability, the optimization of micro hot embossing process should be sought by changing the methodology instead of manipulating the binder composition. This can be carried out by changing the shaping sequences or by replacing the elastomer die with a metallic one.

4.3.1 Replicating microgears by conventional shaping methodology

The 316L feedstock was selected for shaping the microgear geometries (Figures 2.14b and 2.14c) since it was only with this feedstock that the microwall structure was partially replicated (Figure 4.11b). However, replication was not achieved using the transparent elastomer die (Figure 4.19). This failure was attributed to a strong deformation of the thin sections of the transparent elastomer die during compaction. This die was replaced by the beige elastomer (Table 2.12) and the process was repeated for different compaction pressures (Figure 4.20). The new die significantly increased the replicability of the gear teeth. However, the teeth were not all perfect, the root circle was not uniform, and the green gear was easily broken during demoulding, which meant a need for improvement. Figure 4.20 also shows that replicability increases with increasing shaping pressure.

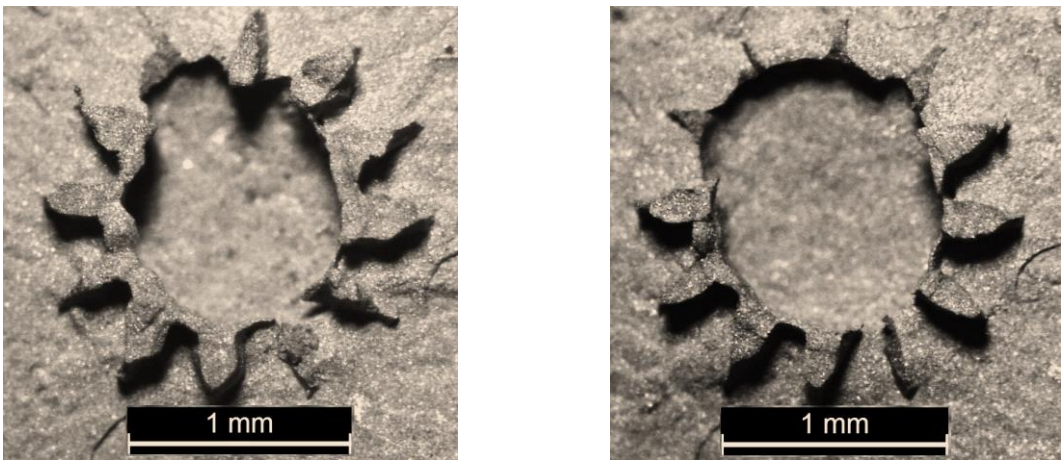

(a) (b)

Figure 4.19 *Convex microgears (316L60M1 feedstock) shaped by the transparent elastomer die using the conventional shaping sequence and the processing conditions of 230 ℃ for 45 minutes, compacted at 5.7 MPa (a) and 8.5 MPa (b) (stereoscopy).*

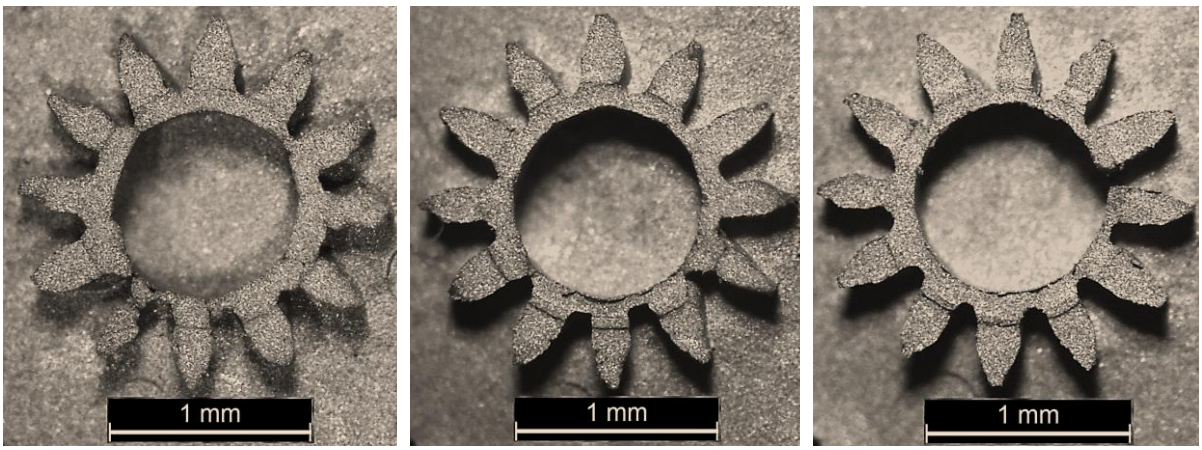

(a) (b) (c)

Figure 4.20 *Convex microgears (316L60M1 feedstock) shaped by the beige elastomer die using the conventional shaping sequence and the processing conditions of 230 ℃ for 45 minutes compacted at 8.5 MPa (a), 11.3 MPa (b) and 14 MPa (c)(stereoscopy).*

4.3.2 Changing the methodology to replicate microgears

The shaping methodology was altered to improve the microgears replicability. This involved delaying the pressure application until the particles become as soft as possible due to the heating up to the shaping temperature (230 ℃). In this way, the possibility of replicability can increase since the feedstock inserted into the die cavity will be softer in the compression stage. Thereby, the new shaping methodology involves preheating the die assembly up to ~50 ℃, placing it in

the tensile machine, subsequent heating up to 230 °C, and applying pressure only when the temperature is stabilized. Figures 4.21a and 4.21b illustrate two specimens shaped by the old and new methodologies, respectively. The thickness of the root circle was produced more uniformly by the second method. The new method seems to produce a gear with a smoother surface; however, production was still limited by the demoulding step (a crack at a tooth tip in Figure 4.21b illustrated by a white arrow). Afterwards, the production of this microgear through the same method using the feedstock with the largest powder concentration (316L65M1) was tested but the replicability was reduced (Figure 4.21c).

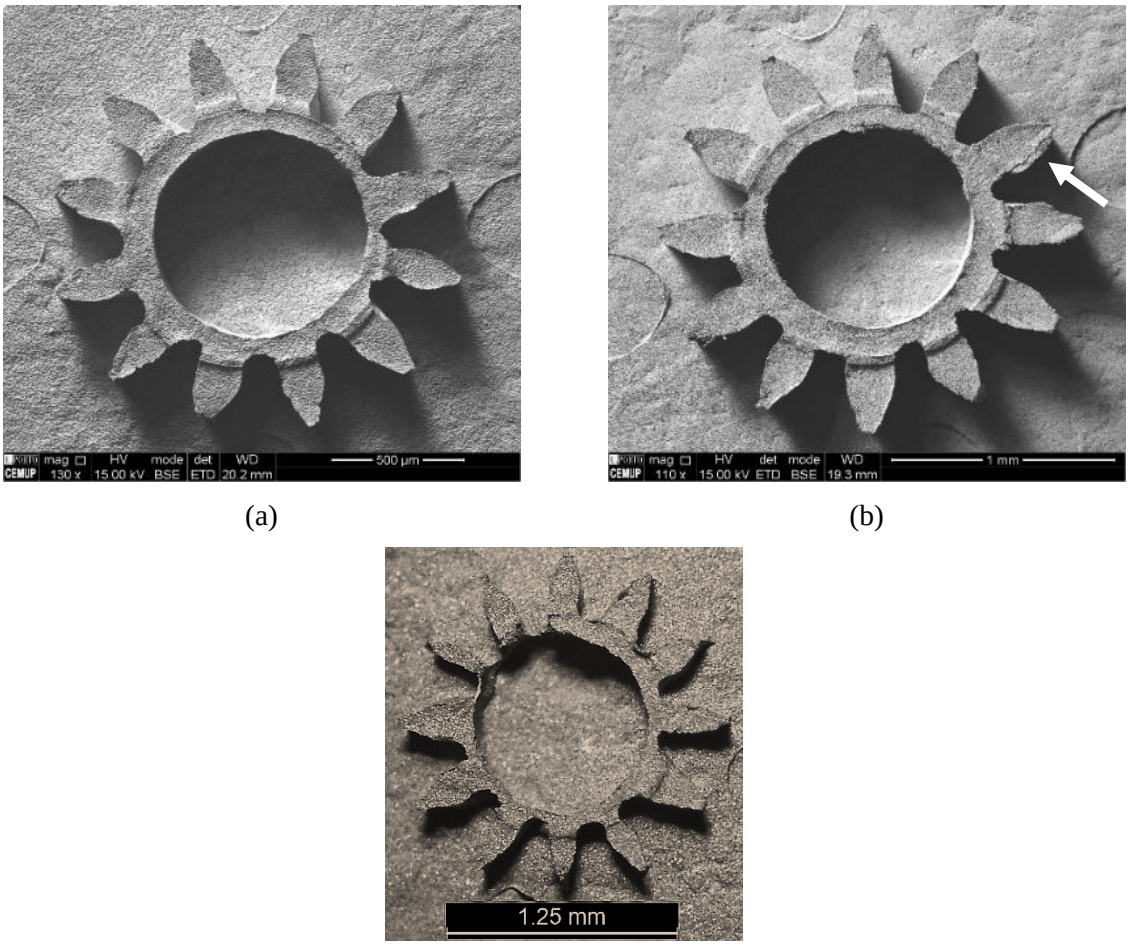

(a) (b)

(c)

Figure 4.21 *Convex microgears shaped in the beige elastomer die at 230 °C, 11.3 MPa for 45 minutes and made in 316L60M1 feedstock through the conventional (a) and new shaping method (b) (SEM/BSE); specimen poorly replicated made of 316L65M1 (c) (stereoscopy).*

The feasibility of the new methodology was also evaluated by replicating the concave microgear geometry. Figure 4.22 illustrates the effect of the pressure on replicability and shows that the best specimen was produced at the highest pressure, 14 MPa. This pressure effect is consistent with the replicability of convex microgears using the conventional shaping method (Figure 4.20) and with a related study [5].

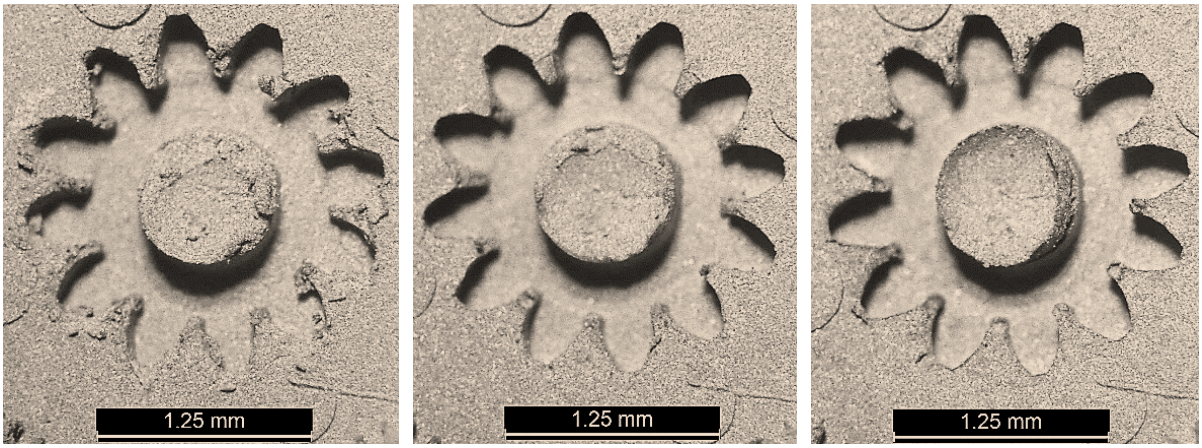

(a) (b) (c)

Figure 4.22 *Concave microgears (316L60M1 feedstock) shaped by the beige elastomer die using the new shaping sequence and the processing conditions of 230 °C for 45 minutes and compacted at 8.5 MPa (a), 11.3 MPa (b) and 14 MPa (c) (stereoscopy).*

Regarding the replicability of the concave microgear, the specimens made by conventional and new methodologies are presented in Figures 4.23a and 4.23b. The new method produced fewer broken parts during demoulding. In addition, a green specimen was successfully shaped using the 316L65M1 feedstock (Figure 4.23c). This material had not allowed the replication of the convex geometry (Figure 4.21c), which means that geometry plays an important role during shaping through micro hot embossing. The potential for replicating a feedstock with a powder concentration greater than the CPVC without having to reduce the viscosity is quite interesting. Previous studies reported the feasibility of shaping a high solid concentrated feedstock, diluted by stearic acid [12, 22].

SEM analysis (Figure 4.23) revealed the presence of black spots only in the 316L60M1 green specimens, which were not observed in the 316L65M1 specimen (Figure 4.23c) and in the 316L60M1 with convex geometry (Figure 4.21). These spots represent heterogeneity, which was also observed in previous experiments (Figure 4.12). Therefore, this suggests that the powder-binder separation in the green specimens made by micro hot embossing may be influenced by the composition.

Regarding the dimensions, the profiles of the master gear die are illustrated in Figure 4.24a, the measured dimensions were represented by colored lines. Measurements were made on the corresponding beige elastomer dies, before and after use, and on the 316L60M1 and 316L65M1 green parts (Figure 4.24b). Considering the dimensional changes and the accumulative of relative differences (Figure 4.24c), the beige elastomer die also changed in size after the shaping process, despite being stiffer than the transparent one. Changing the elastomer dimensions is attributed to its deformation, noticed in the increase of the hardness of the material (Table 4.2). Figure 4.24 also shows that the largest differences were measured in the green convex microgear. The most accurate replicability was obtained for the lower powder concentration.

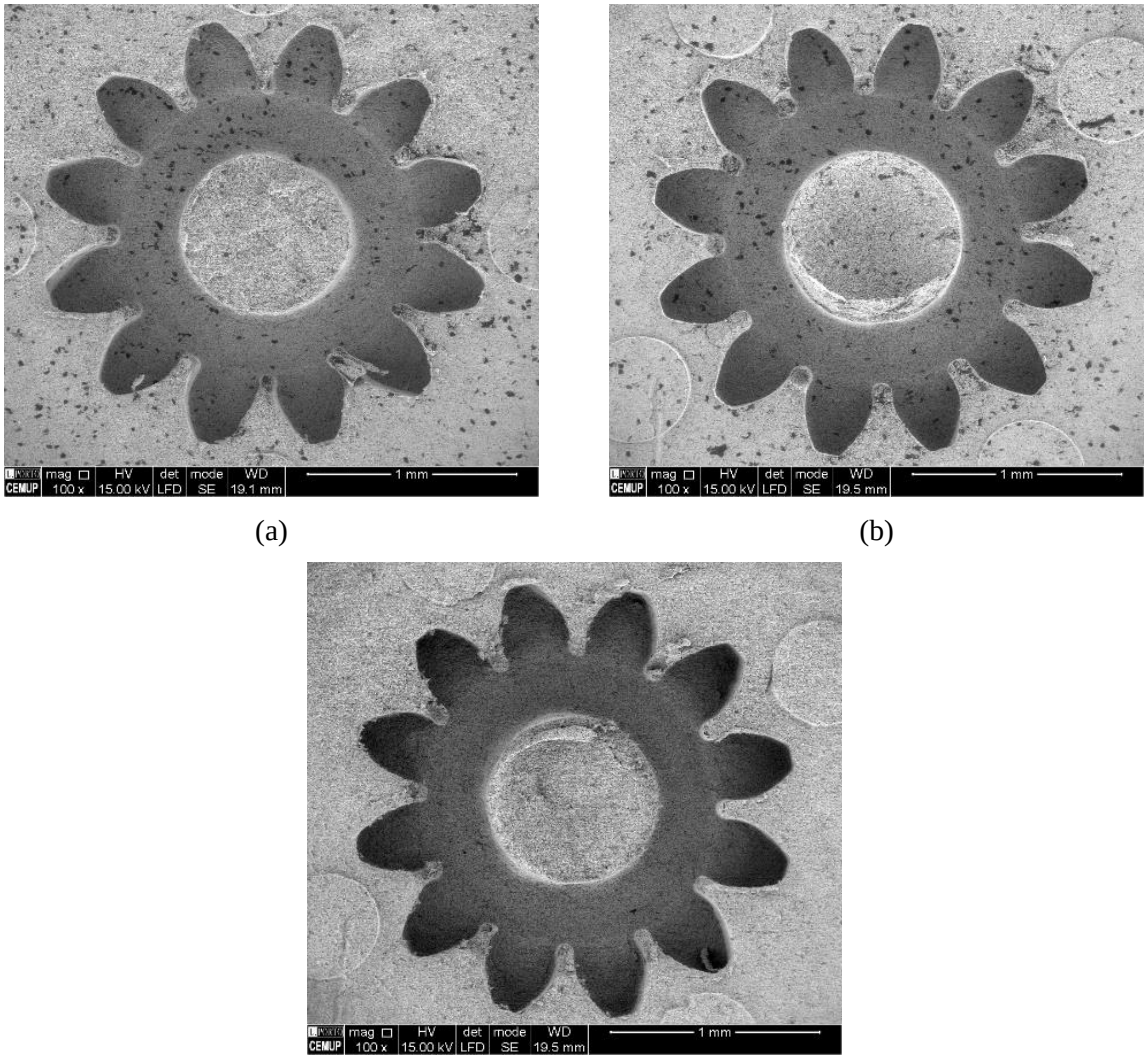

(a) (b)

(c)

Figure 4.23 *Concave microgears shaped in the beige elastomer die at 230 °C and 14 MPa for 45 minutes and made in 316L60M1 feedstock through the conventional (a) and new shaping method (b) and in 316L65M1 feedstock through the new method (c) (SEM/BSE).*

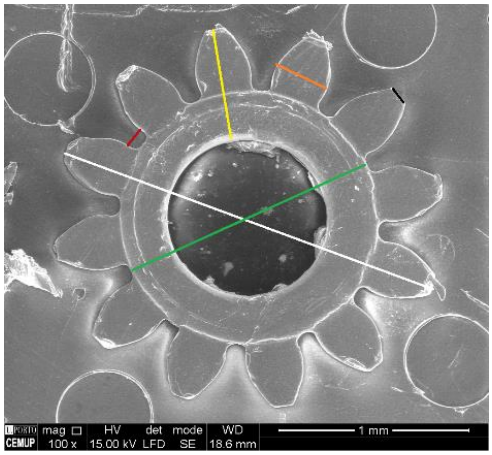

(a)

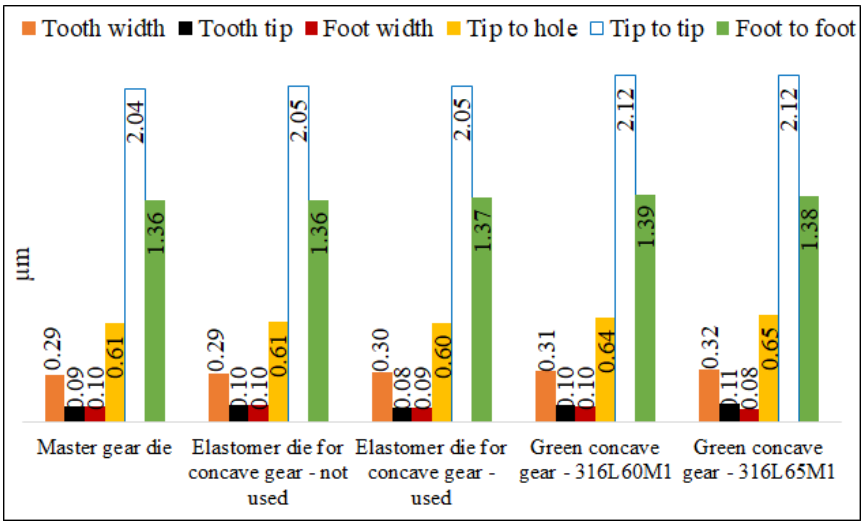

(b)

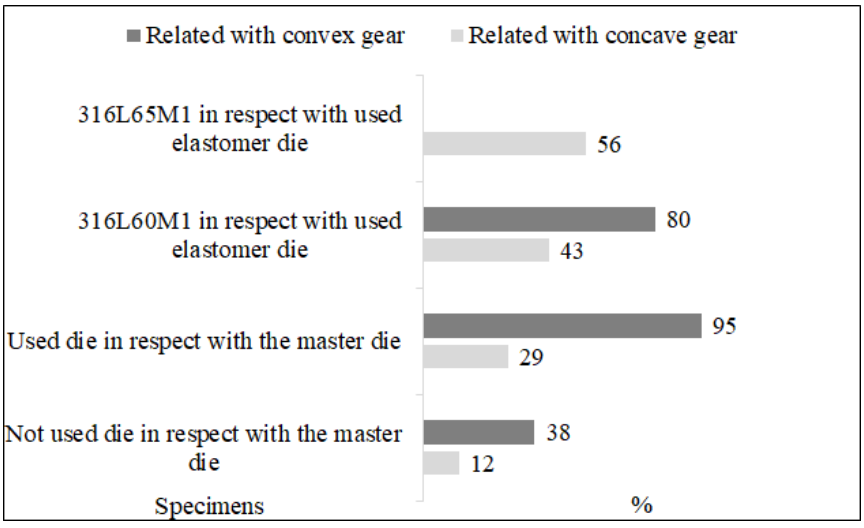

(c)

Figure 4.24 *Microgear profile: tip to tip (white line), foot to foot (green line), foot width (dark red), tip to hole (yellow line), tooth width (orange line) and the tooth tip (black line) (a) (SEM/SE); corresponding measurements made by ImageJ (b); and accumulative of relative dimensional differences (c).*

Table 4.2 Hardness measurements of the beige elastomer die.

Condition	Shore A
Before use	69±1
After shaping	73±1

4.3.3 Replicating microwall feature by metallic die

The replicability of the microwall-half-reservoirs geometry with the elastomer die failed with Al feedstock (Figure 4.11a) and was also limited to those of 316L60M1 (Figure 4.11b). These results indicate that the poor replicability of the microwall geometry is to some extent attributed to powder characteristics (size and shape). However, two other aspects may also influence: the lubrication of the die and its deformation.

Assuming that, this shortcoming was potentiated by the friction between the feedstock and the die, the wall surface of this die was manually lubricated by spraying silicon-free mould release agent or by zinc stearate powder. However, none of these lubricants increased the replicability.

The second hypothesis involves the deformation of the elastomer die during shaping conditions. Therefore, the stiffest available elastomer die (beige elastomer with 69 Shore A) was selected for shaping this microwall feature. The processing conditions were not changed except the pressure being tested different compaction levels. At a low pressure (P= 1.5 MPa) no wall was shaped. For the highest possible pressure (P= 14 MPa), i.e., which did not permanently deform the die, the microwall was stuck within the die cavity and broke during demoulding. The best results were achieved for 11.3 MPa (Figure 4.25a). However, a similar replicability was not achieved with the 316L-MWCNT60M1 feedstock (Figure 4.25b). This behavior can be related to the feedstock characteristics, such as different viscosities (Table 3.1). Replicability did not increase even through the use of the new methodology that is, applying the pressure only when the shaping temperature stabilized (Figure 4.25c).

The width of the green wall aspect of the 316L60M1 specimen is almost half of the corresponding aspect of the die 0.13 ± 0.02 and 0.28 ± 0.01, respectively (Figure 4.25a and 4.25d), measured by ImageJ software.

These different widths are related to the microdeformation of the elastomer die. This happens because the shaping pressure is introduced to the whole surface of the die. Therefore, the width of die channel can become small and the feedstock can hardly fill the die cavity. This is the

weakness of micro hot embossing compared to µPIM in which the injection pressure is applied to die cavity via a feedstock exhibiting shear thinning behavior.

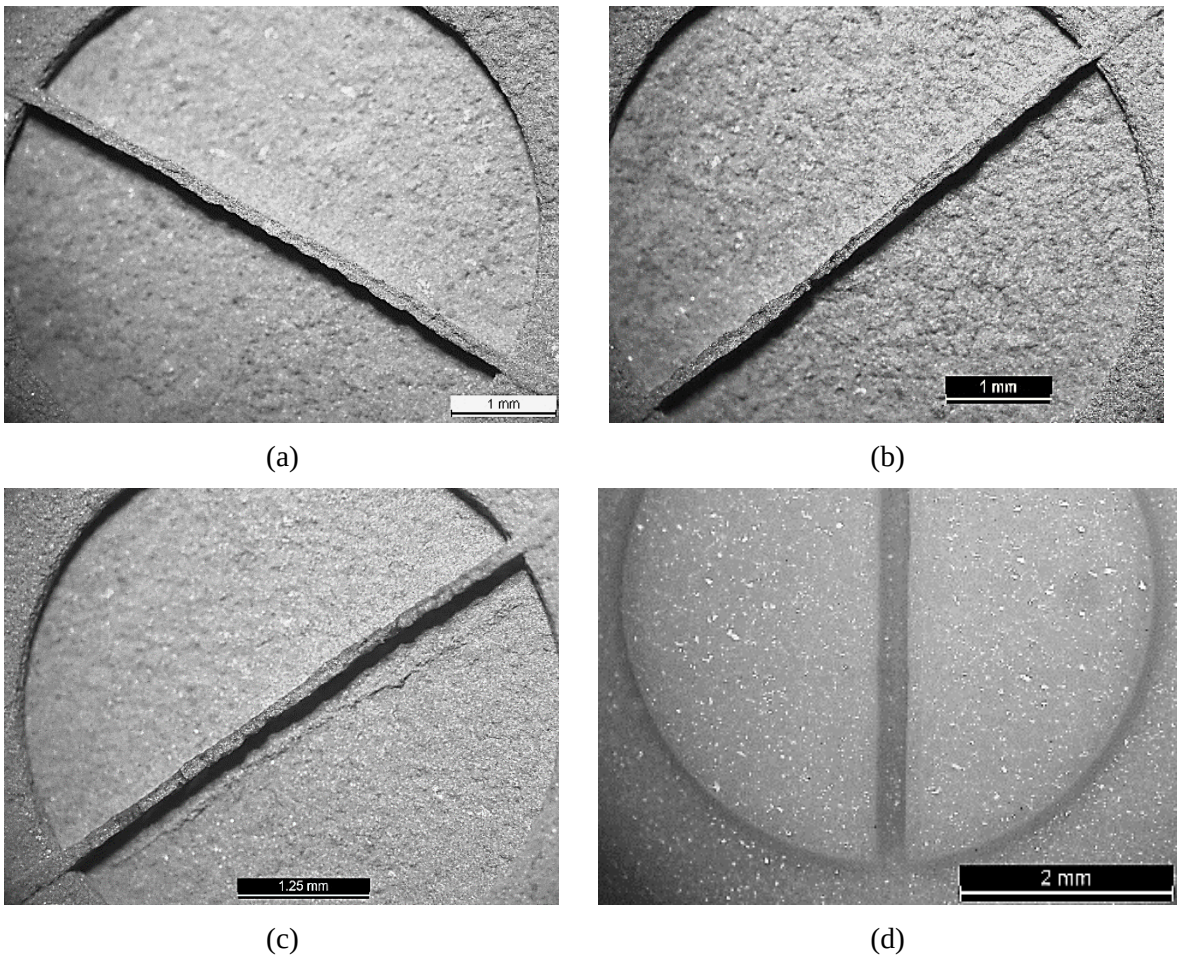

(a) (b)

(c) (d)

Figure 4.25 *Green microwall-half-reservoirs made at 230 ℃, 11.3 MPa for 45 minutes using the feedstocks: 316L60M1 (a), 316L-MWCNT60M1 (b), 316L60M1 shaped through the new methodology (c). Beige elastomer die (d) (stereoscopy).*

The replicating process was modified by replacing the elastomer die by a metallic one, to avoid the deformation of the die during hot embossing. In fact, a related study reported a perfect replicability using a rigid die (silicon wafer) at a suitable pressure-time applications and a modified assembly [1].

A similar approach was tested in this research but, the replicating geometry was maintained on the top face. The new arrangement (Figure 4.26) involves a holding cylinder (part A) in which the die cavity (part B) and the replicating die (part C, with the details illustrated in Figure 2.12) are embedded. This die is placed on the top face of the die cavity which is filled completely with the feedstock.

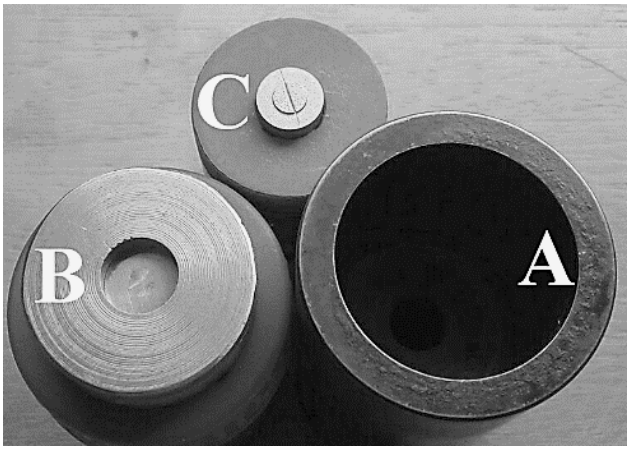

Figure 4.26 *Die assembly: holding cylinder (part A), die cavity (part B), and replicating die (part C).*

The use of the metallic die for replicating process was started with Al feedstock. The first experiment was performed with the same conditions used with the elastomer die (T= 230 ºC, P= 11.3 MPa for 45 min) and failed completely in replicating the microwall aspect. This failure was attributed to the higher thermal conductivity of the metallic die which causes this process to demand less severe processing conditions. Figure 4.27 illustrates two green specimens shaped at lower temperature (150 ºC) and shorter holding time (10 minutes). The microwall aspect was replicated, but there are some unfilled regions and cracks, caused by weak filling and bonding inefficiency of the feedstocks.

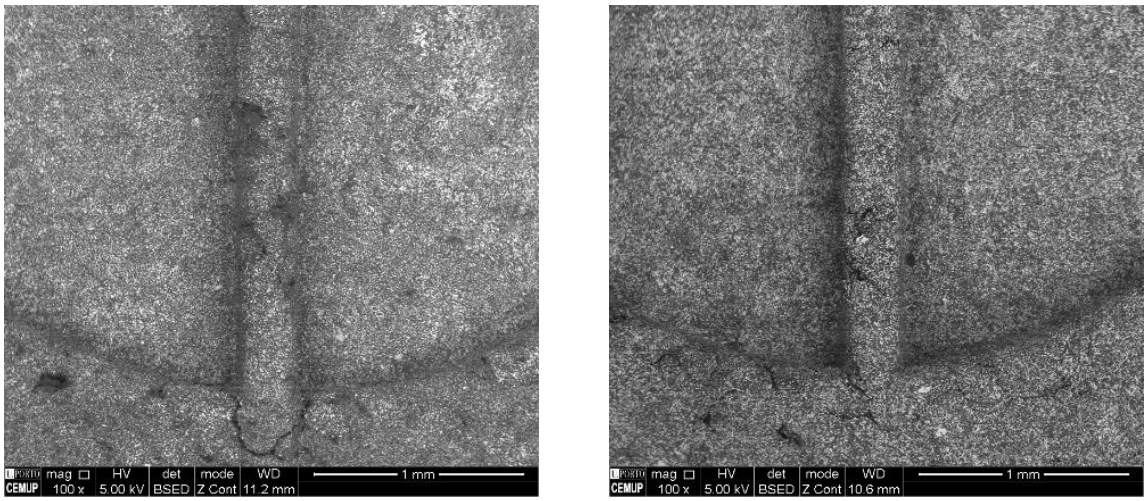

(a) (b)

Figure 4.27 *Microstructure of green microwall-half-reservoirs shaped at 150 ºC, 8.5 MPa for 10 minutes: Al58M1 (a) and Al-MWCNT58M1 (b) (SEM/BSE).*

Holding time did not play a significant role in the removal of the defects detected. Replicability increased by applying a much higher pressure, 76.4 MPa (Figure 4.28) and this level of pressure was required otherwise the green microwall aspect broke during demoulding step.

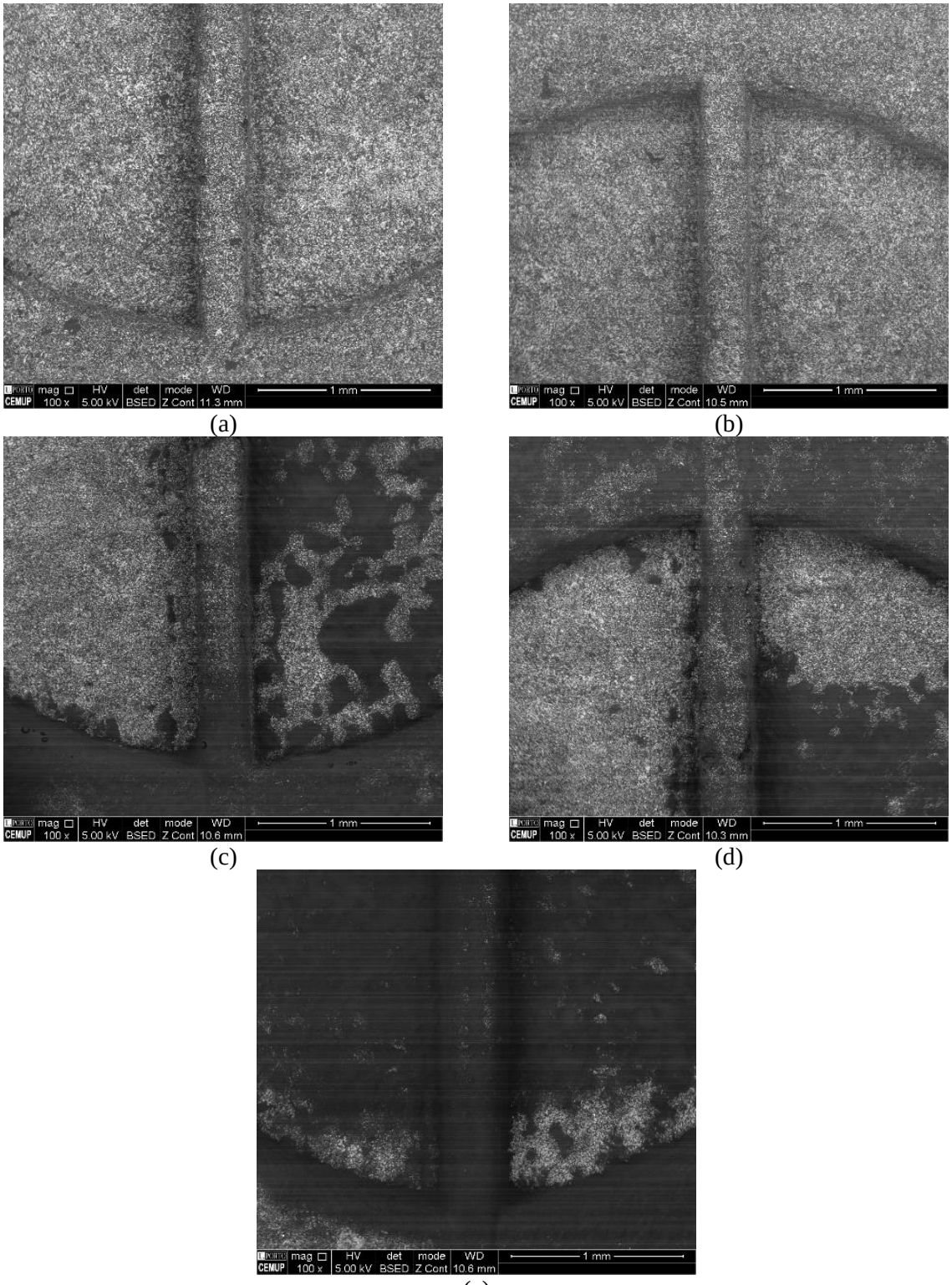

Figure 4.28 *Microwall-half-reservoirs shaped at 150 °C, 76.4 MPa for 8 minutes: Al58M1 (a) and (b), Al-MWCNT58M1 (c) and (d), and Al62M1 (e) (SEM/BSE).*

The microstructural analysis of the Al58M1 (Figures 4.28a and 4.28b) reveals that the constituents are homogeneously dispersed after shaping by the metallic die. The same processing conditions were applied for the Al62M1 and Al-MWCNT58M1 feedstocks, but their microstructures were not homogeneous (Figures 4.28c to 4.28e). This can be correlated with the high softening efficiency of the binder system in the presence of MWCNT, with the increase of thermal conductivity [23], and higher Al content.

Topography measurements (Figure 4.29) showed that the metallic die replicated plane surfaces of green specimens better than the elastomer die (section 4.2.6 and 4.2.7).

However, these images show that the surface roughness has been affected by the feedstock composition; the colour gradient of the Al58M1 feedstock (Figure 4.29a) shows a more homogeneous surface than that of Al-MWCNT58M1 (Figure 4.29b) and Al60M1 (Figure 4.29c).

The cross-section profiles (Figure 4.29d and 2.12b) confirm that the replicability was attained. However, the wall bottom edge is not as sharp as the corresponding aspect of the die.

Figure 4.30 presents the dimensions and roughness values of the green specimens shown in Figure 4.29. The accumulative differences between the green microwall-half-reservoirs and the metallic die reveal that Al58M1 feedstock contributed to a better replicability. This is attributed to the dispersion of the constituents, essential for ensuring good replicability, to be affected by the composition (Figure 4.28).

When the dimensions and surface roughness parameters of green parts made by two dies (elastomer and metallic) are compared to the master die (Figure 4.31), it is clear that shaping by metallic die guarantees better replicability. As already mentioned, this improvement is resulted from the metallic die that does not undergo an early plastic deformation under the feedstock shaping conditions.

4.3.4 Reducing the shaping pressure for the metallic die

The application of high pressure (76.4 MPa) was responsible for avoiding the failure of the microwalls during demoulding, but it caused heterogeneity (see Figure 4.28). By gaining experience, the application of lower temperature and pressure, 150 °C and 11.3 MPa for 8 minutes, functioned without the failure of the microwall aspect during demoulding, but a complete filling of the entire die was not attained.

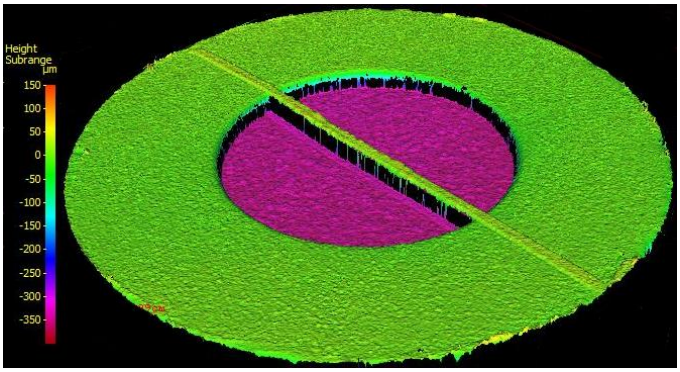

(a)

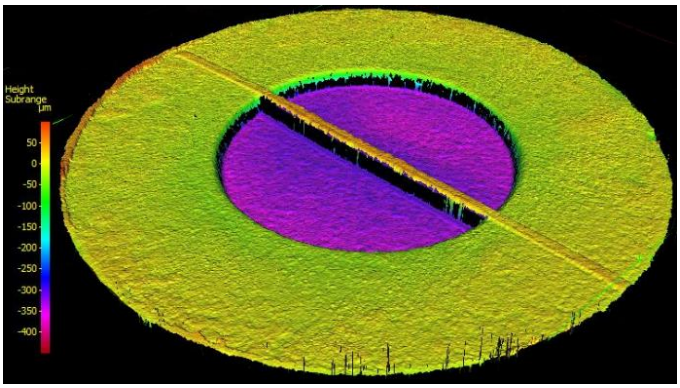

(b)

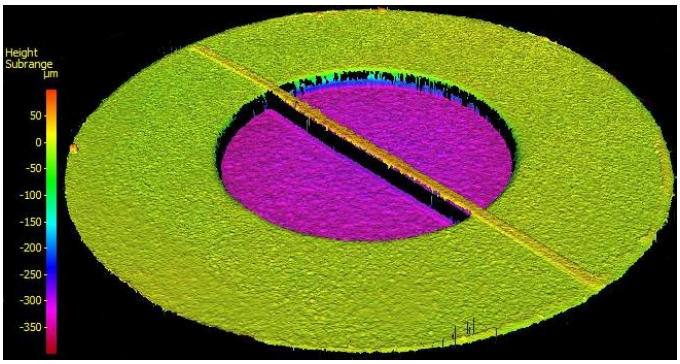

(c)

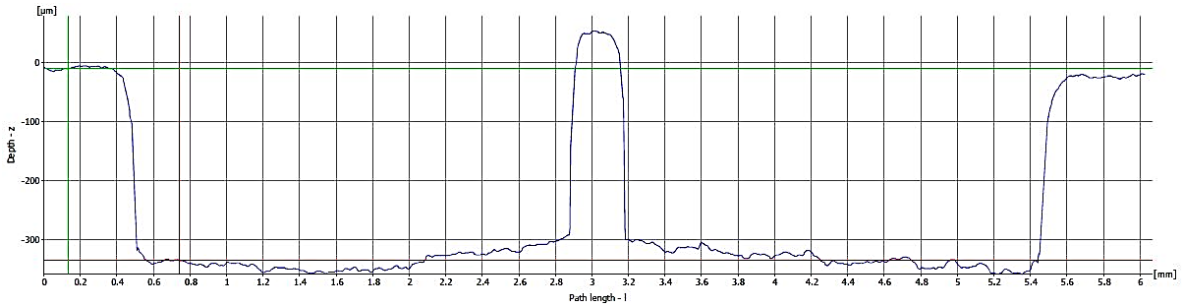

(d)

Figure 4.29 *Roughness maps of microwall-half-reservoirs shaped at 150 °C, 76.4 MPa for 8 minutes with the feedstocks: Al58M1 (a), Al-MWCNT58M1 (b), and Al62M1 (c). Cross section profile of image "b", almost close to center (d) (IFM).*

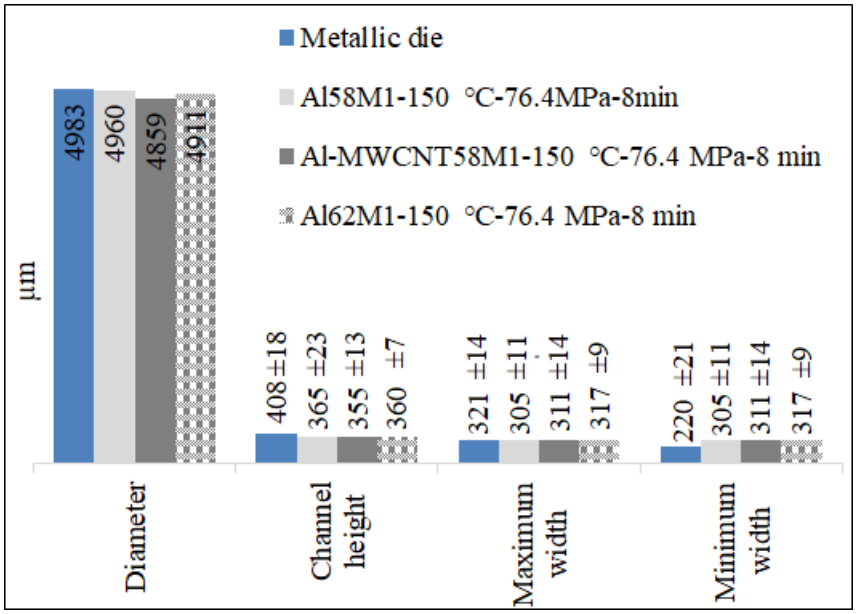

(a)

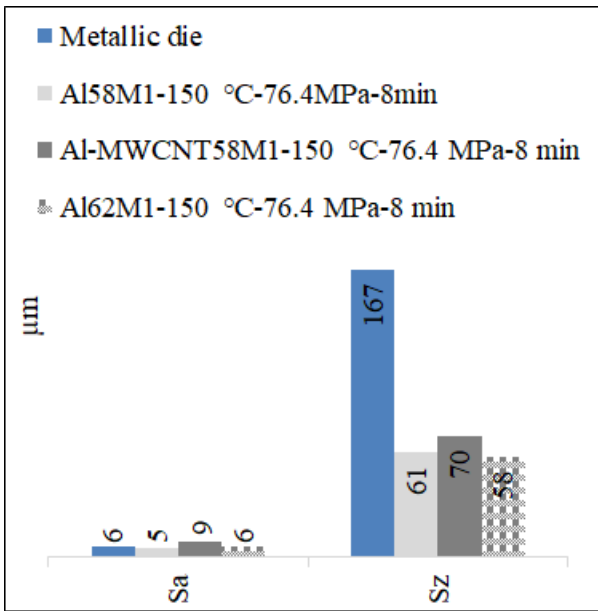

(b)

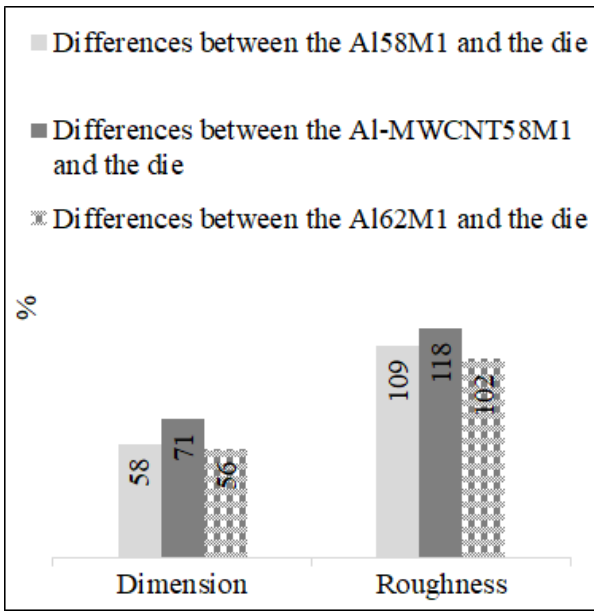

(c)

Figure 4.30 *Dimensions (a), roughness (b), and cumulative relative differences (c) of microwall-half-reservoirs shaped at 150 ℃, 76.4 MPa for 8 minutes with three Al-based feedstocks. (cf. Figure 4.29).*

In order to attain a complete die filling, the shaping temperature and the holding time increased from 150 ℃ to 170 ℃, and from 8 to 10 minutes, respectively, maintaining the same pressure (11.3 MPa). The microstructures (Figure 4.32) show that the powder and binder in the green part made of the feedstock containing MWCNTs were better dispersed than without them.

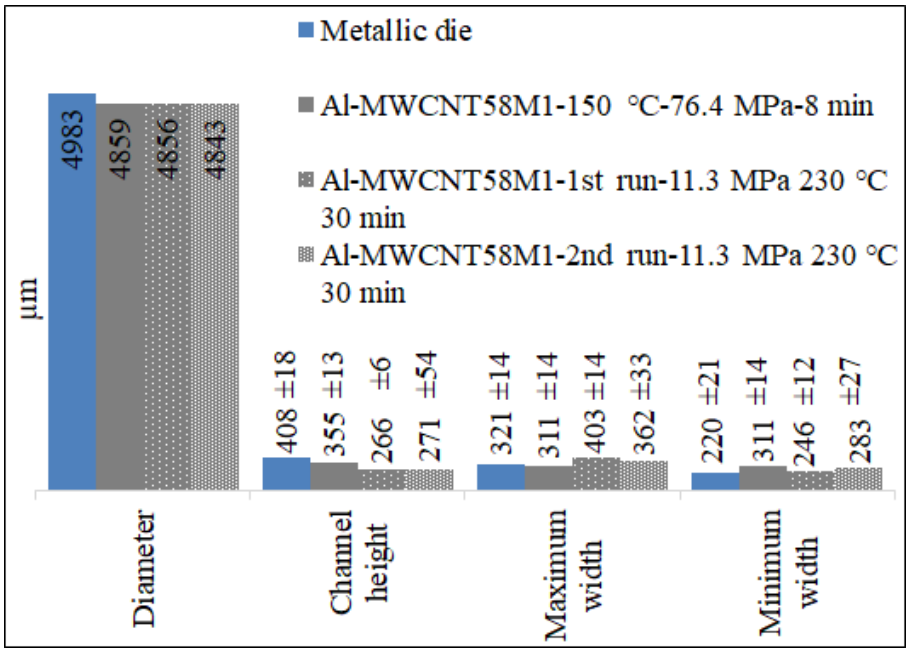

(a)

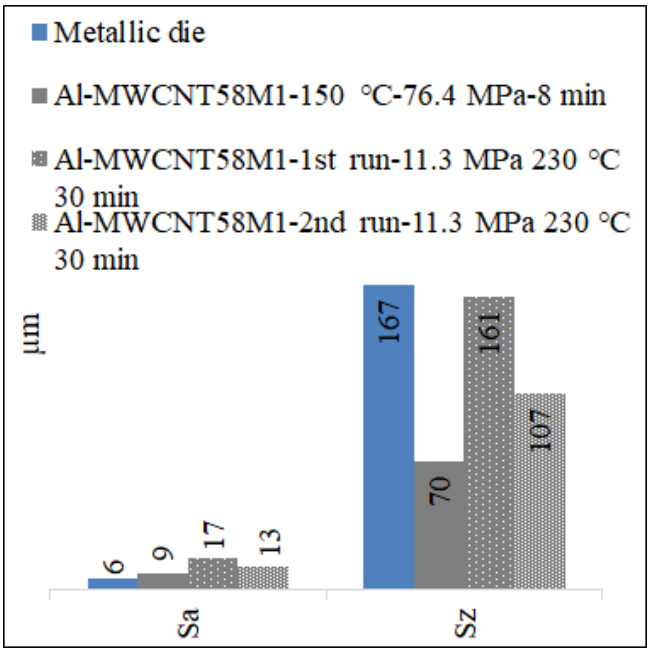

(b)

Figure 4.31 *Comparison between green parts of Al-MWCNT58M1 produced by three conditions and the master die: dimensions (a) and roughness (b) (cf. Figures 4.16 and 4.30).*

This shaping was attained through the application of following procedure:

- preheating the die assembly up to ~50 °C,
- shaping at 170 °C and 11.3 MPa for 10 minutes;
- demoulding the green part at ~90 °C,

- keeping the position of the die assembly upside down relative to the shaping condition (die cavity upwards and the replicating die rod downwards).

The feasibility of the shaping by metallic die was also demonstrated using two 316L-based feedstocks: 316L60M1 and 316L65M1 (Figure 4.33). The last composition corresponds to the higher viscosity (Table 3.1) and seems to be not suitable for a perfect shaping (cf. PIM). However, concave microgear (Figure 4.23c) and microwall (Figures 4.33c and 4.33d) were micro hot embossed using 316L65M1 feedstock. This means that, this procedure can be used for shaping feedstocks with higher viscosity than CPVC.

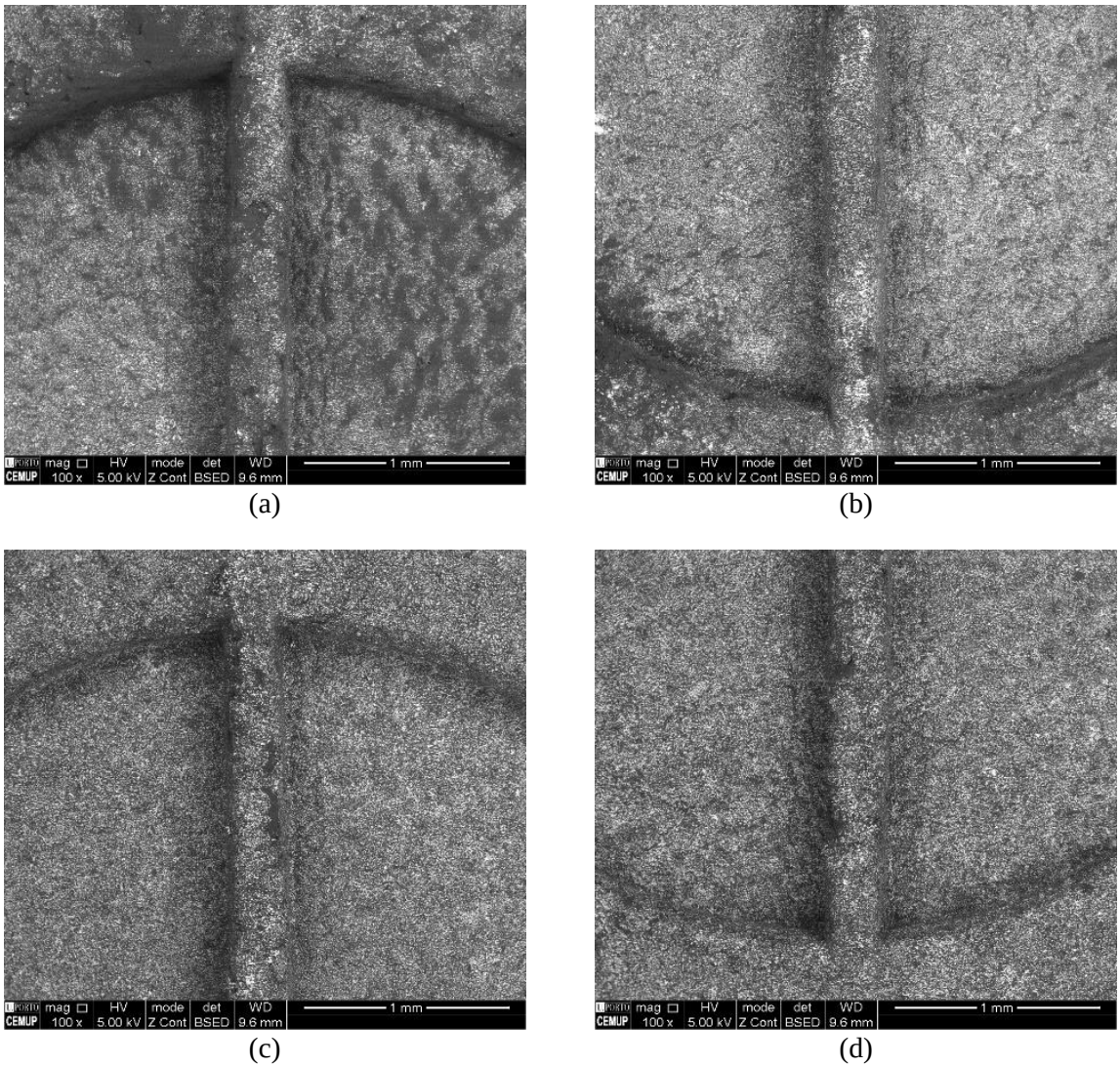

Figure 4.32 *Microstructure of the microwall-half-reservoirs shaped at 170 °C and 11.3 MPa for 10 minutes using: Al58M1 (a) and (b), Al-MWCNT58M1 (c) and (d) (SEM/BSE).*

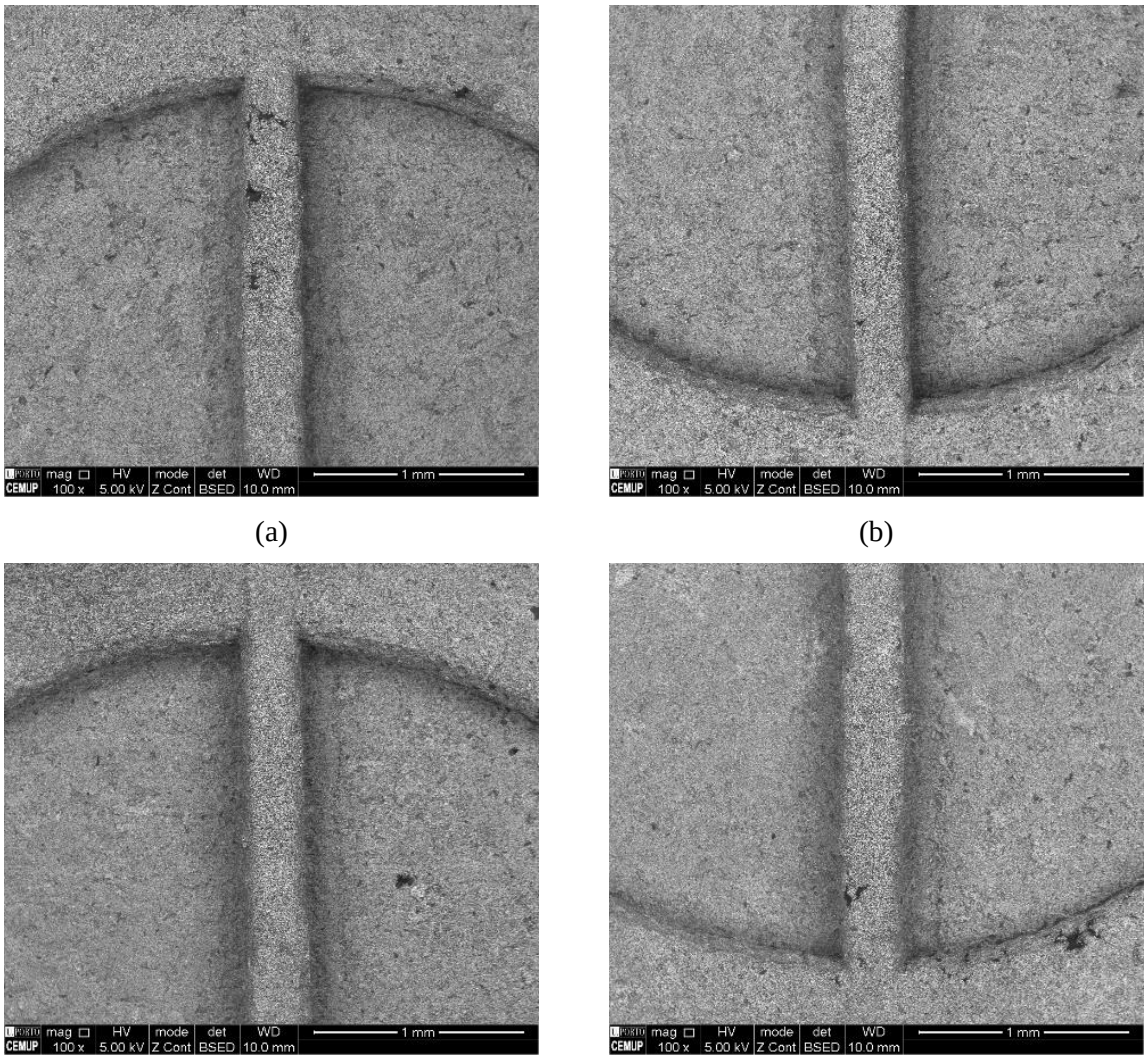

Figure 4.33 *Microstructure of microwall-half-reservoirs shaped at 11.3 MPa and 170 ℃ for 10 minutes made with: 316L60M1 (a) and (b), 316L65M1 (c) and (d) (SEM/BSE).*

4.4 Conclusions

Shaping of green specimens through micro hot embossing is strongly influenced by the particle size of the feedstock being the required mean particle size less than 500 µm. Straight profiles of green specimen were achieved by partially filling of the die cavity and applying a lid to cover it. The lifetime of the elastomer die is also influenced by the die assembly and it was increased by the use of an extra support disk on the top of the elastomer cover.

The most homogeneous dispersion after shaping was obtained using a blender as the granulation technique. The feedstocks with MWCNT attained the most homogeneous dispersion. However, for the 316L feedstock this depended on shaping time.

For Al-based feedstocks, a powder concentration of 58 vol.%, without any additions, guaranteed maximum replicability. The use of higher metallic powder concentrations (62 vol.%) with the addition of an organic material, such as stearic acid, to reduce the viscosity of the feedstock was not found to be suitable.

The increase of the surface roughness after shaping is a characteristic of micro hot embossing with elastomer die. The shaping was performed by compaction and particle bonding, both dependent on the processing conditions. To overcome the stiffness of the feedstock, conditions that induce the plastic deformation of the elastomer die are necessary. The stiffness of the elastomer material was effective for producing microparts, e.g. microtensile specimens.

The elastomer die was suitable to replicate the microchannel-half-flange geometry using Al and 316L feedstocks. The microwall-half-reservoirs were partially replicated with 316L feedstock with 60 vol.% powder concentration, but not with the Al one. This indicates that shaping is influenced by the powder characteristics.

Microgear with convex or concave geometries were also replicated with 316L feedstock using elastomer die. The 316L65M1 feedstock, which contains a powder content higher than CPVC, was also replicated into the concave gear geometry, with the lowest heterogeneity during shaping. This means that the CPVC should only be used as a starting parameter in micro hot embossing.

Micro hot embossing using elastomer die is more proper for replicating concave-like geometries than for convex geometries.

When the elastomer die was replaced by metallic one, the microwall-half-reservoirs geometries were replicated for all the feedstocks. Nevertheless, the distribution of the powder-binder was strongly affected by the process and was very sensitive to segregation. This problem was more pronounced in Al-based feedstocks than in 316L ones. The application of the metallic die provided smoother surfaces and required less demanding conditions, contributing to a sustainable process.

References:

[1] G. Fu, S. Tor, N. Loh, D. Hardt, **Applied Physics A: Materials Science & Processing**, **97** (2009) 925-931, 10.1007/s00339-009-5363-3.

[2] M. Sahli, C. Millot, J.C. Gelin, T. Barrière, **AIP Conference Proceedings**.

[3] M. Sahli, J.C. Gelin, T. Barriere, **Powder Technology**, **246** (2013) 284-302, 10.1016/j.powtec.2013.05.026.

[4] M. Sahli, C. Millot, J.C. Gelin, T. Barrière, **Journal of Materials Processing Technology**, **213** (2013) 913-925, 10.1016/j.jmatprotec.2012.11.007.

[5] E.W. Sequeiros, V.C. Neto, M.T. Vieira, M.F. Vieira, **Powder Metall.**, **57** (2014) 241-244, 10.1179/0032589914z.000000000193.

[6] E.W. Sequeiros, T.J. Ferreira, V.C. Neto, M.T. Vieira, M.F. Vieira, **Euro PM 2014 Congress and Exhibition, Proceedings**.

[7] E.W. Sequeiros, M.T. Vieira, M.F. Vieira, **Proceedings of the International Euro Powder Metallurgy Congress and Exhibition, Euro PM 2012**.

[8] E.W. Sequeiros, T.J. Ferreira, M.T. Vieira, M.F. Vieira, **Euro PM 2011**, Barcelona, Spain, 9 - 12 October 2011.

[9] M. Sahli, J.C. Gelin, T. Barriere, **Materials Science & Engineering C-Materials for Biological Applications**, **55** (2015) 252-266, 10.1016/j.msec.2015.05.019.

[10] J. Zhang, J.-C. Gelin, M. Sahli, T. Barrière, **Journal of Micro and Nano-Manufacturing**, **1** (2013) 041003, 10.1115/1.4025554.

[11] J. Zhang, M. Sahli, J.C. Gelin, T. Barriere, **International Journal of Advanced Manufacturing Technology**, **77** (2015) 2135-2149, 10.1007/s00170-014-6595-8.

[12] M. Sahli, J.C. Gelin, **International Journal of Advanced Manufacturing Technology**, **69** (2013) 2139-2148, 10.1007/s00170-013-5170-z.

[13] H.Z. Ye, X.Y. Liu, H.P. Hong, **Journal of Materials Processing Technology**, **200** (2008) 12-24, 10.1016/j.jmatprotec.2007.10.066.

[14] S.R. Bakshi, D. Lahiri, A. Agarwal, **International Materials Reviews**, **55** (2010) 41-64, 10.1179/095066009x12572530170543.

[15] Z. Baig, O. Mamat, M. Mustapha, **Critical Reviews in Solid State and Materials Sciences**, **43** (2018) 1-46, 10.1080/10408436.2016.1243089.

[16] R.K. Enneti, V.P. Onbattuvelli, S.V. Atre, 4 - Powder binder formulation and compound manufacture in metal injection molding (MIM) A2 - Heaney, Donald F, Handbook of Metal Injection Molding, Woodhead Publishing2012, pp. 64-92.

[17] E.W. Sequeiros, Microfabricação de Componentes Metálicos por Microgravação, Department of Materials and Metallurgical Engineering, **University of Porto**, 2014.

[18] I.M. Meththananda, S. Parker, M.P. Patel, M. Braden, **Dental Materials**, **25** (2009) 956-959, 10.1016/j.dental.2009.02.001.

[19] B. Tay, N.H. Loh, S.B. Tor, F.L. Ng, G. Fu, X.H. Lu, **Powder Technology**, **188** (2009) 179-182, 10.1016/j.powtec.2008.04.047.

[20] H. Saidin, M. Azuddin, **4th International Conference on Mechanical and Manufacturing Engineering, ICME 2013;** , **Applied Mechanics and Materials**, **465-466** (2014) 1250-1254, 10.4028/www.scientific.net/AMM.465-466.1250.

[21] H. Lobo, 8 - Characterization of feedstock in metal injection molding (MIM) A2 - Heaney, Donald F, Handbook of Metal Injection Molding, Woodhead Publishing2012, pp. 183-196.

[22] H.I. Bakan, Y. Jumadi, P.F. Messer, H.A. Davies, B. Ellis, **Powder Metall.**, **41** (1998) 289-291.

[23] Z.D. Han, A. Fina, **Progress in Polymer Science**, **36** (2011) 914-944, 10.1016/j.progpolymsci.2010.11.004.

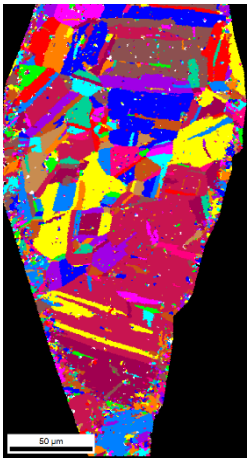

Chapter 5 – Thermal debinding and sintering

5.1 Introduction

In the previous chapter, the characteristics of green parts resulting from Al and 316L feedstocks, with or without MWCNT, were evaluated. The quality of micro hot embossed green parts, dimension and roughness, are dependent factors of several variables as follows: feedstock granulated size (Figure 4.1), die assembly (Figures 4.2, 4.3 and 4.5), feedstock composition (Figures 4.8, 4.21 and 4.28), powder characteristics (Figure 4.11), geometry of parts (Figures 4.10, 4.11, 4.21, 4.23 and 4.24c), elastomer stiffness (Figures 4.15, 4.19 and 4.20, Table 4.1), die material (Figures 4.11 and 4.25 compared with 4.32 and 4.33, Figure 4.31), and MWCNTs reinforcements content (Figures 4.5a, 4.25b, 4.28 and 4.32). The addition of the MWCNT contributes to increase the feedstock homogeneity during shaping, and to decrease the probability of cracking during demoulding (Figures 4.9, 4.12 and 4.32).

For micro hot embossing to be considered as a near-net shape production technique, it is required to control the dimensions and surface roughness, in green parts and, especially, after debinding and sintering. In addition, this control is very important to clarify the contribution of porosity, phase evolution, and MWCNT strengthening effect in the characteristics of the final component.

Thermal debinding was the process selected for the removal of the binder, rather than water/acid solution or catalytic. The behaviour of the nanotubes during binder decomposition was also evaluated. In the thermal debinding process the tubular furnace was evacuated up to ~0.1 Pa with the use of a rotary oil pump, after this step the furnace was purged with Ar-H_2; these actions were repeated three times.

After debinding, the densification was carried out by sintering. Two challenges must be taken into account; the difficulty of sintering Al powders due to a possible superficial and continuous layer of stable aluminium oxide and eventual carbide precipitation in 316L stainless steel due to the reaction of metallic elements with the carbon from MWCNT and/or the binder residue.

Different sintering atmospheres were tested for Al: Ar; Ar-H_2; low vacuum (~0.1 Pa) and high vacuum (< 5×10^{-3} Pa). The sintering was carried out for 2 hours at 640 °C, a temperature higher than the typical 70% of its absolute melting temperature. Some authors have indicated that, this temperature in appropriate for sintering Al in the PIM process (cf. section 1.3.5) and for Al-MWCNT composite production [1]. As regards the 316L powder sintering, it was also carried out for 2 hours at 1250 °C and ~5×10^{-3} Pa.

After sintering, due to the diffusion and porosity reduction, the parts must present shrinkage [2] and, as in green parts, the metallic die should contribute to a smoother surface than the elastomer one, being this more noticeable in the 316L than in the Al powder.

5.2 Thermal debinding

TG curve of the binder (Figure 2.16a) revealed zero residue after heating up to 500 °C at 10 °C/min. This efficiency might be achieved after debinding feedstock through applying long and multistep cycle (Figure 5.1), thus allowing the burnt products to diffuse out of the part.

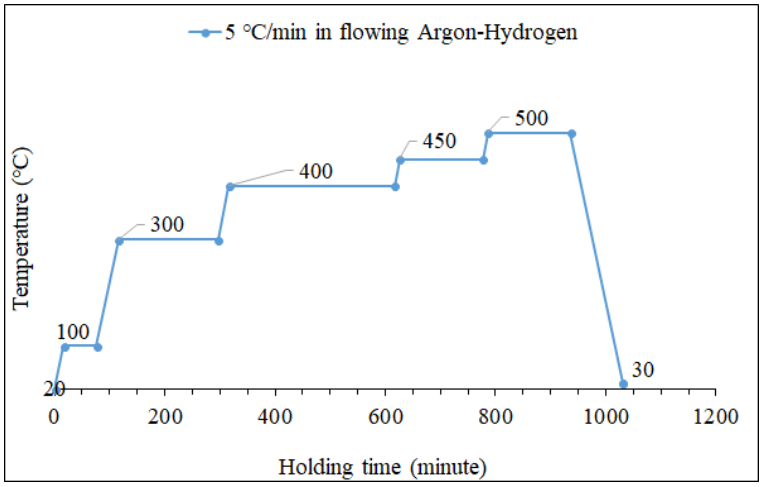

Figure 5.1 *Thermal debinding cycle, homothetic of TGA curve of the binder (M1).*

Brown Al and 316 L parts maintained their geometry (Figure 5.2).

According to the weights of some Al brown parts compared with calculated ones[19], a variation smaller than 4% was observed, being attributed to the binder residue or any phase formation during debinding, like oxidation of Al. Heating rates from 1 °C/min to 5 °C/min, had no significant influence on the efficiency of debinding. Moreover, the presence of 1 vol.% MWCNT contributed to slightly increasing the debinding efficiency. When the Al parts were weighed after sintering, the weights seemed similar before and after the sintering process. This unexpected maintenance of the weight highlights the oxidation of the Al powder during debinding/sintering, and/or the heterogeneity of the Al feedstock (see Figures 4.9 and 4.32).

As regards the brown 316L, they lost weight after sintering by ~3% for all measured parts. This small reduction in weight is attributed to losing the debinding residues or to the eventual phase formation (carbide/oxide) due to the presence of pores and/or carbon, from MWCNT and/or binder residue, in the 316L brown parts, giving rise to new phases with density different from the 316L austenitic steel.

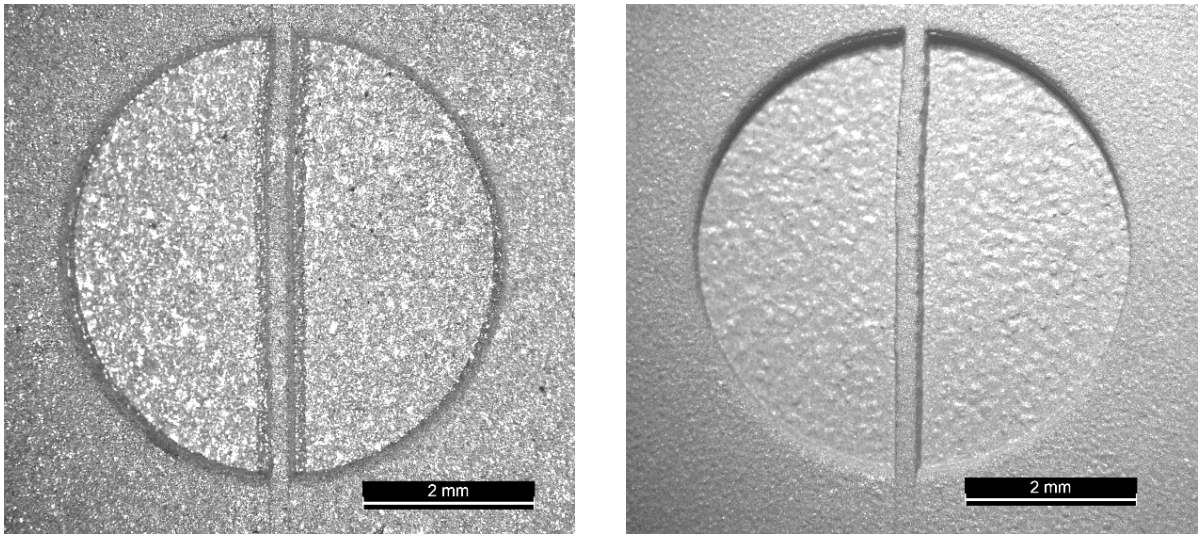

(a) (b)

Figure 5.2 *Brown Al (a) and 316L (b) microwall-half-reservoirs (stereoscopy).*

[19] Cf. equation 2.2.

Part A- Al powders

5A.1 Sintering brown parts

In this sub-chapter different conditions to produce bulk densified aluminium parts during micro hot embossing process, as well as the phase evolution and shape preservation, will be analysed.

5A.1.1 Effect of controlled atmosphere

Preliminary sintering experiments were performed by placing the parts on a porous ceramic plate for debinding, afterwards the parts were controlled for mass and dimensions, and then placed on a clean tray, uncontaminated by the debinding burnt products, and moved to the sintering furnace. The brown parts were not sintered (at 640 ºC for 120 minutes) under low vacuum, in Ar, or in Ar-H_2 constant atmospheres, they were very fragile and easily broken during handling, no shrinkage was observed (Figure 5.3a). The sintering failure can be attributed to the presence of large porosities (Figure 5.3b). Although necks had formed, an indication of the surface diffusion mechanism for low temperature sintering rather than evaporation-condensation, such necks did not grow (Figures 5.4a and 5.4b) indicating that volume material transportation was limited.

Partially-sintered particles (Figures 5.4a and 5.4b) have a rougher surface morphology than pristine powder (Figure 5.4c), which can indicate a composition change, whether oxide or carbide formation.

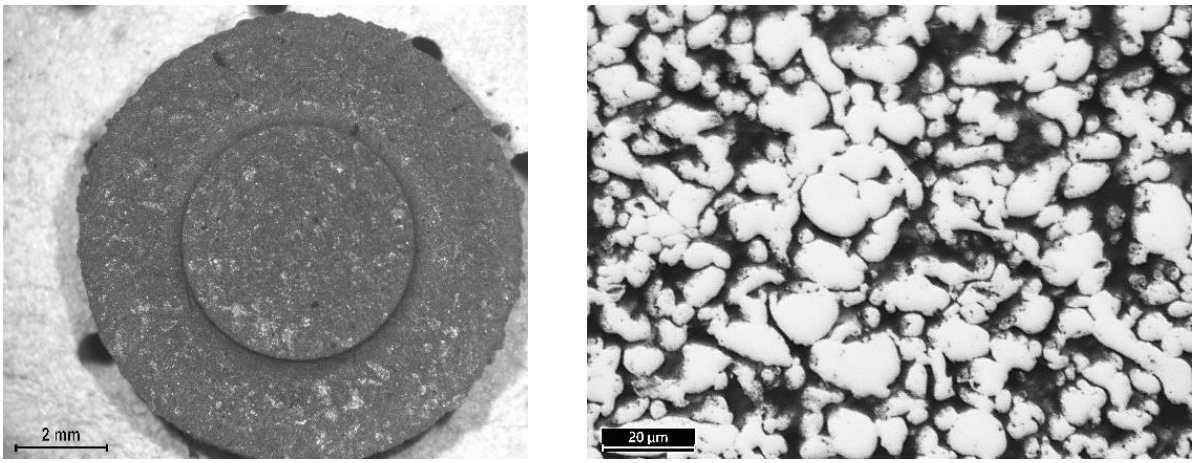

(a) (b)

Figure 5.3 *Brown microblind-flange part made of Al58M1, shaped at 230 ºC/8.5 MPa/45 min, sintered at 640 ºC for 120 minutes in Ar-H_2 (a) (stereoscopy), microstructure of cross section (b) (optical microscopy).*

In addition, it was seen that the number of necks per particle was quite small, almost one per particle (Figure 5.4a), which indicates that each particle is being bound to a very small number of neighbouring particles. Moreover, the neck sizes are mostly less than one-third the size of the powder, resembling neck formation at the earliest step of pressureless sintering [2]. This means that the pressure applied for shaping during micro hot embossing, 8.5 MPa, was not sufficient to bring the powders close enough. Three reasons could contribute to this shortcoming: the powder shape factor, the powder volume concentration in the green part and the low compaction during shaping (Figure 5.5).

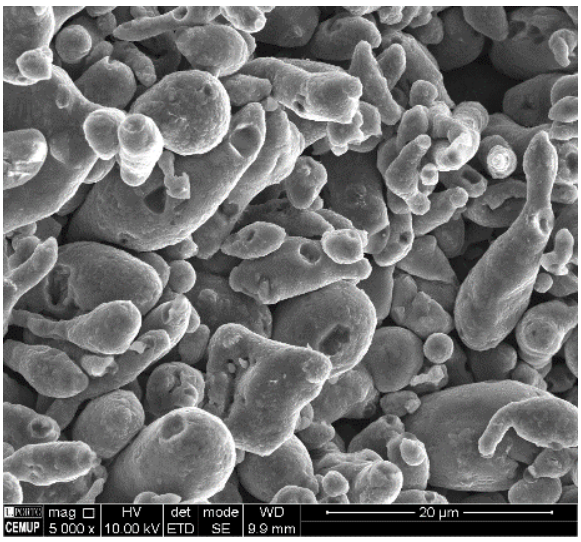

(a)

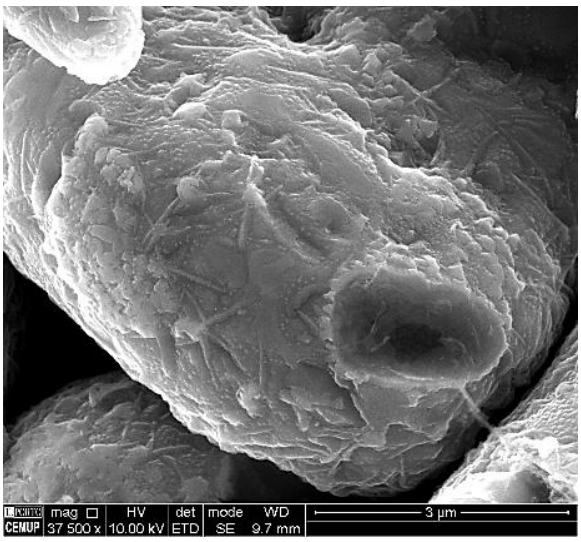

(b)

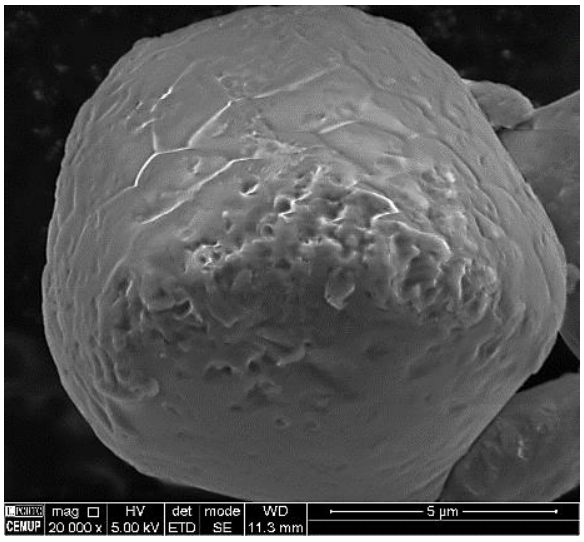

(c)

Figure 5.4 *Partially-sintered Al powders on the broken section of the part (cf. Figure 5.3) with necks and rough morphology (a) and (b); smooth surface of a pristine Al particle (c) (SEM/SE).*

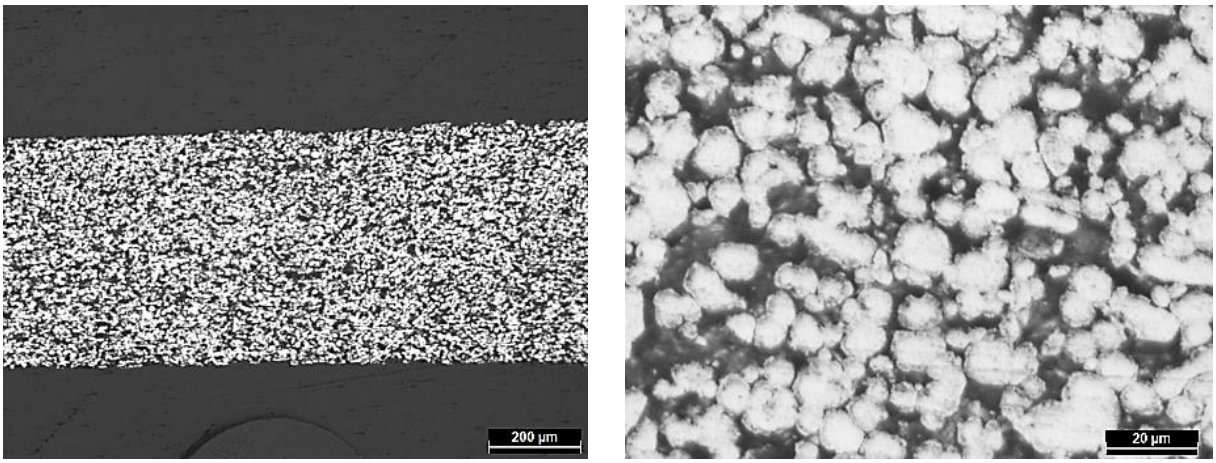

(a) (b)

Figure 5.5 *Green part in Al58M1 shaped at 230 ºC and 8.5 MPa for 30 minutes: cross section (a), in a higher magnification (b) (optical microscopy).*

Besides the large particle interspace, another reason for the sintering failure when using a controlled atmosphere, it can be the trapped air between particles after debinding, occurred during the pause between debinding and sintering. To eliminate this problem, the debinding and sintering were performed consecutively in an Ar-H_2 atmosphere. This experiment was carried out for green parts with 62 vol.% powder and compacted at 76.1 MPa. After sintering, these parts were not very brittle, but broke and the surface of their particles in cross section was rougher than the pristine powder (Figure 5.6).

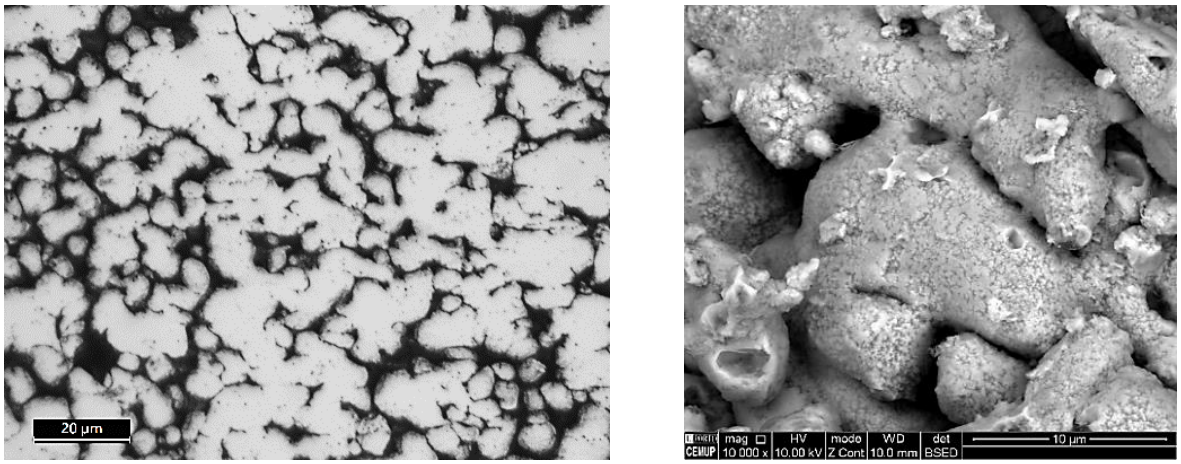

(a) (b)

Figure 5.6. *Cross section of the sintered Al part with 62 vol.% of powder, debound and sintered consecutively in Ar-H_2 at 640 ºC for 2h: as polished (a) and failure surface (b) (OM and SEM/BSE).*

Though the SEM/EDS is not a perfect technique for surface analysis and for quantifying the light elements like oxygen, when the spectra of pristine powder and sintered one are compared, it is evident that the topography of sintered powders can be attributed to oxidation during thermal cycling (Figure 5.7).

Therefore, the failure of sintering the Al in the atmosphere of Ar-H_2 can be caused by the residual oxygen remaining after the primary evacuation (0.1 Pa), and that the hydrogen of the atmosphere did not contribute to the reduction of this partial oxygen. Moreover, another oxidizing resource could be CO_2, or any other carbon compound, in particular those resulting from binder decomposition [3-5]. Thus, the sintering experiments proceeded with high vacuum application.

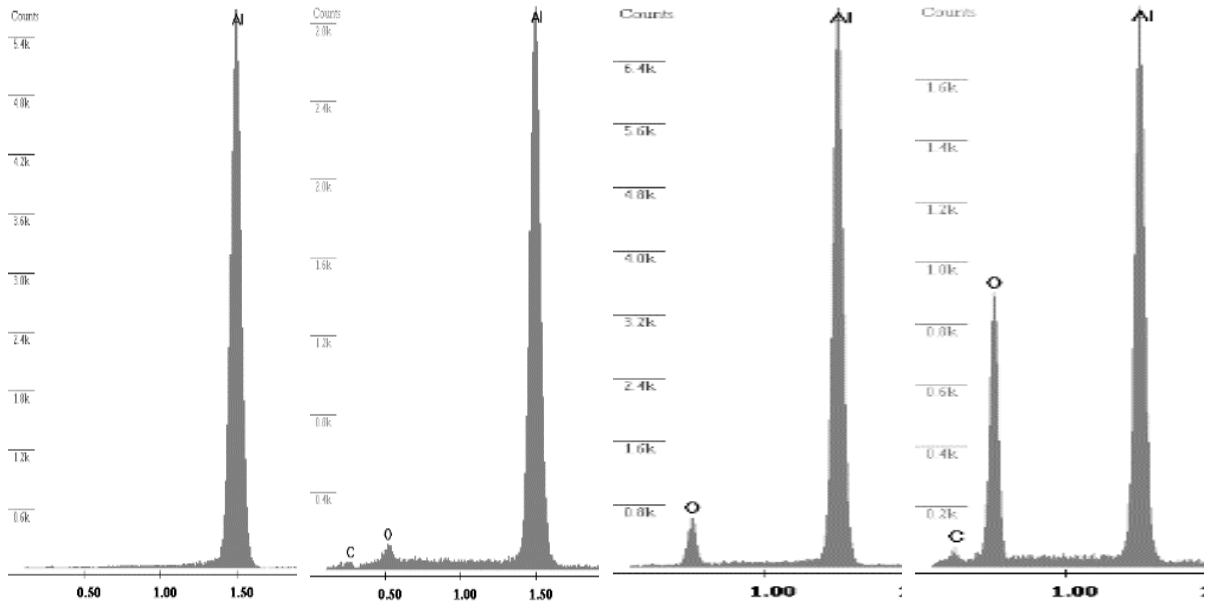

Figure 5.7 *Spectra of the pristine Al powder particle: acquired at 10 keV (a), O_2 peak detected at low voltage, 5 keV (b); spectra of a sintered particle (cf. Figure 5.6): O_2 peak at 10 keV (c) and the peak increase at 5 keV (d) (SEM/EDS).*

5A.1.2 Sintering Al at <5×10^{-3} Pa

Brown parts after weighing and dimensional control were sintered at 640 °C and <5×10^{-3} Pa for 2h. These conditions yielded a diagonal shrinkage of ~15% on the Al part with 58 vol.% powder

content. This part did not break manually although a partially melted zone was observed (Figure 5.8a). Therefore, this densification must be caused by the liquid formation in the presence of the low partial pressure of oxygen in the sintering atmosphere. Microstructural analysis (Figure 5.8b) revealed a porosity of ~17%[20]. The partial melted zone was squeezed out instead of being distributed in the bulk, and it may be caused by any possible heterogeneity of the feedstock. Furthermore, since the Al pristine powder contains some Fe impurity, the formation of the Al-Fe eutectic may have promoted melting at the sintering pressure. The microstructure (Figure 5.8c) shows the Al matrix, porosity and Al-Fe intermetallic (probably $Al_{13}Fe_4$) according to the spectra result (Figures 5.8d and 5.8e).

The pore reduction is affected by the pressure level in the pores. Decreasing this pressure increases the chance of void filling [6]. However, the final porosities were not eliminated because the melted Al did not fill in the internal voids. Besides, the reduction of aluminium oxide and the evaporation of aluminium did not occur at 640 °C. In fact, the aluminium vapour pressure at this sintering temperature is $<\sim 1.3\times10^{-6}$ Pa, according to the Honig curve [7].

From the microscopic observations an entire cross section (e.g. Figure 5.9), it seems that the porosity close to the part faces is slightly higher than in the inner zone, which can be caused by a greater possibility of air contact on the surfaces during the handling of the brown parts, or because the compaction has been affected by the friction between the elastomer die and feedstock during shaping. However, since micro hot embossing is considered as a near net shape process, a finishing process can remove the superficial defects.

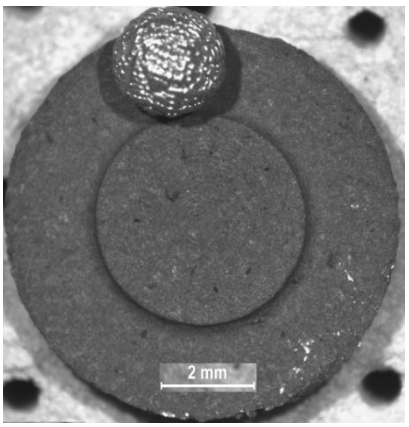

(a)

[20] Obtained by ImageJ from 15 optical microscopy images with 200X magnification, acquired from a polished cross section, these values had a standard deviation of ~1.

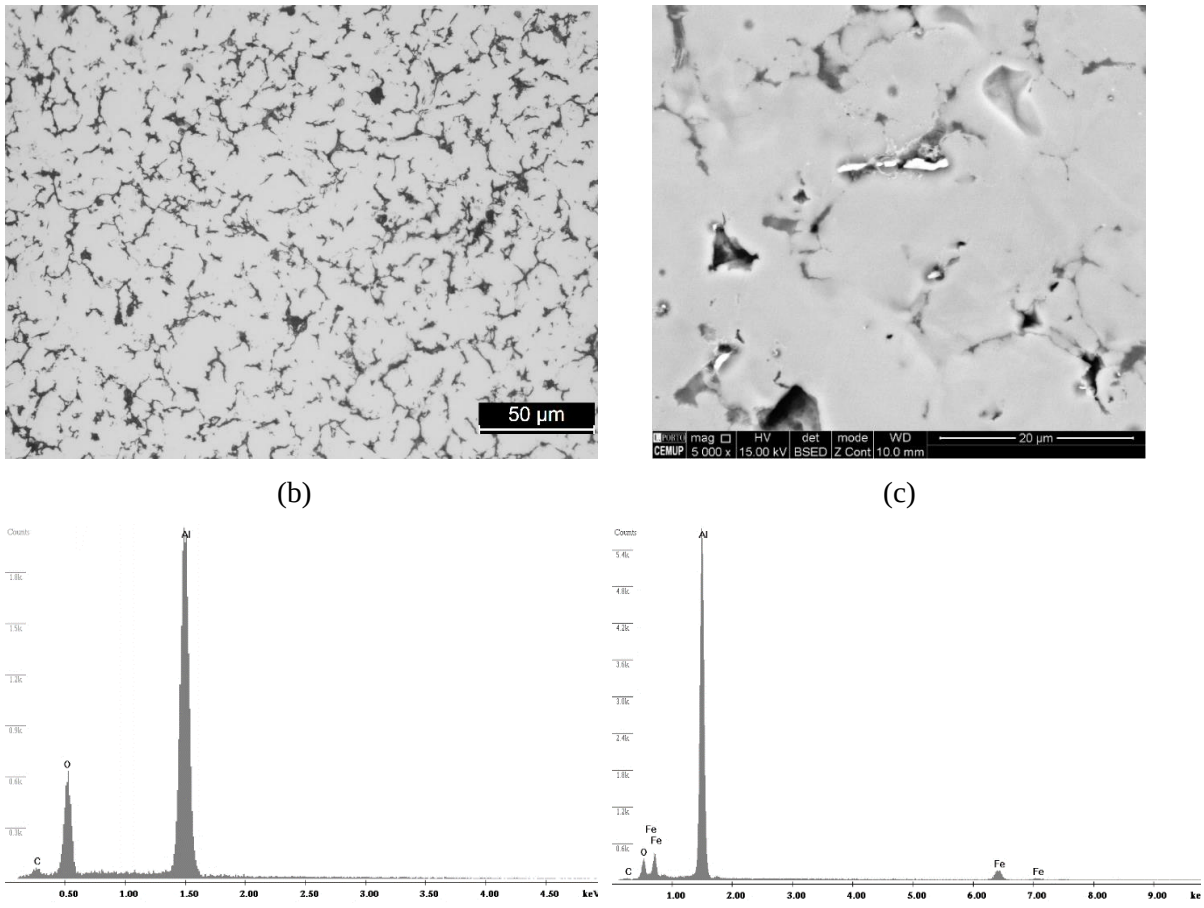

(b) (c)

(d) (e)

Figure 5.8 *Microblind-flange part shaped at 230 ºC and 8.5 MPa for 45 minutes and sintered at 640 ºC for 120 minutes in high vacuum (<5×10^{-3} Pa) (a) (stereoscopy); porosity distribution in the microstructure of a cross section (b) (OM); Al matrix, porosities and white particles as iron intermetallic (c) (SEM/BSE); the spectra of Al matrix (d) and the intermetallic particle (e) (SEM/EDS).*

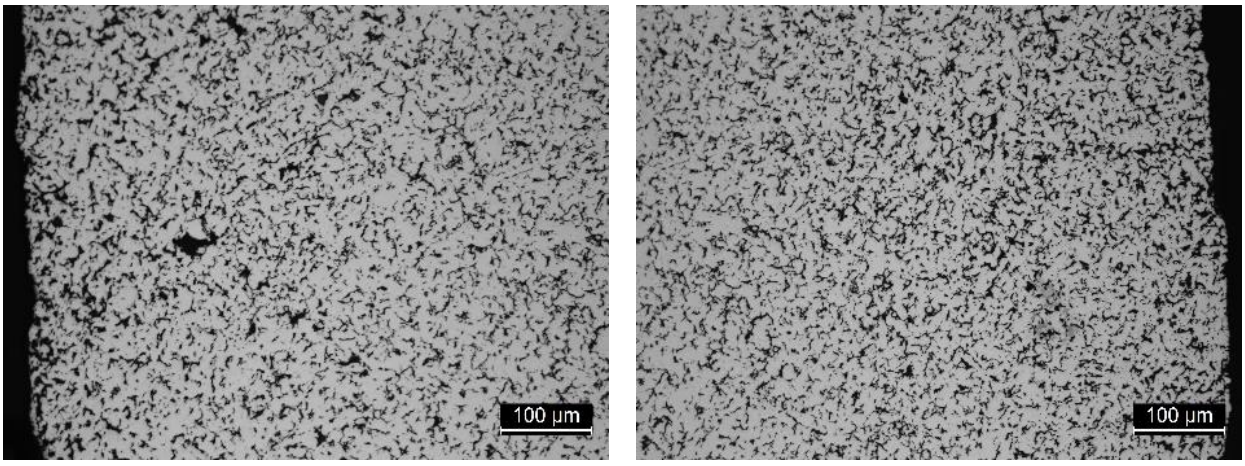

(a) (b)

Figure 5.9 *Porosity distribution in a polished section from one side (a) to another side (b) of the Al sintered part (cf. Figure 5.8) (optical microscopy).*

5A.1.3 Sintering Al-1 vol.% MWCNT at <5×10^{-3} Pa

Brown Al-MWCNT parts shrank ~14%, diagonally, although the partial melting defect was seen again (Figure 5.10).

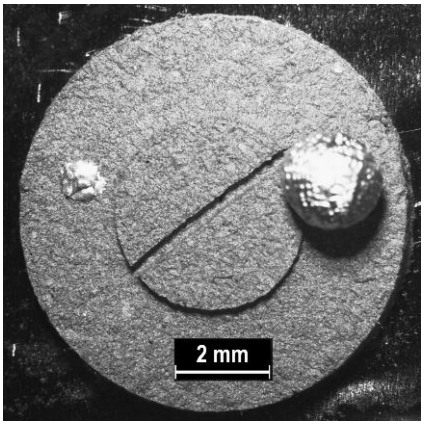

Figure 5.10 *Al-1 vol.% MWCNT microchannel-half-flanges part, shaped at 230 ºC and 11.3 MPa for 30 minutes and sintered at 640 ºC for 120 minutes in high vacuum (<5×10^{-3} Pa) (stereoscopy).*

The densification has been caused by the liquid formation once more. Metallographic analysis revealed a porosity of approximately 26%[21] (Figure 5.11a). This porosity should also be associated with the MWCNT aggregates that are still visible in the parts (Figure 5.11b).

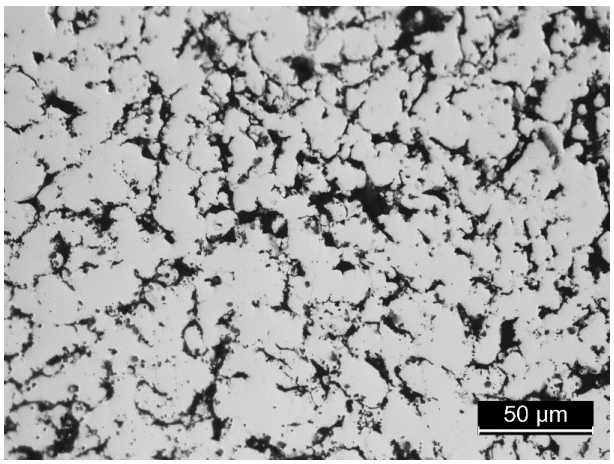

(a)

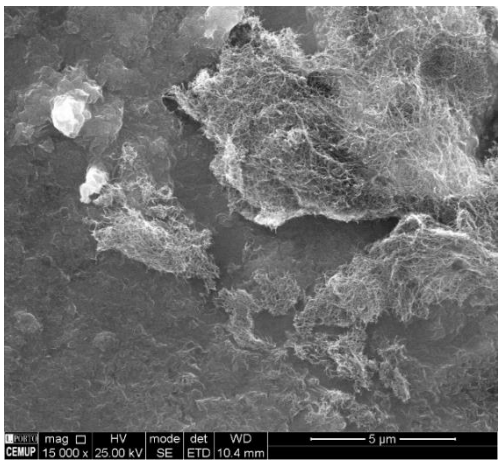

(b)

Figure 5.11 *As polished cross section (a) (OM); and the MWCNT aggregates on the surface of the sintered Al-MWCNT part (b) (SEM/SE).*

[21] Obtained by ImageJ from 16 optical microscopy images with 200X magnification, acquired from the polished cross section, these values had a standard deviation of ~1.

5A.1.4 Elimination of partial melting

Partial melting was eliminated when the brown Al-MWCNT was sintered at a slightly lower temperature, 635 ℃ (Figure 5.12a), although this was achieved in expense of shrinkage, ~10%, with a porosity of ~22%[22] (Figure 5.12b). In comparison with previous condition (section 5.A.1.3), the shrinkage is smaller but the porosity is less too. This apparent contradictory porosity reduction is attributed to the material being preserved in the bulk since no liquid has been squeezed out. However, the sintered part broke manually, Figure 5.12c illustrates the plastically deformed zone which is smoother than the neighbouring region, showing blisters-like features in the particles and clusters of MWCNTs (white arrow in Figure 5.12c).

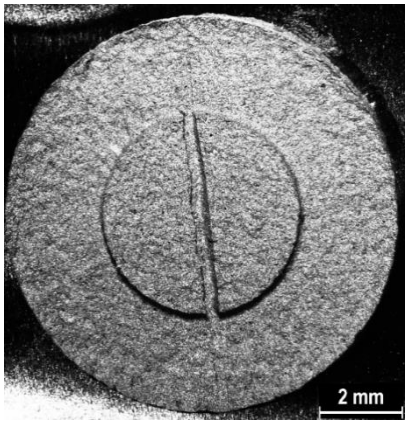

(a)

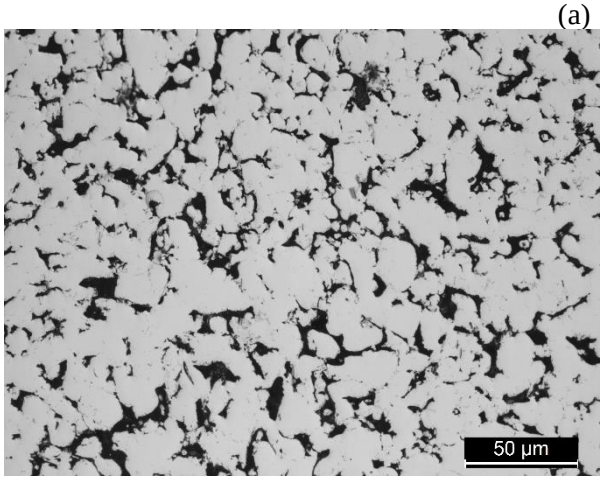

(b)

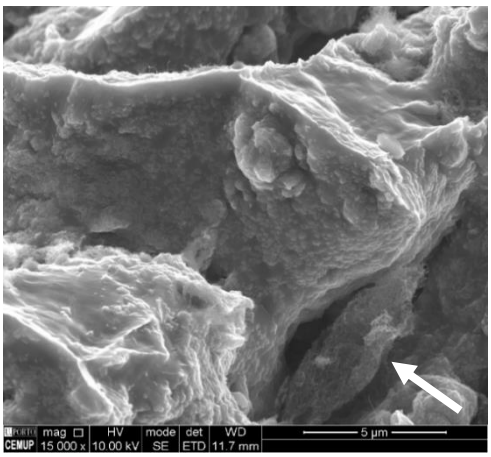

(c)

Figure 5.12 *Sintered microchannel-half-flanges Al-1 vol.% MWCNT (with 58 vol.% powder content, shaped at 230 ℃ and 8.5 MPa for 30 minutes and sintered for 120 minutes in <5×10^{-3} Pa: macroscopic aspect (a) (stereoscopy); porosity on the cross section of the part (b) (OM); morphology of the broken section (c) (SEM/SE).*

[22] Obtained by ImageJ from 18 optical microscopy images with 200X magnification, acquired from the polished cross section, these values had a standard deviation of ~2.

Therefore, the weak sinterability should be associated with the presence of these defects.

When the sintering time was increased to 5 hours maintaining the temperature of 635 ℃, only a diagonal shrinkage increase of about 1% for the Al parts and almost negligible for the Al-MWCNT ones was detected. Since no melt was observed, neck growth could be obtained by the volume diffusion mechanism, occurring at this critical temperature and with the lowest oxygen partial pressure possible [2].

5A.1.5 Effect of MWCNT on the sinterability

Two Al58M1 and AlMWCNT58M1 parts, shaped at equal conditions, were debound and sintered, simultaneously. The diagonal shrinkage and porosity of the Al part equal 11% and ~14%[23], respectively, while those of the Al-MWCNT part equal 8% and 21%[23] (Figure 5.13). This reduction in both shrinkage and densification confirms that the presence of the nanotubes in parts processed by micro hot embossing hindered densification shrinkage, which is consistent with other PM approaches [8, 9]. This is due to the differences between the physical properties of the Al powder and the tangled MWCNT [10].

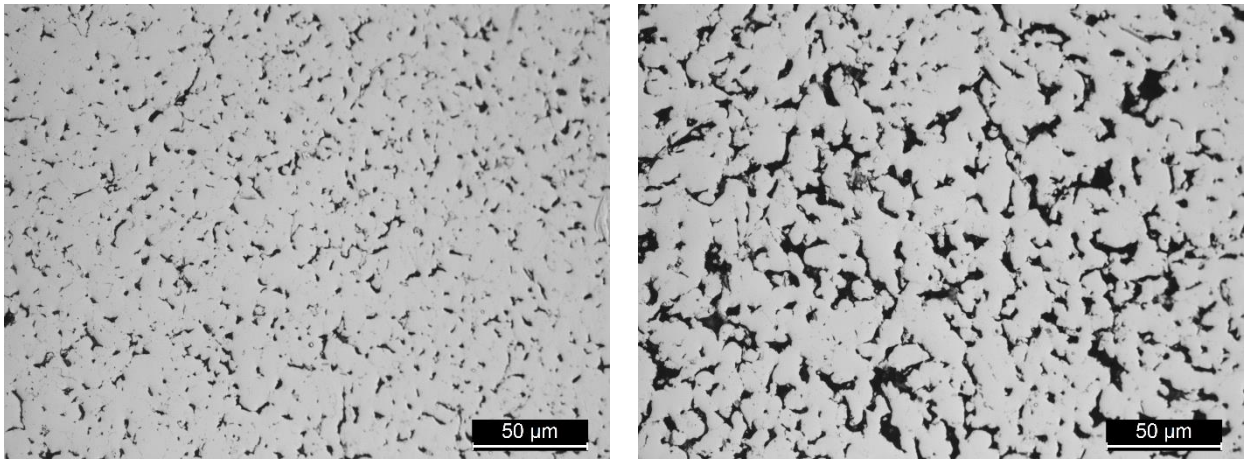

(a) (b)

Figure 5.13 *Cross section of Al (a) and Al-1 vol. % MWCNT (b) parts (optical microscopy), shaped at 170 ℃, 11.3 MPa for 10 minutes, sintered at 637 ℃ and <5×10^{-3} Pa for 2h, without any partial melted zone.*

[23] Obtained by ImageJ from 18 optical microscopy images with 200X magnification, acquired from the polished cross section, these values had a standard deviation of ~3.

Microhardness measurements showed similar values for the Al and Al-MWCNT, 26±0 and 25±3 HV (0.098 N), respectively. The expected hardening effect of the MWCNT should have been neutralized by the presence of porosity and MWCNT aggregates (cf. Figure 5.13). This effect is noticeable in the standard deviation values. This shortcoming will be discussed in Chapter 6 in which the effects of particle size and MWCNT aggregations are explored.

5A.1.6 Effect of using a metallic die

As explained previously (section 4.3.3), shaping with metallic die allowed the use of less demanding conditions (reduction of the shaping time to 10 minutes and the temperature to 150 ºC). Two sets of parts were debound and sintered at equal conditions (637 ºC and $<5\times10^{-3}$ Pa for 2h) and led to diagonal shrinkages of 11% and 12% for the Al, and 8% and 9% for the Al-MWCNT. These values are very similar to those described above, indicating that the use of the metallic die in the shaping did not affect the subsequent processing conditions.

It should be mentioned that the productivity of the shrinkage was strongly dependent on the cleanliness state of the sintering tray and tube, such that shrinkage decreased if they had already been used.

5A.1.7 Oxidation of aluminium powder during thermal cycles

This study attributes the porosity of Al parts sintered in high vacuum not only to the pores inherent to the PM approach [11], but also to the Al oxidation during the thermal cycles. This hypothesis was evaluated by comparing two specimens composed only of Al powder and prepared as follows:

- Pressed with ~8 MPa and sintered,
- Pressed at the same pressure, subjected to the debinding cycle in $Ar+H_2$ atmosphere and then sintered.

Cross sectional observations (Figure 5.14) revealed that the porosity of the pressed and sintered Al powders was much lower than the specimen that had passed through the thermal debinding cycle (Table 5.1).

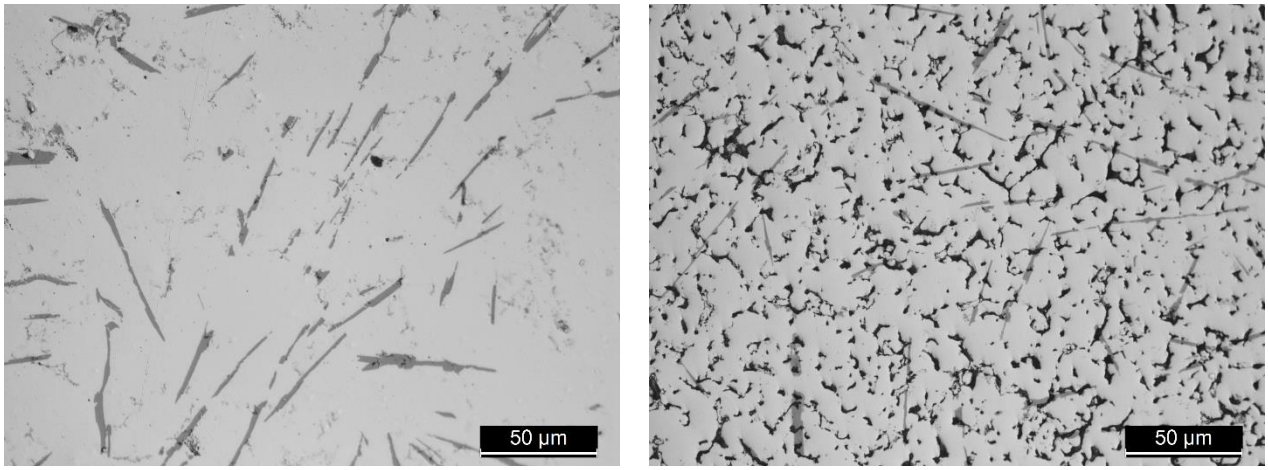

(a) (b)

Figure 5.14 *Microstructure of Al disks: pressed and sintered (a); pressed, subjected to the debinding cycle and then sintered (b), sintered simultaneously at 637 °C and <5×10^{-3} Pa for 2h (OM).*

Table 5.1 Porosity measurements from sintered Al specimens, obtained by ImageJ from 20 to 15 optical microscopy images with 200X magnification, acquired from the polished cross sections (cf. Figure 5.14).

Al Specimen	**Pressed and sintered**	**Pressed, subjected to a thermal cycle similar to debinding and sintered**
Average porosity	4±2	16±4

The needle-like phases (Figure 5.14) should be Al-Fe intermetallics (Figure 5.15) caused during sintering by iron impurities in the pristine powder. The most pronounced presence of these needles in the microstructure occurs because these specimens were prepared from the last amount of purchased powder in which the impurity content of iron was higher.

When these sintered specimens were etched, no grain boundary was revealed in the microstructure of the pressed and sintered powders (Figure 5.16a), but the sintered specimen subjected to the thermal debinding cycle has a microstructure of fine grains (Figure 5.16b), almost as small as the particle size of pristine powder.

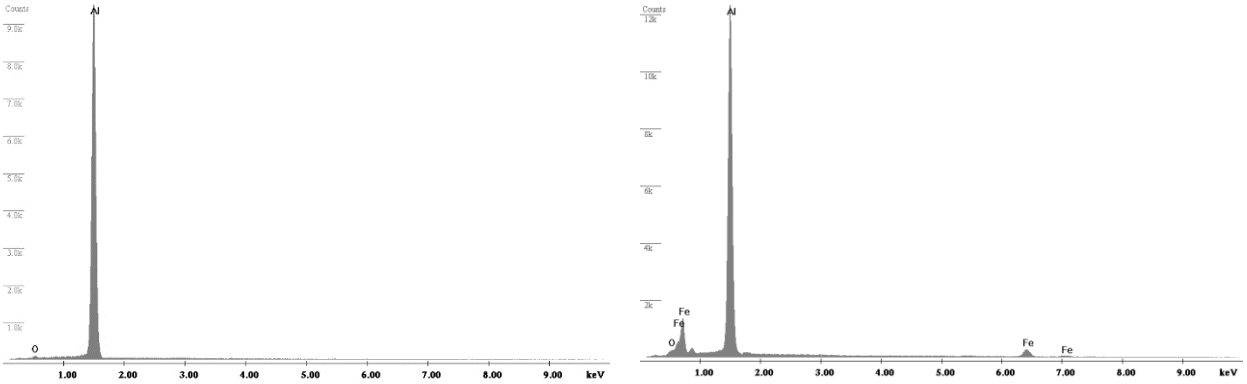

(a) (b)

Figure 5.15 *Spectra of the matrix (a) and of the needles (b) (SEM/EDS).*

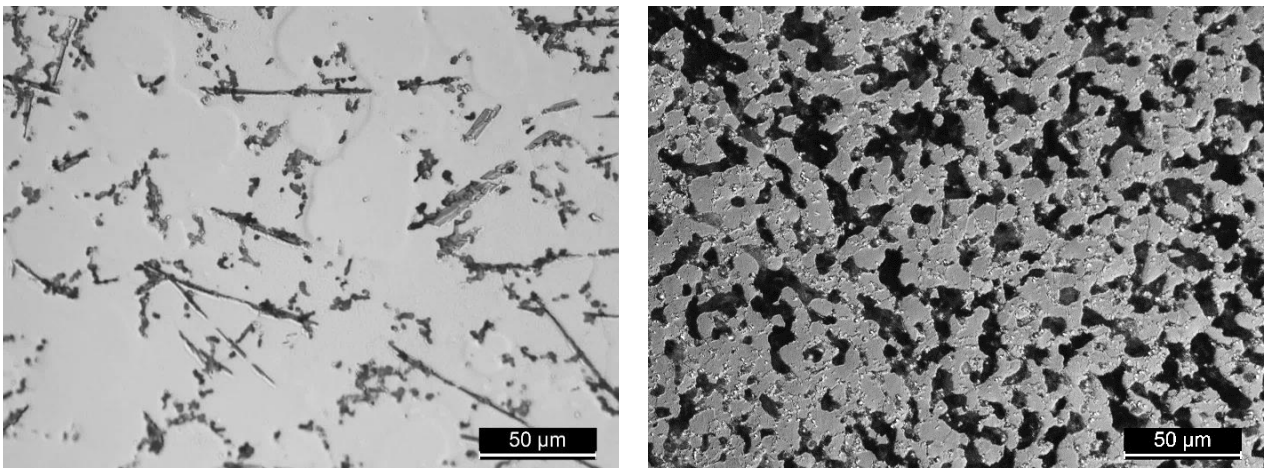

(a) (b)

Figure 5.16 *Microstructure[24] of sintered Al powders pressed and sintered, after etching: without thermal debinding cycle (a), with the debinding cycle (b) (OM).*

5A.1.8 Other phases

When the diffractograms of pressed and sintered Al and Al-MWCNT parts were compared with the micro hot embossed ones (Figure 5.17a), the Al matrix peaks were confirmed for all parts by comparison with the reference pattern number from ICDD 00-004-0787. There was also a peak highlighted at 78.9 º, appearing only for the micro hot embossed parts, which may be attributed to an aluminium oxide.

[24] Etched by H_2O-HNO_3-HF (92:6:2) for 15 minutes at room condition.

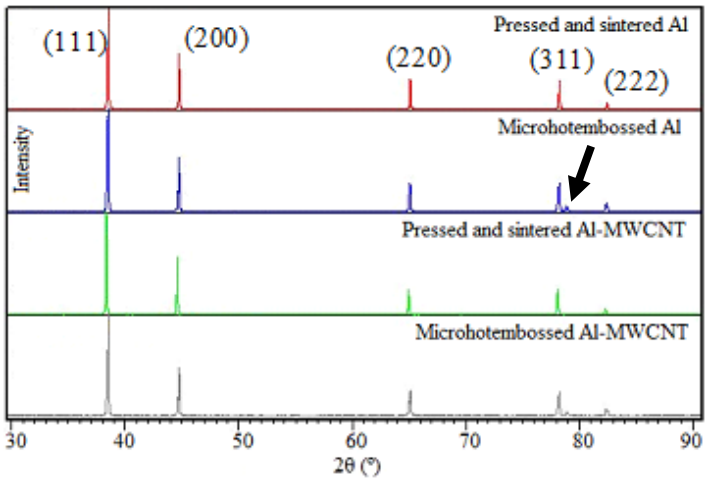

(a)

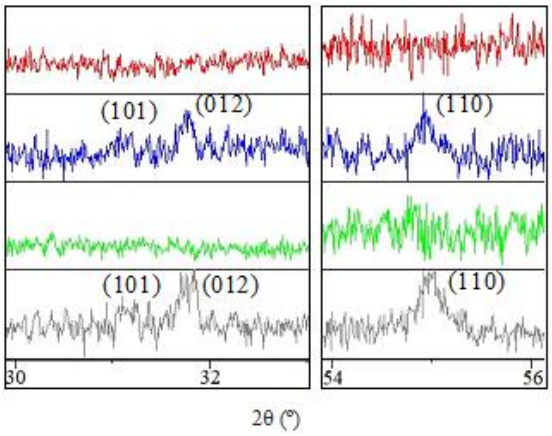

(b)

Figure 5.17 *X-ray powder diffraction[25] of four specimens, black arrow indicates the peak at 78.9º (a), details of different zones of the diffractograms illustrating Al_4C_3 (b).*

Moreover, there were other peaks associated with aluminium carbide (Figure 5.17b), identified by reference pattern number from ICSD 01-079-1736. These peaks were only indexed in the micro hot embossed parts. This phase can support the presence of carbon residues after debinding (cf. 5.2) [12]. The confirmation of aluminium carbide, by XRD, was reported in the sintered aluminium matrix composites reinforced with CNT or carbon black, and subjected to a severe plastic deformation (by ball milling or hot extrusion) [13-15]. A more precise confirmation can be done by TEM.

[25] Specimens weighed <0.3 g, scanning rate was 1 º/s and the specimen was rotating during acquisition.

5A.1.9 Shaping after sintering

Cross section observations of a microwall feature made of Al and sintered at 635 °C (Figure 5.18a) reveal that the porosities in the microwall are larger than in the base, while the same feature made of Al-MWCNT has a homogeneous dispersion, although larger (Figure 5.18b). The higher porosity in the latter specimen is associated with the MWCNT aggregates, as previously mentioned. The dimensions of the microwall feature and of the master die are presented in Table 5.2. These results show that the microwalls are shorter than their die, and they are less conical. There are minor differences between the Al and Al-MWCNT parts. The smaller the dimension, the lower the difference between the die and the part.

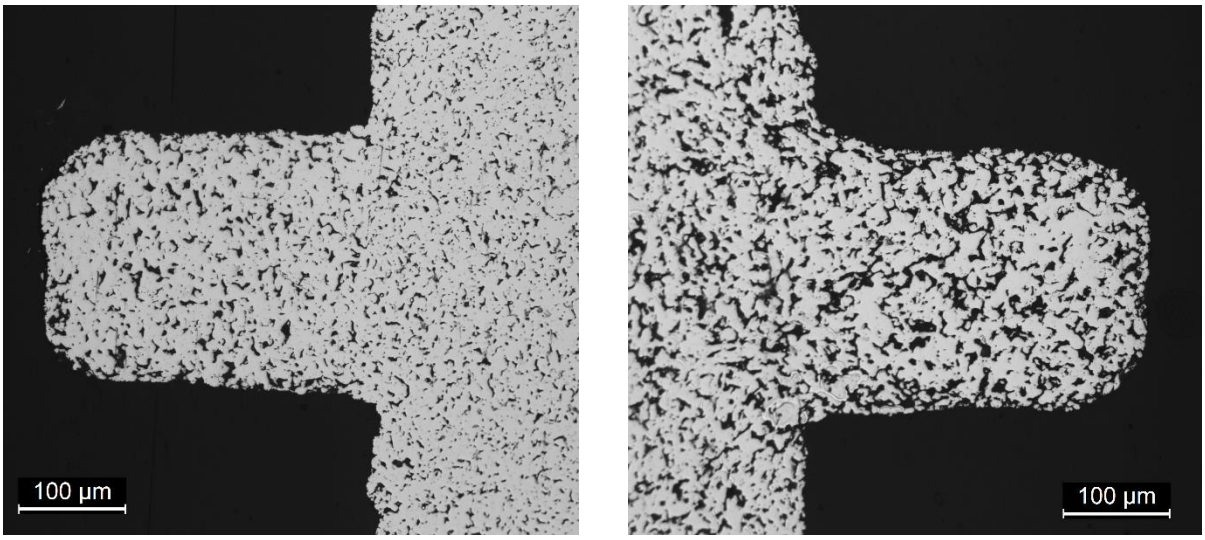

(a) (b)

Figure 5.18 *As polished surface of Al (a) and Al-MWCNT (b) microwall feature (OM).*

Table 5.2 Dimensions of the microwall features (Figure 5.18).

Part	**Height (µm)**	**Maximum width (µm)**	**Minimum width (µm)**
Master die	390	321	220
Al part	302	257	219
Al-MWCNT part	310	278	228

Figure 5.19 illustrates topography measurements of other sintered parts, two microchannel-half-flanges. The analysis of the figure indicates that:

- Channel bottom of the Al-MWCNT seems smoother than that of the Al,

- The flange top surface of the Al part seems slightly more flat than that of the Al-MWCNT,
- Shallower zones on the flanges surface of the Al are less than those of the Al-MWCNT.

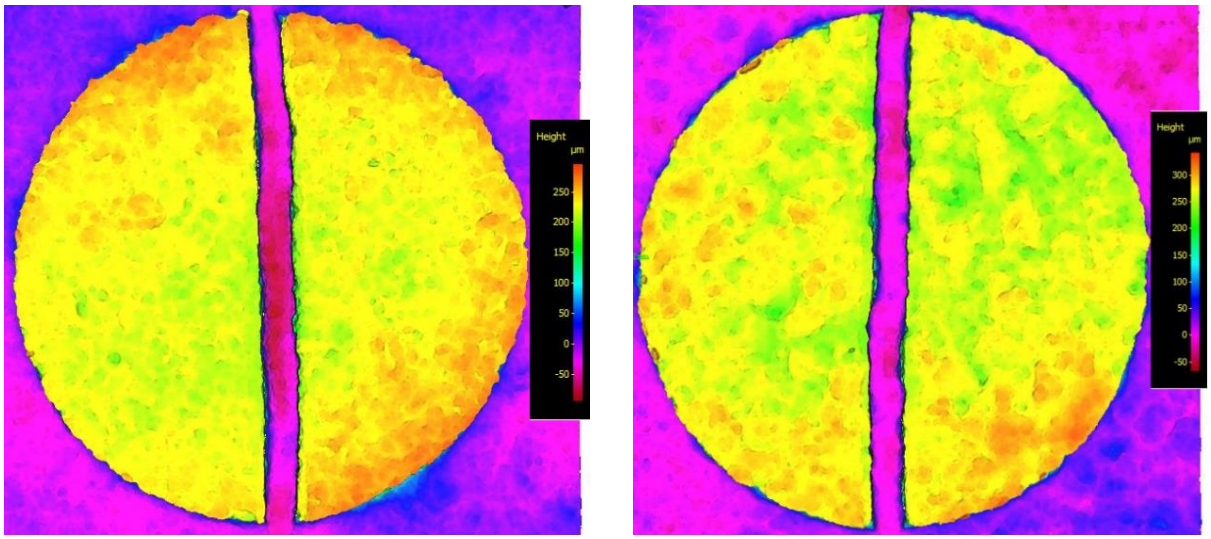

(a) (b)

Figure 5.19 *Roughness map of Al (a) and Al-MWCNT (b) microchannel-half-flanges, shaped at 230 °C/11.3 MPa/30 minutes, and sintered at 640 °C and ~10^{-4} Pa for 30 minutes (IFM).*

Figure 5.20a shows that the Sa of sintered parts is larger than that of the die. This can be correlated with the roughness of the green parts (Figure 4.16b), in addition, the curvatures of bonded powder particles were not smoothed during sintering (Figure 5.20b) due to poor volume diffusion caused by oxidation (cf. section 5A.1.7). However, the Sz of sintered parts reduced, what can be the influence of the plastic deformation of the elastomer die during shaping. The Al-MWCNT is rougher than Al, which can be due to higher porosity and aggregates, and is consistent with green and sinterability results (cf. chapter 4.2.2 and 5A.1.5).

As far as the dimensions are concerned, all features shrank (Figure 5.20c and cf. Figure 4.16a). The diagonal of the sintered Al is smaller than that of the Al-MWCNT due to the porosity and aggregates. The dimensions of the feature preserved the conical-like shape, being the minimum width still slightly larger than the master die, which is attributed to the green part dimensions (Figure 4.16a).

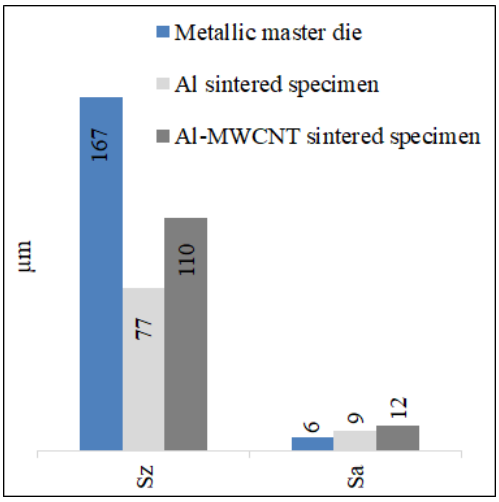

(a)

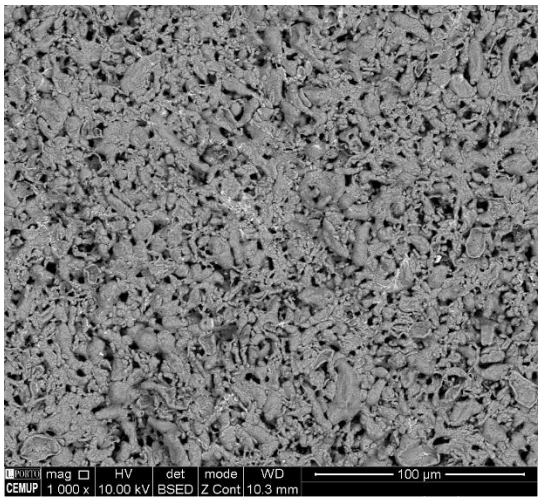

(b)

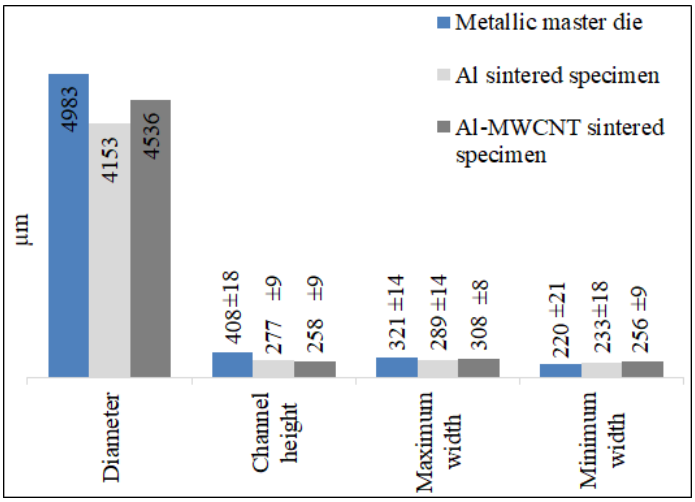

(c)

Figure 5.20 *Quantitative roughness values (a), morphology of the sintered part (b) (SEM/BSE), dimensions compared to those of the metallic master die (c) (cf. Figure 5.19).*

5A.2 Effect of uniaxial pressure on the Al powder sintering

Al powders were pressed uniaxially at different pressures at the rate of 1 mm/minute. Figure 5.21 shows that the larger the compaction, the greater the density after sintering. This figure also shows that the diagonal shrinkage is reduced by increasing pressure since this contributes to the deformation of the soft Al powder and to the cold welding of the particles.

Although pure Al is a very ductile and soft metal, the powder uniaxially compacted at very high pressure (380 MPa) still contained microporosities (Figure 5.22a), which can be the influence of powder characteristics. After sintering the grain size is similar to the powder particle size, which means that the rigid oxide layer hindered grain growth and eventually the large plastic deformation of the powders induced recrystallization inside the particles during sintering.

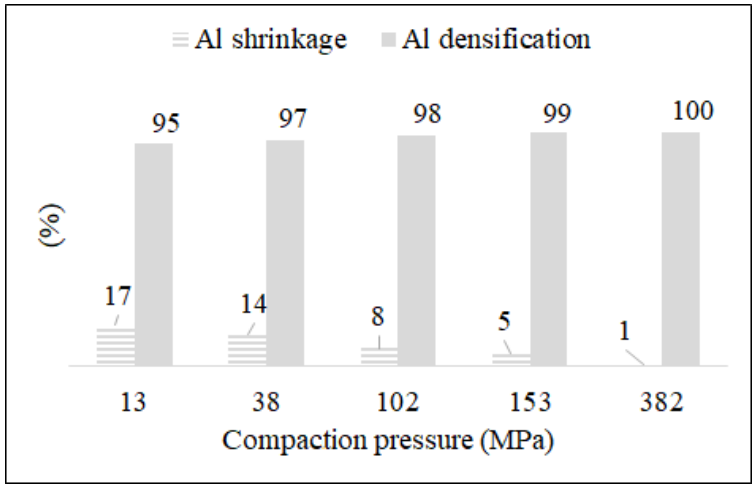

Figure 5.21 *Densification[26] and shrinkage of pressed and sintered Al powder placed on a porous ceramic tray and sintered at 640 °C, <5×10^{-3} Pa for 2h.*

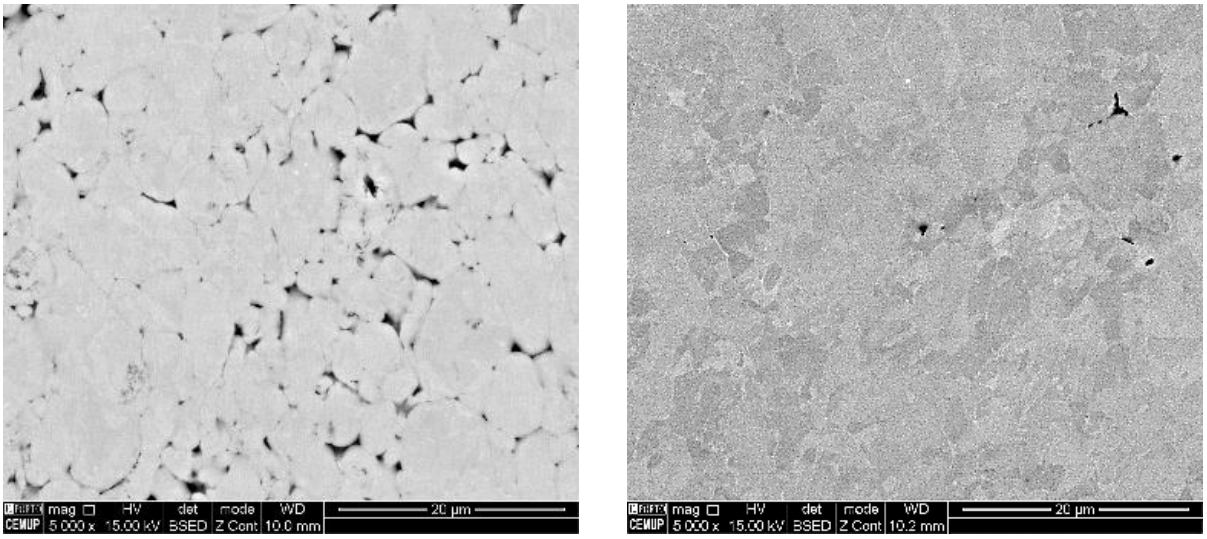

(a) (b)

Figure 5.22 *Microstructure of Al powder pressed at ~382 MPa before (a) and after (b) sintering at 640 °C, <5×10^{-3} Pa for 2h (SEM/BSE).*

Moreover, some micropores were observed (Figure 5.22b) which is not consistent with the densification results. This inconsistency can be attributed to the small mass of the specimens (<1g) that made it difficult to accurately measure the density. The fine grain microstructure (Figure 5.22b) was not observed when the powder was compacted at low pressure (Figure 5.14a). Therefore, this indicates that the particle size effect as a driving force for sintering could

[26] Densification is equal to the density measured, by Archimedes method, over the theoretical density of pure Al, in percentage.

be eliminated at high compaction levels by which the particles are cold welded prior to sintering.

5A.3 Effect of sintering atmosphere

A good efficiency of hydrogen or nitrogen-hydrogen mixture atmospheres for the sintering of Al was not reported [6, 16, 17]. However, the microscopic observations (Figure 5.23) indicate that the Ar-H_2 gas can be a good atmosphere for the sintering of powders pressed with high compaction pressures, although the best method for pore elimination during sintering is with the application of high vacuum ($<5\times10^{-3}$ Pa).

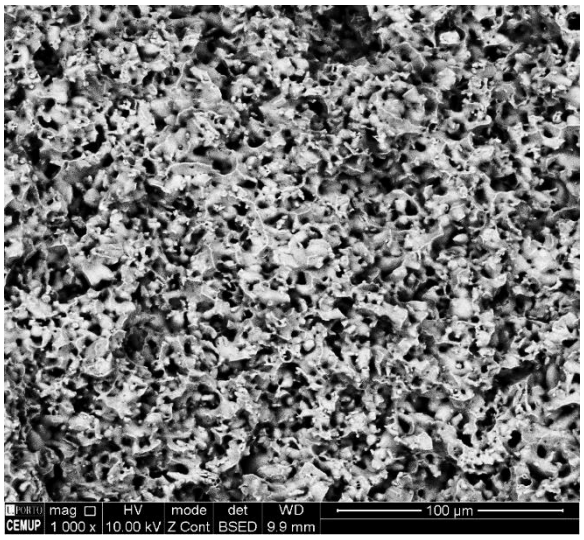

(a)

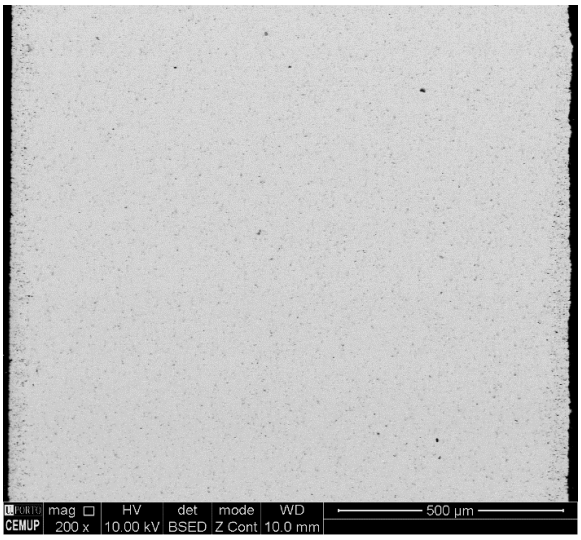

(b)

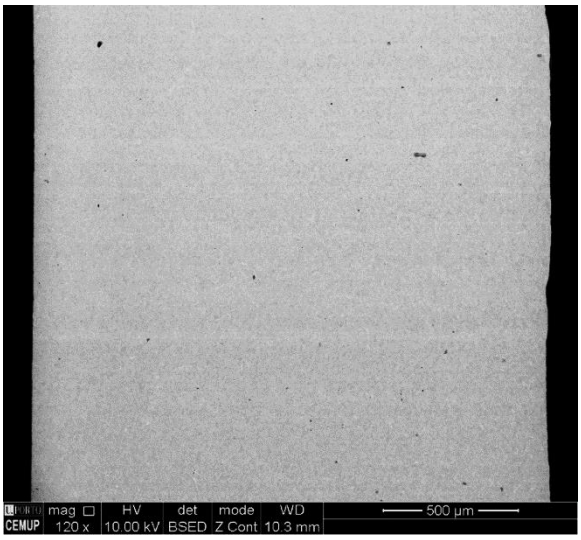

(c)

Figure 5.23 *Al powders uniaxially pressed at: ~12 MPa and sintered in Ar+H_2 (a) ~382 MPa and sintered in Ar+H_2 (b), and ~382 MPa and sintered in high vacuum ($<5\times10^{-3}$ Pa) (c) (SEM/BSE).*

5A.4 Partial conclusions

Al powders, alone or mixed with a binder, form a superficial layer of an aluminium oxide (alumina, boehmite, or other) during a thermal cycle similar to that used for the debinding in micro hot embossing. This implies that these specimens will exhibit a significant porosity and much higher than those that are only pressed and sintered. This porosity should be caused by the trapped air in the low compacted brown parts and cannot ensure a complete surface and volume diffusion during sintering. The presence of MWCNT contributed to the homogeneity of the microstructure particularly about the distribution of porosities; however, some aluminium carbides are reported not as a result of the reaction of the aluminium with the MWCNTs, but also with the carbon residues of the binder after debinding. At 640 ℃ the sintering is accomplished by liquid phase formation, this is transformed into solid state sintering at 637 ℃, but at the expense of densification. A reducing atmosphere of Ar-H_2 is suitable for sintering highly compacted powders and the high vacuum can overcome the porosities in green parts during the sintering. The high compaction of Al powders avoided liquid phase formation during high temperature sintering, and the grain size remained as big as the particle size of the pristine powder.

Part B- 316L powder

5B.1 Sintering

The densification of pressed 316L powders and micro hot embossed parts will be described in this subsection. The microstructure and phase evolution, as well as the shaping of microfeatures of the sintered parts, will also be presented. The sintering conditions were 1250 °C and ~10^{-3} Pa for 2h.

5B.2 Effect of compaction on the 316L densification

Uniaxially pressed 316L powders, with a rate of 1 mm/minute, were sintered and they showed a bright greyish colour. Figure 5.24 shows that the highest densification (98%) was obtained with the lowest compaction pressure (13 MPa). The absence of full densification is attributed to the air trapped within the green parts between the fine particles, which were not perfectly evacuated during sintering. Apparently, evacuation of this trapped air is more difficult for more compacted specimens. Densification problems can also be influenced by any defect, such as microcracking.

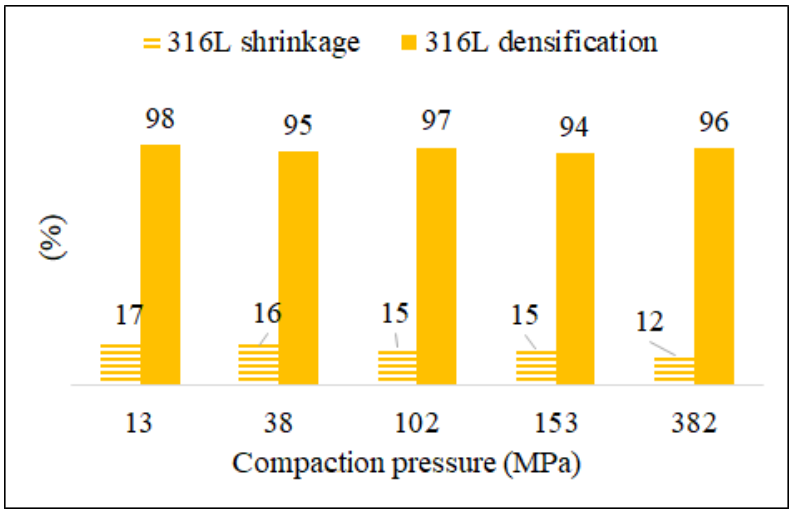

Figure 5.24 *Effect of compaction pressure versus the densification[27] and shrinkage of 316L powder, compacted disks placed on a porous ceramic tray.*

This comparison also shows that the 316L powder pressed at 382 MPa shrank 12% after sintering, this shrinkage did not happen for the Al powder compacted using the same pressure

[27] Densification is equal to the measured density of the sintered part over the measured density of the pristine powder, in percentage. The effect of pristine internal porosities was excluded.

(Figure 5.21), which showed a residual shrinkage of 1%. This difference is correlated with the higher formability of the Al powder that was almost completely densified by this high compression pressure. Meanwhile, the 316L powders compacted at low pressure, 13 MPa densified slightly more than the Al ones (98% and 95% for 316L and Al powders, respectively). This can be attributed to the presence of aluminium oxide, making the diffusion of Al difficult.

5B.3 Phase composition of stainless steel 316L powder

Figure 5.25 shows the XRD diffractogram of pressed and sintered 316L powder. These results, compared with the XRD analysis of the pristine powder (Figure 2.2a), highlights that the 316L powder had some amount of martensite, possibly induced by the atomization process. In fact, the peak observed at 44.4º should be associated with martensite since it is not visible after sintering. The eventual martensite transformation was observed during the heating step in DSC test (Figure 2.1b). If this phase were ferrite instead of martensite, it would be present in Figure 5.25 due to the application of a low cooling rate, slower than 5 °C/min.

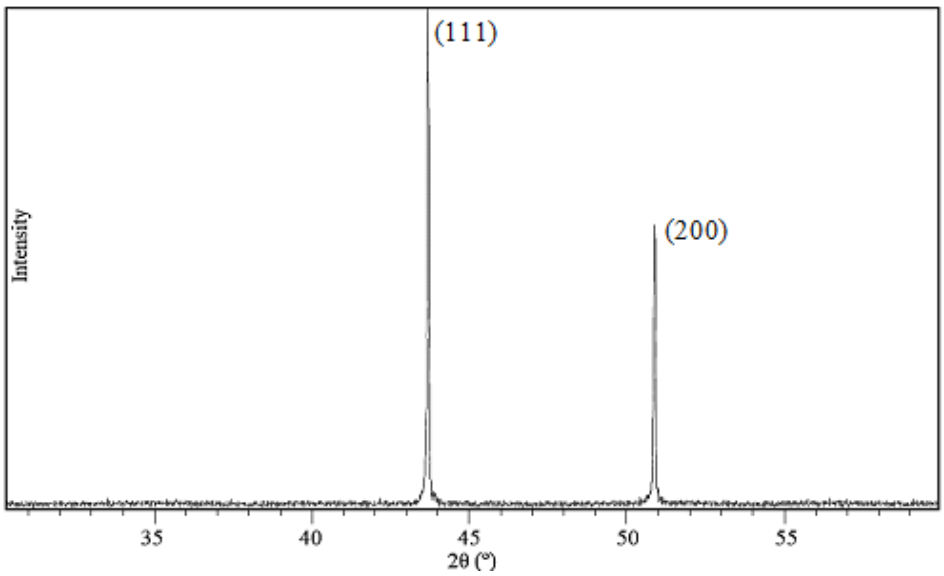

Figure 5.25 *XRD diffractogram of the 316Lpowder pressed (11.3 MPa) and sintered.*

5B.4 Sintering brown parts

5B.4.1 Densification of micro hot embossed parts

The results of the relative densities of 316L and 316L-MWCNT parts are presented in Table 5.3. These results show that both feedstocks led to similar relative density values after sintering and that the size of the microparts had no influence in these values. However, cross section

observations revealed that the MWCNT has reduced the porosity-like spots, which is more pronounced for microtensile (Figure 5.26 and Table 5.3).

Table 5.3 Density measurement and porosity analysis as a function of composition and produced features (sintered parts with 60 vol.% powder content).

Composition	**Feature**	**Shaping pressure (MPa)**	**Theoretical density (kg/m³)**	**Measured density (kg/m³)**	**Relative density (%)**	**Porosity[28]**
316L	Microchannel-half-flanges	11.3	7937[29]	7690±22	97	3.0±0.8
316L-MWCNT			7881[30]	7576±24	96	1.9±0.7
316L	Microtensile specimen	8.5	7937[2]	7591±78	96	6.5±1.1
316L-MWCNT			7881[3]	7570±18	96	0.8±0.2

The microanalysis maps (Figures 5.27 and 5.28)[31] show a uniform distribution of the major alloying elements in the 316L matrix. Moreover, black spots do not represent porosities, but microzones enriched in Mn, Cr and, few in Mo. This indicates that the spots may be chromium carbide (some Cr can be replaced by Fe, Mo and Mn) formed by the reaction of these elements with carbon residues in heterogeneous zones of green parts after debinding and sintering (cf. Figure 4.12). As the MWCNT improved the distribution of powder and binder, the concentration of carbon-rich regions was reduced with the consequent reduction in the number of carbides. Some authors reported these black spots as oxides formed after sintering during PIM process [18].

As regards the composition of the sintered parts, in addition to the maps, Table 5.4 also confirms that the bulk composition has been maintained during micro hot embossing.

[28] Measured by ImageJ from as polished surfaces.

[29] Cf. Table 2.4

[30] Cf. section 2.4, and equation 2.1, the effects of initial porosities, chemical changes (loss of some alloying element) and any phase formation were excluded.

[31] Resolution of ~0.05 µm, declared by the equipment manual, being affected by the incident beam energy and by the atomic weight of the elements analysed

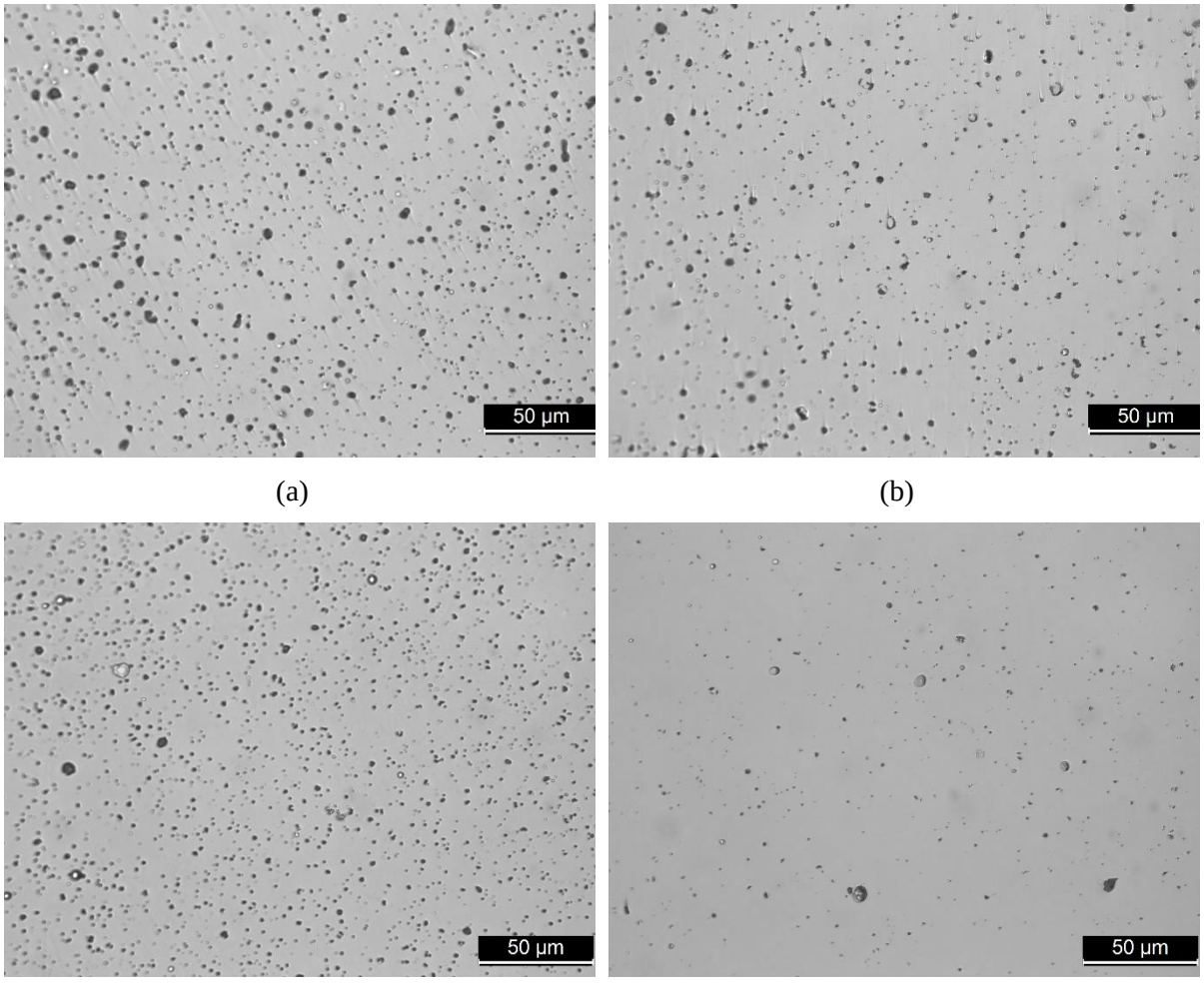

Figure 5.26 *As polished cross sections of 316L (a) and 316L-MWCNT microchannel-half-flanges (b), and 316L (c) and 316L-MWCNT (d) microtensile specimens (OM).*

Table 5.4 Semiquantitative analysis, major elements, of bulks compared to pristine powder (wt.%).

Elements	316L	316L-MWCNT	Pristine powder
Fe	67.8	67.5	Base
Cr	17.6	17.8	17.1
Ni	11.8	11.5	11.1
Mo	2.9	3.2	2.4

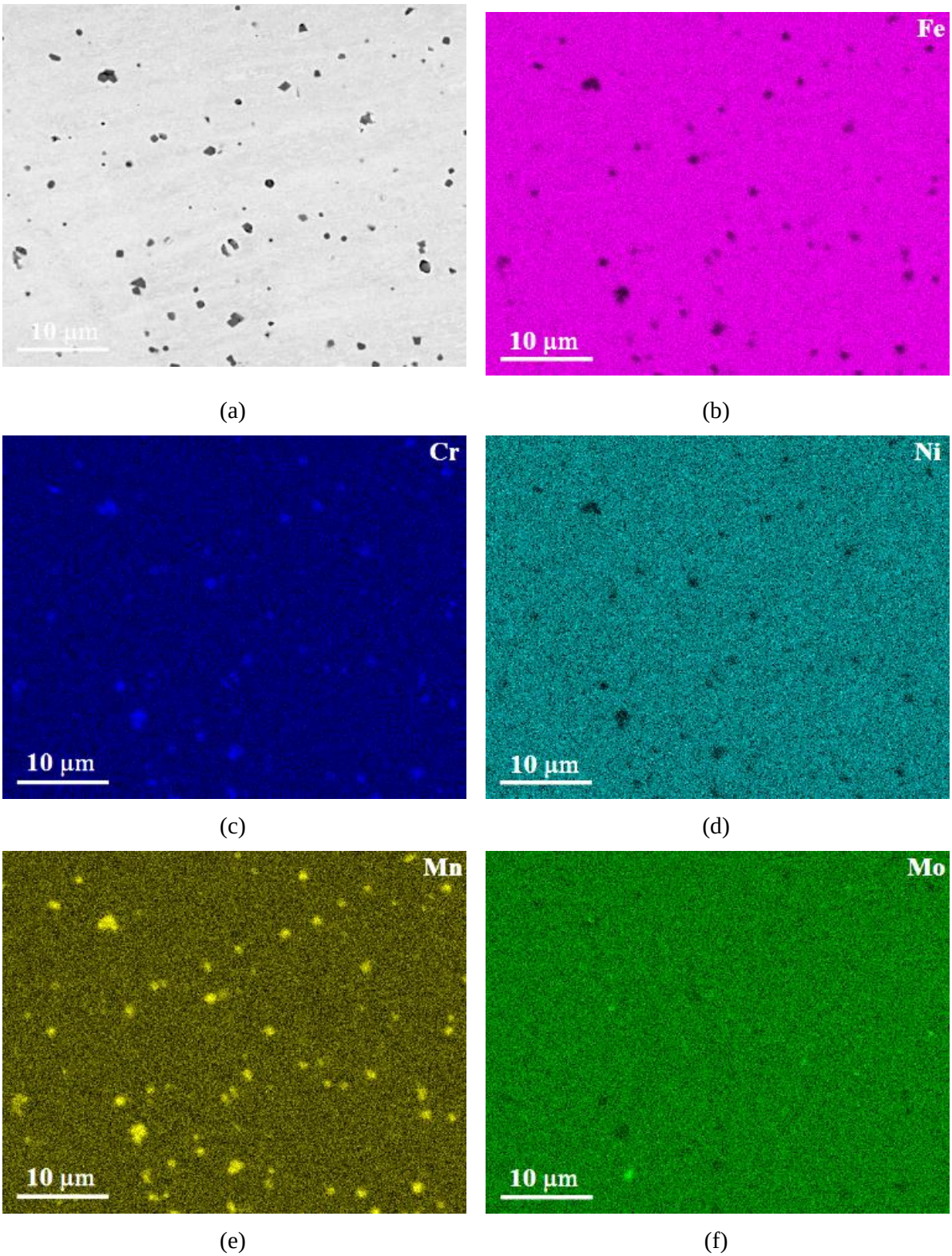

Figure 5.27 *Elemental maps showing the distribution of some elements in the 316L matrix of a microtensile specimen (SEM/EDS map).*

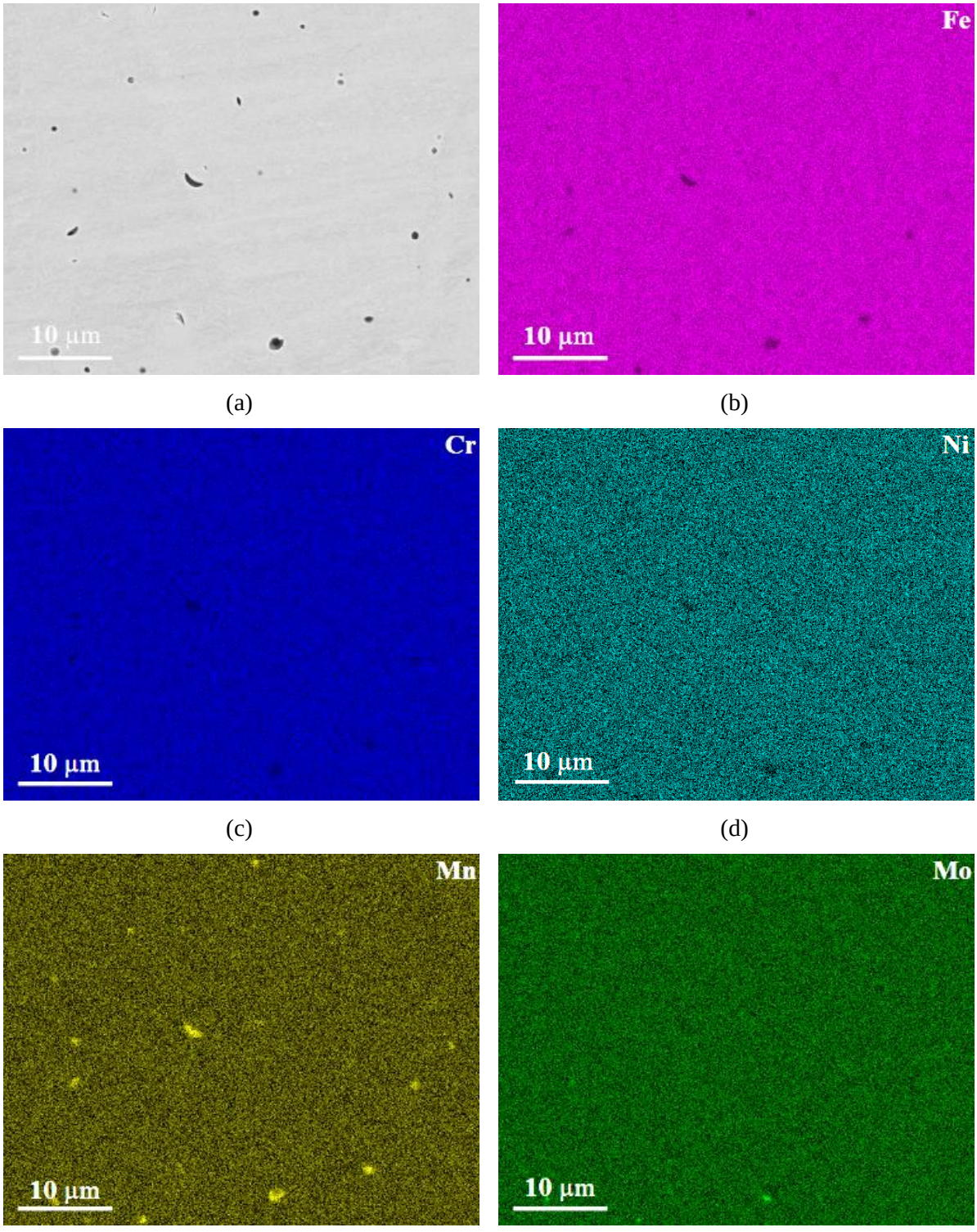

Figure 5.28 *Elemental maps showing the distribution of some elements in the 316L-MWCNT matrix of a microtensile specimen (SEM/EDS map).*

5B.4.2 Microstructure after sintering

Microstructural analysis of surfaces and of cross sections did not reveal the presence of MWCNT after sintering. The sintered parts have austenite grains, some angular dark grey microparticles at boundaries and inside the grains, and very fine white laminated intergranular particles (Figure 5.29).

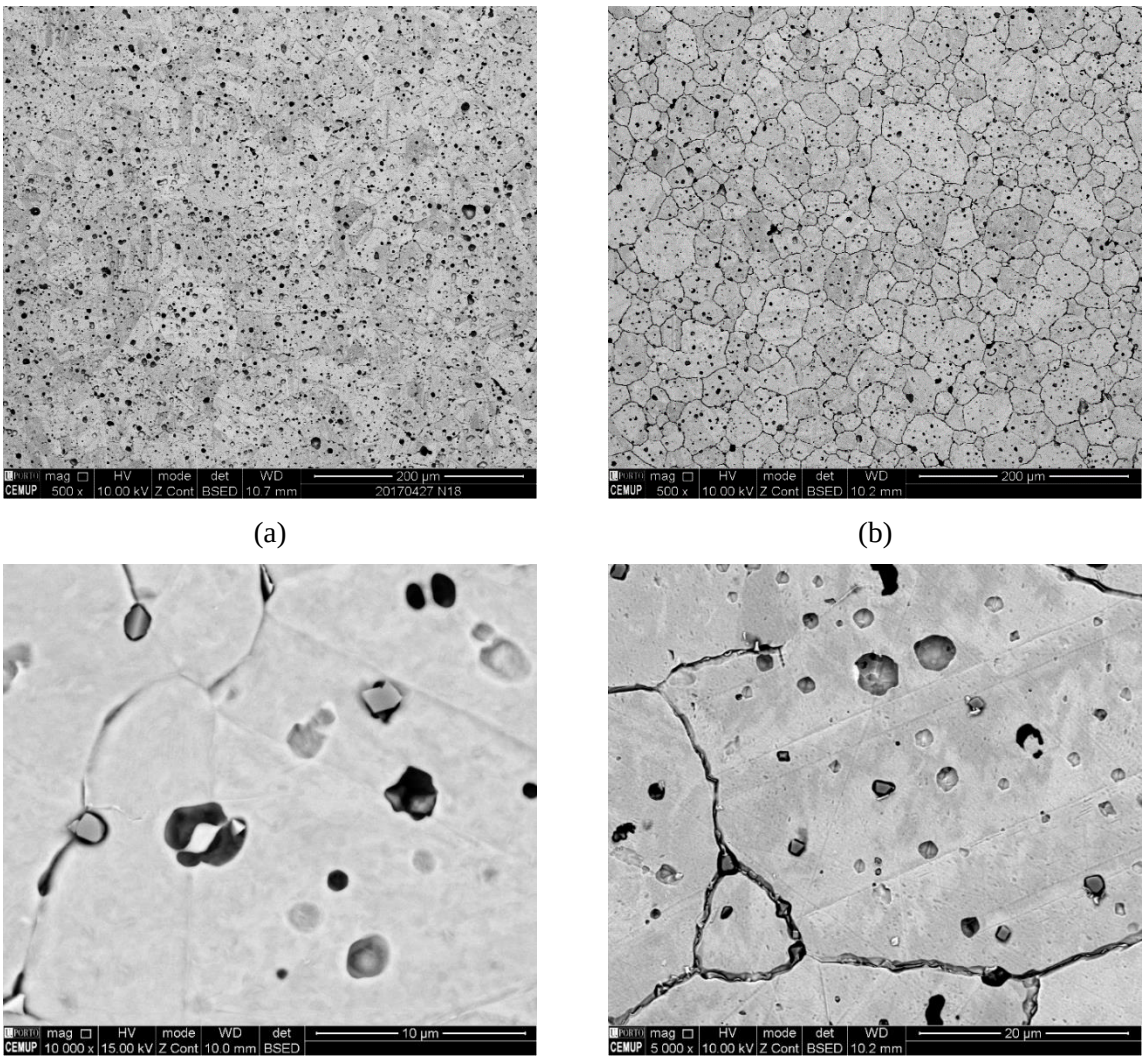

Figure 5.29 *Microchannel-half-flanges made of 316L (a) and 316L-MWCNT (b) (SEM/BSE[32]).*

[32] Etched by H_2O:HNO_3:HCl (1:1:1) in a 35 kHz ultrasonication bath, etching took almost ~10 minutes and one minute for 316L and 316L-MWCNT, respectively. This difference must be caused by changes at grain boundaries, and sample preparation by focused ion beam technique and TEM analysis are needed for further evaluations.

Figures 5.30 and 5.31 show the presence of austenitic grains of different sizes (21.1±17.1 µm and 15.6±11.8 µm for 316L and 316L-MWCNT parts, respectively). This indicates that these parts were densified through a strong volumetric diffusion meanwhile a small grain refinement is observed. In addition, crystalline orientations of the as-polished surfaces confirm that the micro hot embossing process and the presence of MWCNTs did not introduce any preferential orientations in the structure of sintered parts.

Regarding the microspot analysis, Table 5.5 confirms the presence of carbide particles in the microstructure.

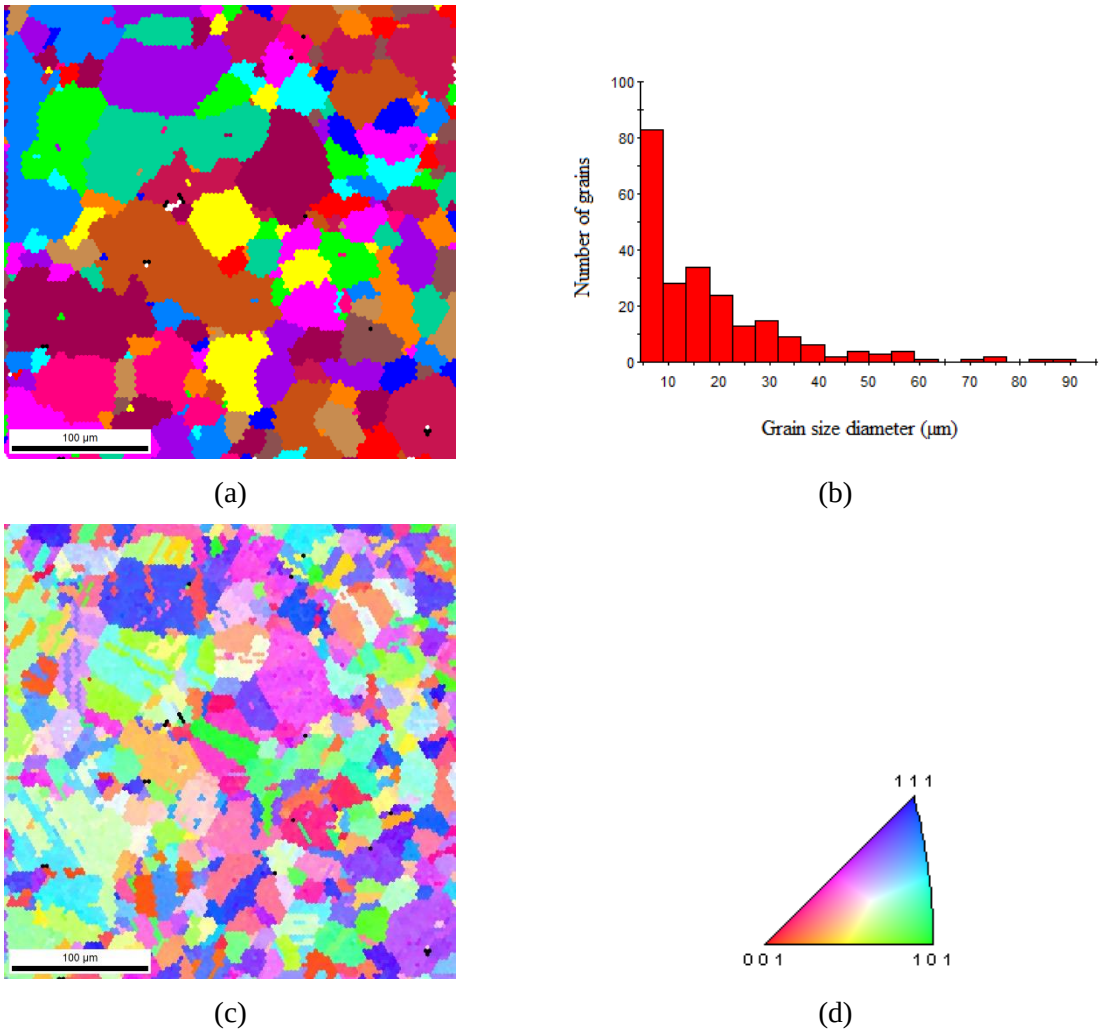

(a) (b)

(c) (d)

Figure 5.30 *Micro hot embossed 316L part: grain size map without twins (a), grain diameter distribution graph (b), IPF (c) and the austenite coded map (d) (SEM/EBSD).*

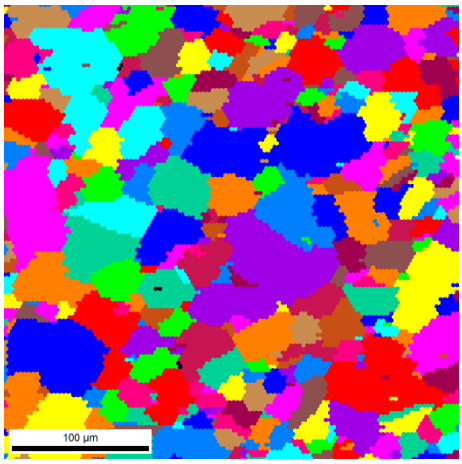

(a)

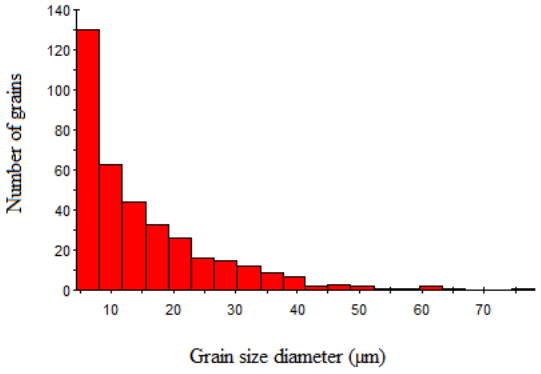

(b)

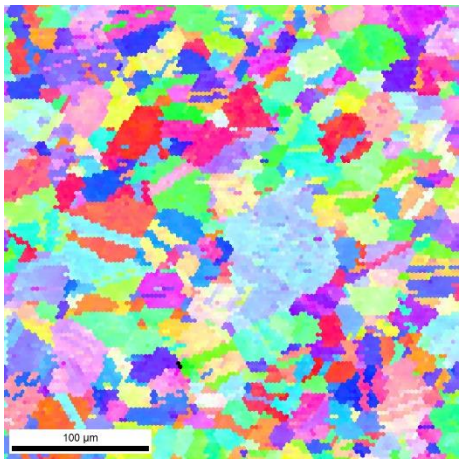

(c)

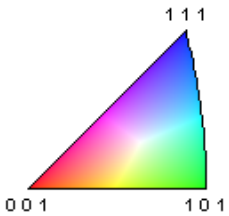

(d)

Figure 5.31 *Micro hot embossed 316L-MWCNT part: grain size map without twins (a), grain diameter distribution graph (b), IPF (c) and the austenite coded map (d) (SEM/EBSD).*

Table 5.5 Chemical composition of carbides in the microstructures.

Elements	**Cr**	**Mn**	**Mo**	**Fe**	**Ni**	**C**
At.%	22	-	4	11	1	Rest

5B.4.3 Phase evolution

The diffractograms of the micro hot embossed 316L and 316-MWCNT parts [33] as compared to the pressed and sintered part, as reference, show equal peak positions (Figure 5.32). These peaks confirm the austenitic matrix, comparing them with the reference pattern number from

[33] They were acquired from the as sintered surfaces.

ICDD/PDF 00-033-0397. There is a peak detected at 79.3 º that may be attributed to chromium carbide.

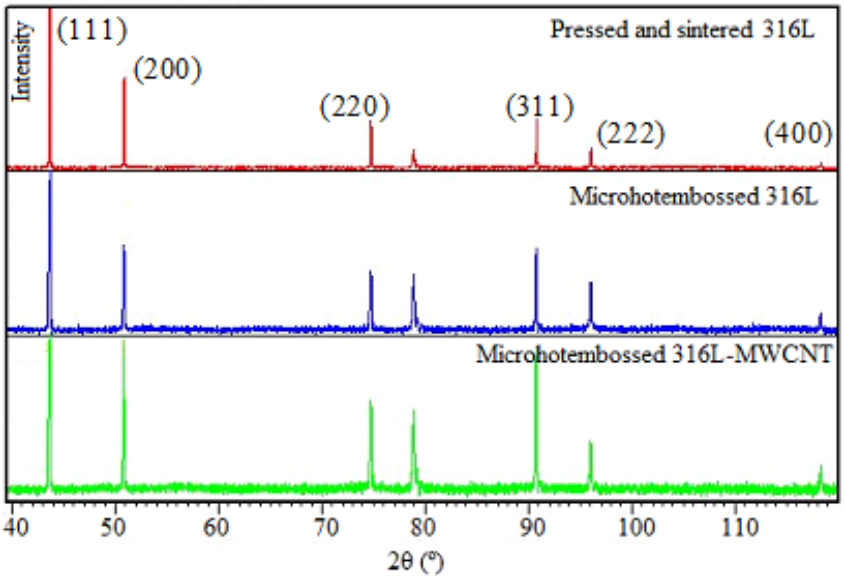

Figure 5.32 *X-ray powder diffraction of sintered specimens*[34].

5B.4.4 Mechanical properties of micro hot embossed tensile specimens

Green microtensile parts (Figure 4.18) were debound (Figure 5.1) and successfully sintered. The specimens were tested at a strain rate of 10^{-4} s^{-1} and a video extensometer recorded the displacement during the test. The corresponding stress-strain curves and the broken tensile specimens (Figure 5.33) illustrate a ductile behavior, as expected for 316L stainless steel.

Comparison of the yield and ultimate strength of the microtensile parts (Table 5.6) with a bulk material [19] shows that the micro hot embossing has not deteriorated the properties of the 316L part; however, when the MWCNT was added to the feedstock , these properties reduced.

SEM failure analysis (Figure 5.34) did not reveal the presence of isolated or aggregated MWCNT. The analysis also highlighted the contribution of dimples to the plastic deformation of the parts and that the dimples of 316L are smaller than those of the 316L-MWCNT. The 316L dimples are full of embedded particles, rich in Cr and Mn. In contrast, the 316L-MWCNT has few particles inside the dimples. These particles acted as reinforcements during the deformation process [18], since they are obstacles to the movement of matrix and/or

[34] Specimens weighed ~0.3 g, scanning rate was 1 º/s and the specimen was rotating.

dislocations, and may explain, in part, the different mechanical response of both materials. Some authors also mentioned these particles within the dimples: some without discussion [20] and others identifying them as $MnCr_2O_4$ [21].

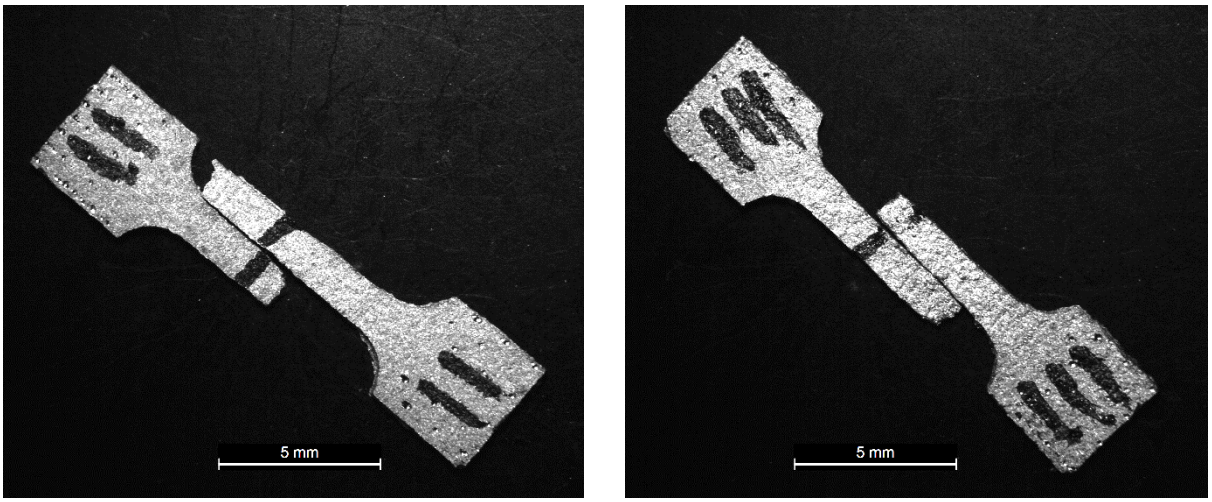

(a) (b)

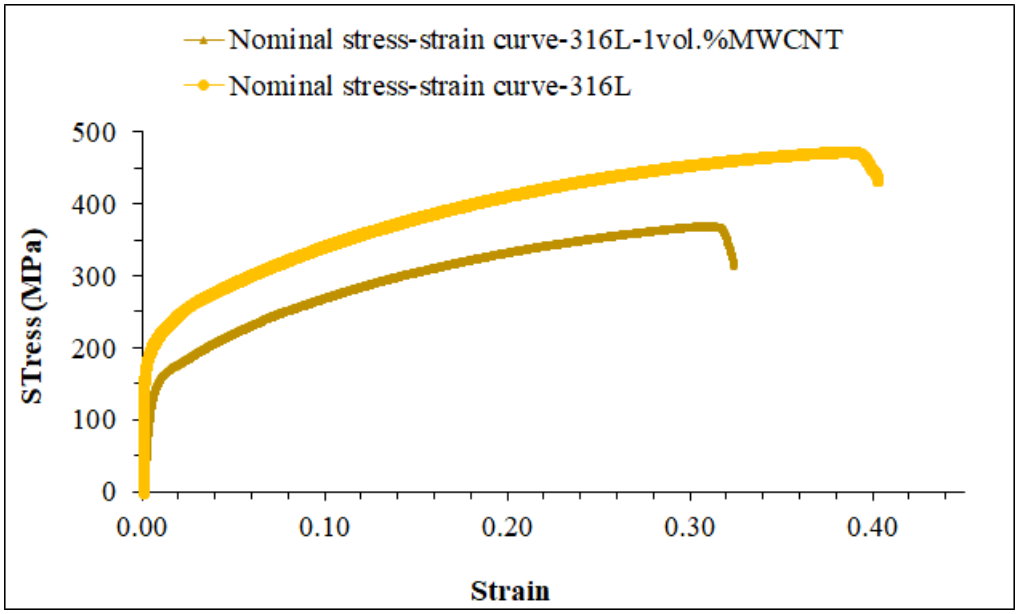

(c)

Figure 5.33 *Tensile specimen tested until rupture: 316L (a) and 316L-MWCNT (b) sintered parts; correspondent stress-strain curves (c).*

Table 5.6 Mechanical properties of the microtensile specimens.

Composition	Ys[35] (MPa)	UTS (MPa)	HV (0.1)
316L	~185	458±15	191±6
316L-MWCNT	~145	371±14	148±4
Bulk 316L	170	485	-

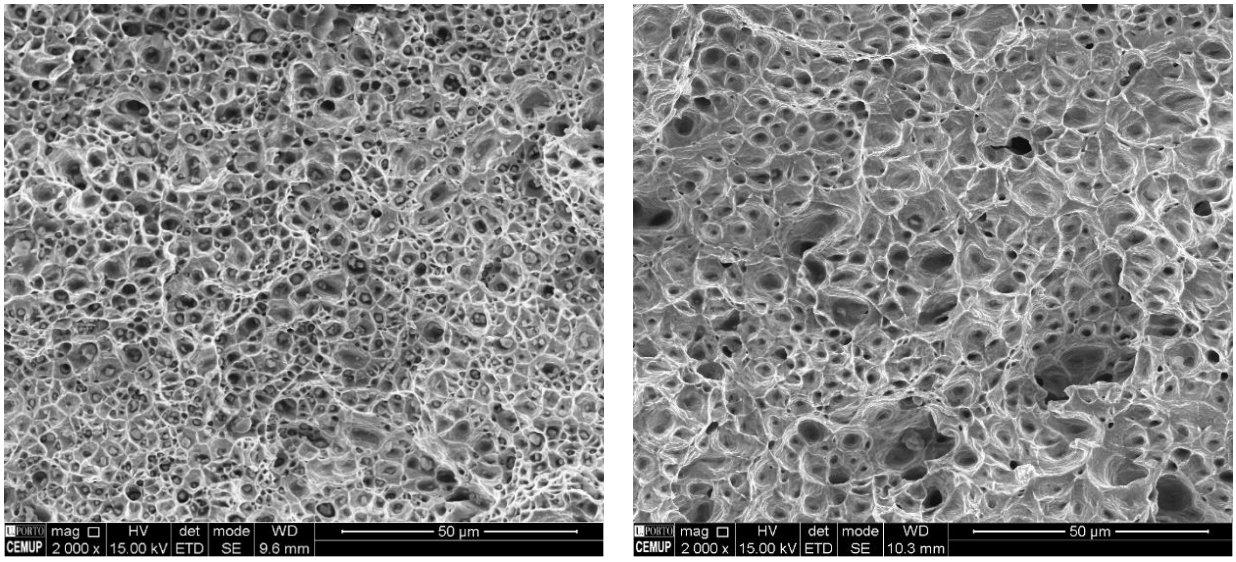

(a) (b)

Figure 5.34 *Morphology of 316L (a) and 316L-MWWCNT (b) failed sections, (SEM/SE).*

5B.4.5 Microstructure of the convex microgear

Microscopic analyses of the sintered convex microgear (Figures 5.35 and 5.36) show that the referred thermal debinding and sintering processes were successful to produce a bulk micropart. The microstructure consists of austenite grains in the interior surrounded by a thin outer region with a very fine grain size, indicated as martensite. This layer can be removed easily by micromilling. The spots inside austenite grains can be attributed to the formation of (Cr, Mn, Fe) carbides. Regarding the grain structure, no preferential crystalline orientation was observed.

[35] It was determined through the 0.2% offset line on the excel file through the regression method.

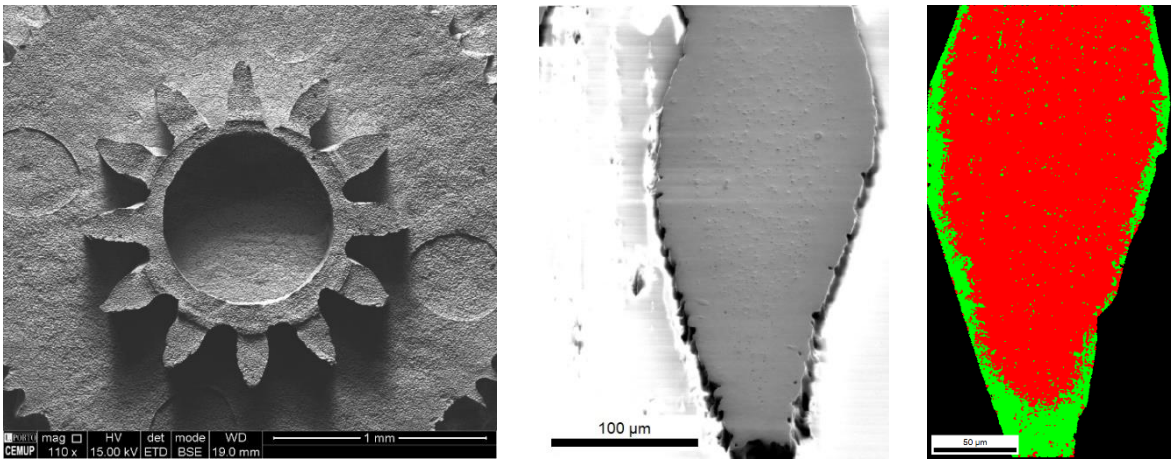

(a) (b) (c)

Figure 5.35 *Shaped microgear (see Figure 4.21) after sintering (a), as polished surface of one tooth (b), the phase distribution in the same tooth feature (c) (SEM/BSE and SEM/EBSD).*

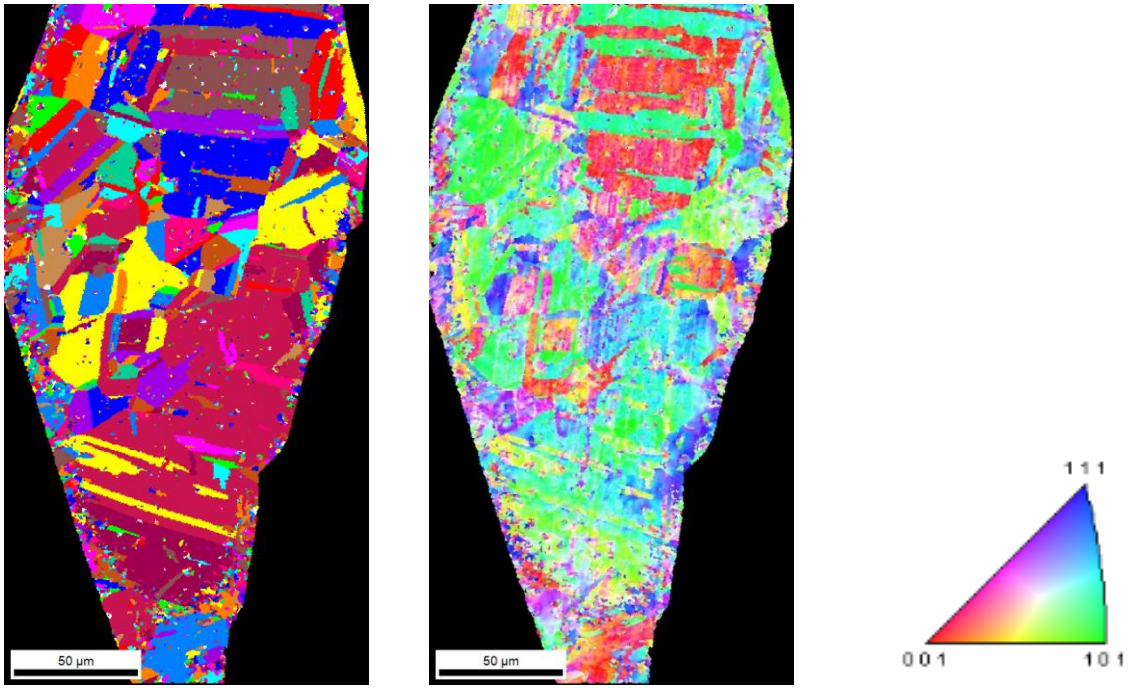

(a) (b) (c)

Figure 5.36 *Grain size (a), IPF (b) and the martensite coded (c) maps of the 316L microgear tooth, (SEM/EBSD).*

5B.4.6 Shaping evaluation after sintering

Brown 316L microchannel-half-flanges and microwall-half-reservoirs retained their shapes without cracking after sintering. As expected (cf. Chapter 4), the parts made by metallic die ended with surfaces smoother than those made by elastomer die. Some superficial discontinuity

and some blister-like regions are observed on the surfaces (yellow arrows in Figure 5.37). These defects must be originated from the heterogeneity existing in the green parts. Figure 5.38 illustrates the cross section of the microwall. Dimensional measurements (Table 5.7) made in the OM show that the specimen made of 65 vol.% powder loading had dimensions closer to the master die than the feedstock with 60 vol.% powder.

Table 5.7 Dimensions of the microchannel-half-flanges metallic die (as reference) and 316L parts (cf. Table 2.11).

Part	**Height (µm)**	**Maximum width (µm)**	**Minimum width (µm)**
Master die	390	321	220
60 vol.%	304	279	241
65 vol.%	302	305	225

In addition, the polished surfaces (Figure 5.38) reveal the presence of an apparently dense, white surface layer of ~ 20 µm thick, followed by a region where the above mentioned black spots (carbides) are visible. This distribution may be explained by a difference in binder removal, with more carbon binder residues in the interior, and by some decarburising effect during sintering, thereby eliminating the carbon in the superficial layer. Other research has also reported the presence of a dense layer in the rim of 316L sintered parts, although this has been associated with diffusion of hydrogen at the limited depth of the part during sintering and its effect of reducing the oxides in this layer [22].

The roughness maps and the information extracted from their analysis (Figures 5.39 and 5.40) show that the Sa and Sz parameters of the sintered 316L and 316L-MWCNT specimens decreased when compared to the green ones (Figure 4.14b). This decrease is the inverse of that was measured in the Al specimens (cf. 5A.1.9). However, the roughness change after sintering is not great being only the result of flattening the semi-spherical surface of the 316L powder by mass transportation and densification.

The effect of the deterioration with the use of the elastomer die is also noted in the measurements of the replicated parts, similarly to that observed in aluminium.

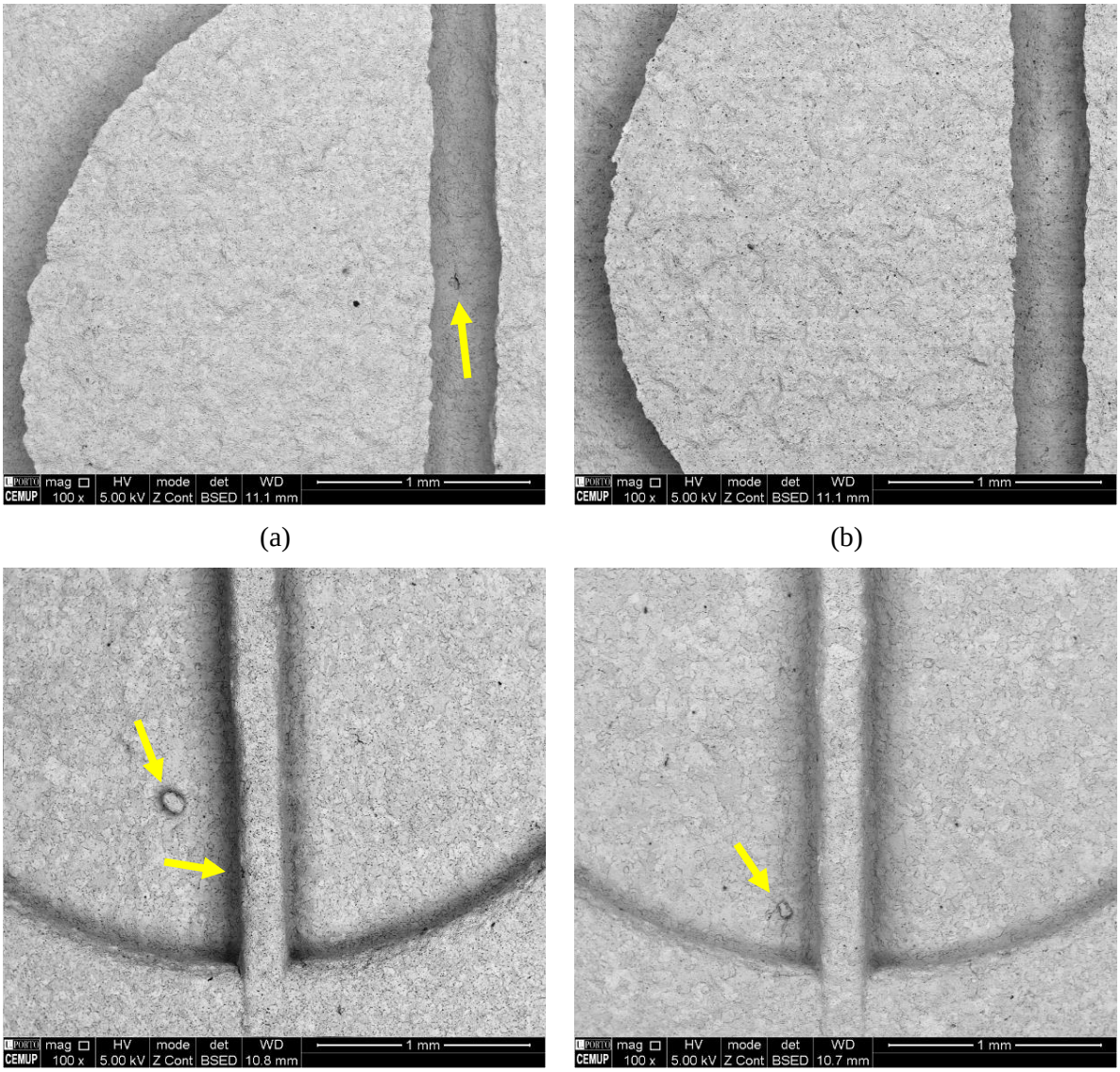

Figure 5.37 *Microchannel-half-flanges made of 316L60M1 (a) and 316L-MWCNT60M1 (b); microwall-half-reservoirs made of 316L60M1 (c) and 316L-MWCNT60M1 (d). The microchannel-half-flanges were shaped at 230 ℃ and 11.3 Pa for 30 minutes and the microwall-half-reservoirs at 170 ℃ and 11.3 Pa for 10 minutes (SEM/BSE).*

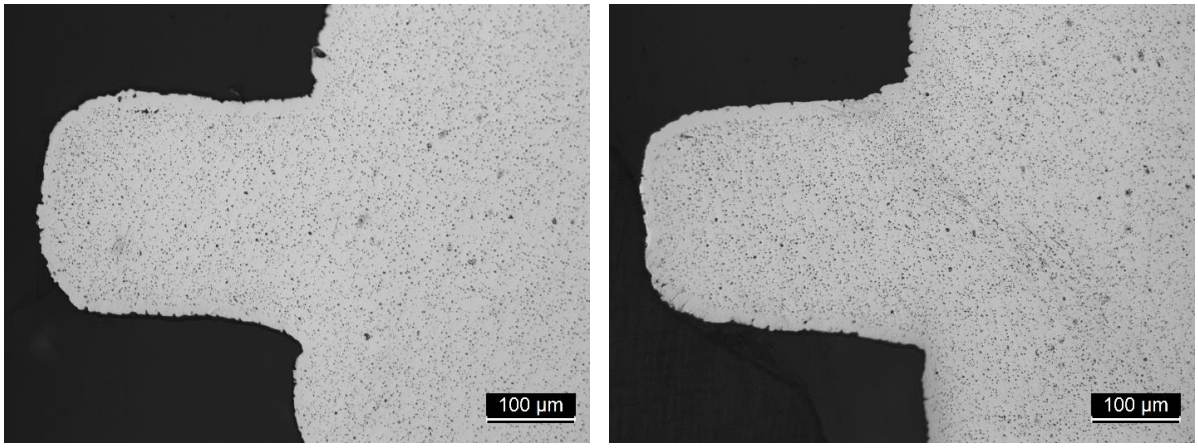

(a) (b)

Figure 5.38 *Microwall feature of 316L 60 vol.% (a) and of 65 vol.% (b) (as polished, OM).*

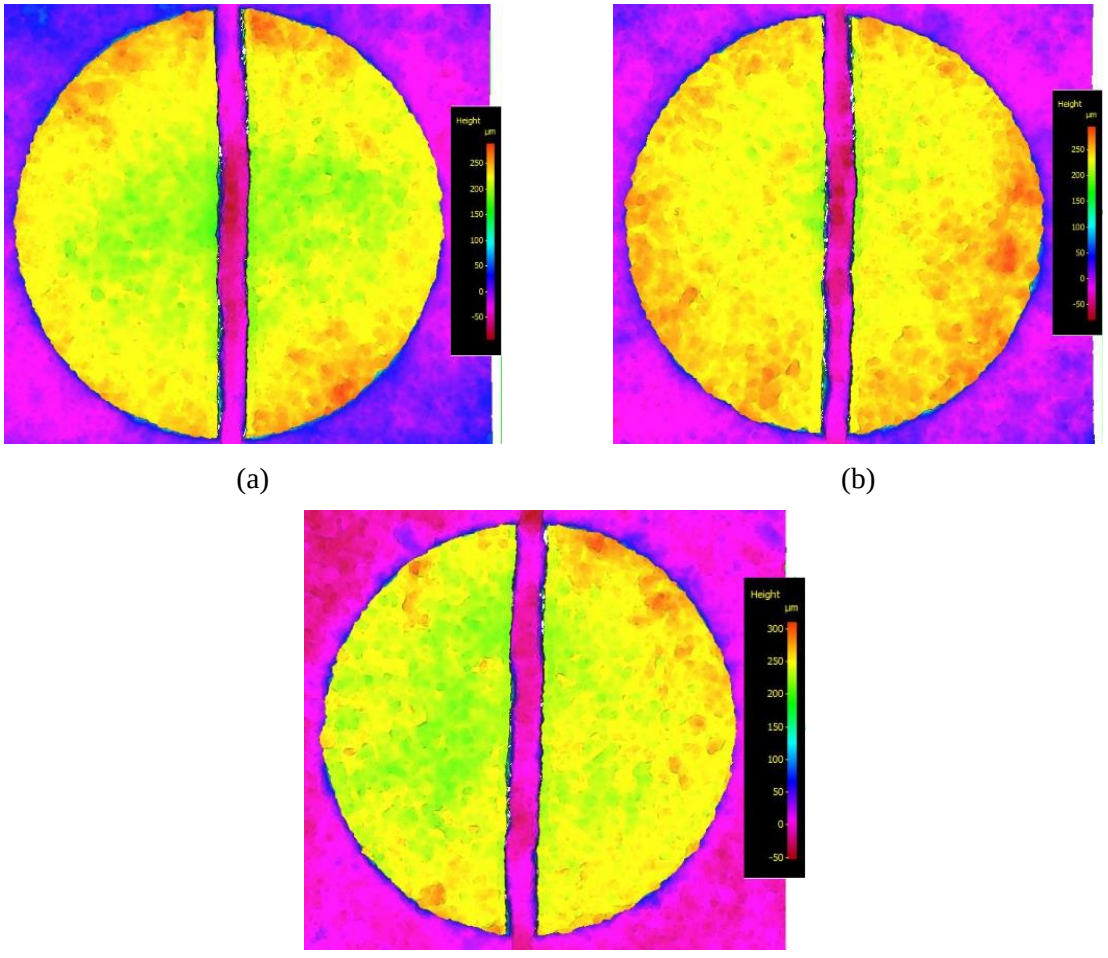

(a) (b)

(c)

Figure 5.39 *Microchannel-half-flanges: 316L shaped at 230 °C, 11.3MPa for 30min by 1st run (a), 316L by 2nd run (b), and 316L-MWCNT also by 2nd run, sintered at 1250 °C/~10-3 Pa/2h (c) (IFM).*

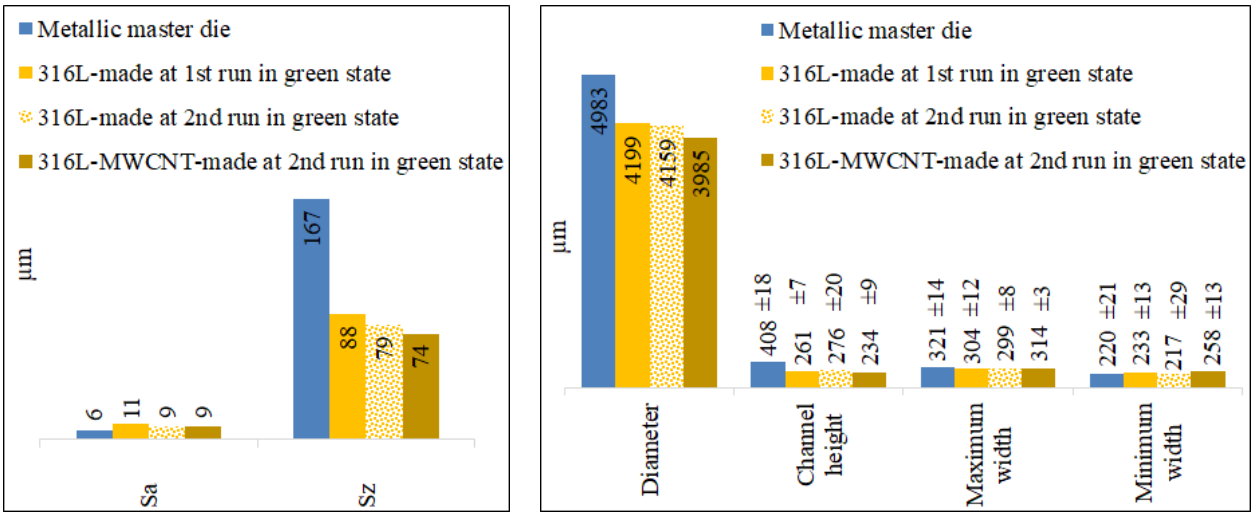

(a) (b)

Figure 5.40 *Quantitative results of roughness parameters (a) and dimensions (b) of three 316L-based materials extracted from the IFM evaluations (cf. Figure 5.39).*

5B.5 Partial conclusions

The 316L powder shrinks during sintering in high vacuum atmosphere, whether it is pressed and sintered or micro hot embossed. The high pressure application during the process does not ensure high densification. The microstructure of the sintered 316L stainless steel after micro hot embossing is mainly austenite. The addition of MWCNT reduced the number of Cr-Mn particles. This effect is mainly caused by the homogeneity of the feedstock, which leads to less carbon residues from the binder after debinding for the component produced with 316L-MWCNT. This homogeneity of binder residues is also the main cause for the absence of Cr-Mn particles in the thin tensile specimens. The carbon nanotubes were not observed in the sintered parts and they did not induce higher mechanical strength. Indeed, the 316L material has higher strength due to the effect of the micro particles distributed in the microstructure and that they are acting as a reinforcement. As regards microfeatures, they were well preserved after sintering.

References:

[1] S. Simões, F. Viana, M.A.L. Reis, M.F. Vieira, **Composite Structures**, **108** (2014) 992-1000, 10.1016/j.compstruct.2013.10.043.

[2] G.R. M., Thermodynamics of sintering, in: Z.Z. Fang (Ed.) Sintering of Advanced Materials - Fundamentals and Processes, Woodhead Publishing2010.

[3] Y. Liu, H. Ren, Q.J. Jiao, Iop, Oxidation mechanism of micron-sized aluminum particles in Al-CO2 gradually heating system, 2017 International Conference on Structural, Mechanical and Materials Engineering2017.

[4] X.Y. Zhu, M. Schoenitz, E.L. Dreizin, **Journal of Physical Chemistry C**, **113** (2009) 6768-6773, 10.1021/jp809816u.

[5] X.Y. Zhu, M. Schoenitz, E.L. Dreizin, **Journal of Physical Chemistry C**, **114** (2010) 18925-18930, 10.1021/jp105363v.

[6] G.B. Schaffer, B.J. Hall, S.J. Bonner, S.H. Huo, T.B. Sercombe, **Acta Materialia**, **54** (2006) 131-138, 10.1016/j.actamat.2005.08.032.

[7] N. Yoshimura, Outgassing, Vacuum Technology: Practice for Scientific Instruments, Springer Berlin Heidelberg, Berlin, Heidelberg, 2008, pp. 123-174.

[8] M.K. Habibi, A.M.S. Hamouda, M. Gupta, **Composites Science and Technology**, **72** (2012) 290-298, 10.1016/j.compscitech.2011.11.015.

[9] S. Simões, F. Viana, M.A.L. Reis, M.F. Vieira, **Metals**, **7** (2017) 11, 10.3390/met7070279.

[10] L. Vaisman, H.D. Wagner, G. Marom, **Advances in Colloid and Interface Science**, **128** (2006) 37-46, 10.1016/j.cis.2006.11.007.

[11] G. RM., Powder metallurgy science, 2nd ed. ed., Princeton, NJ: Metal Powder Industries Federation.

[12] I. Pinwill, M. Edirisinghe, M. Bevis, **Journal of materials science letters**, **10** (1991) 1107-1110.

[13] H. Arik, **Materials & Design**, **25** (2004) 31-40, 10.1016/s0261-3069(03)00163-8.

[14] D. Poirier, R. Gauvin, R.A.L. Drew, **Composites Part A: Applied Science and Manufacturing**, **40** (2009) 1482-1489, https://doi.org/10.1016/j.compositesa.2009.05.025.

[15] F. Rikhtegar, S.G. Shabestari, H. Saghafian, **Journal of Alloys and Compounds**, **723** (2017) 633-641, 10.1016/j.jallcom.2017.06.222.

[16] T. Pieczonka, T. Schubert, S. Baunack, B. Kieback, **Proc. Conf. 'Sintering'05**, (2005) 331-334.

[17] T. Pieczonka, T. Schubert, S. Baunack, B. Kieback, **Materials Science and Engineering a-Structural Materials Properties Microstructure and Processing**, **478** (2008) 251-256, 10.1016/j.msea.2007.06.002.

[18] J.M. Jang, W. Lee, S.H. Ko, C. Han, H. Choi, **Archives of Metallurgy and Materials**, **60** (2015) 1281-1285, 10.1515/amm-2015-0114.

[19] https://www.azom.com/article.aspx?ArticleID=2382 2018 22/06/2018.

[20] M.R. Raza, F. Ahmad, N. Muhamad, A. Sulong, M.A. Omar, M.N. Akhtar, M. Aslam, **Powder Technology**, **289** (2016) 135-142, 10.1016/j.powtec.2015.11.063.

[21] J. Weise, D. Lehmhus, J. Baumeister, R. Kun, M. Bayoumi, M. Busse, **Steel Research International**, **85** (2014) 486-497, 10.1002/srin.201300131.

[22] L. Liu, N.H. Loh, B.Y. Tay, S.B. Tor, **Powder Technology**, **206** (2011) 246-251, 10.1016/j.powtec.2010.09.027.

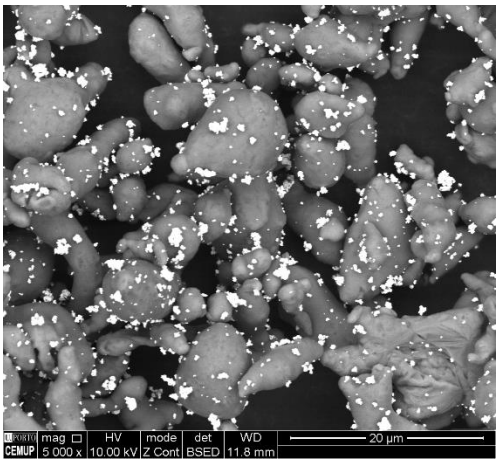

Chapter 6 – A comparative study with other reinforcements

6.1 Introduction

This study used the pure aluminium (Al), which is a light metal with a high workability, widely used and recycled. As mentioned above, the Al is applied as an alloy and composite in automotive and aeronautic structural applications. Since Al has a low melting temperature, it can be very applicable in the PM industry if it is sufficiently reinforced to exhibit specific mechanical properties. In this way, the role of other reinforcements besides MWCNT in the final properties should be evaluated. Up to now, the discussion included the feedstock preparation and producing bulk parts through shaping by feedstock, debinding and sintering, using MWCNT as the reinforcement. However, it was demonstrated that the producing technique may not have been the most adequate to cause a significant improvement in the Al mechanical properties. In order to evaluate whether the micro hot embossing was the reason for this shortcoming, the following two sets of tests were carried out:

- Dispersing Al and MWCNTs by a sonication based approach, pressing and sintering,
- Using other reinforcements (Graphene nanosheets, nanoalumina and ultrafine tungsten carbide) since they represent different types of reinforcement materials (cf. Chapter 2.3.2), applying the same dispersing method used for MWCNT, followed by pressing and sintering.

In this chapter, the microhardness measurement was considered as the criterion for the evaluation of the reinforcing effect of MWCNT after sintering, being this affected by the dispersion method and pressing. The first set of tests started with the procedure explained in

Chapter 2.4; when the mixtures were uniaxially pressed, their densification was attained by applying high vacuum sintering (cf. Chapter 2.9). Subsequently, the composition that produced the composite with the greatest hardness was selected and the dispersion conditions were changed by using an ultrasonication bath to assist sonication. The best condition (reinforcement quantity and dispersion procedure) was selected for dispersing other reinforcements in the Al powder. The hardest nanocomposite was analyzed to determine the reinforcing mechanism and to evaluate its mechanical and wear properties.

6.2 Hardening of Al-MWCNT dispersed by sonication

Microhardness measurements of the preliminary Al-MWCNT nanocomposites (Table 6.1) showed that the Al-0.5 wt.% MWCNT became the hardest, in respect to the non-reinforced matrix. Comparing these results with the related study, the same preparation conditions and the same MWCNT [1] having been applied but with a different pure Al powder, indicates that the metallic powder characteristics (surface area, size distribution and shape factor that are called 3S) significantly influenced the strengthening, i.e. 14% hardness increase by 0.5 wt.% MWCNT unlike the related study in which the increase of 47% was reported by 0.75 wt.% MWCNT.

Table 6.1. Microhardness values of the specimens, compacted at ~300 MPa and sintered.

MWCNT (vol.%)	**0.00**	**0.33**	**0.66**	**1.00**	**1.32**	**2.64**
MWCNT (wt.%)	**0.00**	**0.25**	**0.50**	**0.75**	**1.00**	**2.00**
HV (0.098N)	35	38	40	38	39	39
SD	3	2	2	3	3	3

Microscopy observations from the cross sections of these preliminary sintered specimens revealed that the more the MWCNT concentration was used, the larger were the MWCNT agglomerates observed. Observations also revealed some nanotubes joining two separate zones in a fractured zone in the Al matrix, which shows the CNT bridging (Figures 6.1a and 6.1b) that was not enough for a strong strengthening. Some authors reported a similar bridging effect at the fracture surface of strengthened specimens [2-5].

It will be noted that before compaction the MWCNT agglomerates surrounded fine and large Al particles, some agglomerates were larger than the powder average particle size (Figure 6.1c), and that some short ones were apparently placed on individual Al particles (Figure 6.1d). Agglomerates are heterogeneous regions that cause very weak CNT/matrix interfaces and

therefore, the load transfer mechanism does not work [6]. Furthermore, this agglomeration of the nanotubes does not allow them to be embedded in the aluminium matrix as individual nanotubes and thus strengthening by reducing the mean free path of dislocations is removed.

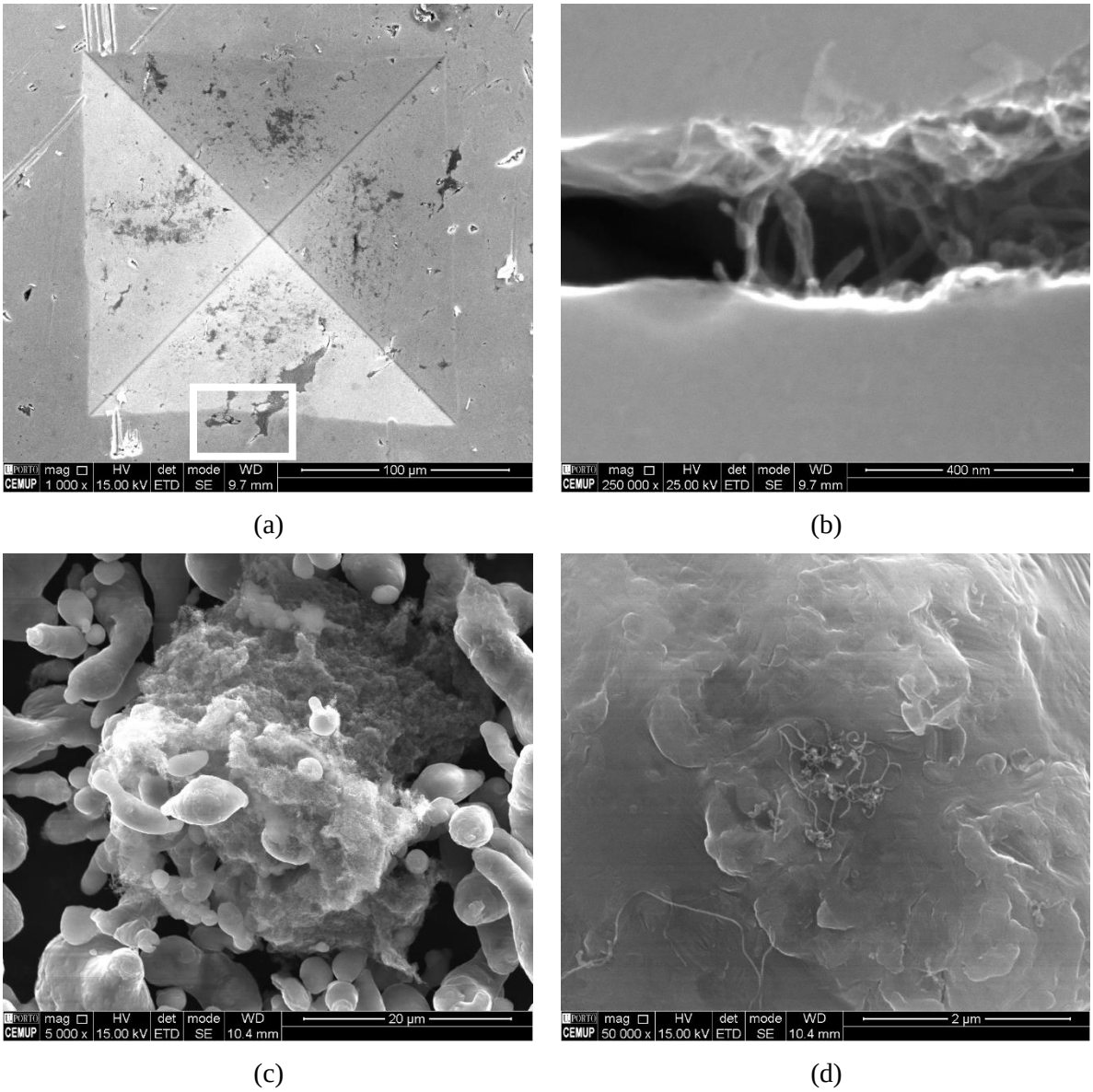

(a) (b)

(c) (d)

Figure 6.1 *A hardness indentation with MWCNT agglomerates and a crack that propagated from agglomerates to the matrix (white square inset) (a), carbon nanotubes bridging the tip of the crack (b); dispersion of MWCNT and Al powder before compaction: powder particles surrounded by the nanotubes agglomerates (c) and some MWCNTs placed on an individual Al particle (d) (SEM/BSE&SE images of Al 1.00 vol.% MWCNT).*

Sonication is a physical dispersing method through which sound waves are converted into a high energy stirring that causes strong shear forces in the solution. Due to this, bubbles form

and break down the MWCNT agglomerates [7]. In the presence of the metallic powders, these should also be associated with the deagglomeration process. However, it seems that the interaction of the Al powders, with a D_{50} of 10 μm and shape factor larger than one, has not been sufficient to break down the pristine agglomerates, by sonication at 340 Hz (20400 rpm) for 15 minutes.

6.3 Changing the dispersing conditions for the Al-MWCNT system

In order to surpass the hardness measured in the preliminary results (Table 6.1), the dispersing conditions of the MWCNT were changed. Although the Al-0.75 wt.% MWCNT composition did not led to the greatest hardness increase, but it was selected for applying new dispersing conditions in order to establish a comparison with related studies [1, 8].

Table 6.2 presents the hardness values for the new dispersing conditions. New changes involved the speed and time of mixing, the order of adding constituents into isopropanol, using Stearic Acid (SA) and Hydrogen Peroxide (H_2O_2) as surfactants, and increasing the compaction level (from 300 MPa to 400 MPa) to eliminate possible green porosities.

It is seen that the hardness of the pure Al and of the reinforced specimen increased slightly (comparing the specimens Nos. 1 and 2 in Table 6.2 with corresponding specimens in Table 6.1), as the compaction pressure had increased. Meanwhile, the mixture quantity in the mixing dish influenced the hardness (comparing specimens Nos. 2 and 3 in Table 6.2). This condition was carried out for large scale processing, and the SEM evaluation hardly revealed any MWCNT placed on the individual Al particles (like Figure 6.1d).

Applying post mixing treatment, such as Turbula over a long period, or even changing the order of mixing (No. 4 to No. 8 in Table 6.2) did not increase the hardening effect. Adding SA to isopropanol or using H_2O-5 vol.% H_2O_2, as the dispersing solution was not helpful either (No. 9 and No. 10 in Table 6.2).

It was reported that increasing the sonication time, for better dispersing, was not useful because MWCNTs were damaged [8]. This damage is important because defects on MWCNTs are prone to form aluminium carbide [9-11]. Thus, to improve the dispersion of Al and nanotubes the ultrasonication bath method was chosen.

Table 6.2. Microhardness values of Al-1 vol.% MWCNT specimens, dispersed by sonication at 20400 rpm, compacted at ~400 MPa, and sintered.

No.	Conditions	HV (0.098N)	SD
1	Pure Al	36	1
2	Sonicated like preliminary condition	39	3
3	Sonicated like preliminary condition but in an amount approximately 10 times greater in the mixing dish	37	5
4	Sonicated like preliminary condition and then 24 hours in Turbula	39	3
5	MWCNTs and Al sonicated 5 minutes separately and then 10 minutes together	36	4
6	Like No. 5 and then 6 hours in Turbula	37	3
7	Sonicated like preliminary condition and then magnetic stirring	36	3
8	MWCNTs and Al sonicated 10 minutes separately and then 5 minutes together followed by magnetic stirring	39	6
9	Sonicated like preliminary condition with 5 wt.% SA	36	3
10	Sonicated like preliminary condition in H_2O-5 vol % H_2O_2	37	2

6.4 Application of ultrasonication bath to assist sonication

Since the MWCNT agglomerations affect the matrix strengthening [6], the ultrasonication technique was applied to facilitate the MWCNT deagglomeration. An isopropanol-MWCNT mixture with a very small concentration (~$1.5*10^{-4}$ g/ml) of MWCNT was placed in the ultrasonication bath for 60 minutes, and specimens were taken for microscopy observations after 0, 15 and 60 minutes' dispersion. The analysis of Figures 6.2a to 6.2d and 2.5a shows that the longer the ultrasonication time, the smaller the agglomerates. Microscopy observations also highlighted the fact that the MWCNTs, after being processed for 60 min, were not exfoliated even when they were processed by the high speed sonication (340 Hz) for 15 minutes (Figure 6.2e).

These results confirm that the formation of shock waves, due to bubble collapsing, by the ultrasonication bath [12] at 35 kHz for 60 minutes was not as aggressive as the shear bubbles generated by the focused and uniform energy provided by the high speed sonication [8]. Therefore, the new methodology can involve assisted sonication by ultrasonication bath.

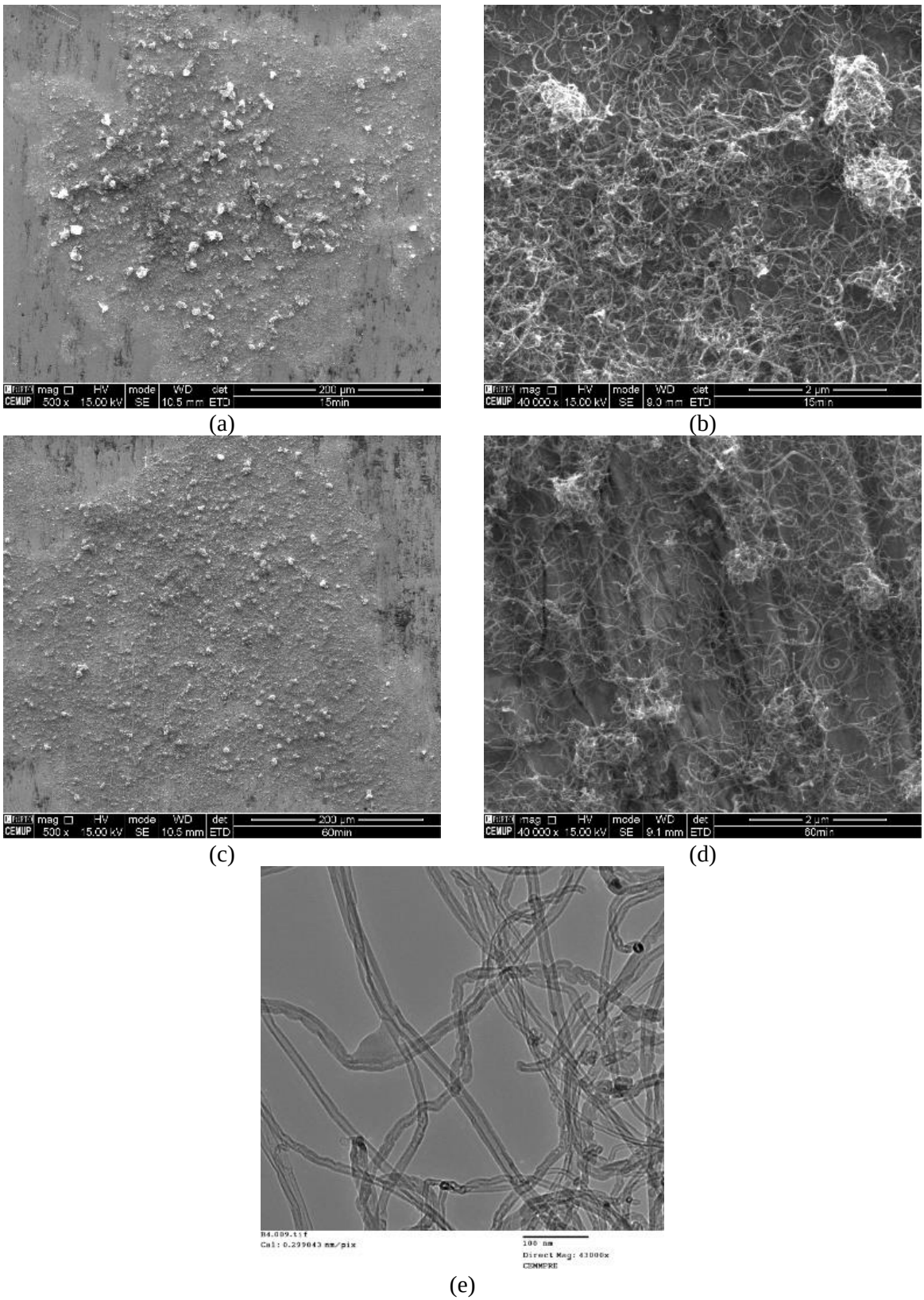

Figure 6.2 *Images from ~1.7 g/ml MWCNT in isopropanol solution treated in ultrasonication bath after 15 minutes (a) and (b), 60 minutes (c) and (d) (SEM/SE); MWCNTs dispersed in isopropanol by the assisted sonication approach (60 minutes of ultrasonication followed by a simultaneous sonication for 15 minutes of 20400 rpm) (e)(TEM).*

The ultrasonication bath itself was not able to disperse the Al powder particles with MWCNTs completely, and some Al was always deposited on the bottom of the dispersing dish. To ensure a complete dispersion a new approach, the "assisted sonication", was tested in such a way that firstly the ultrasonication bath was applied to disperse the MWCNTs in isopropanol, and secondly the Al powder, that was previously deagglomerated in a separate dish, was added and the dispersion proceeded by applying the sonication and ultrasonication simultaneously (Table 6.3). This application was not effective in increasing the hardness for the ultimate and medium speed stirring conditions (Nos. 1 and 2 in Table 6.3). It can be seen that when the dispersing speed of the final mixing step decreased, the microhardness increased slightly (No.3 in Table 6.3). It improved a little when the primary dispersing time decreased, and the dispersing speed for the second step increased (No.4 in Table 6.3).

Applying common sonication and assisted sonication resulted in a hardness increases of 8% and 14%, respectively (No. 2 in Table 6.2 and No. 4 in Table 6.3). This improvement is attributed to the dispersion and size of the MWCNT agglomerates (Figure 6.3). The largest cluster size measured in the images decreased from ~75 μm to ~20 μm by changing the dispersion methodology; however, some porosities may have been associated.

This hardness increase is still far from what should be expected and indicates, as mentioned above, that the 3S of the powder should play an important role in the strengthening.

Table 6.3. Microhardness values of Al-1 vol.% MWCNT specimens mixed by the assisted sonicated method, compacted at ~400 MPa and sintered.

No.	Conditions	HV (0.098N)	SD
1	MWCNT in Ultrasonic bath for 60 minutes, 3000 rpm for 5 min with Al, and then 20400 rpm together for 15 min cooperated by ultrasonication	36	2
2	MWCNT in Ultrasonic bath for 60 minutes, 3000 rpm for 5 min with Al, and then 11000 rpm together for 15 min cooperated by ultrasonication	36	3
3	MWCNT in Ultrasonic bath for 60 minutes, 3000 rpm for 5 min with Al, and then 1500 rpm together for 15 min cooperated by ultrasonication	38	2
4	MWCNT in Ultrasonic bath for 15 minutes, 3000 rpm for 5 min with Al, and then 11000 rpm together for 5 minutes cooperated by ultrasonication	41	2

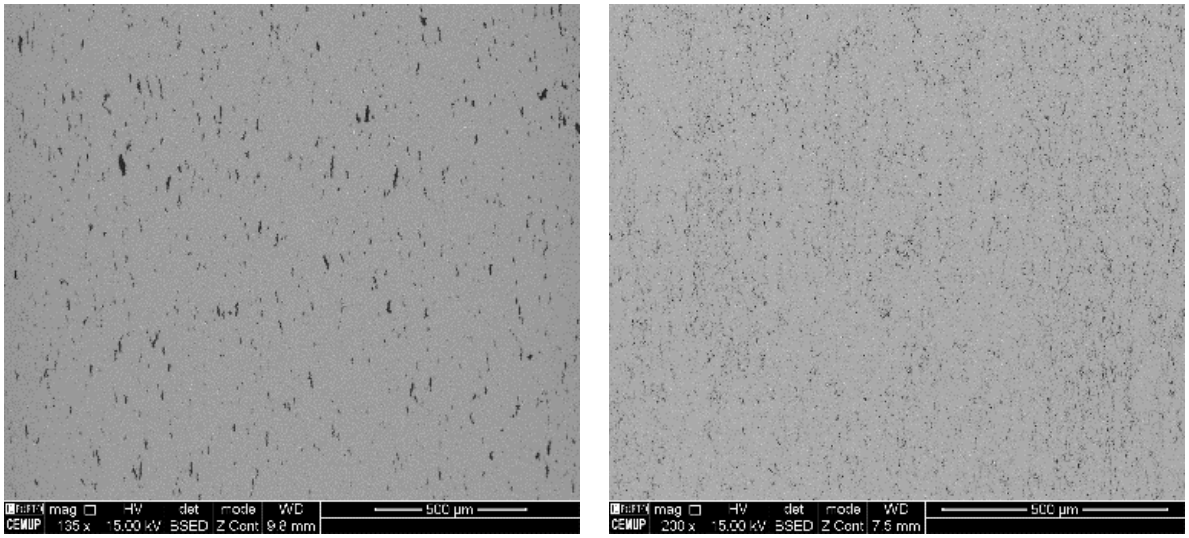

(a) (b)

Figure 6.3 *As polished cross section observations from sintered Al-1 vol.% MWCNT prepared through sonication method (No 2 in Table 6.2) (a) and assisted sonication method (No. 4 in Table 6.3) (b) (SEM/BSE).*

6.5 Raman analysis of MWCNT

Raman spectroscopy was used to evaluate the effect of the assisted sonication technique on the MWCNT, and whether the nanotubes were affected by the interaction of the Al powder during dispersion. This was carried out by testing three specimens: the pristine MWCNT, the nanotube processed by means of assisted sonication, and the Al-1 vol.% MWCNT dispersed by assisted sonication (Figure 6.4). The changes of intensity ratios of the three specimens, I_D/I_G, show a slight reduction for the assisted sonication MWCNT, and an increase for the Al-1 vol.% MWCNT mixture (Table 6.4). It was also observed that the frequency of the D band, disorder-induced feature, decreased with the sonication but remained the same for the powder mixture. The frequency of the G band, representing the tangential vibration, was upshifted after each experiment.

Table 6.4. The positions of D and G bands, and the I_D/I_G.

Specimen	**D (cm^{-1})**	**G (cm^{-1})**	**I_D/I_G**
Pristine	1365.5	1566.9	0.55
Assisted sonication	1358.3	1571.6	0.50
Assisted sonication with powder	1358.3	1578.7	0.64

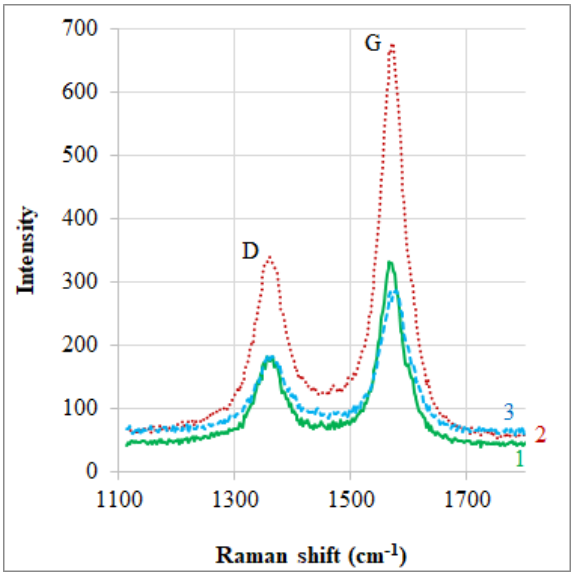

Figure 6.4 *Raman spectra, first order region, taken from pristine MWCNT (No. 1 in green), assisted sonication MWCNT (No. 2 in red), and assisted sonication Al-1vol.%MWCNT (No. 3 in blue).*

As regards the integrity of MWCNTs after applying the assisted sonication method, the MWCNT agglomerates were broken through bubble collapsing, whereby the nanotubes were forced to face a certain level of strain during the process. The Raman analysis revealed the consequences of this effect, i.e. an association of bands shifting over the entire process, and this was pronounced for the G band in the presence of the Al powder. Band shifting due to the strain has already been mentioned in related studies [11, 13, 14]. Moreover, the I_D/I_G ratio, as a criterion for determining the disorder level [15], decreased for the MWCNT in the absence of powder, and the G band upshifted a little (Table 6.4). This could mean that the assisted sonication method has acted as a sort of cleaning process, i.e. the interlocked impurities could be eliminated, thereby facilitating the tangential vibration. This study indicates that the assisted sonication seems to be less aggressive to MWCNTs than ball milling [14] and if the ratio is slightly greater than that of the ratio reported in the related study [1], this can be attributed to the associated effect of the powder characteristics (3S).

6.6 Al powder mixed with Graphene, Nanoalumina and Ultrafine WC

The ultrasonication technique is used to produce high quality Graphene nanosheets by means of liquid-phase exfoliation of graphite particles [16] and ultrasonication bath followed by probe sonication of graphene solution results in stable suspension of graphene nanosheets even after one month [17]. Based on this information and the results obtained in the dispersion of the tubes, assisted sonication was selected to disperse 1 vol.% (0.83 wt.%) Graphene nanoparticles.

The conditions chosen were those that led to better dispersion results of the MWCNT (no. 4 in Table 6.3). The same method was also used for the dispersion of 1 vol.% of nanoalumina and ultrafine WC in (1.48 and 5.60 wt.%, respectively). However, the solid concentration of the WC mixture in the isopropanol was almost 4 times greater than the other reinforcements, due to the preparation limitations.

The hardening caused by each of these reinforcements is seen in Table 6.5. The Al-WC system showed the highest hardening, although the produced composite had some porosity (the effect of any phase evolution has been ignored for the theoretical calculations). Meanwhile, the hardness of the Al-MWCNT composite is smaller than in the previous condition (No. 4 Table 6.3). This should be the effect of the lower compaction pressure used in these tests, which is also consistent with its densification value.

Table 6.5. Microhardness and densification values of Al specimens mixed with 1 vol.% of reinforcements, pressed (152 MPa) and sintered.

Material	**Pure**	**MWCNT**	**Graphene**	**Al_2O_3**	**WC**
HV (0.098)	30±1	31±2	36±1	36±1	46±2
Density (kg/m^3)	2639±21	2538±4	2633±10	2568±18	2723±10
Densification (%)	99	95	99	96	97

6.6.1 Characterization of the Al-Graphene nanocomposite

Detailed observations revealed that multilayer Graphene sheets still persist after ultrasonication, after applying the assisted sonication process with Al powder and even after sintering (Figure 6.5). However, high-resolution TEM is needed for a more precise analysis, e.g. to reveal whether the nano sheets were damaged by the process. Qualitative observations indicated that the graphene and the processing conditions did not introduce any preferential crystallographic orientation because no colour was predominant in the IPF (Figure 6.6).

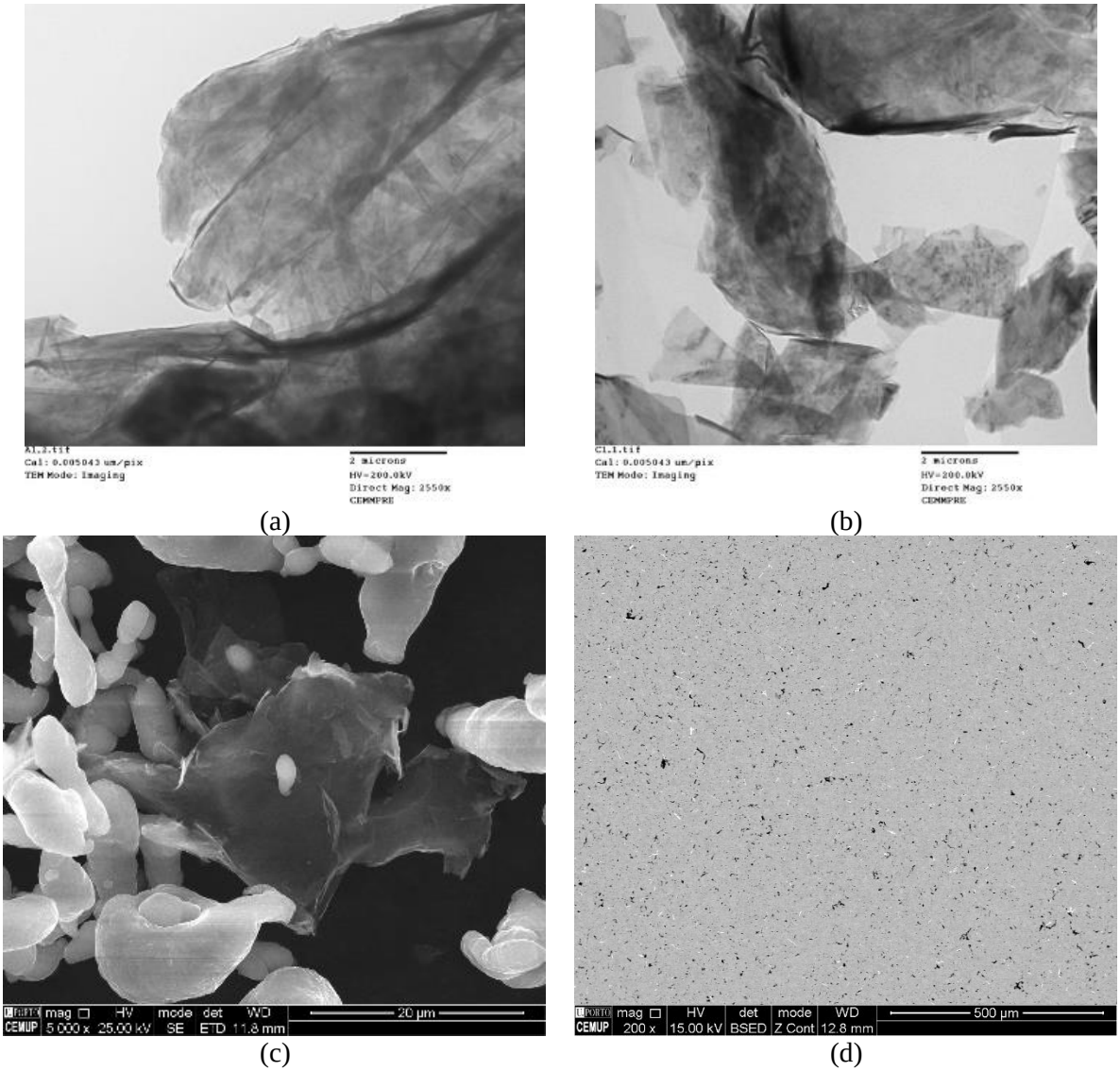

Figure 6.5 *Graphene nanosheets in different conditions: pristine (a), after 15 minutes ultrasonication (b) (TEM), agglomerates among Al powder after assisted sonication process (c) and the polished surface of the sintering Al-1 vol.% Graphene specimen (d) (SEM/SE&BSE).*

The 20% of hardness increase for the Al-Graphene nanocomposite could be attributed to the Graphene rigidity itself and the grain refinement (7.0±3.6 µm for the Pure Al to 5.7±3.1 µm for the Al-Graphene, analysed by SEM/EBSD). Related studies reported a growth in hardness of ~15% for Al composite mixed with 1 wt.% graphene nanosheets, produced by 4 hours of dispersing through ultrasonication followed by spark plasma sintering at 400 ℃ in a vacuum with the application of a uniaxial pressure of 50 MPa [18]. Some authors reported a growth of 43% in hardness for the Al composite, mixed with 0.15 wt.% exfoliated graphene nanosheets. The preparation involved 48 h dispersal by magnetic stirring of the as-prepared graphene with Al powder, compacting at 560 MPa and sintering at 600 ℃ for 4 hours in an Argon atmosphere

[19]. The difference between these reports and the results of this study (graphene nanocomposite in Table 6.5) could be attributed to the dispersion methods, characteristics of the Al powder, type and volume fraction of the graphene, and the thermomechanical history of the nanocomposites.Meanwhile, the application of the assisted sonication method for the graphene nanocomposite led to a higher hardening effect than that of the MWCNT (20% as compared with 14%).

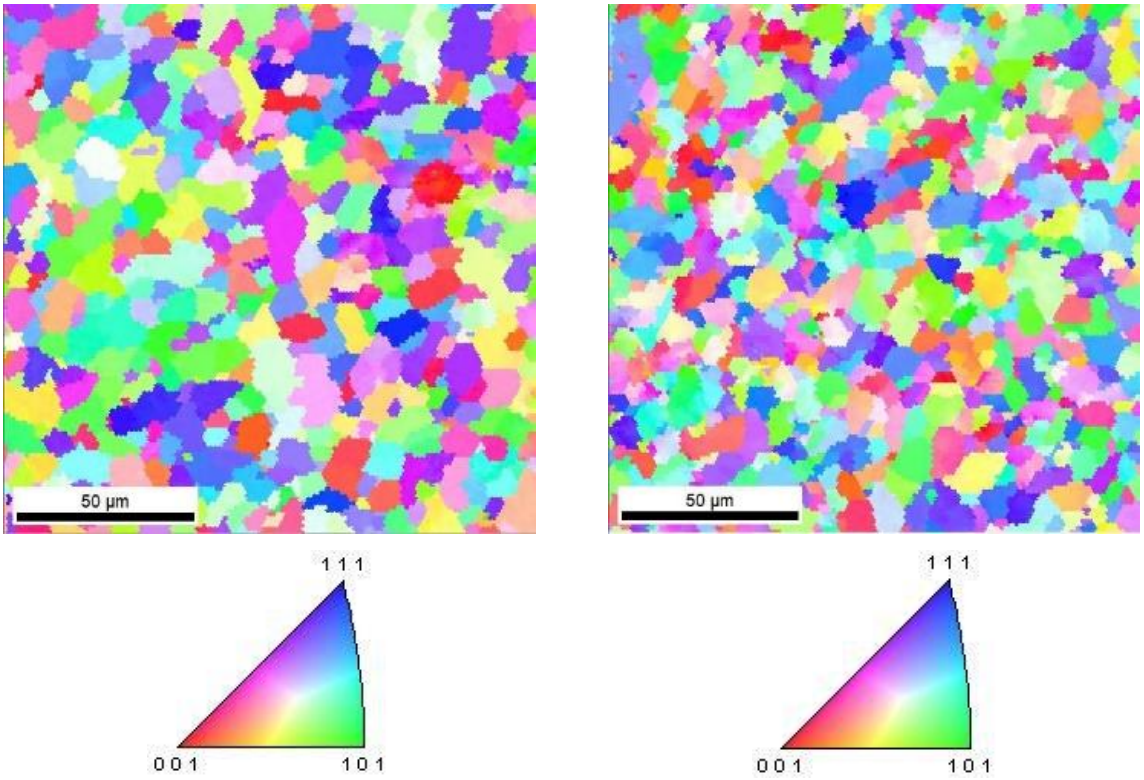

(a) (b)

Figure 6.6 *The inverse pole figures (IPF)and coded maps of the sintered pure Al (a) and Al-1 vol.% Graphene (b) (SEM/EBSD with a step size of 1.2 µm).*

6.6.2 Characterization of the Al-Al_2O_3 nanocomposite

As far as the Al-Al_2O_3 nanocomposite is concerned, although this resulted in a hardness value similar to the Al-Graphene composite, it presented a lower densification than the pure Al (Table 6.5). This reduction could be explained by the dispersion of the nanoalumina particles among the Al powder (Figure 6.7); they are seen in agglomerates as big as Al particles, and also in very fine distributions on the Al particle surfaces, i.e. they could behave as a barrier against the volume diffusion of aluminium during sintering. A related study [20] reported a hardness growth of 109% for an Al reinforced by 4 vol.% Al_2O_3. This large difference in strengthening could be related only to the volumetric portion of the reinforcement, but also to the processing

conditions (combination of wet mixing, cold isostatic pressing, sintering proceeded by hot extrusion and annealing).

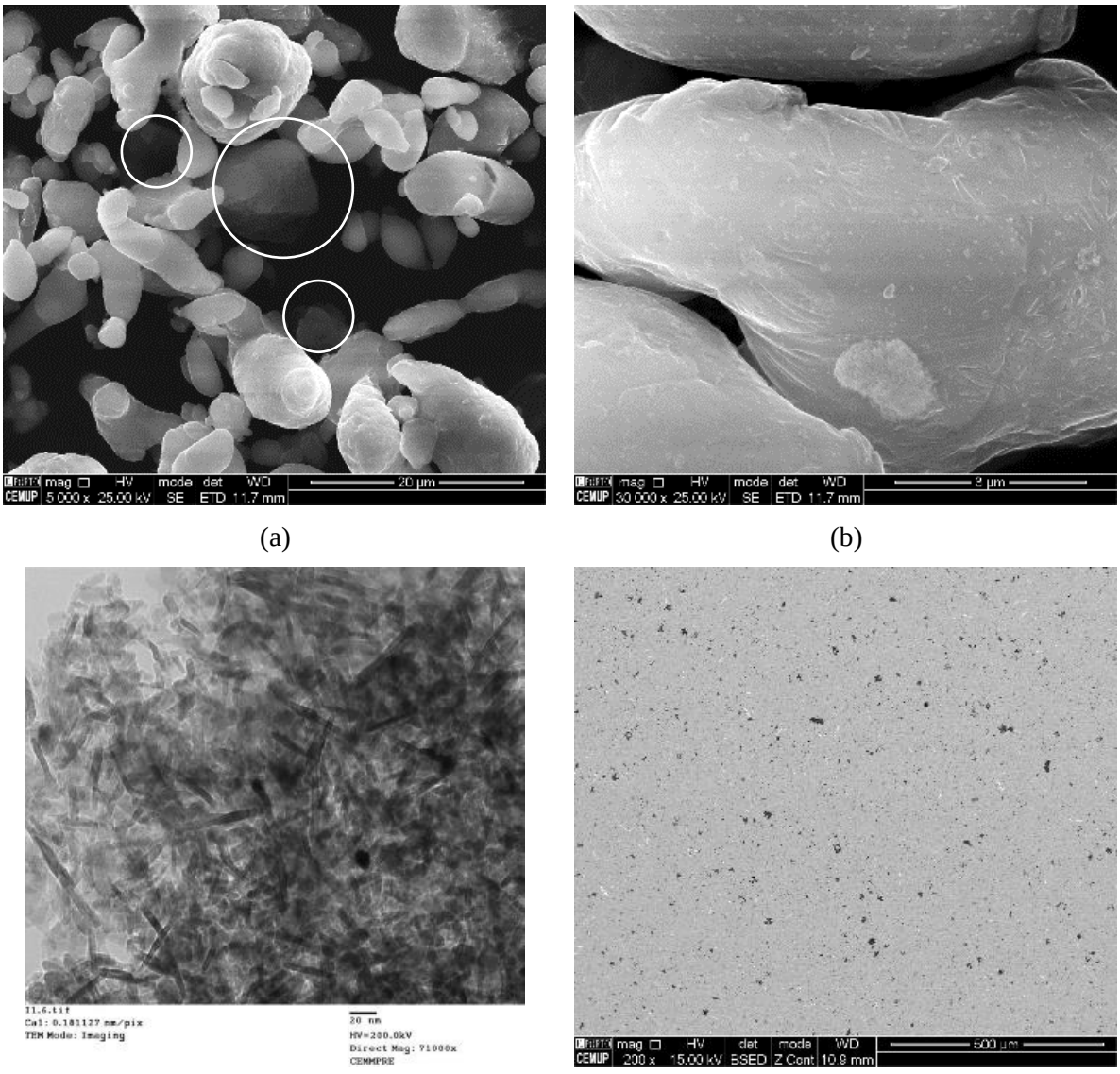

(a) (b)

(c) (d)

Figure 6.7 *Nanoalumina agglomerates (white circles) among Al powders after dispersion (a), fine distribution on the surface of individual powders (b) (SEM/SE), nanoalumina agglomerate after ultrasonication for 15 minutes (c) (TEM), as polished surface of the sintered cross section specimen (d) (SEM/BSE).*

6.6.3 Characterization of the Al-WC nanocomposite

According to microhardness measurements (Table 6.5), the Al matrix attained a hardness increase of 53% by means of ultrafine WC. This is the strongest reinforcing effect that the Al matrix received, compared to the same concentration of MWCNT, Graphene nanosheet and

nanoalumina. The relative density of the Al-WC showed incomplete densification. However, the decrease in relative density could be the effect of porosity formation and/or the formation of a new phase. In fact, when the primary mixture (Figure 6.8a) is compared to the microstructure of the sintered specimen (Figure 6.8b), it appears that the size of the second phase is larger than the WC particles and their agglomerates.

The microstructure of the Al-WC composite comprises the Al matrix with a new greyish phase, larger than the primary WC particle size, and non-reacted WC particles (Figure 6.8c).

Microscopy analyses also reveal that the new phase can contribute to the reduction of densification in respect to the pure Al.

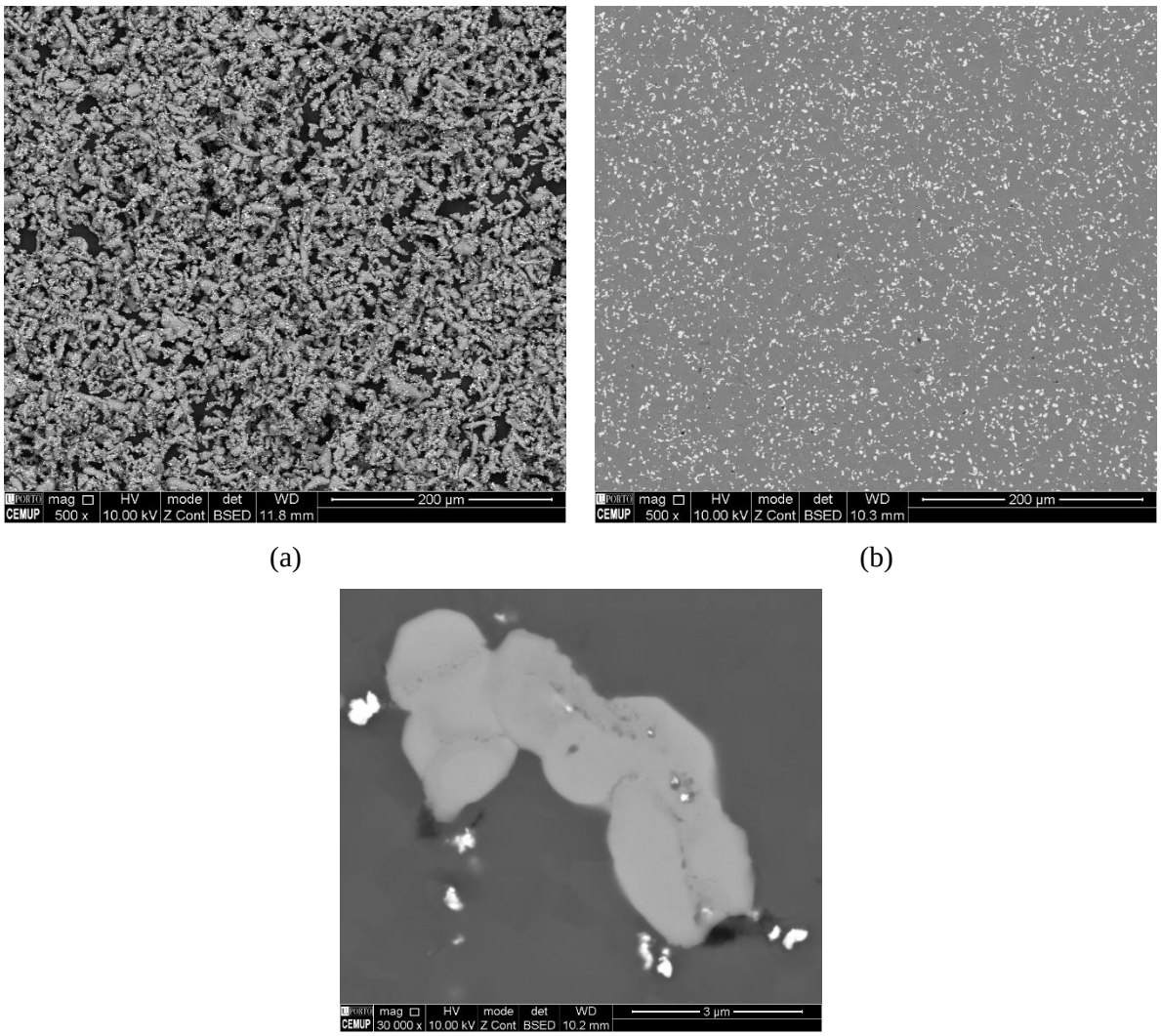

Figure 6.8 *Microstructure of the Al-WC composite before (a) and after sintering (b) and (c) (SEM/BSE).*

Figure 6.8a also reveals that the assisted sonication method has been able to disperse WC particles that are much heavier than the Al particles, although the reinforcement concentration in the dispersion solution was almost four times higher than that of the other reinforcements used in this study.

The grain size analysis, conducted using the SEM/EBSD technique, indicated a grain size refinement from 7.0±3.6 µm, for the pure Al, to 4.3±2.7 µm, for the Al-WC composite. Meanwhile, no preferential crystallography orientation was confirmed (Figure 6.9).

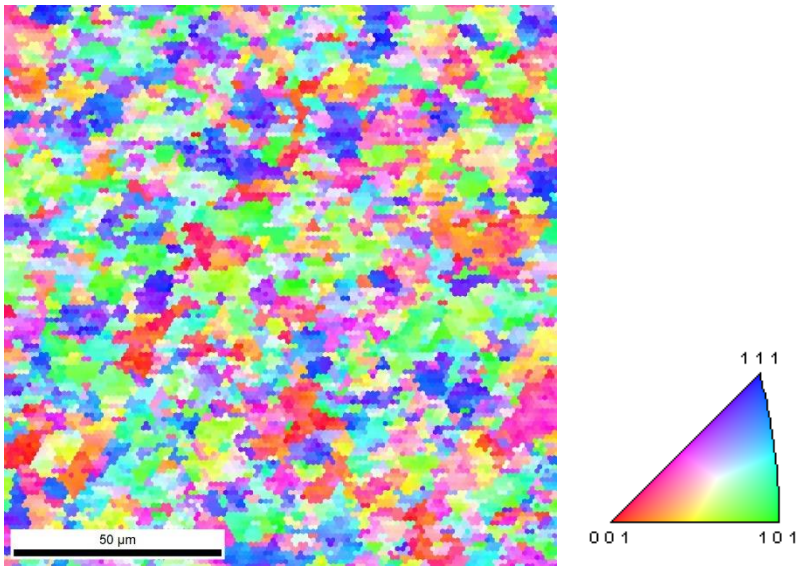

Figure 6.9 *IPF and the coded maps of the Al-WC nanocomposite on a cross section (SEM/EBSD with a step size of 1.2 µm).*

The chemical analysis map revealed the presence of only one phase, although the resolution limitation did not allow to identify finer interphases (Figure 6.10). The carbon trace is only seen in the WC position, indicating that the formed phase consists of Al and W. This phase is indicated as $Al_{12}W$, according to stoichiometry obtained by electron dispersive spectroscopy analysis, and it is consistent with other studies [21, 22].

The XRD analysis (Figure 6.11) confirmed the formation of $Al_{12}W$ (indexed by reference pattern number 00-008-0331 from ICSD files) in addition to the Al matrix and non-transformed WC (reference pattern number 00-004-0787 from ICDD, and 01-072-0097 from ICSD, respectively). However, other intermetallic can have formed in the intermediate positions [23] but the TEM analyses is needed, e.g. the dark spots in the greyish phase are not porosities (Figure 6.8c).

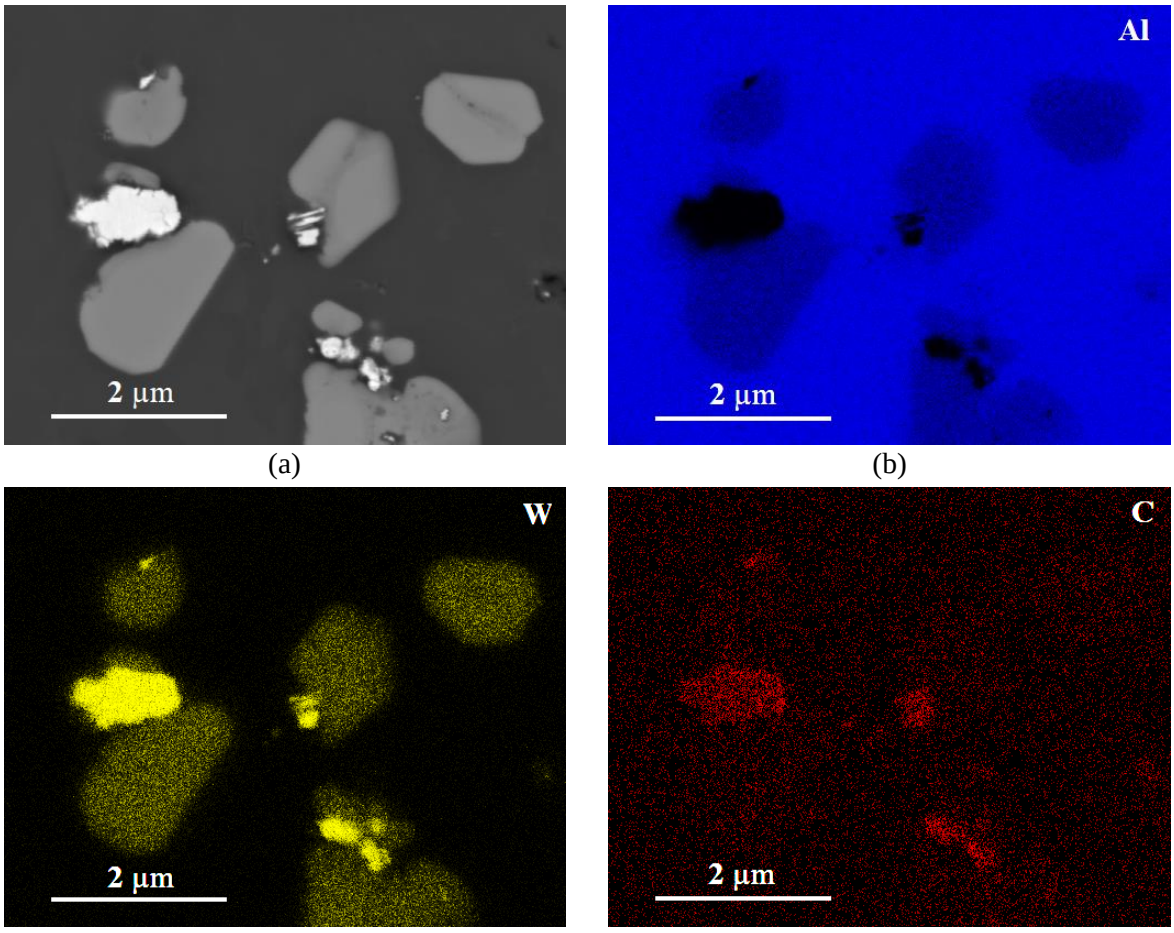

Figure 6.10 *Localized analysis maps highlighting the matrix and the reinforcing elements.*

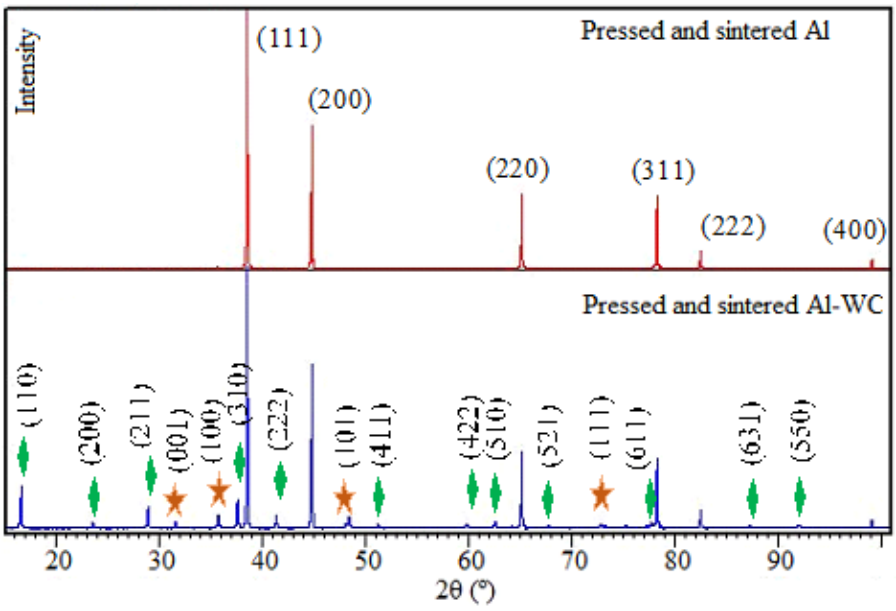

Figure 6.11 *Diffractograms showing Al peaks as well as $Al_{12}W$ (green inset) and WC (brown inset).*

Thus, the hardening effect in Al-WC can be caused by three occurrences: the grain size refinement, phase transformation, and the non-reacted dispersed WC particles.

Related studies reported the strengthening effect of the WC in the Al matrix through other PM approaches, e.g. ball milling, it being reported that the hardness increases with the increase in both the milling time and the WC content [21]; ~23% increase in the hardness obtained by 15 wt.% WC, with a reverse effectiveness caused by increasing the milling time [22]; a hardness increase of 40% by 10 wt.% WC [24]; or an incremental hardness growth resulting from increasing the amount of WC with an opposite effect on tensile strength and densification [25]. It is seen that all these high hardness increases were obtained by adding large amounts of WC through which the density is affected considerably, while the hardening effect in this study was obtained by 1 vol.%.

6.6.3.1 Mechanical properties

Pure Al was strengthened by WC maintaining much of its ductility in both flexural and extension conditions (Figure 6.12 and Table 6.6). No cracks were observed in the flexion test at the permanent deflection. The failure analyses of the tensile specimen (Figure 6.13) revealed the presence of a ductile fracture.

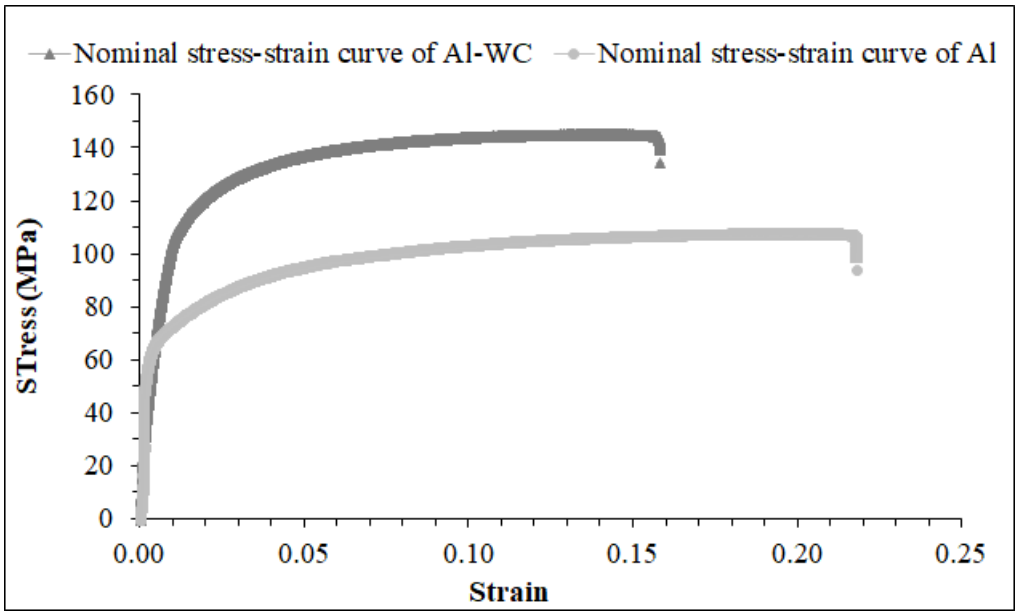

Figure 6.12 *Stress-strain curves of pure Al and Al-WC nanocomposite obtained at a strain rate of* $10^{-4}\ s^{-1}$.

Table 6.6 Mechanical properties of pure Al and Al-1 vol.% WC nanocomposite.

Composition	**Ys[36] (MPa)**	**UTS (MPa)**	**Elongation (%)**	**Flexural strength (MPa)[37]**
Pure Al	~63	110±2	19	336±1
Al-WC	~110	148±4	16	532±11

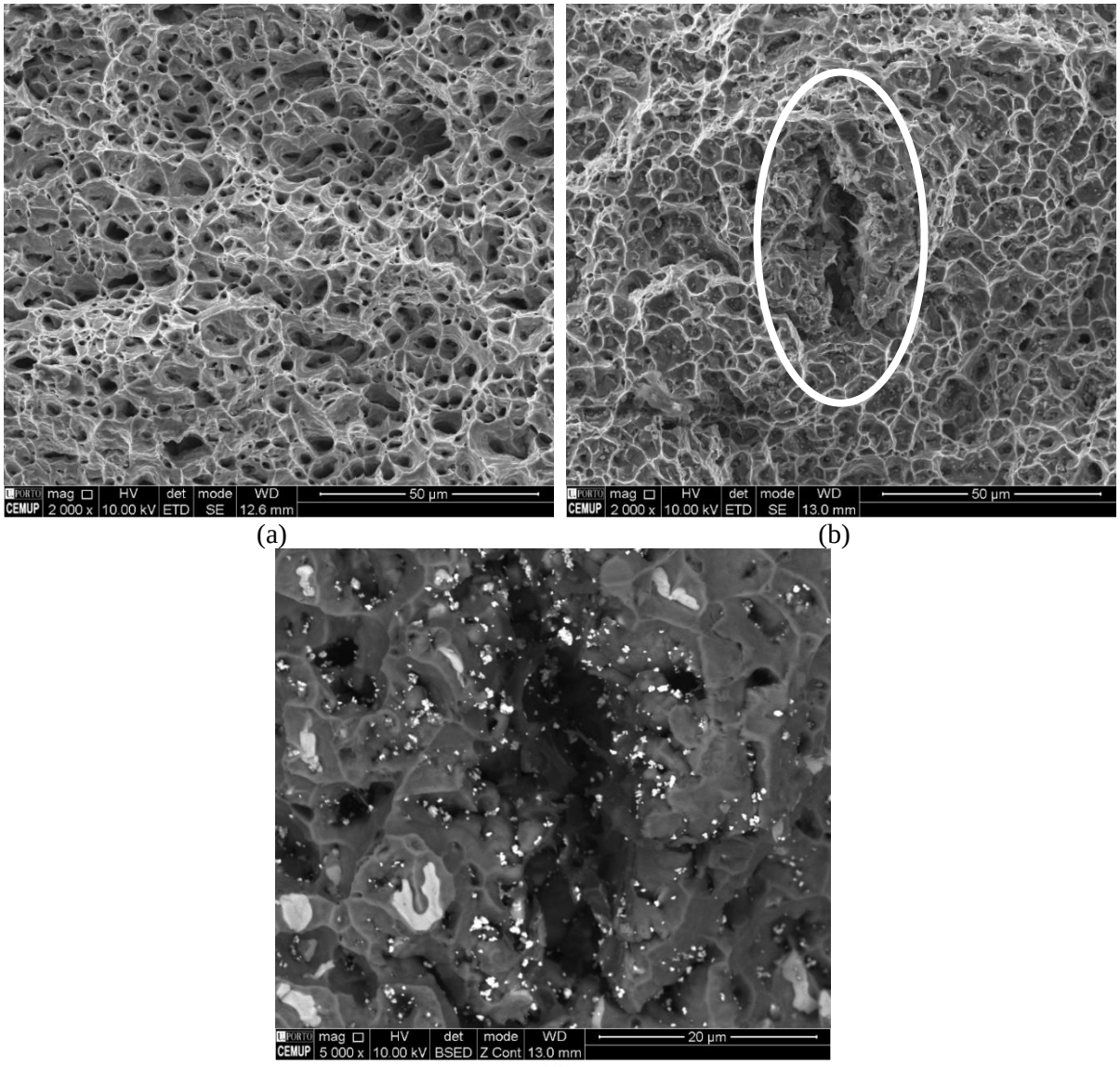

(a) (b)

(c)

Figure 6.13 *Fracture surfaces of Al (a) and Al-WC (b), high magnification of the inset in previous image showing a rupture zone (c) (SEM/SE and SEM/BSE).*

[36] Ys was determined through the 0.2% offset line on the excel file by regression method.

[37] (1.5×Force×distance between support)/(Width×Thickness^2) through 3 points bending test.

The magnification of the zone where the rupture was more evident does not indicate the presence of any new phase or even a particular concentration of the WC and $Al_{12}W$ phases.

6.6.3.2 Wear abrasion evaluation through ball cratering test

Unlike the mechanical strength, the composite did not present a good resistance to abrasive wear (Figure 6.14).

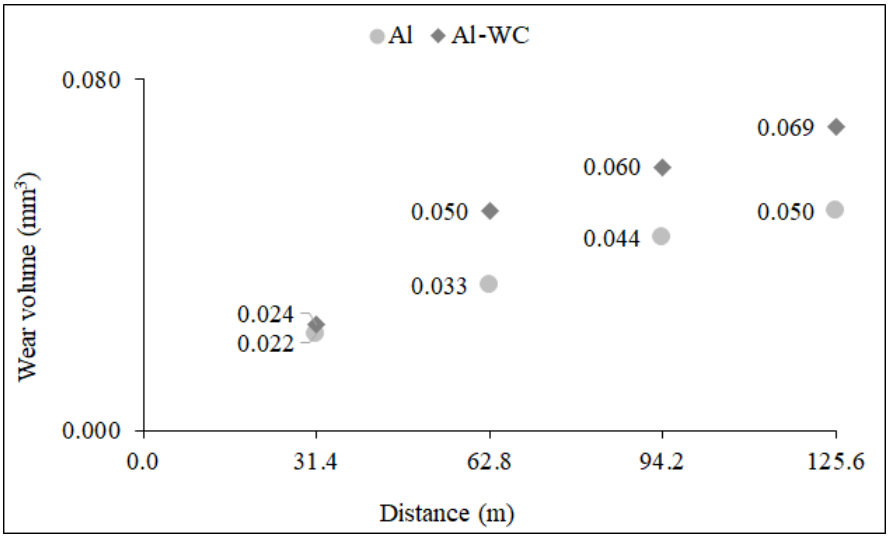

(a)

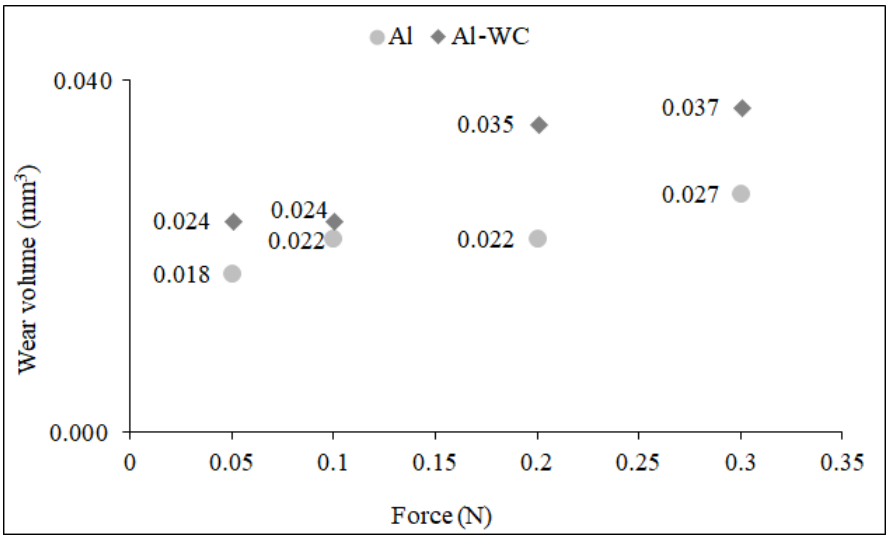

(b)

Figure 6.14 *Wear abrasive resistance[38] results for different distances at 0.1 N force (a), and for different forces during 31.4 m distance.*

[38] Test was performed at 80 rpm with a hard steel ball of 24.98 mm diameter and a 2 vol.% SiC mixture in ionized water (adapted from BS EN 1071_6_2007). The wear volume equals to 3.1416×(crater diameter^4)/(64×ball radius).

The wear mechanism was grooving for both materials, the depth of the grooves in the Al-WC composite appears larger than that of the pure Al (Figure 6.15). This shortcoming can be caused by the contribution of the hard WC particles and/or the $Al_{12}WC$ phase in the Al matrix, acting as a supplementary abrasive.

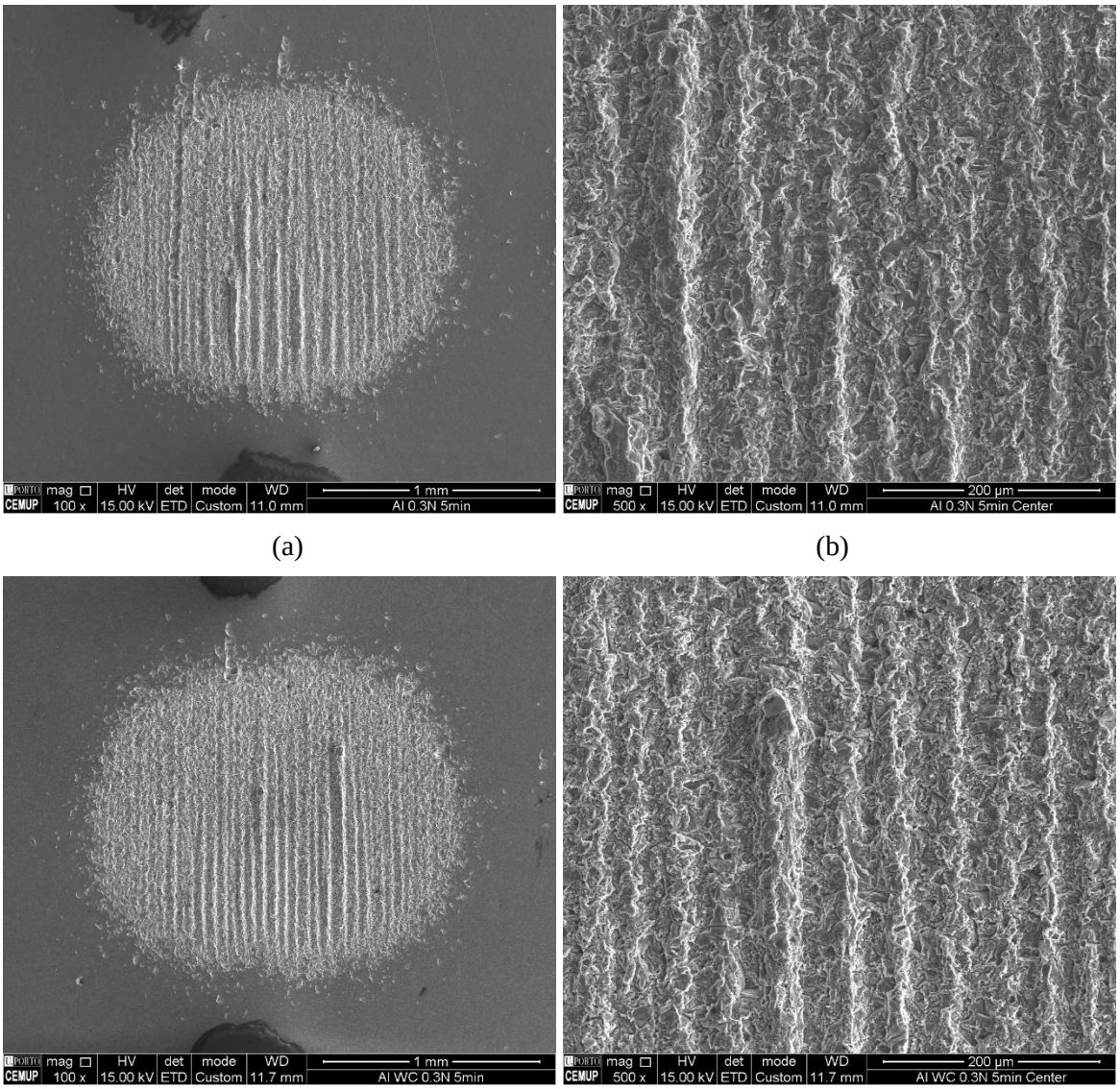

Figure 6.15 *Craters and morphology of the grooves on the Al (a), (b), and Al-WC (c) and (d) specimens for 31.4 m (5 min) with an applied force of 0.3 N.*

6.7 Conclusions

In this study, aluminium powders, with D_{50} of 10 µm, were mixed by carbon nanotubes, graphene nanosheets, nanoalumina and ultrafine tungsten carbide.

Mechanical characterization of Al–MWCNT nanocomposites reveals a weak hardening effect with the maximum hardness obtained for 0.5 wt.% MWCNT after sonication and sintering. Comparison with other studies indicates a strong influence of the aluminium powder characteristics (surface area, size distribution and shape factor, as 3S) in the mechanical response of the nanocomposite.

This study shows that sonication assisted by an ultrasonication bath is the most appropriate method for dispersing MWCNTs without causing damage. This dispersal method has been effective for dispersing the other reinforcements.

Under the same processing conditions and with similar volume percentages, the greatest hardening effect was achieved by using the ultrafine WC particles coming after by graphene nanosheets, nanoalumina and MWCNT. This was obtained by a good dispersion of dense WC in Al powder through the assisted sonication method. The strengthening can be a combination of phase formation, grain refinement, and fine WC particle dispersion.

The Al-WC composite had a ductile failure under a uniaxial tensile test and a flexural strength almost twice the pure Al. The weakening wear abrasive resistance of the composite is attributed to the role of the reinforcement components as cumulated abrasives.

References:

[1] S. Simões, F. Viana, M.A.L. Reis, M.F. Vieira, **Composite Structures**, **108** (2014) 992-1000, 10.1016/j.compstruct.2013.10.043.

[2] F. Rikhtegar, S.G. Shabestari, H. Saghafian, **Journal of Alloys and Compounds**, **723** (2017) 633-641, 10.1016/j.jallcom.2017.06.222.

[3] B. Boesl, D. Lahiri, S. Behdad, A. Agarwal, **Carbon**, **69** (2014) 79-85, 10.1016/j.carbon.2013.11.061.

[4] H. Kwon, M. Estili, K. Takagi, T. Miyazaki, A. Kawasaki, **Carbon**, **47** (2009) 570-577, 10.1016/j.carbon.2008.10.041.

[5] Z. Xia, L. Riester, W. Curtin, H. Li, B. Sheldon, J. Liang, B. Chang, J. Xu, **Acta Materialia**, **52** (2004) 931-944.

[6] P. Barai, G.J. Weng, **International Journal of Plasticity**, **27** (2011) 539-559, 10.1016/j.ijplas.2010.08.006.

[7] Q.H. Cheng, S. Debnath, E. Gregan, H.J. Byrne, **Journal of Physical Chemistry C**, **114** (2010) 8821-8827, 10.1021/jp101431h.

[8] S. Simões, F. Viana, M.A.L. Reis, M.F. Vieira, **Composite Structures**, **126** (2015) 114-122, 10.1016/j.compstruct.2015.02.062.

[9] L.J. Ci, Z.Y. Ryu, N.Y. Jin-Phillipp, M. Ruhle, **Acta Materialia**, **54** (2006) 5367-5375, 10.1016/j.actamat.2006.06.031.

[10] R.P. Bustamante, M.M. Yoshida, R.M. Sánchez, J.B. Martinez, J.G. Cantu, **Microscopy and Microanalysis**, **18** (2012) 1914, 10.1017/S1431927612011427.

[11] D. Poirier, R. Gauvin, R.A.L. Drew, **Composites Part A: Applied Science and Manufacturing**, **40** (2009) 1482-1489, https://doi.org/10.1016/j.compositesa.2009.05.025.

[12] Y.Y. Huang, E.M. Terentjev, **Polymers**, **4** (2012) 275-295, 10.3390/polym4010275.

[13] M.A.L. Reis, N.M.B. Neto, M.E.S. de Sousa, P.T. Araujo, S. Simoes, M.F. Vieira, F. Viana, C.R.L. Loayza, D.J.A. Borges, D.C.S. Cardoso, P.D.C. Assuncao, E.M. Braga, **Aip Advances**, **8** (2018) 10.1063/1.5018745.

[14] F. Ostovan, K.A. Matori, M. Toozandehjani, A. Oskoueian, H.M. Yusoff, R. Yunus, A.H.M. Ariff, **Materials**, **9** (2016) 10.3390/ma9030140.

[15] S. Costa, E. Borowiak-Palen, M. Kruszynska, A. Bachmatiuk, R.J. Kalenczuk, **Materials Science-Poland**, **26** (2008) 433-441.

[16] A. Ciesielski, P. Samori, **Chemical Society Reviews**, **43** (2014) 381-398, 10.1039/c3cs60217f.

[17] R. Durge, R.V. Kshirsagar, P. Tambe, Effect of sonication energy on the yield of graphene nanosheets by liquid-phase exfoliation of graphite, in: M.A. Xavior, P. Yarlagadda (Eds.) 12th Global Congress on Manufacturing and Management2014, pp. 1457-1465.

[18] W.M. Tian, S.M. Li, B. Wang, X. Chen, J.H. Liu, M. Yu, **International Journal of Minerals Metallurgy and Materials**, **23** (2016) 723-729, 10.1007/s12613-016-1286-0.

[19] J.H. Liu, U. Khan, J. Coleman, B. Fernandez, P. Rodriguez, S. Naher, D. Brabazon, **Materials & Design**, **94** (2016) 87-94, 10.1016/j.matdes.2016.01.031.

[20] Y.C. Kang, S.L.I. Chan, **Materials Chemistry and Physics**, **85** (2004) 438-443, 10.1016/j.matchemphys.2004.02.002.

[21] A. Evirgen, M.L. Ovecoglu, **Journal of Alloys and Compounds**, **496** (2010) 212-217, 10.1016/j.jallcom.2010.02.136.

[22] A. Simon, D. Lipusz, P. Baumli, P. Balint, G. Kaptay, G. Gergely, A. Sfikas, A. Lekatou, A. Karantzalis, Z. Gacsi, **Archives of Metallurgy and Materials**, **60** (2015) 1517-1521, 10.1515/amm-2015-0164.

[23] H.Z. Zhang, P.Z. Feng, F. Akhtar, **Scientific Reports**, **7** (2017) 10.1038/s41598-017-12302-w.

[24] S.J.A. Fabian, B. Selvam, **Journal of Mechanical Engineering and Technology**, **Volume 6 No. 2** (2014) 1-11.

[25] M. Razavi, I. Mobasherpour, **International Journal of Materials Research**, **105** (2014) 1103-1110, 10.3139/146.111126.

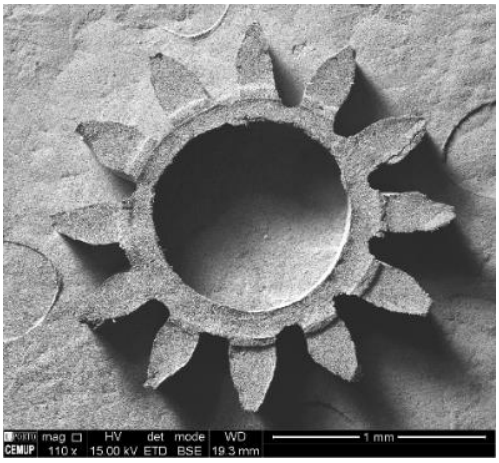

Chapter 7 – Conclusions & Future works

7.1 Conclusions

This study had aimed at producing components with microfeatures through micro hot embossing using pure Al and stainless steel 316L powders reinforced with MWCNT. The effect of the MWCNT in the following processing steps was also evaluated: feedstock preparation, shaping and sintering. The state of the art highlighted the availability of diverse information on the reinforcement of Al by this carbon allotrope by different techniques. However, there was no information on the use of a feedstock of this composite for the (μ)PIM or micro hot embossing techniques, with the exception of the polyester assisted technique for dispersing the powder and MWCNT. The processing of 316L through (μ)PIM or micro hot embossing is a more referenced subject and some studies reported the composite processing. The addition of MWCNT to the 316L feedstock for PIM and its effect on the feedstock characteristics had also been mentioned.

The used Al and 316L powders had a particle size distribution of 10 and 3.5 μm and shape factors close to one for 316L and larger than one for Al, respectively. These powders were mixed with a commercial multicomponent binder, being the volume of solids (metal powders and reinforcement) optimized by a torque mixing technique, considering the critical powder volume concentration values. Feedstocks with two compositions for the Al, 58 and 62 vol.%, and one for the 316L, 60 vol.%, stainless steel, were prepared. The stainless steel feedstock with higher solid volume, 65 vol.%, was also selected for shaping to increase the efficiency of the process. In addition, feedstocks with 1 vol.% MWCNT, replacing equal volume of powder portion in the feedstock, were prepared.

For the Al system, stearic acid was selected to decrease the feedstock viscosity. The torque values required for mixing feedstocks were affected by the powder content and additives; the stability of torque during mixing was achieved for all feedstocks. However, microscopic observations revealed that Al feedstocks required a complimentary mixing step having a single screw extrusion proved to be suitable for this purpose, since porosities were eliminated, and the powder-binder dispersion increased.

The torque mixing technique was proper to produce homogeneous 316L feedstock. The homogeneity of the feedstock was not influenced by MWCNT, being dispersed in the binder even when they had been premixed with the metallic powders. Granulation of Al feedstock was challenging; Al powders were deformed or cut when the feedstock was crushed into small particles by a commercial granulator or mortar and pestle.

At the maximum possible shaping temperature (230 ℃), whatever the pressure and holding time, the shaping was achieved with feedstock particulates smaller than 500 µm. Green parts, e.g. microblind-flanges with the maximum possible flatness, were shaped when the die cavity was partially filled and then covered by a lid, otherwise a boat-like cross section would be made.

Micro hot embossing was able to even replicate the concentric circles caused by master die turning. The shaping process confirmed that the optimized solid volume was 58 vol.% and 60 vol.% for Al and 316L feedstocks, respectively. The Al feedstock with 62 vol.% was not shaped to the microblind-flange. With regard to the shaping of the geometries in green parts, the following conclusions were obtained:

- The shaping of micro-half-flanges and microreservoirs, representing geometries with small aspect ratios, was successfully attained with Al and 316L stainless steel feedstocks.
- Microwall and microchannel, as geometries of large aspect ratio, did not follow same trend; the first failed to shape the Al feedstock and was poor for the 316L, the microchannel was shaped by both materials. Moreover, the microwall was not replicated even though the die with the most rigid elastomer (~ 64 Shore A) was used, and only a metallic die ensured good results.
- The use of a metallic die can produce green parts closer to the die than the elastomer one. With this die it is also possible to reduce the shaping conditions due to the higher thermal conductivity of the metal. A perfect demoulding was done with the application of high shaping pressure or demoulding when the die was still warm (~ 90 ℃). This method was

also able to shape the microwall using higher solid volumes (62 and 65 vol.% for Al and 316L, respectively).

- Microtensile parts were made using the most rigid elastomer, trimming was always needed.
- Shaping microgear features was only obtained by the most rigid elastomer, the concave geometry was also shaped by the 65 vol.% 316L feedstock being not sensible to segregation.
- All green parts were also made with feedstocks containing MWCNT. The nanotubes increased the demoulding efficiency for the elastomer die, although they contributed to roughness increase.
- Changes in the dimensions and roughness of green parts is the characteristic of micro hot embossing, being more pronounced using an elastomer die due to its plastic deformation during the shaping.

The effect of the composition in the shaping has the following points that deserve to be highlighted:

- The more homogeneous green parts were attained by the feedstocks granulated by the blender equipment.
- The addition of stearic acid to the Al feedstock reduced its viscosity, but deteriorated its shaping, even with the optimum feedstock composition. This addition caused a powder-binder segregation.
- The presence of MWCNT increased the homogeneity of the green parts, regardless of the die type and the metallic powder.
- Using metallic die increased the sensibility of feedstock to segregation during shaping and it required a compromise between the critical processing conditions (T, P and t). This problem was pronounced in the Al green parts.

A long thermal debinding cycle (five heating steps in total ~17 hours) was acceptable in terms of shape maintenance. However, the application of a temperature of 500 ℃ did not result in a perfect debinding efficiency, that is, some oxidation for the Al parts and some carbon residue for the 316L ones were observed.

Al brown parts, with or without MWCNT, were only sintered in high vacuum condition ($\leq 5\times10^{-3}$ Pa). The sintering mechanism at 640 ℃ involved liquid phase formation and it changed to volume transportation with the temperature decrease, 637 ℃, at the expense of shrinkage.

The maximum diagonal shrinkage, after sintering the brown parts, was only ~15%. This low efficiency was due to the oxidation of the Al powder during the thermal debinding cycle. The presence of MWCNT contributed to the porosities; they were observed mostly in aggregates and their reinforcing effect was not obtained. The nanotubes and the carbon residue of the binder contributed to the aluminium carbide formation after sintering.

The densification mechanism in high temperature sintering of Al powders was dependent on the compacting pressure, i.e. the liquid forming mechanism was activated for less compacted powders while the volume transportation functioned for high pressure compacted powders. The high vacuum is suitable for the sintering of low compacted powders, while the Ar-H_2 reducing atmosphere is efficient for highly compacted powders.

As far as the sintering of pressed 316L stainless steel powder is concerned, the application of a high compaction pressure did not ensure a perfect densification. The brown powders compacted with a low pressure were densified by almost 97%. Micro hot embossing did not change the composition of the sintered parts having these microparts presented a tensile strength of 458 MPa with 40% elongation, consistent with the bulk alloy.

Microscopic observations did not confirm the presence of MWCNTs in the 316L matrix after sintering. However, they are responsible for a cleaner microstructure in terms of carbide/oxide phase formation. This should be due to providing a more homogeneous feedstock reducing the carbon-rich zones that lead to carbide formation. Nevertheless, the mechanical properties of the 316L sintered part had benefitted by the presence of those phases. Microfeatures preserved their geometries after sintering.

This study also evaluated the strengthening of Al powder by MWCNT and other reinforcements, namely Graphene nanosheets, nanoalumina and ultrafine tungsten carbide. Sonication assisted by an ultrasonication bath has proved to be the most appropriate method for dispersing MWCNTs without causing strong damage. This dispersal method has been effective for dispersing the other reinforcements.

The pristine powder used for this study was not significantly reinforced with any of the nanometric reinforcements, even with the specially developed assisted sonication mixing technique.

Under the same processing conditions and with similar volume percentages, the greatest hardening effect was achieved by using the ultrafine WC particles coming after by graphene

nanosheets, nanoalumina and MWCNT. This was obtained by a good dispersion of dense WC in Al powder through the assisted sonication method. The strengthening can be a combination of phase formation, grain refinement, and fine WC particle dispersion. However, this composite was less wear resistant than the pure Al, grooving was the most abundant abrasive mechanism.

7.2 Future works

Despite the high number of experiments and results obtained throughout this research, there are several open questions and suggestions for future works that should be mentioned:

- The more intense use of TEM is essential to evaluate the potential formation of intermediate phases in the Al-WC composite, and to characterize the carbide/oxide phases observed in the micro hot embossed 316L stainless steel, and the small grains at the peripheral zone of sintered microgear part.
- Preparing micro hot embossed tensile parts made of the feedstock with 65 vol.% of powder to evaluate the effect of powder concentration on the mechanical properties.
- Apply cold isostatic pressure on Al green parts to eliminate possible microporosities, considering a pressure limitation to avoid powder-binder segregation.
- Use a gas flow rate greater than 0.833×10^{-5} m^3s^{-1} (0.5 ml/min) for thermal debinding cycle of Al.
- Apply hot/cold isostatic pressure on sintered Al parts after micro hot embossing.
- Use a longer ultrasonication time and maximum sonication energy to the WC, then mix this reinforcement with the Al powder using the maximum energy of assisted sonication method, followed by pressing and sintering.
- Utilize a ball mill to produce WC nanoparticles and then disperse them in Al.
- Use lower Graphene nanosheets content for Al reinforcement (e.g. 0.025 wt.%), improving dispersion using higher energy or time.
- Applying longer ultrasonication time and maximum sonication energy to nanoalumina, then mix with Al/316L powders using the maximum energy of assisted sonication method, followed by ball milling, pressing and sintering.
- Evaluate the effect of different particle size of metal powder on the strengthening, using same nanoreinforcement and processing method.
- Produce parts by micro hot embossing or (μ)PIM components using the conditions that led to the best results in the above mentioned tasks.
- Perform HRTEM analysis of compacted Al powders to evaluate the effect of compaction on the interparticles boundaries.
- Determination of kinetics of the in-situ reaction in the Al-1 vol.% WC composite.

Annex A – XRD reference files

Name and formula

Reference code:	00-033-0397
Common name:	304-stainless steel
PDF index name:	Chromium Iron Nickel
Empirical formula:	$Cr_{0.19}Fe_{0.7}Ni_{0.11}$
Chemical formula:	$Cr_{0.19}Fe_{0.7}Ni_{0.11}$

Crystallographic parameters

Crystal system:	Cubic
Space group:	Fm-3m
Space group number:	225
a (Å):	3.5911
b (Å):	3.5911
c (Å):	3.5911
Alpha (°):	90.0000
Beta (°):	90.0000
Gamma (°):	90.0000
Volume of cell (10^6 pm^3):	46.31
Z:	4.00
RIR:	-

Subfiles and Quality

Subfiles:	Inorganic Alloy, metal or intermetalic
Quality:	Star (S)

Comments

Color:	Black
General comments:	Austenitic Steel. Synthetic taenite is Ni-Fe rich analog.
Analysis:	Quantitative analysis by Atomic Absorption Spectroscopy: chromium 17.9%, nickel 11.4%, molybdenum <0.01%, silicon 0.88%.
Additional pattern:	To replace 31-619.

References

Primary reference: Pfoertsch, Ruud, Penn State University, University Park, Pennsylvania, USA., ICDD Grant-in-Aid, (1982)

Peak list

No.	h	k	l	d [A]	2Theta[deg]	I [%]
1	1	1	1	2.07500	43.583	100.0
2	2	0	0	1.79610	50.792	45.0
3	2	2	0	1.26970	74.699	26.0
4	3	1	1	1.08280	90.697	30.0
5	2	2	2	1.03680	95.968	12.0
6	4	0	0	0.89790	118.161	3.0

Stick Pattern

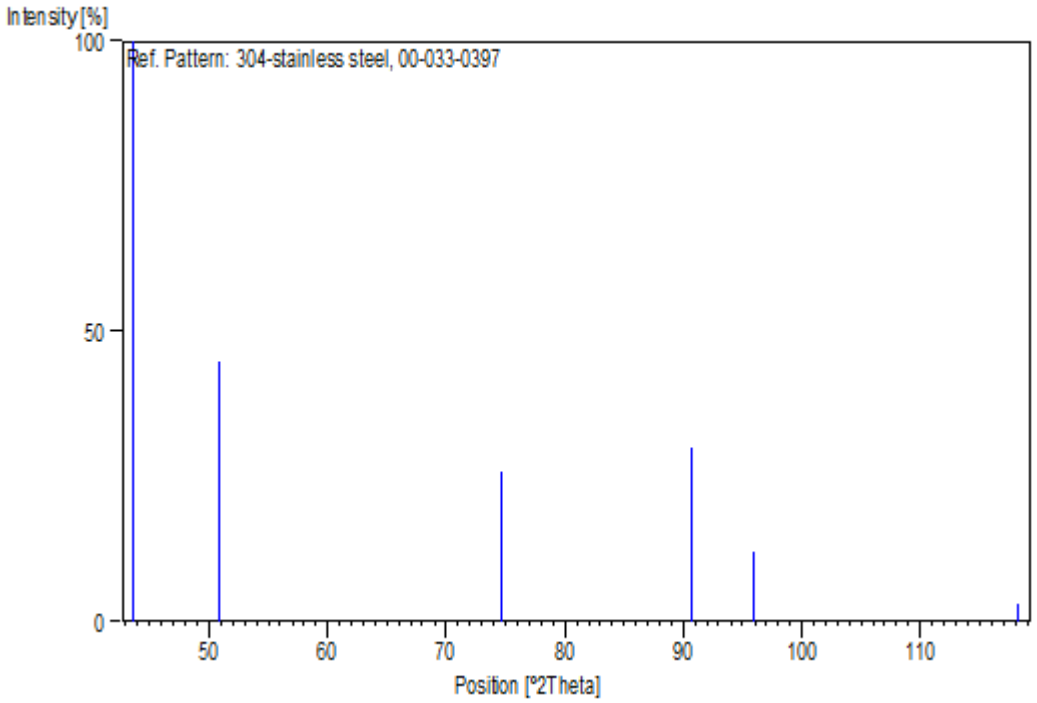

Name and formula

Reference code:	01-087-0721
Mineral name:	Iron
ICSD name:	Iron
Empirical formula:	Fe
Chemical formula:	Fe

Crystallographic parameters

Crystal system:	Cubic
Space group:	Im-3m
Space group number:	229
a (Å):	2.8662
b (Å):	2.8662
c (Å):	2.8662
Alpha (°):	90.0000
Beta (°):	90.0000
Gamma (°):	90.0000
Calculated density (g/cm^3):	7.88
Measured density (g/cm^3):	7.87
Volume of cell (10^6 pm^3):	23.55
Z:	2.00
RIR:	10.77

Subfiles and Quality

Subfiles:	Inorganic Mineral Alloy, metal or intermetalic Corrosion Modelled additional pattern
Quality:	Calculated (C)

Comments

ICSD collection code:	064998
Test from ICSD:	Calc. density unusual but tolerable. No R value given. At least one TF missing.

References

Primary reference: Calculated from ICSD using POWD-12++, (1997)
Structure: Owen, E.A., Williams, G.I., J. Sci. Instrum., 31, 49, (1954)

Peak list

No.	h	k	l	d [A]	2Theta[deg]	I [%]
1	1	1	0	2.02671	44.677	100.0
2	2	0	0	1.43310	65.028	11.5
3	2	1	1	1.17012	82.342	17.4

Stick Pattern

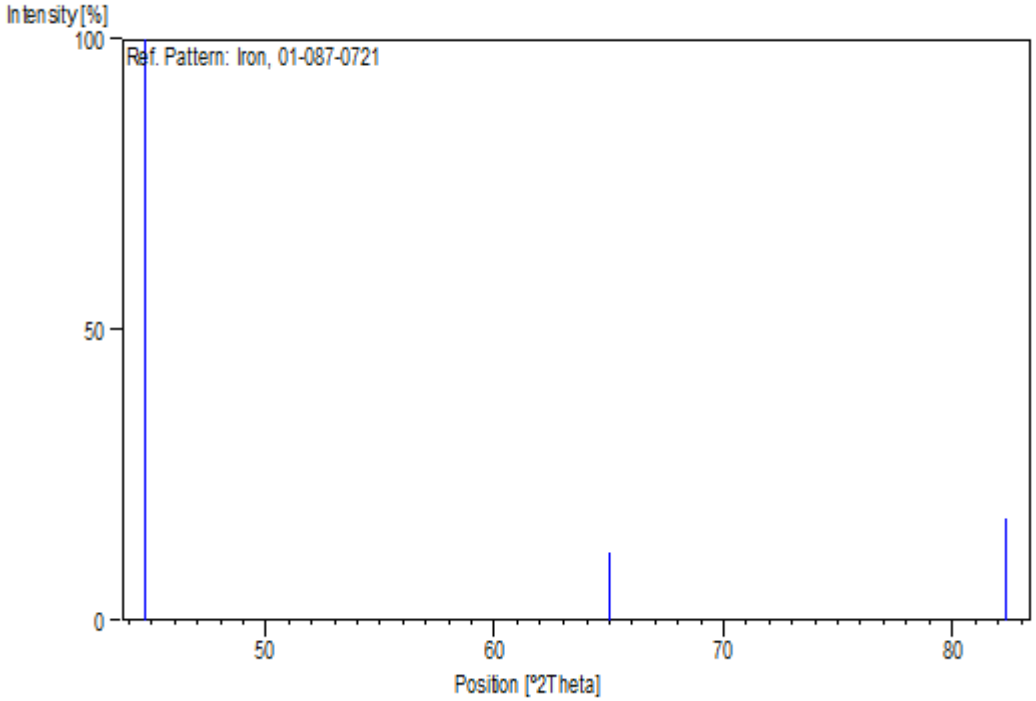

Name and formula

Reference code: 00-004-0787

Mineral name: Aluminum, syn
PDF index name: Aluminum

Empirical formula: Al
Chemical formula: Al

Crystallographic parameters

Crystal system: Cubic
Space group: Fm3m
Space group number: 225

a (Å): 4.0494
b (Å): 4.0494
c (Å): 4.0494
Alpha (°): 90.0000
Beta (°): 90.0000
Gamma (°): 90.0000

Calculated density (g/cm^3): 2.70
Volume of cell (10^6 pm^3): 66.40
Z: 4.00

RIR: 3.62

Subfiles and Quality

Subfiles: Inorganic
Mineral
Alloy, metal or intermetalic
Common Phase
Educational pattern
Explosive
Forensic
NBS pattern
Pigment/Dye
Quality: Star (S)

Comments
Color: Light gray metallic
General comments: Mineral species of doubtful validity, Am. Mineral., 65 205 (1980).

Sample preparation: The material used for the NBS sample was a melting point standard sample of aluminum prepared at NBS, Gaithersburg, MD, USA.
Analysis: The chemical analysis (%): Si 0.011, Cu 0.006, Fe 0.007, Ti 0.0001, Zr 0.003, Ga 0.004, Mo 0.00002, S 0.0001, Al 99.9+ (by difference).
Temperature: Pattern taken at 25 C.

References

Primary reference: Swanson, Tatge., Natl. Bur. Stand. (U.S.), Circ. 539, I, 11, (1953)

Peak list

No.	h	k	l	d [A]	2Theta[deg]	I [%]
1	1	1	1	2.33800	38.473	100.0
2	2	0	0	2.02400	44.740	47.0
3	2	2	0	1.43100	65.135	22.0
4	3	1	1	1.22100	78.230	24.0
5	2	2	2	1.16900	82.438	7.0
6	4	0	0	1.01240	99.081	2.0
7	3	3	1	0.92890	112.046	8.0
8	4	2	0	0.90550	116.574	8.0
9	4	2	2	0.82660	137.463	8.0

Stick Pattern

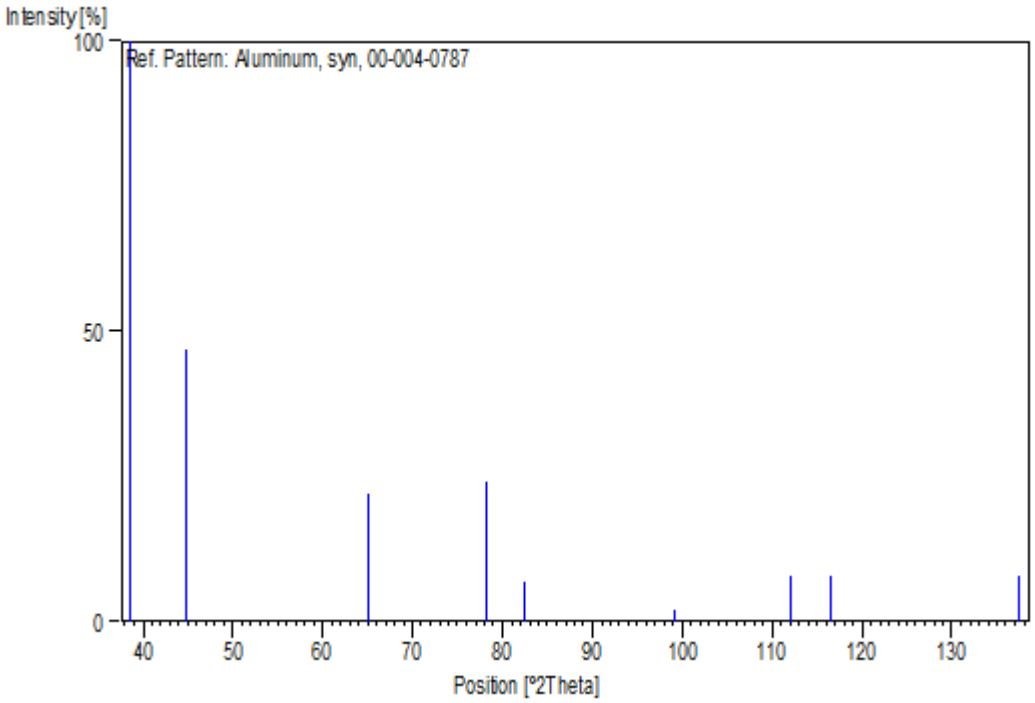

Name and formula

Reference code: 01-079-1736

ICSD name: Aluminum Carbide

Empirical formula: Al4C3
Chemical formula: Al4C3

Crystallographic parameters

Crystal system: Rhombohedral
Space group: R-3m
Space group number: 166

a (Å): 3.3350
b (Å): 3.3350
c (Å): 24.9670
Alpha (°): 90.0000
Beta (°): 90.0000
Gamma (°): 120.0000

Calculated density (g/cm^3): 2.98
Volume of cell (10^6 pm^3): 240.49
Z: 3.00

RIR: 1.07

Subfiles and Quality

Subfiles: Inorganic
Alloy, metal or intermetalic
Corrosion
Modelled additional pattern
Quality: Calculated (C)

Comments

ICSD collection code: 066751

References

Primary reference: Calculated from ICSD using POWD-12++, (1997)

Structure: Gesing, T.M., Jeitschko, W., Z. Naturforsch., B: Chem. Sci., 50, 196, (1995)

Peak list

No.	h	k	l	d [A]	2Theta[deg]	I [%]
1	0	0	3	8.32233	10.622	0.8
2	0	0	6	4.16117	21.336	8.0
3	1	0	1	2.86906	31.148	45.9
4	0	1	2	2.81387	31.775	100.0
5	0	0	9	2.77411	32.243	5.5
6	1	0	4	2.62118	34.180	0.1
7	0	1	5	2.50011	35.890	42.1
8	1	0	7	2.24457	40.142	51.5
9	0	1	8	2.11975	42.617	1.9
10	0	0	12	2.08058	43.460	8.2
11	1	0	10	1.88880	48.137	15.3
12	0	1	11	1.78460	51.143	2.1
13	1	1	0	1.66750	55.026	94.1
14	0	0	15	1.66447	55.135	51.0
15	1	1	3	1.63500	56.216	0.2
16	1	0	13	1.59924	57.589	2.1
17	1	1	6	1.54785	59.690	1.6
18	0	1	14	1.51740	61.014	6.7
19	0	2	1	1.44169	64.593	3.4
20	2	0	2	1.43453	64.955	9.1
21	0	2	4	1.40693	66.392	0.1
22	2	0	5	1.38725	67.459	7.3
23	1	0	16	1.37288	68.261	0.2
24	0	2	7	1.33855	70.266	8.4
25	0	1	17	1.30912	72.089	0.7
26	1	1	12	1.30117	72.599	8.3
27	0	2	10	1.25005	76.081	2.8
28	2	0	11	1.21840	78.429	0.5
29	1	0	19	1.19608	80.185	0.1
30	0	0	21	1.18890	80.768	0.1
31	1	1	15	1.17803	81.671	0.1
32	0	2	13	1.15421	83.731	0.5
33	0	1	20	1.14589	84.479	0.1
34	2	0	14	1.12229	86.686	1.9
35	2	1	1	1.09059	89.872	2.2

Stick Pattern

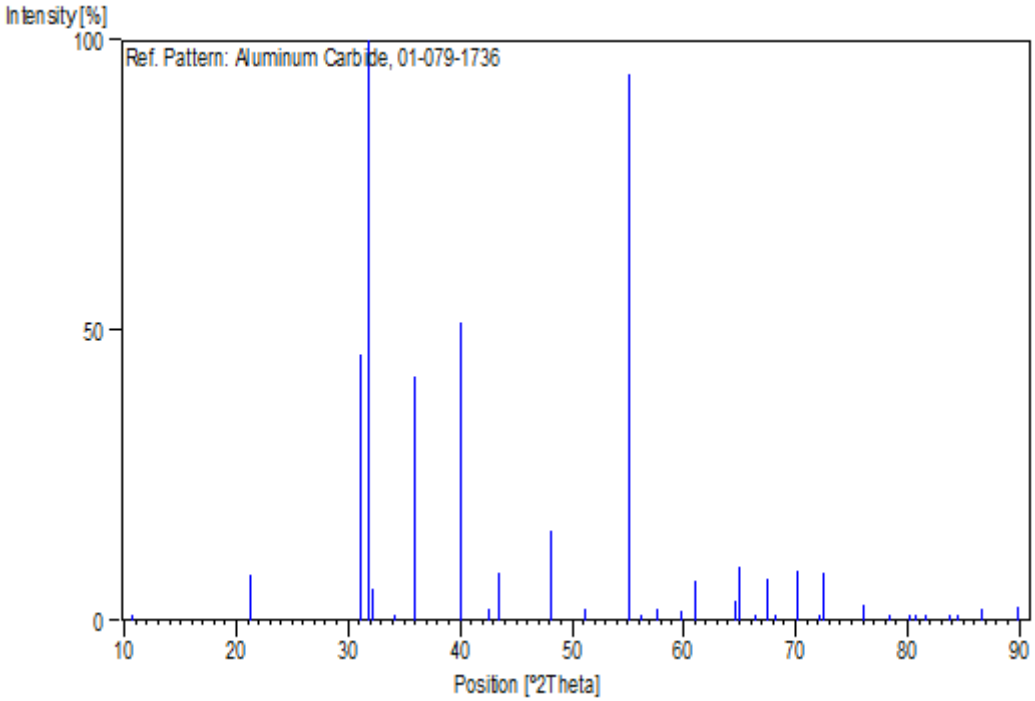

Name and formula

Reference code:	01-072-0097
ICSD name:	Tungsten Carbide
Empirical formula:	CW
Chemical formula:	WC

Crystallographic parameters

Crystal system:	Hexagonal
Space group:	P-6m2
Space group number:	187
a (Å):	2.9065
b (Å):	2.9065
c (Å):	2.8366
Alpha (°):	90.0000
Beta (°):	90.0000
Gamma (°):	120.0000
Calculated density (g/cm^3):	15.67
Volume of cell (10^6 pm^3):	20.75
Z:	1.00
RIR:	14.58

Subfiles and Quality

Subfiles:	Inorganic Alloy, metal or intermetalic Corrosion Modelled additional pattern
Quality:	Calculated (C)

Comments

ICSD collection code:	015406

References

Primary reference:	Calculated from ICSD using POWD-12++, (1997)
Structure:	Leciejewicz, J., Acta Crystallogr., 14, 200, (1961)

Peak list

No.	h	k	l	d [A]	2Theta[deg]	I [%]
1	0	0	1	2.83660	31.514	44.0
2	1	0	0	2.51710	35.640	100.0
3	1	0	1	1.88273	48.302	83.2
4	1	1	0	1.45325	64.018	15.3
5	0	0	2	1.41830	65.792	4.6
6	1	1	1	1.29339	73.106	15.2
7	2	0	0	1.25855	75.476	7.1
8	1	0	2	1.23565	77.129	13.2
9	2	0	1	1.15040	84.071	10.5

Stick Pattern

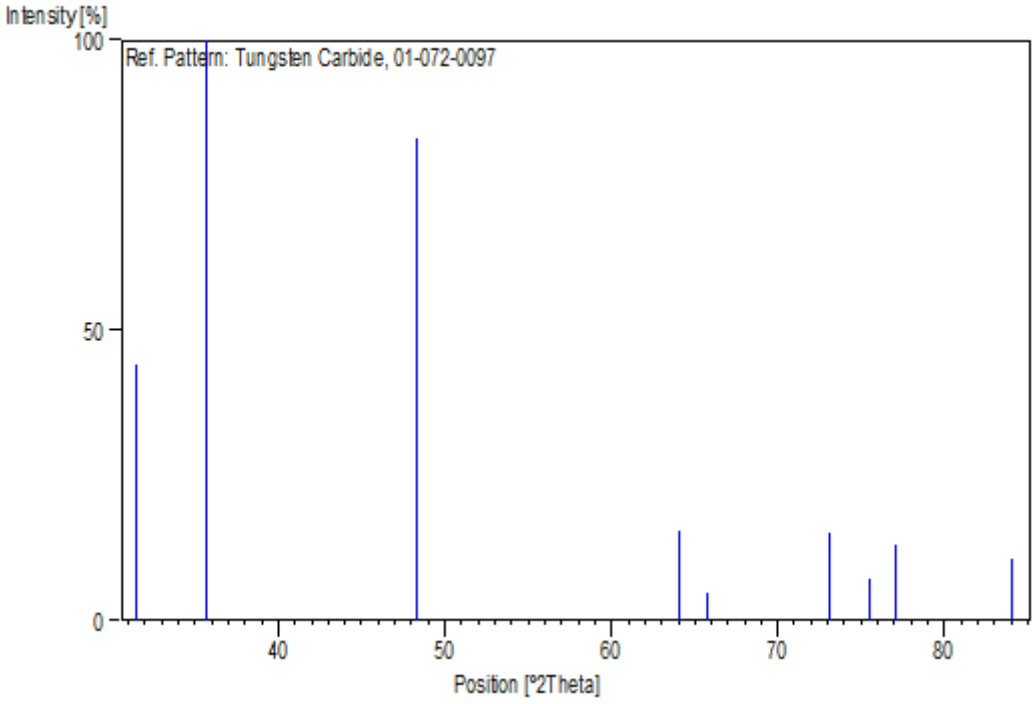

Name and formula

Reference code:	00-008-0331
PDF index name:	Aluminum Tungsten
Empirical formula:	$Al_{12}W$
Chemical formula:	WAl_{12}

Crystallographic parameters

Crystal system:	Cubic
Space group:	Im3
Space group number:	204
a (Å):	7.5803
b (Å):	7.5803
c (Å):	7.5803
Alpha (°):	90.0000
Beta (°):	90.0000
Gamma (°):	90.0000
Calculated density (g/cm^3):	3.88
Volume of cell (10^6 pm^3):	435.57
Z:	2.00
RIR:	-

Subfiles and Quality

Subfiles:	Inorganic Alloy, metal or intermetalic
Quality:	Indexed (I)

Comments

Structure:	Isomorphous with molybdenum aluminum-$MoAl_{12}$ and chromium manganese aluminum alloy-(Mn , Cr) Al_{12} .
Additional diffraction line(s):	Plus 6 additional reflections to 0.7818.

References

Primary reference:	Adam, Rich., Acta Crystallogr., 7, 813, (1954)

Peak list

No.	h	k	l	d [A]	2Theta[deg]	I [%]
1	1	1	0	5.36000	16.525	100.0
2	2	0	0	3.79000	23.454	18.0
3	2	1	1	3.09000	28.871	55.0
4	2	2	0	2.68000	33.408	6.0
5	3	1	0	2.40000	37.442	75.0
6	2	2	2	2.19000	41.187	35.0
7	3	2	1	2.03000	44.600	90.0
8	4	0	0	1.89500	47.969	14.0
9	4	1	1	1.78700	51.069	20.0
10	4	2	0	1.69500	54.060	8.0
11	3	3	2	1.61600	56.936	6.0
12	4	2	2	1.54700	59.726	20.0
13	5	1	0	1.48700	62.399	40.0
14	5	2	1	1.38400	67.639	10.0
15	4	4	0	1.34000	70.178	6.0
16	5	3	0	1.30000	72.675	30.0
17	6	0	0	1.26300	75.164	18.0
18	6	1	1	1.23000	77.549	50.0
19	6	2	0	1.19900	79.950	6.0
20	5	4	1	1.17000	82.352	10.0
21	6	2	2	1.14300	84.742	6.0
22	6	3	1	1.11800	87.102	20.0
23	4	4	4	1.09400	89.516	4.0
24	5	5	0	1.07200	91.872	30.0
25	6	4	0	1.05100	94.264	10.0
26	7	2	1	1.03200	96.562	16.0
27	6	4	2	1.01300	99.002	8.0
28	7	3	0	0.99530	101.418	6.0
29	7	3	2	0.96270	106.288	16.0
30	7	4	1	0.93310	111.284	20.0
31	8	2	0	0.91920	113.861	8.0
32	6	5	3	0.90600	116.471	30.0
33	8	2	2	0.89330	119.154	35.0
34	8	3	1	0.88120	121.889	45.0
35	6	6	2	0.86950	124.728	4.0
36	7	5	2	0.85830	127.655	20.0
37	8	4	0	0.84750	130.710	1.0

Stick Pattern